frontiers | Research Topics

Recent advances in pediatric neuroradiology

Edited by
Sahar Ahmad, Ye Wu and Yunzhi Huang

Published in
Frontiers in Pediatrics
Frontiers in Neurology
Frontiers in Radiology

ISSN 1664-8714
ISBN 978-2-8325-6462-2
DOI 10.3389/978-2-8325-6462-2

About Frontiers

Frontiers is more than just an open access publisher of scholarly articles: it is a pioneering approach to the world of academia, radically improving the way scholarly research is managed. The grand vision of Frontiers is a world where all people have an equal opportunity to seek, share and generate knowledge. Frontiers provides immediate and permanent online open access to all its publications, but this alone is not enough to realize our grand goals.

Frontiers journal series

The Frontiers journal series is a multi-tier and interdisciplinary set of open-access, online journals, promising a paradigm shift from the current review, selection and dissemination processes in academic publishing. All Frontiers journals are driven by researchers for researchers; therefore, they constitute a service to the scholarly community. At the same time, the *Frontiers journal series* operates on a revolutionary invention, the tiered publishing system, initially addressing specific communities of scholars, and gradually climbing up to broader public understanding, thus serving the interests of the lay society, too.

Dedication to quality

Each Frontiers article is a landmark of the highest quality, thanks to genuinely collaborative interactions between authors and review editors, who include some of the world's best academicians. Research must be certified by peers before entering a stream of knowledge that may eventually reach the public - and shape society; therefore, Frontiers only applies the most rigorous and unbiased reviews. Frontiers revolutionizes research publishing by freely delivering the most outstanding research, evaluated with no bias from both the academic and social point of view. By applying the most advanced information technologies, Frontiers is catapulting scholarly publishing into a new generation.

What are Frontiers Research Topics?

Frontiers Research Topics are very popular trademarks of the *Frontiers journals series*: they are collections of at least ten articles, all centered on a particular subject. With their unique mix of varied contributions from Original Research to Review Articles, Frontiers Research Topics unify the most influential researchers, the latest key findings and historical advances in a hot research area.

Find out more on how to host your own Frontiers Research Topic or contribute to one as an author by contacting the Frontiers editorial office: frontiersin.org/about/contact

Recent advances in pediatric neuroradiology

Topic editors
Sahar Ahmad — University of North Carolina at Chapel Hill, United States
Ye Wu — Nanjing University of Science and Technology, China
Yunzhi Huang — Nanjing University of Information Science and Technology, China

Citation
Ahmad, S., Wu, Y., Huang, Y., eds. (2025). *Recent advances in pediatric neuroradiology*. Lausanne: Frontiers Media SA. doi: 10.3389/978-2-8325-6462-2

Table of contents

Frontiers in Radiology

TYPE Editorial
PUBLISHED 03 June 2025
DOI 10.3389/fradi.2025.1632995

OPEN ACCESS

EDITED AND REVIEWED BY
Sotirios Bisdas,
University College London, United Kingdom

*CORRESPONDENCE
Sahar Ahmad
✉ sahar967@email.unc.edu

RECEIVED 22 May 2025
ACCEPTED 23 May 2025
PUBLISHED 03 June 2025

CITATION
Ahmad S, Huang Y and Wu Y (2025) Editorial: Recent advances in pediatric neuroradiology.
Front. Radiol. 5:1632995.
doi: 10.3389/fradi.2025.1632995

Editorial: Recent advances in pediatric neuroradiology

Sahar Ahmad[1,2]*, Yunzhi Huang[3] and Ye Wu[4]

[1]Department of Radiology, The University of North Carolina at Chapel Hill, Chapel Hill, NC, United States, [2]Biomedical Research Imaging Center (BRIC), The University of North Carolina at Chapel Hill, Chapel Hill, NC, United States, [3]School of Artificial Intelligence and Future Technology, Nanjing University of Information Science and Technology, Nanjing, China, [4]School of Computer Science and Technology, Nanjing University of Science and Technology, Nanjing, China

KEYWORDS

pediatric, neuroimaging, disease, radiology, brain development

Editorial on the Research Topic
Recent advances in pediatric neuroradiology

Pediatric neuroradiology is crucial for identifying abnormalities, tracking disease course, and planning treatment and assessing its efficacy in children and adolescents. The advancements in imaging techniques [magnetic resonance imaging (MRI), computed tomography (CT), and ultrasound (US)] and the latest integration of artificial intelligence (AI) have dramatically improved the pediatric neuroradiology field in both research and clinical practice. This Research Topic brings together novel studies that advance our current knowledge on pediatric imaging techniques, diagnostic procedures, and early brain development.

One of the key challenges in studying neonatal brain architecture is that during early postnatal period, brain tissue contrast and structural morphology (size, shape, and complexity) change dynamically. Since ultra-high field MRI at 7T effectively improves signal-to-noise ratio (SNR) and tissue contrast in adult brains, it appears to be a viable solution for neonatal brains. However, safety issues and regulatory constraints preclude 7T MRI acquisition from neonates. To account for this, Bridgen et al., proposed a safe 7T imaging protocol for neonates and demonstrated its improved performance for neonatal brain imaging.

Early personalized intervention remains a cornerstone in pediatric care and thus requires accurate disease diagnosis. Congenital hydrocephalus is one of the most prevalent neurological conditions in fetuses and neonates, and its incidence has increased in lower and middle-income countries (LMIC). MRI is a powerful diagnostic tool for this condition; however, it has limited availability in LMIC. An alternative is a portable ultra-low field MRI at 0.064 T, allowing bedside imaging. The application of this imaging technique was presented in a case report by Groteklaes et al., to diagnose pathologies in neonates born with congenital hydrocephalus. Another study (Sidorenko et al.) developed a predictive model based on measured clinical parameters and mathematically computed cerebral blood flow to stratify preterm infants at increased risk of developing intraventricular hemorrhage.

By capturing precise structural changes, neuroimaging biomarkers facilitate the detection of atypicalities early on. Ciceri et al., investigated the fetal brain gyrification process by quantifying different shape descriptors of cortical surfaces and predicted gestational age as a means to monitor normal fetal brain growth and identify deviations manifested in ill-formed cortical plate due to several pathologies such as spina bifida. Trimarco et al. studied the growth of thalamic volumes in very preterm infants and the neurodevelopmental outcomes at 2 years of age. Segmentation plays a key role in getting regional predictive markers. To this end, Xi et al., developed a deep learning segmentation model for CT scans of the 2-year-olds and analyzed region-specific volumes. In addition to macrostructural properties of the brain, microstructural properties computed from diffusion MRI are also important. Verschuur et al., assessed the feasibility of constrained spherical deconvolution (CSD) in reconstructing crossing fibers from neonatal data and also analyzed the impact of spatial and angular resolution, as well as processing parameters, on tractography and quantitative metrics.

This Research Topic also includes two review articles: (i) Shen and Zhou, discussed advancements in studying attention-deficit/hyperactivity disorder (ADHD), including insights from neuroimaging, and (ii) Zhang et al., presented a pediatric case on myelin oligodendrocyte antibody-associated transverse myelitis (MOG-TM) and discussed their findings in the context of previous observations.

To summarize, this special issue covers a breadth of topics in pediatric neuroradiology that will inform the readers about the latest advancements in neuroimaging, image analysis, brain development, and disease diagnosis.

Author contributions

SA: Writing – original draft, Writing – review & editing. YH: Writing – review & editing. YW: Writing – review & editing.

Conflict of interest

The authors declare that the research was conducted in the absence of any commercial or financial relationships that could be construed as a potential conflict of interest.

Generative AI statement

The author(s) declare that no Generative AI was used in the creation of this manuscript.

Publisher's note

frontiers | Frontiers in Radiology

TYPE Original Research
PUBLISHED 18 January 2024
DOI 10.3389/fradi.2023.1327075

High resolution and contrast 7 tesla MR brain imaging of the neonate

Philippa Bridgen[1,2], Raphael Tomi-Tricot[1,3,4,5], Alena Uus[3,4], Daniel Cromb[3], Megan Quirke[2,3], Jennifer Almalbis[2,3], Beya Bonse[2,3], Miguel De la Fuente Botella[2,3], Alessandra Maggioni[2,3], Pierluigi Di Cio[1,2], Paul Cawley[2,3], Chiara Casella[3], Ayse Sila Dokumaci[4], Alice R. Thomson[3,6], Jucha Willers Moore[3,6], Devi Bridglal[3], Joao Saravia[3], Thomas Finck[3], Anthony N. Price[2,3], Elisabeth Pickles[1,2,4], Lucilio Cordero-Grande[3,4,7], Alexia Egloff[2,3], Jonathan O'Muircheartaigh[3,6,8], Serena J. Counsell[3], Sharon L. Giles[1,2,4], Maria Deprez[3,4], Enrico De Vita[1,3,4,9], Mary A. Rutherford[2,3,6], A. David Edwards[2,3,6], Joseph V. Hajnal[1,3,4], Shaihan J. Malik[1,3,4†] and Tomoki Arichi[2,3,6*†]

[1]London Collaborative Ultra High Field System (LoCUS), King's College London, London, United Kingdom, [2]Guys and St Thomas' NHS Foundation Trust, London, United Kingdom, [3]Centre for the Developing Brain, School of Biomedical Engineering and Imaging Sciences, King's College London, London, United Kingdom, [4]Biomedical Engineering Department, School of Biomedical Engineering and Imaging Sciences, King's College London, London, United Kingdom, [5]MR Research Collaborations, Siemens Healthcare Limited, London, United Kingdom, [6]MRC Centre for Neurodevelopmental Disorders, King's College London, London, United Kingdom, [7]Biomedical Image Technologies, ETSI Telecomunicación, Universidad Politécnica de Madrid and CIBER-BBN, ISCIII, Madrid, Spain, [8]Department of Forensic and Neurodevelopmental Sciences, Institute of Psychiatry, Psychology and Neuroscience, King's College London, London, United Kingdom, [9]MR Physics, Radiology Department, Great Ormond Street Hospital for Children, London, United Kingdom

Introduction: Ultra-high field MR imaging offers marked gains in signal-to-noise ratio, spatial resolution, and contrast which translate to improved pathological and anatomical sensitivity. These benefits are particularly relevant for the neonatal brain which is rapidly developing and sensitive to injury. However, experience of imaging neonates at 7T has been limited due to regulatory, safety, and practical considerations. We aimed to establish a program for safely acquiring high resolution and contrast brain images from neonates on a 7T system.

Methods: Images were acquired from 35 neonates on 44 occasions (median age 39 + 6 postmenstrual weeks, range 33 + 4 to 52 + 6; median body weight 2.93 kg, range 1.57 to 5.3 kg) over a median time of 49 mins 30 s. Peripheral body temperature and physiological measures were recorded throughout scanning. Acquired sequences included T2 weighted (TSE), Actual Flip angle Imaging (AFI), functional MRI (BOLD EPI), susceptibility weighted imaging (SWI), and MR spectroscopy (STEAM).

Results: There was no significant difference between temperature before and after scanning ($p = 0.76$) and image quality assessment compared favorably to state-of-the-art 3T acquisitions. Anatomical imaging demonstrated excellent sensitivity to structures which are typically hard to visualize at lower field strengths including the hippocampus, cerebellum, and vasculature. Images were also acquired with contrast mechanisms which are enhanced at ultra-high field including susceptibility weighted imaging, functional MRI, and MR spectroscopy.

EDITED BY
Sahar Ahmad,
University of North Carolina at Chapel Hill,
United States

REVIEWED BY
Xianjun Li,
The First Affiliated Hospital of Xi'an Jiaotong University, China
Martina Di Stasi,
University of Naples Federico II, Italy
Yunzhi Huang,
Nanjing University of Information Science and Technology, China

*CORRESPONDENCE
Tomoki Arichi
✉ tomoki.arichi@kcl.ac.uk

[†]These authors have contributed equally to this work and share last authorship

RECEIVED 24 October 2023
ACCEPTED 29 December 2023
PUBLISHED 18 January 2024

CITATION
Bridgen P, Tomi-Tricot R, Uus A, Cromb D, Quirke M, Almalbis J, Bonse B, De la Fuente Botella M, Maggioni A, Cio PD, Cawley P, Casella C, Dokumaci AS, Thomson AR, Willers Moore J, Bridglal D, Saravia J, Finck T, Price AN, Pickles E, Cordero-Grande L, Egloff A, O'Muircheartaigh J, Counsell SJ, Giles SL, Deprez M, De Vita E, Rutherford MA, Edwards AD, Hajnal JV, Malik SJ and Arichi T (2024) High resolution and contrast 7 tesla MR brain imaging of the neonate.
Front. Radiol. 3:1327075.
doi: 10.3389/fradi.2023.1327075

Discussion: We demonstrate safety and feasibility of imaging vulnerable neonates at ultra-high field and highlight the untapped potential for providing important new insights into brain development and pathological processes during this critical phase of early life.

KEYWORDS

magnetic resonance imaging (MRI), ultra-high field MRI, neonate, infant, brain, neuroradiology

Introduction

During the neonatal period (the time of birth and the first few weeks of postnatal life), the human body undergoes a series of highly programmed yet rapid sequences of physiological and anatomical maturation which enable adaption to the demands of the new ex utero environment. In this critical juncture, dramatic developmental changes are similarly seen within the human brain, as the cortex rapidly expands and folds and axonal projections proliferate within the white matter (1), neurotransmitter action and receptor density evolve (2), and distinct correlated network patterns of functional activity emerge (3). The fundamental importance of this period is emphasized by the effects of congenital or acquired perinatal brain pathology, which invariably result in life-long alterations in brain structure and function and can lead to later neurodisability. Furthermore, multiple lines of evidence now suggest that the previously unknown underpinnings of the brain abnormalities that underlie mental health disorders and neurological diseases in adulthood also likely begin in the perinatal period, well before symptoms or behavioural difficulties manifest later in life (4). There is therefore a clear need for tools which can not only accurately identify pathology in the neonatal period but can also act as novel biomarkers for later outcome and provide mechanistic insight into pathophysiological processes to inform potential treatments.

In recent years, MR imaging at ultra-high field [7 Tesla (T) or higher] has become increasingly used in adult subjects due to the significant gains in signal-to-noise-ratio (SNR) and differences in tissue contrast it offers over standard MR systems (1.5 or 3T) (5). The increased SNR can then be used to increase image resolution whilst maintaining image quality. This has proved to be particularly clinically beneficial for enhancing diagnosis and understanding about diseases which affect the cortex such as drug-resistant focal epilepsy where no relevant lesion has been identified at standard field strengths (6) and cerebral vasculature such as small-vessel stroke (7). Furthermore, numerous studies have demonstrated that ultra-high field imaging can provide profound new insights into brain physiology, particularly using contrast mechanisms based on magnetic susceptibility such as blood-oxygen-level-dependent (BOLD) functional MRI (fMRI), where the increased sensitivity and spatial specificity enable characterization of neural activity at a cortical laminar level (8); and Magnetic Resonance Spectroscopy (MRS) where there is improved separation of overlapping frequency peaks (9). Imaging at 7T for neonates is therefore a compelling prospect, as it could theoretically enable more detailed visualization of key developing brain structures, improved understanding about pathophysiological processes, and reduced prognostic uncertainty.

Despite the likely benefits, regulatory barriers and safety concerns have thus far prevented widespread application of 7T MR imaging in neonates, with only a single study previously demonstrating feasibility (10). Furthermore, detailed safety modelling has demonstrated that careful planning is required as there are higher risks associated with increased specific absorption rate (SAR) and temperature instability in neonates compared to adults under the same conditions at 7T (11). A further consideration is that the composition of neonatal brain tissue differs markedly from that of the mature adult brain, and thus image acquisition sequence parameters must be adapted accordingly to account for significantly different field-dependent tissue relaxation times (12). With these factors in mind, we aimed to establish a 7T imaging program for neonates following a comprehensive safety assessment. We describe our resulting safety approach, initial experiences, and results, and demonstrate the potential gains in anatomical and pathological sensitivity for the neonatal population.

Materials and methods

All examinations took place on a Siemens Magnetom Terra 7T system (Siemens Healthineers, Erlangen, DE) in the London Collaborative Ultra-high field System (LoCUS) centre at St Thomas' Hospital London. National ethics committee approval (NHS REC: 19/LO/1384) was attained for the work and all images were acquired following parental consent.

Safety

Previous neonatal modelling suggests that close monitoring of infant body temperature is imperative for MRI scanning, as neonates can become rapidly hypothermic if not sufficiently insulated (due to reduced subcutaneous fat in comparison to adults) (13) or could become hyperthermic due to systemic heating inherent in prolonged radiofrequency (RF) exposure (11, 14). The latter is an important consideration at ultra-high field as in addition to their small body size, the higher water content of neonatal tissue leads to significantly different dielectric properties in comparison to adults. Taking this into account, a recent detailed RF safety simulation using a head-centered model within a local transmit coil of the generic type deployed in the Siemens Terra scanner, has shown that SAR is likely elevated in neonates at ultra-high field in comparison to adults being scanned under the same conditions (11). This is in contrast to lower field strengths (3 Tesla or less) where heating was predicted to be less. As the study for 7T indicated that systemic (rather than localized) heating posed the most likely risk, further mitigation was achieved by mandating continuous monitoring of axillary temperature in addition to heart rate and oxygen saturation throughout the examination. This was achieved using a Philips Invivo Expression MR400 monitor (Philips Healthcare, Gainesville, FL) which was tested to verify safety/efficacy for use at 7T (15).

To further mitigate the risk of potential temperature effects and following a local risk assessment, the scanner software was modified for imaging neonates to use a more conservative SAR estimation. Following IEC guidelines (60601-2-33) the head-average SAR is subject to a limit of 3.2 W/kg and local 10 g averaged SAR is subject to limits of either 10 W/kg or 20 W/kg when operating in normal or first level controlled modes respectively, as selected by the operator. SAR is estimated within the scanner software by multiplying measured RF power (P_{RF}) by a multiplicative factor (k) fixed within the scanner software. This factor is typically determined by simulation, but is only valid for the range of body types/positions simulated by the manufacturer. Since for larger subjects the local SAR is expected to be the limiting factor, the Siemens Terra scanner is configured to actively control local SAR (not head averaged SAR) when the head coil is used. However, our simulation study (11) suggested that as power is increased, the limiting factor for neonates would actually be head-averaged SAR exceeding the 3.2 W/kg limit. To account for this we modified the k value within the scanner to take a value of 2.8, which we calculated would mean that the head-averaged SAR would not exceed IEC guideline limits. Further details are given in Appendix 1. A robust process was developed to allow this configuration change to occur safely: software changes result in the displayed name of the coil changing (as a visual check) and then updated SAR estimates are experimentally confirmed by scanning a phantom before and after switching. The process is set out using a detailed checklist which must be signed-off before each scanning session by two authorized personnel.

Acoustic noise testing was carried out using an OptiSLM device (Optoacoustics Ltd, Israel) to measure the sound pressure level (dBA) of each acquisition sequences whilst scanning a phantom with the microphone attached to the phantom (*measured sound pressure levels associated with each sequence are detailed within* Table 1). The maximum sound pressure level recorded for the sequences used was 95 dBA.

Image acquisition

Images were successfully acquired from 35 neonates (24 male) of median postmenstrual age at scan: 40 + 0 weeks (range 33 + 4–52 + 6 weeks); median gestational age at birth: 35 weeks (range 27 + 64–42 + 1 weeks); median body weight at scan: 2.9 kg (range 1.64–5.3 kg) (*study population details can be seen in* Table 2, *with individual clinical diagnoses outlined in the* Supplementary Table). Examinations took place on 44 occasions lasting a median total of 49 min 30 s (range 20–77 min), with 41 min 15 s of active scanning when the full core protocol was completed. 9 infants were imaged both in the preterm period and at term equivalent age; and one infant with congenital heart disease was imaged both pre-operatively and post-operatively. 18 infants additionally had images acquired on a 3T system (Achieva, Philips, Best NL) with 32ch receive head coil, with a further subset of 5 infants having the 3T scan within 24 h of the 7T scanning session for direct comparison. T2 images were acquired on the 3T system with a turbo spin echo (TSE) sequence with parameters 0.8 mm × 0.8 mm × 1.6 mm, TR/TE 12,000/156 ms and a SENSE factor of 2.11. This corresponds to an overall reduction in voxel volume of factor 2.4 in comparison to those acquired on the 7T system. All Images were reviewed by experienced neonatal neuroradiologists (AE, JS, TF, MAR).

Participants were positioned supine headfirst in the isocenter of a 1TX-32RX Nova head coil with the aid of foam and inflatable pads (Pearltec, Zurich CH) to help reduce head movement and to ensure that maximum signal was received from all elements of the head coil. Participants were scanned during natural sleep following feeding and were then swaddled and immobilized inside 2 pre-warmed blankets and a vacuum evacuated bag (Pearltec, Zurich CH). Hearing protection was applied using molded dental putty in the external auditory meatus (President Putty, Coltene Whaledent, Mahwah, NJ, USA) which provides 22dB of acoustic protection (16). Together with additional acoustic protection from the inflatable pads (~7 dB), the combination brings sound pressure levels to well below those defined in UK MHRA guidance (https://assets.publishing.service.gov.uk/government/uploads/system/uploads/attachment_data/file/958486/MRI_guidance_2021-4-03c.pdf). Two infants with congenital cardiac disease were receiving a continuous intravenous prostaglandin E1 (PGE1) infusion (with the infusion pumps outside the examination room) during image acquisition to maintain patency of the ductus arteriosus. All scans were supervised by experienced clinical staff (a doctor and nurse) with appropriate training in neonatal care and resuscitation who also reviewed the neonates' temperature and vital sign measurements throughout scanning.

In all infants, the following were acquired high-resolution 2D T2-weighted images (T2W) in at least 2 orthogonal planes, mid brain and cerebrum, MR spectroscopy (MRS) including metabolite T1 estimation, 3D susceptibility weighted imaging (SWI), and Blood Oxygenation Level Dependent (BOLD) functional MRI (fMRI) were acquired. Actual Flip angle Imaging (AFI) B_1^+ mapping (17) was obtained in 15/44 cases (due to time constraints). Sequence parameters were selected initially from those optimized at 3T for the developing Human Connectome Project (18) and were then iteratively adapted to maximize SNR and resolution (*parameters for all acquisitions are detailed in* Table 1).

To address intra-volume motion artifacts, as well as provide increased signal-to-noise ratio (SNR) and image resolution, T2

TABLE 1 Acquisition sequence parameters.

Sequence	Resolution (mm)	FOV frequency	TR (ms)	TE (ms)	Acceleration factor	FA (deg)	Other parameters	Acquisition time (min)	Measured sound pressure level (dBA)
Localizer	0.7 × 0.7 × 5.0	250 × 250 mm	4,000	107	GRAPPA 4	115		0:22	92.0
B0 map	5.0 × 5.0 × 5.0	210 × 220 mm	10.0	1.02, 2.26, 4.08	none	10		019	95.0
T2—axial	0.6 × 0.6 × 1.2	141 × 151 mm	8,640	156	GRAPPA 2	120	–	2:37	93.3
T2—sagittal	0.6 × 0.6 × 1.2	154 × 125 mm	8,640	156	GRAPPA 2	120	–	3:12	90.8
T2—coronal	0.6 × 0.6 × 1.2	154 × 125 mm	8,640	156	GRAPPA 2	120	–	3:29	94.7
AFI	2.2 × 2.2 × 3.0	140 × 140	141	1.93, 3.62, 9.00	GRAPPA 3	60		1:54	90.5
MRS (STEAM)	16 × 16 × 16	–	3,000	20	none	90	TM = 10 ms	2:45	60.0
BOLD fMRI (GRE-EPI)	1.0 × 1.0 × 1.0	125 × 125 mm	2,560	43	GRAPPA 3 Multiband 3	90 (exc) 110 (deg)	–	7:26	94.2
Susceptibility weighted imaging (SWI)	0.2 × 0.2 × 1.2	122 × 150 mm	22	15	GRAPPA 3	15	–	2:12	95.2

FOV, field of view; TR, repetition time; TE, echo time; FA, flip angle; TI, inversion time; GRAPPA, GeneRalized autocalibrating partial parallel acquisition; TM, mixing time; STEAM, STimulated echo acquisition mode; AFI, actual flip-angle imaging; GRE-EPI, gradient echo echo planar imaging.

TABLE 2 Summary clinical characteristics of the patient population imaged on the 7 tesla MR system.

Total number of examinations	44
Total number of subjects (sex)	35 (24 male; 11 female)
Median gestational age at birth in weeks + days (range)	35 weeks + 0 days (range 27 + 6–42 + 1)
Median post-menstrual age at scan in weeks + days (range)	40 weeks + 0 days (range 33 + 4–52 + 6)
Median weight at scan in kg (range)	2.9 kg grams (range 1.6–5.3 kg)
Median head circumference at scan in cm (range)	34 cm (range 28–39.5 cm)
Clinical background:	
Healthy control delivered at full term	5
Preterm birth	17
Congenital cardiac disease	5
Antenatally diagnosed brain abnormality	5
(agenesis of the corpus callosum; ventriculomegaly; congenital viral infection)	
Other (hypoxic ischaemic injury, intracerebral hemorrhage, inherited metabolic disease)	3
Median total examination duration in minutes, second (range)	49 min 30 s (range 20–77 min)

images of different orientations were combined into a single high-resolution volume with isotropic resolution 0.45 mm using Slice to Volume Reconstruction (SVR) as implemented in SVRTK (https://svrtk.github.io). Each acquired image was split into odd and even stacks of slices, and heavily motion corrupted resulting stacks were excluded after visual inspection. Remaining stacks were co-aligned using volumetric registration and reconstructed into a single isotropic volume using a super-resolution algorithm (19). Reconstructed images were then tissue segmented, region parcellated and surfaces generated using the developing Human Connectome Project (dHCP) structural pipeline (https://github.com/BioMedIA/dhcp-structural-pipeline) (20). Native and SVR image quality were assessed by visual review of the T2-weighted images with two reviewers (PB, TA) using a grading system of 1–4 previously used in the dHCP (20): where (1) is a poor quality image, (2) is an image with significant motion artifact, (3) is an image with negligible motion artifact; and (4) is a good quality image (*example images shown in* Figure 1A).

BOLD fMRI resting state networks were delineated following standard preprocessing steps including rigid body motion correction, high pass temporal filtering, slice time correction, and spatial smoothing (Gaussian filter of full-width half maximum 3 mm) and using independent component analysis (ICA) as implemented in MELODIC v3.0, part of the FSL software library (www.fmrib.ox.ac.uk/fsl) (21). Minimum intensity projection (MIP) images were prepared from the magnitude and phase SWI data using CLEAR-SWI (22). Metabolite concentrations were estimated from the MRS data following pre-processing using Suspect-MRS (https://suspect.readthedocs.io/en/latest/) including optimal channel-combination (23), eddy current correction, spectral registration and outlier rejection (24). LCModel (25) was then used for metabolite fitting with basis sets generated by Tarquin (brain + Gly + Glth) (26).

Results

All infants tolerated scanning on the 7T system, with stable vital signs throughout the scan session. There were no adverse events during image acquisition and there were no concerns expressed about discomfort or altered behaviour reported by clinical staff or parents either during or in the 24 h subsequent to the scanning session. Infant axillary temperature remained stable throughout image acquisition, with no significant difference in temperature measurements at the start of scanning (median 36.9 degrees centigrade, range 35.5–37.4) and at the end of scanning (median 36.8 degrees centigrade, range 35.6–37.7)

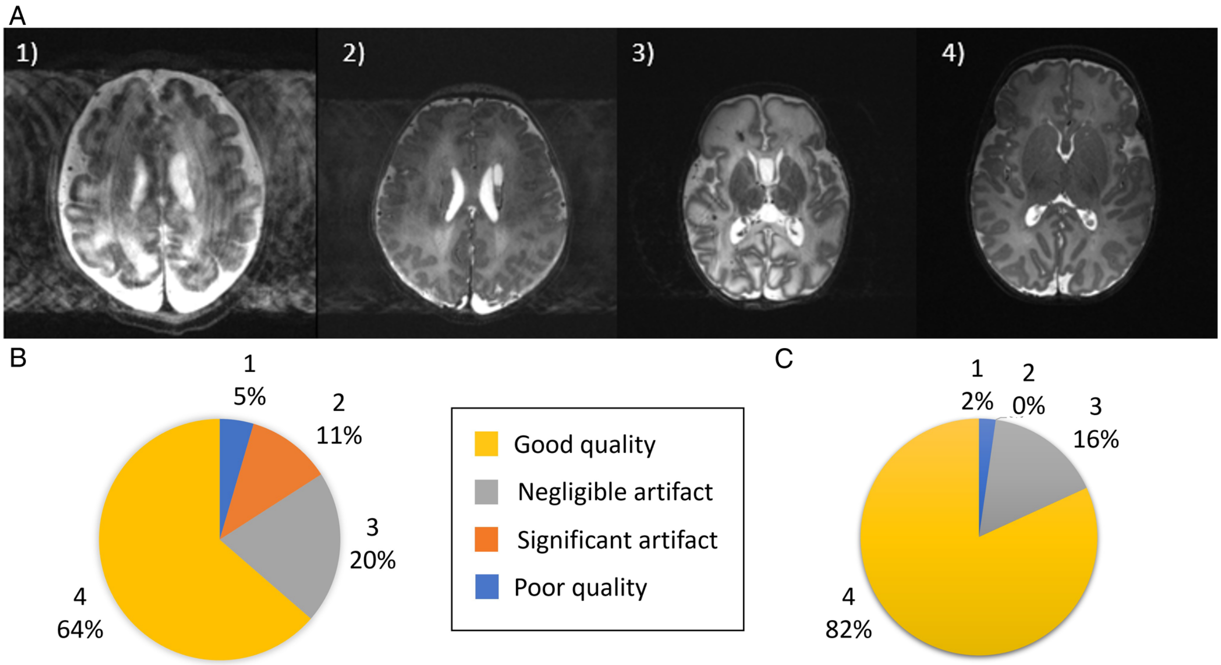

FIGURE 1
Image quality assessment. (A) Shown are representative images depicting quality of the native images as assessed using a previously described score (20), where (1) is a poor quality image (2) image contains significant motion artefact, (3) image with negligible motion artefact and (4) good quality image. (B) Image quality assessment results for the native T2-weighted images and (C) for the slice-to-volume reconstructed T2-weighted images.

on the 7T system (paired *t*-test: $p = 0.76$, Figure 2). This included the youngest preterm infant studied, who weighed 1.58 kg.

Images from the AFI sequence (Figure 3*)* show that relative B_1^+ magnitude is non-uniform over the brain. The example map shown (Figure 3A) is typical of what was seen across all infants studied, with a “center brightening” of the B_1^+ magnitude, and lower values seen peripherally, particularly in superior regions. The FSL brain extraction tool (BET) (27) was used to define a brain mask to then compute whole-brain histograms of B_1^+ magnitude, shown in Figure 3B. The histograms are consistent across all

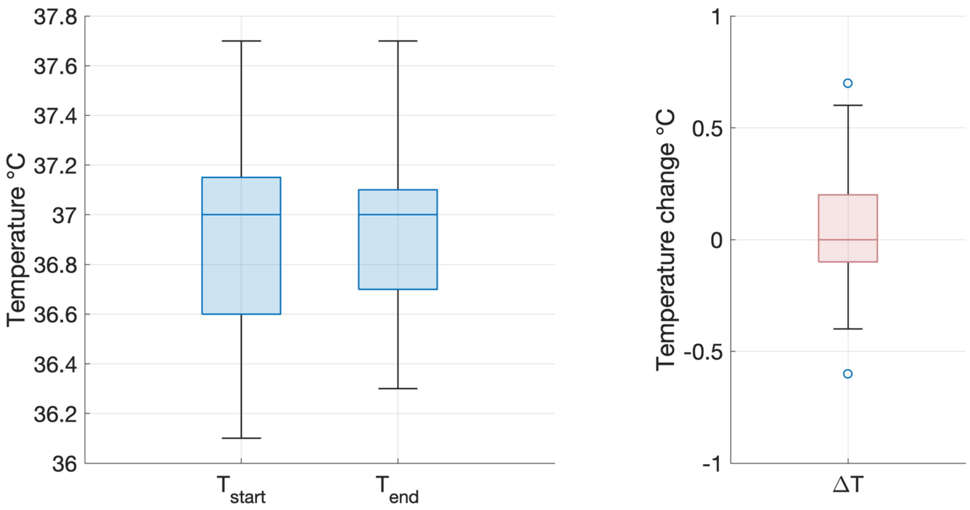

FIGURE 2
Infant temperature during scanning on the 7T system. There was no significant difference between infant axillary temperature at the start (*left*) and end (*right*) of the imaging session on the 7T system (paired two tailed *t*-test: $p = 0.76$). Box and whisker plots showing data median (bold line), 25th and 75th centile (box borders) and data range (whiskers). Data outliers are denoted by circles.

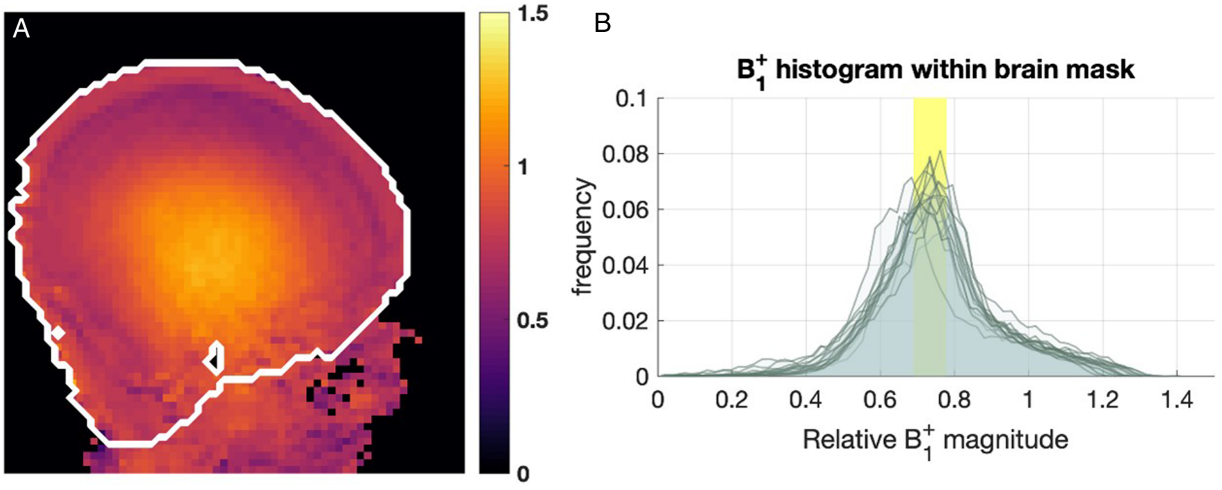

FIGURE 3
B_1^+ maps from 15 infants. (**A**) Example B_1^+ map obtained with AFI sequence, shown in relative units (i.e., relative to nominal B_1^+). The white contour marks the approximate brain outline. (**B**) Histograms of relative B_1^+ magnitude within the brain mask in 15 subjects. The yellow box shows the range of median relative B_1^+ (0.69–0.78).

infants and show that the median B_1^+ over the brain was in the range 0.69−0.78 (relative to nominal value) with the central bright spot reaching values approximately 20%−30% higher than nominal value.

In infants with paired studies, expert neuroradiology review of the T2 weighted anatomical images acquired at 7T was considered in all cases to be equivalent or higher in comparison to those acquired at 3T. In addition, the higher tissue contrast and spatial resolution of the 7T images resulted in improved visualization of specific structures which are typically challenging to delineate at lower field strengths (Figure 4). These included the hippocampi, greater definition of substructures within the deep grey matter structures (thalami and basal ganglia), and cortical folding in areas where it tends to be particularly convoluted and therefore difficult to delineate (i.e., the occipital lobe). Furthermore, additional detail which is not appreciated at lower field strengths could be seen, including the white matter medullary veins and cerebellar folia.

Specific pathological features that could be clearly visualized on 7T images included cystic lesions and septi in periventricular leukomalacia (PVL), areas of micro-hemorrhage, subdural cerebral hemorrhage, cortical polymicrogyria, and absence of the cavum septum pellucidum (Figure 5). SVRTK reconstructed images further improved image contrast and quality by correcting motion and inter-slice artifacts (Figures 6A–C), enabling robust automated tissue segmentation and surface generation (Figure 6D). Image quality of the native T2-weighted images was assessed to be good in 64% of the acquisitions (Figure 1B), which increased further to 82% following SVR reconstruction (Figure 1D), which compares favorably against equivalent figures assessed with the same criteria on state-of-the-art images acquired for the dHCP with a 3T system and dedicated neonatal receive coil (20).

The higher static magnetic field strength at 7T additionally led to marked gains in sensitivity in image contrasts dependent on magnetic susceptibility such as SWI. In addition to providing detailed visualization of the cerebral vasculature including both the arteries and veins (Figure 7A), the clinical value of SWI acquisitions was evident for identification of small areas of intracerebral hemorrhages in infants with congenital cardiac disease, in a preterm infant with a white matter cystic lesion where the hemorrhagic origin of the lesion could be appreciated (Figure 7B), and in a preterm infant with extensive intracerebral hemorrhage in the distribution of the deep medullary veins (Figure 7C). Gains in sensitivity and spatial specificity could also be appreciated using BOLD fMRI, with more cortically localized and broader repertoire of resting-state networks in comparison to 3T (3) (Figure 8). Expected gains in sensitivity and spectral resolution were also realised with MRS indicating the possibility of resolving spectral contributions of GABA, glutamate and glutamine that would usually require an edited acquisition scheme at lower field strengths (Figure 9).

Discussion

We report our first experiences and demonstrate feasibility of imaging neonates on a 7T system and the potential gains in anatomical and pathological sensitivity in brain images. In all cases, infants tolerated image acquisition at ultra-high field with stable vital signs and body temperature throughout the examination. Acquired high resolution anatomical images demonstrated high tissue contrast enabling visualization of several structures which are typically challenging to delineate in neonates at standard field strengths. The potential of ultra-high field imaging to provide new insight about the developing

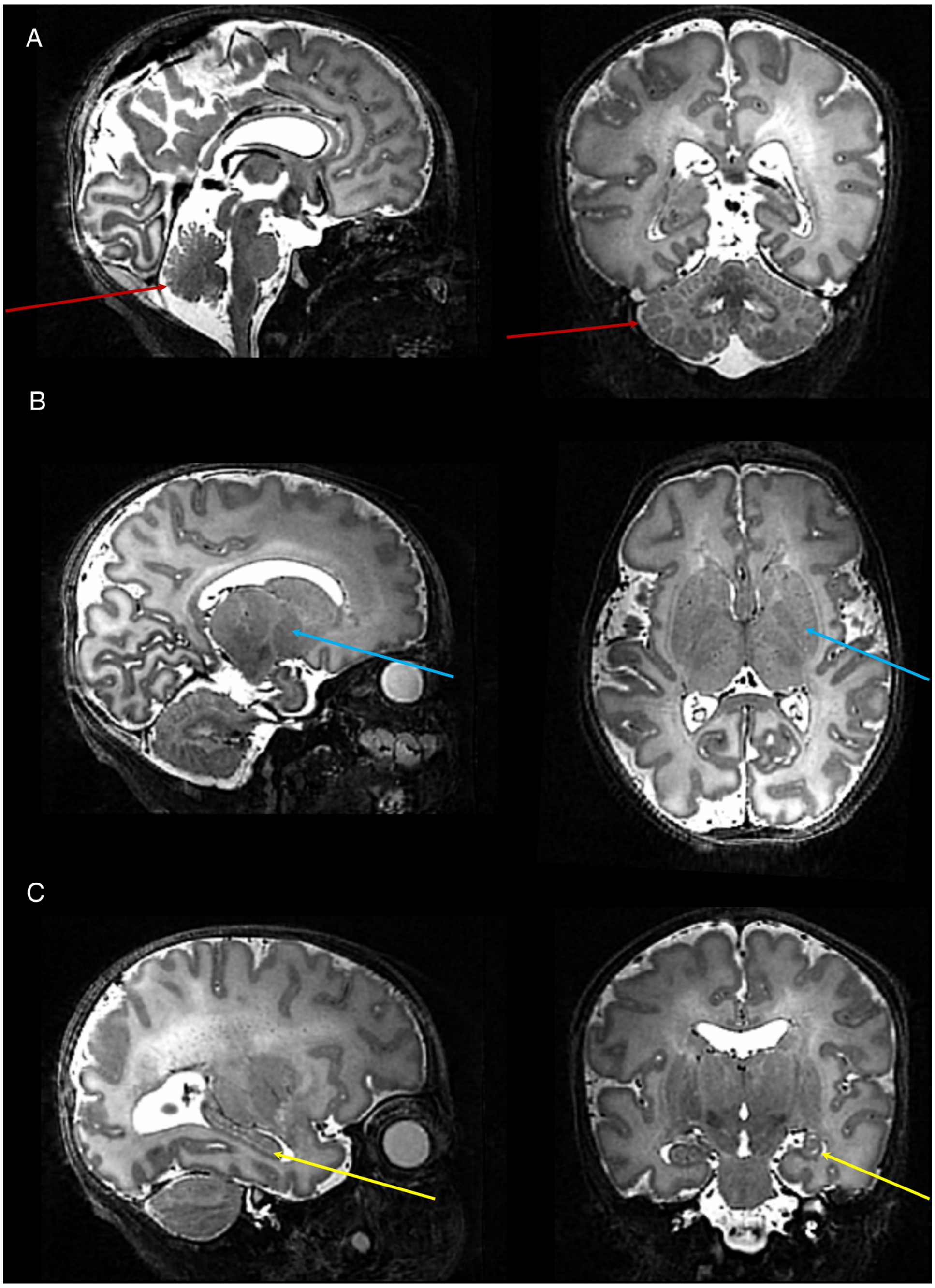

FIGURE 4
High resolution T2 weighted 7T image acquired from a preterm infant. Images show excellent visualisation of the: (A) cerebellar vermis and folia (*red arrows*); (B) deep gray matter nuclei within the basal ganglia and thalamus (*blue arrows*); (C) hippocampus (*yellow arrow*).

neonatal brain was further highlighted using contrasts dependent on tissue magnetic susceptibility including SWI and fMRI; and for MRS data which benefits both from increased SNR and spectral dispersion.

Recent studies of electromagnetic and radiofrequency exposure for 7T imaging of neonates suggested that in contrast to imaging at standard field strengths, more conservative operational limits should be used to limit SAR at ultra-high field in comparison to adults (11). Addressing the potential risks of body temperature heating is further complicated in neonates by their under-developed thermal regulation and high surface-to-volume body ratio, which means that they can also become rapidly hypothermic if not appropriately insulated with clothes and/or blankets (13, 28). Accounting for these factors is imperative as not only can neonates not directly indicate if they are uncomfortable or feeling cold/warm in the scanner, but thermal instability can result in significant physiological stress including increased oxygen consumption, decreased cardiac output and

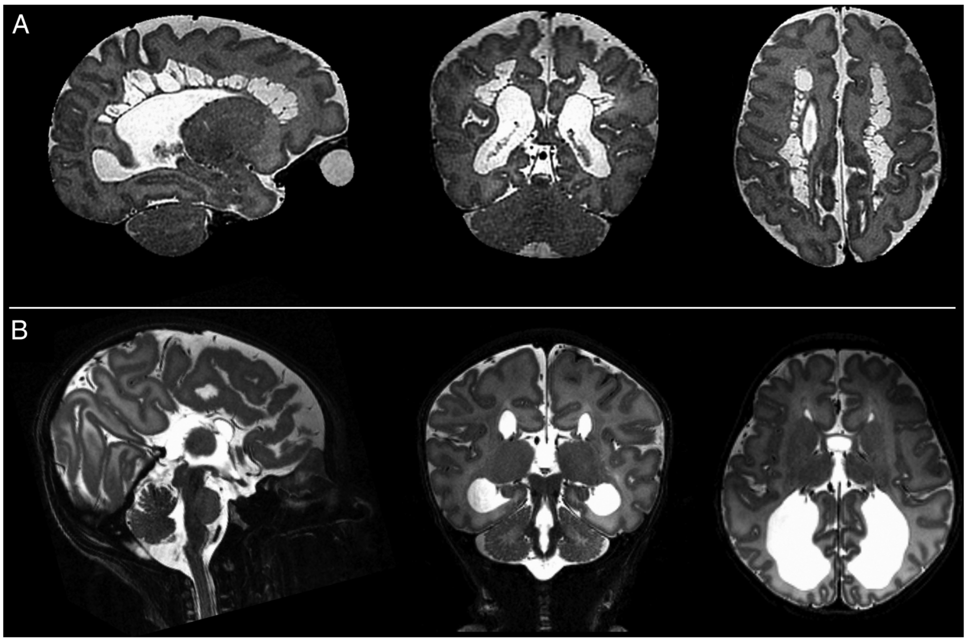

FIGURE 5
Examples of intracranial pathology identified on T2 weighted images at 7T. *(from left to right: illustrative slices in the sagittal, coronal, and axial planes)*. Shown are: (**A**) Cystic PVL; (**B**) Complete agenesis of the corpus callosum.

metabolic acidosis (29). Here we demonstrate that neonatal body temperature remained stable during ultra-high field imaging, whilst using a combination of appropriate adaptation of scanner software models and practical steps including swaddling and continuous monitoring using MR compatible equipment.

In addition to informing our safety assessment, the prior modelling study (11) predicted that B_1^+ would be non-uniform for neonates using the 7T head coil, contrary to expectations that the small size of neonatal subjects might mitigate this problem. The measured B_1^+ distributions (Figure 3) from the current study are consistent with predictions from the aforementioned modelling study. Figure 5 in Clarke et al. shows equivalent measurements from adults using the same coil (30); it is noticeable that while the centre-brightening effect is comparable between neonates and adults, areas of significant B_1^+ drop-out are less extreme in neonates than adults. These characteristics should be factored in when optimizing sequences for this cohort.

The clinical value of ultra-high field brain imaging has become relatively well established in older children and adults, particularly in applications and pathologies where the higher spatial resolution and improved tissue contrast has proven to increase sensitivity and offer new insight. Key examples include management of drug-resistant epilepsy where it can markedly improve detection and differentiation of potentially treatable epileptogenic lesions in comparison to imaging at standard field strengths, leading to international consensus recommendations for 7T imaging for this specific application (31); improved delineation of vascular pathology such as aneurysms or arteriovenous malformations (32); detailed visualization of the deep grey matter structures which can help guide the insertion of deep brain stimulation electrodes (33); and detection and differentiation of lesions in multiple sclerosis (34).

Whilst the clinical indications for 7T imaging of neonates are yet to be established, our initial experiences similarly suggest that there is clear potential through improving sensitivity for conditions which impact the developing cortex, vasculature, and smaller structures. This includes following preterm birth, which globally now represents greater than 15 million births annually and has significant implications for later neurodevelopmental outcome in survivors (35). In addition to the traditionally recognized patterns of direct white matter injury such as cystic PVL, preterm birth is also associated with subtle abnormalities such as punctate white matter lesions or micro-hemorrhages for which the underlying pathophysiology and clinical meaning remain uncertain (36). Furthermore, it is increasingly appreciated that adverse neurocognitive outcomes following preterm birth are related to lifelong alterations in cortical development, thalamic growth and connectivity (37). Infants with congenital cardiac disease are at high risk of peri-operative hemorrhage or ischemic injury, and often have chronically reduced cerebral oxygenation (38). These factors have also been found to result in profound life-long effects on cortical maturation which are similarly associated with adverse neurodevelopmental outcomes (39). Thus, imaging neonates at 7T could not only enhance detection of injuries in these high-risk populations, but also holds clear potential to provide marked new mechanistic insight into the pathophysiology underlying their neurodevelopmental consequences.

We also highlight the potential of gaining new insights into the developing brain using specific image contrasts which benefit from

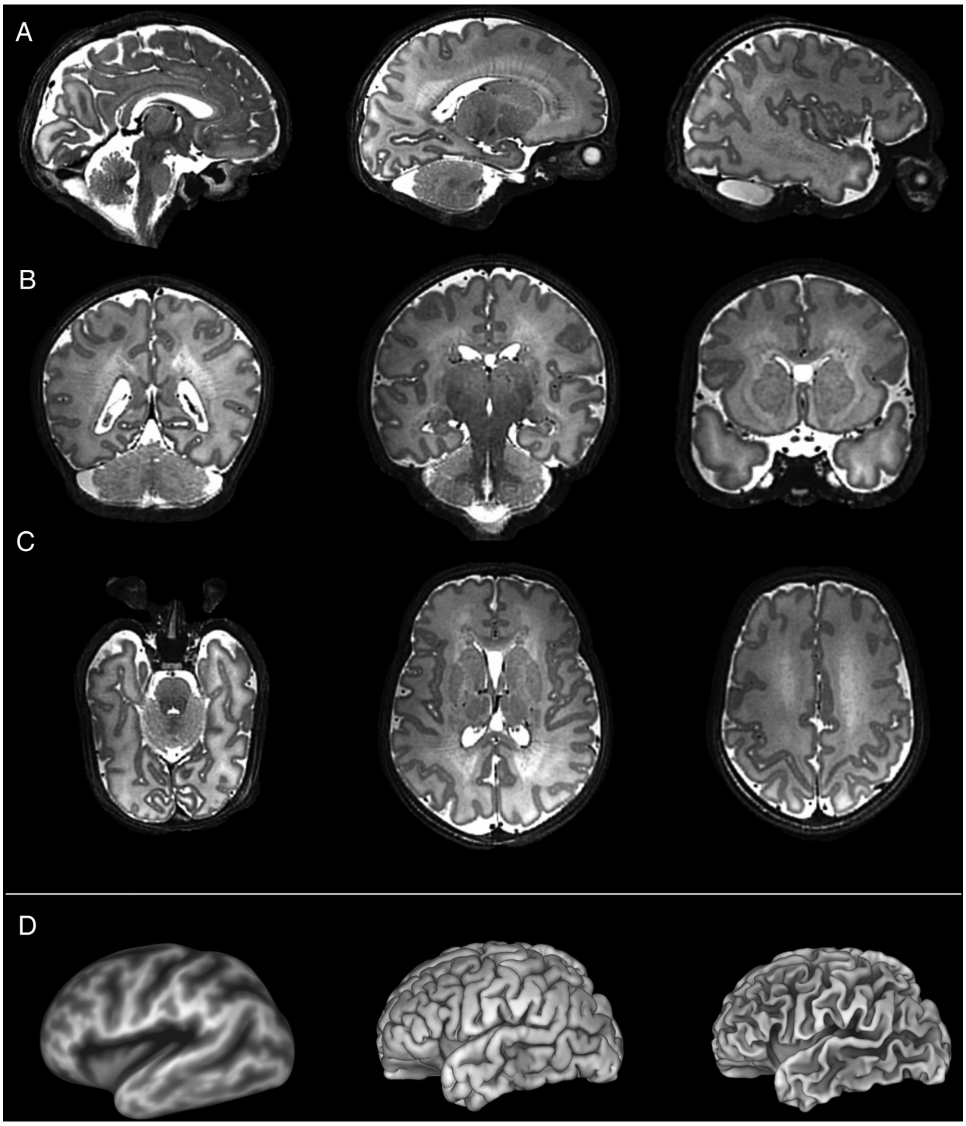

FIGURE 6
Slice to volume reconstructed T2 weighted images acquired from a preterm infant shown in the (A) sagittal, (B) coronal and (C) axial planes. These high contrast, high resolution images are amenable for further processing such as the generation of (D) (*from left to right*) inflated, pial, and white matter surfaces.

the increased field strength such as SWI, MRS and fMRI. The SWI method in particular has been shown to have particular value at 7T, where it has broad clinical applications including improved characterization of gliomas for surgical planning and epileptogenic foci (31), but additionally has potential to provide important new insights into the pathophysiology of common conditions such as dementia (40). Here, we show that SWI in neonates not only has high sensitivity for detecting areas of hemorrhage, but additionally can provide detailed visualization of the cerebral vasculature including both the arterial and venous systems (see Figure 7). This knowledge could provide novel insight about the specific role of the vascular system and cerebral perfusion in regional brain development and how this relationship is altered by pathology. fMRI BOLD contrast is similarly enhanced at ultra-high field and has been shown to enable fine-scale studies of the brain's functional architecture at higher resolution and sensitivity compared to standard field strengths, including delineation of activity within cortical columns, layers and specific deep grey matter nuclei (8). The ability to characterize brain activity at this level of detail in the neonatal brain is a compelling prospect, as this is a crucial time for the establishment of the brain's life-long framework of functional connectivity, with studies at 3T demonstrating rapid maturation of resting state networks in the time leading up to birth (3). Importantly, early-life alterations in functional connectivity such as those associated with preterm birth persist into later life and correlate with adverse neurodevelopmental outcome (4, 37). Significantly increased sensitivity and spectral resolution at 7T with 1H-MRS have been well described in adults (9), which we were also able to demonstrate in neonates. Wider

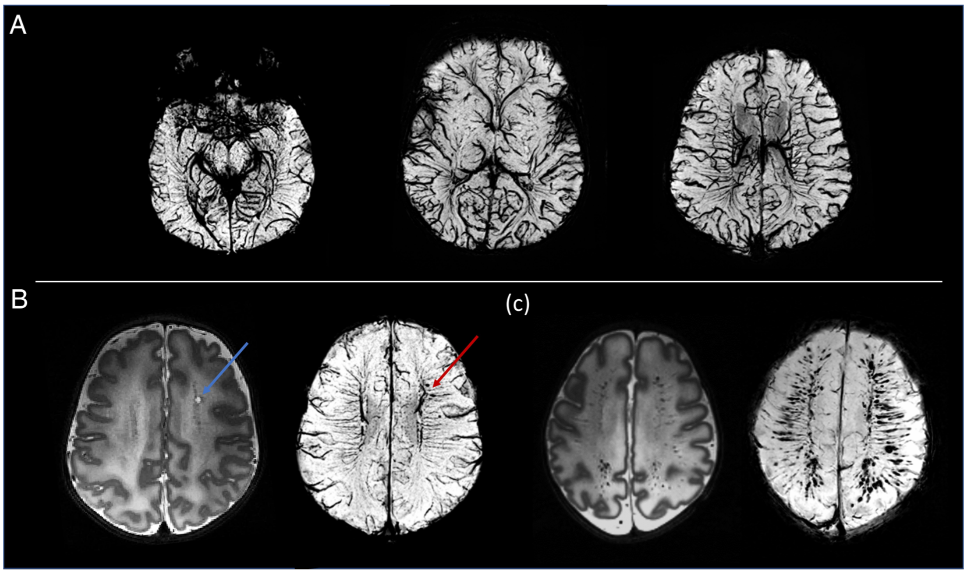

FIGURE 7
Susceptibility weighted images (SWI). (**A**) Example MIP axial slices from the SWI data acquired from a healthy neonate imaged at term equivalent age. (**B**) A cystic lesion (blue arrow) noted on T2-weighted images (*bottom left*) in a preterm infant. SWI demonstrated the hemorrhagic origin of the lesion (red arrow) and gives possible insight into the underlying pathophysiology through its adjacent location to the deep medullary veins. (**C**) Preterm infant with extensive intracerebral hemorrhage in the distribution of the medullary veins. The extent of this is visualized more clearly on the SWI image (bottom right).

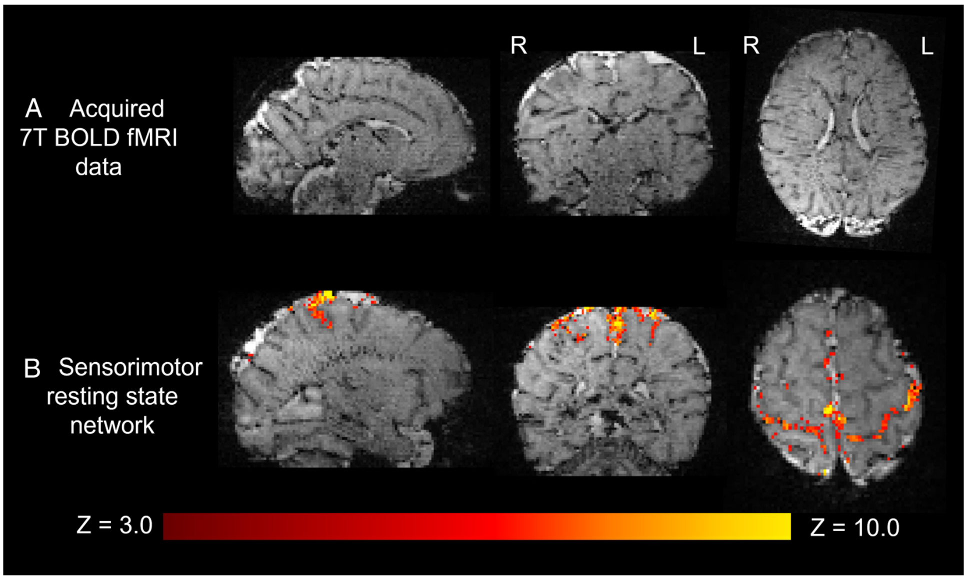

FIGURE 8
Resting state functional MRI data acquired from a preterm infant at 7T. (A) High spatial resolution (1 mm isotropic) high contrast whole brain BOLD fMRI data acquired at 7T from a preterm infant. (B) The sensorimotor resting state network derived using independent component analysis. Activation can be seen to clearly localize to the cortical ribbon, following the configuration of the sulci.

application could potentially inform about how inhibitory-excitatory neurotransmitter balance evolves across early development and about its possible role in the pathophysiology of neurodevelopmental disorders such as autism (4).

We describe our initial experiences and demonstrate feasibility of 7T neonatal imaging with a limited range of sequences optimized for this population. Although the acquired images had high SNR, an important consideration for this work is that we

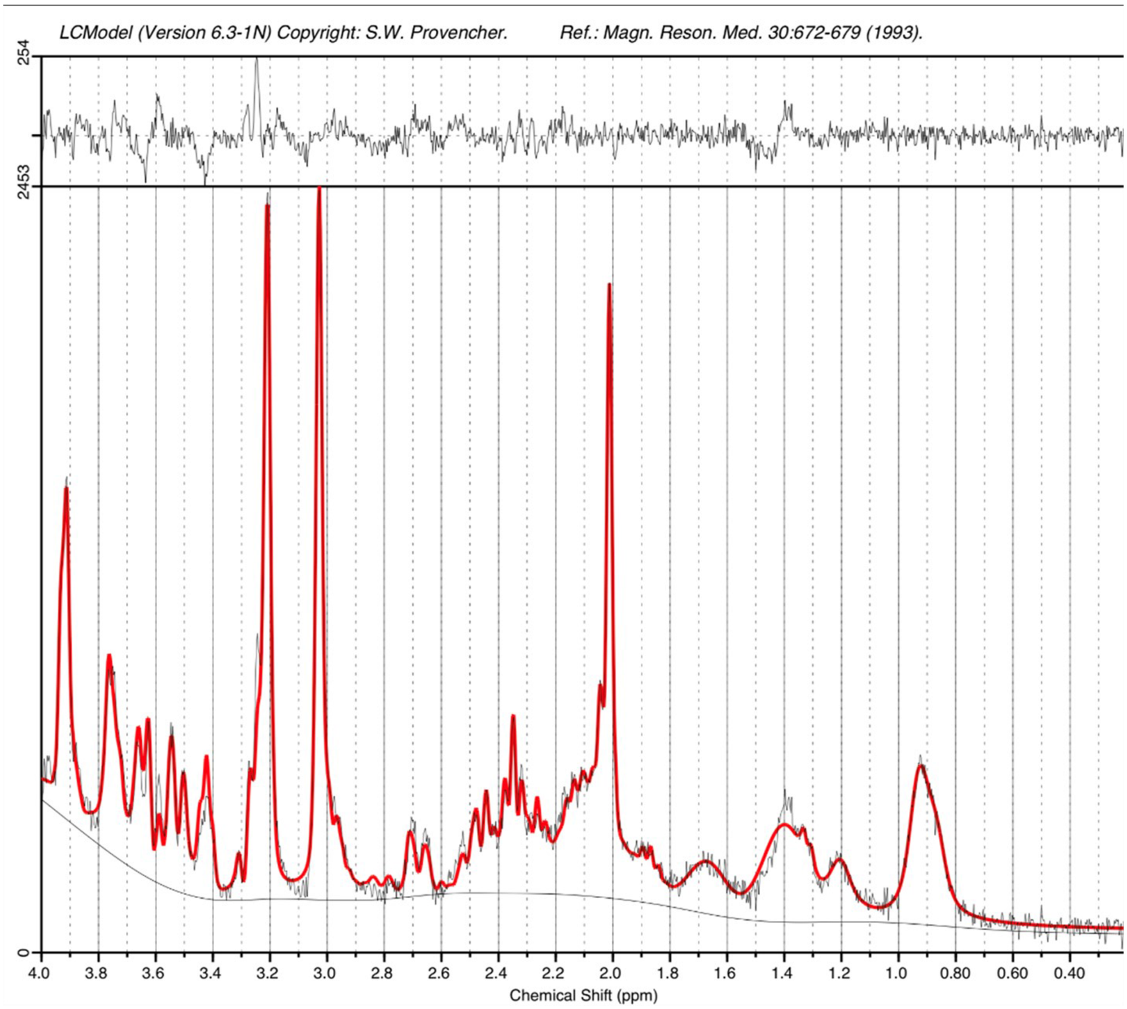

FIGURE 9
STEAM MRS spectrum acquired from the left thalamus of an infant at term equivalent age on the 7T system. A narrow linewidth (4.8Hz) and high SNR (26) as estimated by LCModel are observed. The acquisition time was just 2′24″.

used a standard adult transmit and receive head coil. Previous work at 3T has demonstrated that SNR, image homogeneity and head immobilization can all be considerably improved with a head coil which is appropriately sized so that the receive elements are closer to the neonatal head (18). Work is thus underway to develop a neonatal specific head coil for 7T scanning in our center (41). Whilst we demonstrate significant gains in anatomical detail and sensitivity with high-resolution T2-weighted imaging, high contrast T1-weighted imaging was found to be challenging to acquire at 7T without knowledge of neonatal-specific tissue T1 values. Systematic data collection is therefore underway to establish brain tissue T1 and T2 relaxation values across the perinatal period in both preterm and term born neonates and will be reported separately. Nevertheless, our work highlights the clear potential of ultra-high field brain imaging in neonates to improve diagnosis and understanding of pathological mechanisms during this key stage of life. This has important implications not only for the clinical management of conditions known to originate in this period (such as cerebral palsy) but also for other common but hitherto poorly understood conditions like autism and mental health disorders which likely have their origin in the perinatal period.

Data availability statement

The anonymised raw data supporting the conclusions of this article will be made available by the authors on completion of a data sharing agreement as stipulated by institutional governance regulations.

Ethics statement

The studies involving humans were approved by NHS Health Research Authority London—City and East Research Ethics Committee. The studies were conducted in accordance with the local legislation and institutional requirements. Written informed consent for participation in this study was provided by the participants' legal guardians/next of kin.

Author contributions

PB: Conceptualization, Data curation, Formal analysis, Investigation, Methodology, Project administration, Writing – original draft, Writing – review & editing, Resources. RT-T: Software, Writing – review & editing, Investigation, Methodology. AU: Methodology, Software, Writing – review & editing. DC: Data curation, Methodology, Writing – review & editing, Investigation. MQ: Methodology, Writing – review & editing, Investigation. JA: Methodology, Writing – review & editing, Investigation. BB: Methodology, Writing – review & editing, Investigation. MDF: Methodology, Writing – review & editing, Investigation. AM: Methodology, Writing – review & editing, Investigation. PDC: Data curation, Project administration, Writing – review & editing, Investigation. PC: Data curation, Methodology, Project administration, Supervision, Writing – review & editing, Investigation. CC: Formal analysis, Writing – review & editing, Methodology. AD: Data curation, Writing – review & editing, Formal analysis, Methodology. AT: Formal analysis, Writing – review & editing, Investigation. JM: Data curation, Formal analysis, Writing – review & editing, Investigation, Methodology. DB: Formal analysis, Writing – review & editing. JS: Formal analysis, Writing – review & editing. TF: Formal analysis, Writing – review & editing. AP: Data curation, Formal analysis, Methodology, Project administration, Writing – review & editing. EP: Data curation, Formal analysis, Methodology, Writing – review & editing, Investigation, Software. LCG: Formal analysis, Software, Writing – review & editing. AE: Formal analysis, Writing – review & editing. JO: Formal analysis, Methodology, Project administration, Software, Writing – review & editing. SC: Data curation, Methodology, Writing – review & editing. SG: Methodology, Supervision, Writing – review & editing. MD: Formal analysis, Software, Writing – review & editing, Methodology. EV: Data curation, Formal analysis, Methodology, Writing – review & editing, Investigation, Software. MR: Formal analysis, Writing – review & editing. DE: Methodology, Supervision, Writing – review & editing, Funding acquisition. JH: Data curation, Methodology, Supervision, Writing – review & editing, Funding acquisition. SM: Conceptualization, Data curation, Formal analysis, Funding acquisition, Investigation, Methodology, Project administration, Resources, Software, Supervision, Writing – original draft, Writing – review & editing. TA: Conceptualization, Data curation, Formal analysis, Funding acquisition, Investigation, Methodology, Project administration, Resources, Software, Supervision, Writing – original draft, Writing – review & editing.

Funding

The author(s) declare financial support was received for the research, authorship, and/or publication of this article.

The work was supported a project grant awarded by Action Medical Research [GN2728]. TA is also supported by an MRC Clinician Scientist Fellowship [MR/P008712/1] and Transition Support Award [MR/V036874/1]. PC, AT, JOM, MAR, ADE and TA received support from the Medical Research Council Centre for Neurodevelopmental Disorders, King's College London [MR/N026063/1]. LCG received support by project PID2021-129022OA-I00, funded by MCIN/AEI/10.13039/501100011033/FEDER, EU. The authors also acknowledge support in part from the Wellcome Engineering and Physical Sciences Research Council (EPSRC) Centre for Medical Engineering at Kings College London [WT203148/Z/16/Z].

Acknowledgments

The authors are grateful for discussion and advice from Jonathan Polimeni, David Carmichael, Essa Yacoub and colleagues at Utrecht University. We acknowledge significant input and support from colleagues at Siemens Healthineers without whom this work would not have been possible. We are also grateful for assistance from Philips Invivo, and Pearltec. This research was funded/supported by the National Institute for Health and Care Research (NIHR) Clinical Research Facility at Guy's and St Thomas' NHS Foundation Trust. The views expressed are those of the author(s) and not necessarily those of the NHS, the NIHR or the Department of Health and Social Care. The funders had no role in the design and conduct of the study; collection, management, analysis, and interpretation of the data; preparation, review, or approval of the manuscript; and decision to submit the manuscript for publication.

Conflict of interest

The authors declare that the research was conducted in the absence of any commercial or financial relationships that could be construed as a potential conflict of interest.

Publisher's note

Supplementary material

The Supplementary Material for this article can be found online at: https://www.frontiersin.org/articles/10.3389/fradi.2023.1327075/full#supplementary-material

References

1. Kostovic I, Jovanov-Milosevic N. The development of cerebral connections during the first 20–45 weeks' gestation. *Semin Fetal Neonatal Med*. (2006) 11(6):415–22. doi: 10.1016/j.siny.2006.07.001

2. Ben-Ari Y, Gaiarsa JL, Tyzio R, Khazipov R. GABA: a pioneer transmitter that excites immature neurons and generates primitive oscillations. *Physiol Rev*. (2007) 87(4):1215–84. doi: 10.1152/physrev.00017.2006

3. Doria V, Beckmann CF, Arichi T, Merchant N, Groppo M, Turkheimer FE, et al. Emergence of resting state networks in the preterm human brain. *Proc Natl Acad Sci U S A*. (2010) 107(46):20015–20. doi: 10.1073/pnas.1007921107

4. Batalle D, Edwards AD, O'Muircheartaigh J. Annual research review: not just a small adult brain: understanding later neurodevelopment through imaging the neonatal brain. *J Child Psychol Psychiatry*. (2018) 59(4):350–71. doi: 10.1111/jcpp.12838

5. Pohmann R, Speck O, Scheffler K. Signal-to-noise ratio and MR tissue parameters in human brain imaging at 3, 7, and 9.4 tesla using current receive coil arrays. *Magn Reson Med*. (2016) 75(2):801–9. doi: 10.1002/mrm.25677

6. van Lanen R, Colon AJ, Wiggins CJ, Hoeberigs MC, Hoogland G, Roebroeck A, et al. Ultra-high field magnetic resonance imaging in human epilepsy: a systematic review. *Neuroimage Clin*. (2021) 30:102602. doi: 10.1016/j.nicl.2021.102602

7. Geurts LJ, Zwanenburg JJM, Klijn CJM, Luijten PR, Biessels GJ. Higher pulsatility in cerebral perforating arteries in patients with small vessel disease related stroke, a 7T MRI study. *Stroke*. (2018) 50(1):62–8. doi: 10.1161/STROKEAHA.118.022516

8. Dumoulin SO, Fracasso A, van der Zwaag W, Siero JCW, Petridou N. Ultra-high field MRI: advancing systems neuroscience towards mesoscopic human brain function. *Neuroimage*. (2018) 168:345–57. doi: 10.1016/j.neuroimage.2017.01.028

9. Tkac I, Oz G, Adriany G, Ugurbil K, Gruetter R. In vivo 1H NMR spectroscopy of the human brain at high magnetic fields: metabolite quantification at 4T vs. 7T. *Magn Reson Med*. (2009) 62(4):868–79. doi: 10.1002/mrm.22086

10. Annink KV, van der Aa NE, Dudink J, Alderliesten T, Groenendaal F, Lequin M, et al. Introduction of ultra-high-field MR imaging in infants: preparations and feasibility. *AJNR Am J Neuroradiol*. (2020) 41(8):1532–7. doi: 10.3174/ajnr.A6702

11. Malik SJ, Hand JW, Satnarine R, Price AN, Hajnal JV. Specific absorption rate and temperature in neonate models resulting from exposure to a 7T head coil. *Magn Reson Med*. (2021) 86(3):1299–313. doi: 10.1002/mrm.28784

12. Williams LA, Gelman N, Picot PA, Lee DS, Ewing JR, Han VK, et al. Neonatal brain: regional variability of in vivo MR imaging relaxation rates at 3.0 T–initial experience. *Radiology*. (2005) 235(2):595–603. doi: 10.1148/radiol.2352031769

13. Plaisier A, Raets MM, van der Starre C, Feijen-Roon M, Govaert P, Lequin MH, et al. Safety of routine early MRI in preterm infants. *Pediatr Radiol*. (2012) 42 (10):1205–11. doi: 10.1007/s00247-012-2426-y

14. Malik SJ, Beqiri A, Price AN, Teixeira JN, Hand JW, Hajnal JV. Specific absorption rate in neonates undergoing magnetic resonance procedures at 1.5 T and 3 T. *NMR Biomed*. (2015) 28(3):344–52. doi: 10.1002/nbm.3256

15. Bridgen P, Malik S, Wilkinson T, Cronin JN, Bhagat T, Hart N, et al. Reliability and safety of anaesthetic equipment around an high-field 7-tesla MRI scanner. *Br J Anaesth*. (2023) 130(6):e490–e2. doi: 10.1016/j.bja.2023.02.019

16. Merchant N, Groves A, Larkman DJ, Counsell SJ, Thomson MA, Doria V, et al. A patient care system for early 3.0 tesla magnetic resonance imaging of very low birth weight infants. *Early Hum Dev*. (2009) 85(12):779–83. doi: 10.1016/j.earlhumdev.2009.10.007

17. Yarnykh VL. Actual flip-angle imaging in the pulsed steady state: a method for rapid three-dimensional mapping of the transmitted radiofrequency field. *Magn Reson Med*. (2007) 57(1):192–200. doi: 10.1002/mrm.21120

18. Hughes EJ, Winchman T, Padormo F, Teixeira R, Wurie J, Sharma M, et al. A dedicated neonatal brain imaging system. *Magn Reson Med*. (2017) 78(2):794–804. doi: 10.1002/mrm.26462

19. Kuklisova-Murgasova M, Quaghebeur G, Rutherford MA, Hajnal JV, Schnabel JA. Reconstruction of fetal brain MRI with intensity matching and complete outlier removal. *Med Image Anal*. (2012) 16(8):1550–64. doi: 10.1016/j.media.2012.07.004

20. Makropoulos A, Robinson EC, Schuh A, Wright R, Fitzgibbon S, Bozek J, et al. The developing human connectome project: a minimal processing pipeline for neonatal cortical surface reconstruction. *Neuroimage*. (2018) 173:88–112. doi: 10.1016/j.neuroimage.2018.01.054

21. Smith SM, Jenkinson M, Woolrich MW, Beckmann CF, Behrens TE, Johansen-Berg H, et al. Advances in functional and structural MR image analysis and implementation as FSL. *Neuroimage*. (2004) 23(Suppl 1):S208–19. doi: 10.1016/j.neuroimage.2004.07.051

22. Eckstein K, Bachrata B, Hangel G, Widhalm G, Enzinger C, Barth M, et al. Improved susceptibility weighted imaging at ultra-high field using bipolar multi-echo acquisition and optimized image processing: cLEAR-SWI. *Neuroimage*. (2021) 237:118175. doi: 10.1016/j.neuroimage.2021.118175

23. Rodgers CT, Robson MD. Coil combination for receive array spectroscopy: are data-driven methods superior to methods using computed field maps? *Magn Reson Med*. (2016) 75(2):473–87. doi: 10.1002/mrm.25618

24. Near J, Harris AD, Juchem C, Kreis R, Marjanska M, Oz G, et al. Preprocessing, analysis and quantification in single-voxel magnetic resonance spectroscopy: experts' consensus recommendations. *NMR Biomed*. (2021) 34(5):e4257. doi: 10.1002/nbm.4257

25. Provencher SW. Estimation of metabolite concentrations from localized in vivo proton NMR spectra. *Magn Reson Med*. (1993) 30(6):672–9. doi: 10.1002/mrm.1910300604

26. Wilson M, Reynolds G, Kauppinen RA, Arvanitis TN, Peet AC. A constrained least-squares approach to the automated quantitation of in vivo (1)H magnetic resonance spectroscopy data. *Magn Reson Med*. (2011) 65(1):1–12. doi: 10.1002/mrm.22579

27. Smith SM. Fast robust automated brain extraction. *Hum Brain Mapp*. (2002) 17 (3):143–55. doi: 10.1002/hbm.10062

28. Soll RF. Heat loss prevention in neonates. *J Perinatol*. (2008) 28(Suppl 1):S57–9. doi: 10.1038/jp.2008.51

29. Wood T, Thoresen M. Physiological responses to hypothermia. *Semin Fetal Neonatal Med*. (2015) 20(2):87–96. doi: 10.1016/j.siny.2014.10.005

30. Clarke WT, Mougin O, Driver ID, Rua C, Morgan AT, Asghar M, et al. Multi-site harmonization of 7 tesla MRI neuroimaging protocols. *Neuroimage*. (2020) 206:116335. doi: 10.1016/j.neuroimage.2019.116335

31. Opheim G, van der Kolk A, Markenroth Bloch K, Colon AJ, Davis KA, Henry TR, et al. 7T epilepsy task force consensus recommendations on the use of 7T MRI in clinical practice. *Neurology*. (2021) 96(7):327–41. doi: 10.1212/WNL.0000000000011413

32. Radojewski P, Slotboom J, Joseph A, Wiest R, Mordasini P. Clinical implementation of 7T MRI for the identification of incidental intracranial aneurysms versus anatomic variants. *AJNR Am J Neuroradiol*. (2021) 42 (12):2172–4. doi: 10.3174/ajnr.A7331

33. Xiao Y, Zitella LM, Duchin Y, Teplitzky BA, Kastl D, Adriany G, et al. Multimodal 7T imaging of thalamic nuclei for preclinical deep brain stimulation applications. *Front Neurosci*. (2016) 10:264. doi: 10.3389/fnins.2016.00264

34. Kolb H, Absinta M, Beck ES, Ha SK, Song Y, Norato G, et al. 7T MRI differentiates remyelinated from demyelinated multiple sclerosis lesions. *Ann Neurol*. (2021) 90(4):612–26. doi: 10.1002/ana.26194

35. Cao G, Liu J, Liu M. Global regional and national incidence and mortality of neonatal preterm birth, 1990−2019. *JAMA Pediatr*. (2022) 176(8):787–96. doi: 10.1001/jamapediatrics.2022.1622

36. de Bruijn CAM, Di Michele S, Tataranno ML, Ramenghi LA, Rossi A, Malova M, et al. Neurodevelopmental consequences of preterm punctate white matter lesions: a systematic review. *Pediatr Res*. (2023) 93(6):1480–90. doi: 10.1038/s41390-022-02232-3

37. Rogers CE, Lean RE, Wheelock MD, Smyser CD. Aberrant structural and functional connectivity and neurodevelopmental impairment in preterm children. *J Neurodev Disord*. (2018) 10(1):38. doi: 10.1186/s11689-018-9253-x

38. Bonthrone AF, Stegeman R, Feldmann M, Claessens NHP, Nijman M, Jansen NJG, et al. Risk factors for perioperative brain lesions in infants with congenital heart disease: a European collaboration. *Stroke*. (2022) 53(12):3652–61. doi: 10.1161/STROKEAHA.122.039492

39. Kelly CJ, Christiaens D, Batalle D, Makropoulos A, Cordero-Grande L, Steinweg JK, et al. Abnormal microstructural development of the cerebral Cortex in neonates with congenital heart disease is associated with impaired cerebral oxygen delivery. *J Am Heart Assoc*. (2019) 8(5):e009893. doi: 10.1161/JAHA.118.009893

40. van Rooden S, Versluis MJ, Liem MK, Milles J, Maier AB, Oleksik AM, et al. Cortical phase changes in Alzheimer's disease at 7T MRI: a novel imaging marker. *Alzheimers Dement*. (2014) 10(1):e19–26. doi: 10.1016/j.jalz.2013.02.002

41. Clement J, Tomi-Tricot R, Malik SJ, Webb A, Hajnal JV, Ipek O. Towards an integrated neonatal brain and cardiac examination capability at 7 T: electromagnetic field simulations and early phantom experiments using an 8-channel dipole array. *MAGMA*. (2022) 35(5):765–78. doi: 10.1007/s10334-021-00988-z

Appendix 1: SAR estimation

Our simulation study (11) suggested that head average SAR is proportional to RF power with factor 0.45, i.e.,:

$$\mathrm{hdSAR} = 0.45\ \mathrm{P_{RF}}$$

The Siemens Terra scanner estimates local SAR and subjects this to a limit of $20\,\mathrm{W\ kg^{-1}}$ when in first-level controlled mode (the worst case), i.e.,:

$$\mathrm{SAR_{est}} = \mathrm{P_{RF}k}$$

$$\mathrm{SAR_{est}} \leq 20\ \mathrm{W\ kg^{-1}}$$

Hence, to ensure that $\mathrm{hdSAR} \leq 3.2\mathrm{W\ kg^{-1}}$ we modified k to be $\mathrm{k} = \frac{20}{3.2} \times 0.45 = 2.8\ \mathrm{kg^{-1}}$.

With this value of k, the maximum power allowed by the scanner would be $\mathrm{P_{RF}} = \frac{20}{2.8} = 7.1\mathrm{W}$ and according to our simulation study, this would result in $\mathrm{hdSAR} = 0.45 \times 7.1 = 3.2\ \mathrm{W\ kg^{-1}}$ as required. This is over a factor of 2 times more limiting than the value set by the manufacturer.

Frontiers in Pediatrics

TYPE Review
PUBLISHED 10 June 2024
DOI 10.3389/fped.2024.1400468

OPEN ACCESS

EDITED BY
Sahar Ahmad,
University of North Carolina at Chapel Hill,
United States

REVIEWED BY
Francesca Felicia Operto,
University of Salerno, Italy
Luis Nuñez-Jaramillo,
University of Quintana Roo, Mexico

*CORRESPONDENCE
Hui Zhou
✉ 1103570489@qq.com

RECEIVED 13 March 2024
ACCEPTED 20 May 2024
PUBLISHED 10 June 2024

CITATION
Shen F and Zhou H (2024) Advances in the etiology and neuroimaging of children with attention deficit hyperactivity disorder.
Front. Pediatr. 12:1400468.
doi: 10.3389/fped.2024.1400468

Advances in the etiology and neuroimaging of children with attention deficit hyperactivity disorder

Fang Shen and Hui Zhou*

Department of Pediatrics, West China Second University Hospital, Sichuan University, Key Laboratory of Birth Defects and Related Diseases of Women and Children of Ministry of Education, Chengdu, China

Attention deficit hyperactivity disorder (ADHD) is the most common neurodevelopmental disorder in children, characterized by age-inappropriate inattention, hyperactivity, and impulsivity, which can cause extensive damage to children's academic, occupational, and social skills. This review will present current advancements in the field of attention deficit hyperactivity disorder, including genetics, environmental factors, epigenetics, and neuroimaging features. Simultaneously, we will discuss the highlights of promising directions for further study.

KEYWORDS

attention deficit hyperactivity disorder, genetics, environmental risk factors, epigenetics, neuroimaging features, further research directions

1 Introduction

Attention deficit hyperactivity disorder (ADHD) is a prevalent neurodevelopmental disorder, characterized by extensive hyperactive, impulsive and/or inattentive behaviors that impair daily functioning. Notably, it is estimated the global prevalence of ADHD as 7.2% (1, 2). And in China specifically, ADHD affected around 6.4% of children (3). Long-lasting clinical symptoms are present in between 50% and 60% of ADHD patients, frequently coexisting with additional disorders, namely anxiety, oppositional defiant disorder, and tic disorders. These conditions can increase the risk of suicide and delinquency and have a major negative influence on families and society (4, 5). The complicated etiology of ADHD is frequently attributed to a confluence of hereditary and environmental variables (6, 7). Research has demonstrated that structural abnormalities in the brain, such as decreased brain volume and cortical surface area in ADHD, can cause disturbances in brain function, which can result in executive dysfunction and a variety of clinical symptoms, including impulsivity, hyperactivity, and inattention (7, 8).

2 The etiology and pathogenesis of ADHD

Although the exact cause of ADHD remains unidentified, most researchers contend that it is a result of a combination of hereditary and environmental factors. Besides, ADHD has a comparatively variable clinical presentation, by thoroughly examining its various etiology and pathogenesis, new treatment approaches can be developed and researched more easily.

2.1 Genetic factors

The development of ADHD is largely influenced by genetic factors, and investigations involving twins and family lines have demonstrated a distinct familial clustering in the disorder's development. Additionally, research conducted by Uchida et al. (9) found that children whose parents had ADHD were more likely than their non-ADHD parents to experience ADHD and other cognitive and psychiatric disorders. Faraone et al. demonstrated that the heritability of ADHD in twins is approximately 74% (10). Through a genome-wide association study (GWAS) of ADHD, Demontis et al. (11) presented a significant research paper in 2019 which achieved substantial progress in identifying genetic risk factors and refining the genetic architecture of the disease. The research revealed 12 independent genome-wide significant loci associated with ADHD by combining a genome-wide association meta-analysis of ADHD risk genes with data from the Danish Integrative Psychiatric Research (iPSYCH) and 11 ADHD cohorts from various nations that were gathered by the Psychiatric Genomics Consortium (PGC), totaling 20,183 ADHD patients and 35,191 controls.

Primarily, the identified risk genes are clustered in the cerebral cortex and are associated with early brain development, principally involving several brain-specific neuronal subtypes and midbrain dopaminergic neurons. The risk gene loci are linked to neurodevelopment, neurotransmitter transmission, and regulation of gene expression. The aforementioned study provides compelling evidence that ADHD is a polygenic disorder, with several risk genes working together to determine the development of the condition and varying degrees of illness risk associated with each gene. In 2023, Demontis et al. identified 27 risk loci, comprising both the common loci from the 2019 analysis and recently found rarer genetic loci. Simultaneously, after examining the expression of ADHD risk genes in different tissues and cell types, the researchers discovered that many of these genes were enriched in excitatory and inhibitory brain neuronal cell types. Additionally, it was demonstrated that genes expressed in dopaminergic mesencephalic neurons and genes related to ADHD were significantly correlated ($P = 0.005$) based on the results of single-cell RNA sequencing data and cell type-specific analysis (12).

Furthermore, the ongoing advancement of research on disease risk gene loci (13) will gradually lead to the genetic elucidation of the effects of risk genes on the development of particular neuronal subtypes and brain network connections, as well as the further clarification of the connection between attention-deficit, hyperactivity, and impulsive behaviors in children with ADHD and abnormalities in brain development. Based on prior research, an estimated 300 candidate genes have been linked to the onset of ADHD. These genes are primarily found in midbrain interneurons. We will then describe in detail three common interneurons including dopaminergic neurons, noradrenergic neurons, and 5-hydroxytryptamine (5-HT) neurons.

2.1.1 Association of dopaminergic genes, dopamine neurotransmission pathway and ADHD symptoms

2.1.1.1 Dopamine receptor genes

Dopamine receptor D4 (DRD4) is the most studied candidate gene associated with increased risk of ADHD, DRD4 receptor regulates dopamine signaling in the CNS and plays important roles in attention, reward, and motivation. Chang et al. (14) found that children with the DRD4 GG genotype were more likely to experience ADHD than children with the DRD4 GA/AA. Notably, variable Number Tandem Repeats (VNTR) is a repeated section of the DNA sequence that is the main target of variations in the DRD4 gene. The 7 repeat (7R) and the 4 repeat (4R) are two of the most prevalent variation types. Research has identified a correlation between the 7R variation and a higher likelihood of developing ADHD. According to some research, those who have the DRD4 7R variation may be more prone to ADHD in specific groups. However, the results are inconsistent, as the association's intensity and direction changed based on populations and research. Thus, the DRD4 gene's connection to ADHD remains debatable, and other genetic and environmental variables may influence how the gene functions. The relationship between DRD5 gene variations and ADHD has not been researched adequately. Despite this, Tong et al. (15) have suggested that some variations in the DRD5 gene may be associated with an increased chance of developing ADHD. Whereas other research has suggested that the DRD5 gene and ADHD do not appear to be correlated. Therefore, to validate the DRD5 gene's involvement in the pathogenesis of ADHD, additional research is required.

2.1.1.2 Dopamine transporter genes

An increased risk of ADHD has also been linked to variations in dopamine transporter genes, such as those in the dopamine transporter 1 (DAT1, also known as *SLC6A3*) gene. One of the most extensively researched potential genes in the pathophysiology of childhood ADHD is DAT1 (16). Research has indicated that the 10R of the 40 bp VNTR in the 3′ untranslated region (3′ UTR) of DAT1 is strongly correlated with clinical symptoms in ADHD children, particularly those with attention deficits and that DAT1 haplotypes comprising the 10R of the 40 bp VNTR of the 3′UTR/the 6R of the 30 bp VNTR of the intron 8 are strongly correlated with cognitive impairments in ADHD. The 10R/10R genotype of DAT1 VNTR is related to ADHD in Korean children (17). Study in Jordan children showed that the 10R allele of *DAT1* was associated with ADHD in the children (18). On the other hand, conflicting results were reported in the studies in the Omani children, Han Chinese children, Iranian population and Turkish population which showed no association significant between VNTR polymorphism with ADHD (19–22). Meanwhile, it has been reported that there is no association between VNTR polymorphism of *DAT1* genes and ADHD among Indonesian children based on a case-control study (23). In 2020, Kuc et al. also found that the *SLC6A3* gene polymorphism was not associated with the presence of ADHD (24).

2.1.2 Genes associated with the 5-hydroxytryptaminergic system

The frontal orbital-striatal pathway is regulated by 5-hydroxytryptamine (5-HT), and 5-hydroxytryptamine receptors (5-HTR) are mainly located in the brain's prefrontal cortex, amygdala, and hippocampus (25). Deviations from normalcy in these brain regions have a substantial impact on children with ADHD's hyperactivity, impulsivity and attention span. The presence of two crucial 5-HT receptors, specifically 5-hydroxytryptamine 1A and 2A receptors, have been identified as closely related to the behaviors associated with ADHD (26). Additionally, the 5-hydroxytryptamine transporter (SERT), 5-HTR 1B and 5-HTR 2A genes are involved in the pathophysiology of ADHD (27). The 5-hydroxytryptamine transporter gene (SLC6A4/5-HTT) encodes the 5-hydroxytryptamine transporter (SERT) and regulates the effectiveness of 5-HT. This gene promoter region (5-HTTLPR) is associated with ADHD pathogenesis as the long allele (L) and the short allele (S). Children with ADHD exhibit more evident behavioral issues and hyperactivity when they have the "S" allele and the "S/S" genotype, and a greater degree of executive function impairment when they have the "L" allele (28).

2.1.3 Genes connected to the noradrenergic system

The norepinephrine transporter (NET, SLC6A2) was discovered to reuptake sympathetically released norepinephrine (NE) into the presynaptic membrane via active transport. Since norepinephrine transporter antagonists can affect the effectiveness of pharmacological treatment in children with ADHD, the norepinephrine transporter gene has emerged as the most extensively researched noradrenergic system gene. According to Shang et al. (29), children with ADHD can have their intrinsic brain activity, attention, and visual memory regulated by the norepinephrine transporter gene. Shirama et al. (30) concluded that NE modulation of serum concentrations and gene interactions alter alertness in ADHD patients, leading to an increased likelihood of dangerous behaviors in ADHD patients. The findings of Hawi et al. (31) revealed a high correlation between the development of ADHD and SLC6A2. Wang et al. (32) found that the α-2A adrenergic receptor (ADRA2A) gene is also a candidate gene, and children with the ADRA2A rs553668 GG/GA genotype were more likely to develop ADHD than those with the ADRA2A rs553668 AA genotype.

2.2 ADHD environmental risk factors

Environmental risk factors, which mostly include psychosocial variables, pregnancy, and perinatal risk factors, are directly linked to the development of ADHD.

2.2.1 Pregnancy and perinatal risk factors

The development of children with ADHD has been discovered to be influenced by perinatal circumstances, environmental variables, intrauterine factors, and maternal self-factors throughout pregnancy. For example, children are more likely to acquire ADHD if their mothers smoke, drink excessively, or are exposed to air pollutants (polycyclic aromatic hydrocarbons), or field nonionizing nonionizing radiation when they are pregnant (33–36). Acetaminophen exposure during pregnancy has been reported to be highly related to a high incidence of ADHD in children (37). There have also been reports of possible risk factors for ADHD in children, including maternal pre-pregnancy overweight or obesity, severe mental illness in the parents, hypothyroxinemia, depression, and gestational diabetes mellitus (38–43).

2.2.2 Psychosocial factors

Psychosocial factors primarily include parental mental health, marital harmony, parental relationships, and family education methods. However, the impact of the natural physical environment, including the children's living conditions and family's financial status on the onset of symptoms and overall course of ADHD patients should not be discounted. For instance, Nilsen et al. (44) discovered that children who are exposed to cigarette smoke may be more likely to experience symptoms of ADHD. The financial status of a family may also effect a child's likelihood of developing ADHD (45). Low family income has often been linked to an elevated risk of ADHD in children within research (46, 47). Meanwhile, the development of ADHD can also be influenced by parental mental health, marital status, and parental relationship status. A study (48) confirmed that mothers of ADHD children exhibit more pronounced symptoms of anxiety and depression than their fathers. Furthermore, children with ADHD are frequently exposed to inappropriate educational techniques for extended periods, which makes them increasingly likely to exhibit abnormal behavioral patterns.

Scholars have studied the mechanisms by which environmental factors contribute to the development of ADHD in children. It was found that children whose mothers smoked during pregnancy had reduced volumes of cortical gray matter, cerebellum, and corpus callosum, and thinning of frontal, temporal, and parietal regions, along with alterations in the white matter microstructure of several major connective bundles. Importantly these alterations in brain regions have also been associated with deficits in cognitive performance, auditory processing, social development and ADHD. At the same time, studies have shown that adolescents whose mothers smoked during pregnancy showed inefficient recruitment of relevant brain regions (including the temporal lobe, hippocampus and cerebellum) during response inhibition, attention and memory tasks (49). Prenatal alcohol-exposed children have reduced brain volumes and abnormalities in the frontal, parietal, and temporal lobes in terms of volume, gray matter density, shape, and cortical thickness (50), which have been associated with attention deficits and impulsive behavior (51).

Peterson et al. applied magnetic resonance imaging studies have found that prenatal exposure to PAH air pollutants disrupts the development of white matter in the left hemisphere of children, particularly in the frontal, parietal, and temporal lobes, which can lead to ADHD symptoms and externalizing problems since this white matter contributes to attention and impulse control (33). Non-clinical studies have shown evidence of various potential mechanisms for the deleterious effects of acetaminophen on neurodevelopment. Blecharz-Klin et al. (52) found that rats receiving therapeutic doses of acetaminophen significantly modulated neurotransmission in brain structures (prefrontal cortex, hypothalamus, and striatum) associated with behavior and working memory.

The contribution of maternal overweight/obesity to unfavorable brain development is partly influenced by inflammatory phenomena. Thus, inflammation may play a role in the association between maternal overweight/obesity and ADHD in children and adolescents. Obese pregnant women have higher circulating levels of pro-inflammatory cytokines than normal-weight pregnant women, and the normal developmental trajectory of the fetal brain may be interrupted by exposure to infections and high levels of pro-inflammatory cytokines, with long-lasting or persistent consequences for gray matter volume and white matter integrity (53, 54). This leaves the fetus vulnerable to psychiatric complications, and thus ADHD is associated with elevated levels of inflammatory cytokines (55, 56).

Recent data from the existing literature suggests that gestational diabetes mellitus (GDM) promotes altered structural brain morphology in the offspring. Van Dam et al. found reduced neuronal excitability and neuronal plasticity in children whose mothers had GDM, suggesting that GDM may lead to central nervous system dysfunction, which may be further associated with impaired cognitive and motor outcomes (57). In a recent study, researchers used diffusion tension imaging studies to show that infants of mothers with GDM exhibited microstructural white matter abnormalities associated with impaired neurocognitive abilities (58). Lynch et al. found that reduced hippocampal volume in specific subregions of children exposed to GDM *in utero* is accompanied by specific alterations in hippocampal morphology (59). In another recent study, Ahmed et al. observed reduced cortical thickness in multiple brain structures and poorer overall cognitive performance in diabetes-exposed offspring (60).

2.3 Epigenetic involvement in the pathogenesis of ADHD

In the field of genetics, epigenetics focuses on gene expression and functional regulation rather than alterations to the DNA sequence. The most popular topics of study in epigenetics include DNA methylation, histone modification and non-coding RNA (61). Neurodevelopmental disorders are diseases in which epigenetics plays a prominent role.

2.3.1 DNA methylation

DNA methylation is one of the most researched types of modification in the field of epigenetics. By adding methyl groups to the DNA bases, it controls the expression of genes. Research has revealed that the DRD4 gene exhibits evidence of methylation, with varying levels of methylation among individuals diagnosed with ADHD (61). Moreover, variations in the DNA methylation of genes associated with the dopamine signaling pathway may result in modified expression levels of the relevant genes, which could impact dopamine signaling and neurodevelopment, ultimately linking them to the pathogenesis of ADHD (62, 63). In the methylome analysis of salivary DNA from children with ADHD, Wilmot et al. (64) discovered altered DNA methylation of the vasoactive intestinal peptide receptor 2 (VIPR2). Additionally, methylation of cytosine-phosphate-guanine (CpG), a crucial location upstream of DRD4, plays a significant part in dopamine's ability to regulate. Meanwhile, Wilmot also demonstrated that male children with ADHD had higher levels of CpG methylation in their peripheral tissues, indicating that DNA methylation markers in these children's peripheral tissues may be useful for research in the future. While the study by Walton et al. (65) did not find evidence of differential methylation of DRD4 and VIPR2, it discovered that potential symptomatic changes in children with ADHD have been distinguished by DNA methylation at birth at multiple genomic locations.

Additionally, early-life methylation patterns in the peroxisome network may impair the production of docosahexaenoic acid (DHA), which may contribute to the symptoms of ADHD in children and adolescents. Chen et al. (66) studied twin children with ADHD and discovered several different methylated genes between ADHD and non-ADHD siblings. In contrast to the Wilmot result of hypomethylation of the VIPR2 gene, differential methylation of the VIPR2 gene was also discovered, with hypermethylation in three afflicted twins.

2.3.2 Histone modification

Another significant epigenetic mechanism that alters the modification marks on histone proteins to control gene expression is histone modification. Common histone modifications linked to gene activation and expression include acetylation, methylation and phosphorylation. They play an important role in different nuclear processes, such as replication, DNA repair, transcription, and chromatin structure stabilization (67). However, relatively little work has been done on the role of histone modifications in the pathogenesis of ADHD. Xu et al. (62) studied blood samples from Chinese Han children and found increased expression of histone deacetylase 1 (HDAC1) in children with ADHD compared to healthy controls, suggesting that protein acetylation is reduced in the group of children with ADHD. Histone methylation and acetylation abnormalities, can all result in aberrant gene expression, which can then influence neurodevelopment, synaptic function, and dopamine signaling, impacting the pathogenesis of ADHD.

2.3.3 Non-coding RNAs

Non-coding RNAs are also implicated in the pathophysiology of ADHD, in addition to DNA methylation and histone modification. The expression and function of genes can be controlled by these non-coding RNA molecules (68). Notably, individuals with ADHD may have different levels of several non-coding RNAs' expression. These non-coding RNAs have the potential to impact neurodevelopment, synaptic function, and dopamine signaling pathways through controlling the expression of particular genes. Srivastav et al. (69) observed that peripheral microRNA concentrations were different in both animal models and children with ADHD. In 2023, Dypås et al. discovered 32 microRNAs that were strongly linked to features related to ADHD, including hyperactivity (29) and inattention (3) (70).

3 Comorbidities of ADHD

Comorbidity refers to the presence of more than one disease diagnosis in a patient, and ADHD is frequently comorbid with other disorders, both psychiatric disorders and non-mental diseases, with up to 70%–80% of individuals with ADHD experiencing concomitant psychiatric disorders throughout their lives (71), including oppositional defiant disorder (ODD), conduct disorder (CD), major depressive disorder (MDD), bipolar disorder (BD), anxiety disorders (AD), and substance use disorders (SUD). In addition, ADHD is highly comorbid with other neurodevelopmental disorders, such as autism spectrum disorders (ASD), learning disabilities (LD), and tic disorders (TD). According to recent research, non-mental disorders are very common in individuals with ADHD and greatly lower quality of life. Research on non-mental diseases that co-occur with ADHD has demonstrated a strong correlation with obesity, diabetes mellitus, sleep disorders, epilepsy, and allergic diseases (72–74). Comorbidities frequently cause children with ADHD to have significantly impaired social functioning and complicate their clinical presentation, diagnosis, and course of treatment. For this reason, it is critical to understand why comorbidity between ADHD and other diseases is so common.

Studies have revealed a biological explanation for the co-occurrence of ODD in children with ADHD. This includes a shared genetic basis involving the genes encoding androgen receptors and adrenal hormones. Additionally, it has been proposed that there is a strong correlation between serum 5-hydroxytryptamine concentrations and aggressive behavior in individuals. Furthermore, Noordermeer et al. demonstrated that children with comorbid ODD and ADHD displayed genetic variations in working memory, facial expression detection, and temporal processing, indicating neurocognitive impairment (75). According to an etiological study of children with co-occurring CD and ADHD, there may be hereditary and environmental factors that contribute to both conditions (76). The persistent weight of linked emotional and cognitive features in people with ADHD, as well as the association between psychosocial and functional stressors in daily life, may be the cause of ADHD and mood disorders and the prevalence of comorbid anxiety and SUD (77–79). Moreover, rather than being the result of exposure to these exposures, mental comorbidity may also be a direct expression of common genetic variables between ADHD, comorbid conditions, and related emotional, cognitive, and behavioral features. Fraporti et al. (80) reported that the interaction between the ADORA2A gene and the DRD2 gene affects anxiety disorders in children with ADHD. Demontis et al. discovered an association between anxiety disorders and the DRD2 gene in children with ADHD. A GWAS meta-analysis of ADHD revealed that obesity, insomnia, ASD, schizophrenia, MDD, and cannabis use disorders have significant genetic correlations with ADHD, and there is genetic overlap between them (74). Therefore, a major contributing factor to the explanation of the correlation between co-occurring features and comorbid psychiatric disorders and ADHD is genetics.

One of the most widely studied co-occurring nonmental diseases in ADHD patients is epilepsy. The prevalence of epilepsy ranges from 0.5% to 0.9% in children worldwide (81), and it is often comorbid with other psychiatric disorders, such as ASD, ADHD, and AD, with ADHD being the most common. Some researchers have also suggested that the relationship between epilepsy and ADHD is bidirectional (82) and that ADHD may contribute to an elevated risk of seizures, while chronic recurrent abnormal discharges in children with epilepsy may exacerbate symptoms of ADHD, such as poor attentional control and impulsive and hyperactive behavior. The pathogenesis of epilepsy co-occurring with ADHD is often caused by a combination of factors and may include related mechanisms such as structural brain abnormalities, genetic factors, and neurobiochemical mechanisms.

In terms of brain structure, Karalok et al. (83) reported that both children with benign childhood epilepsy with centrotemporal spikes (BECTs) and children with BECTs with comorbid ADHD showed cortical structure abnormalities (cortical area thinning), but comorbid ADHD in children with epilepsy was more strongly associated with cortical area thinning. In terms of genetic factors, the genotypic association between ADHD and epilepsy is extremely high, and this correlation can be explained by the influence of family aggregation, mainly on the maternal side, as well as by individual-specific environmental factors (84). A number of studies have suggested that epilepsy comorbid with ADHD may be due to the presence of common genetic abnormalities between the two, mainly in the IQSec2 gene, the SLC6A1 gene, the SLC9A9 gene, the Dlg4 gene, and the Vamp2 gene (85–87). In terms of neurobiochemistry, abnormalities in dopamine receptor function or dopamine overproduction in the central nervous system are currently considered to be the main mechanisms for the co-occurrence of epilepsy and ADHD.

4 Neuroimaging features

Based on some studies, cortical maturation in ADHD patients involves multiple regions and cortical dimensions. Primarily, this is manifested in ADHD patients as delayed developmental trajectories. Previously, Shaw et al. (88) also demonstrated that cortical maturation in ADHD patients is significantly delayed. Likewise, Qian et al. (89) found developmentally relevant delays in inhibitory and transfer functions in children with ADHD. Children with ADHD are more affected by subcortical abnormalities; the more delayed subcortical structure development, the more prominent the hyperactivity and impulsivity symptoms in the child, and the slower the cortical thinning of the prefrontal and cingulate regions (90, 91). Besides, a report published in 2021 identified that children with ADHD had smaller cerebral cortex total surface area, cortical thickness and subcortical areas (7). Simultaneously, the developmental trajectory of gray matter volume and cortical thickness is correlated with changes in symptoms of ADHD. The more severe the symptoms, the slower the brain matures (65, 92). Therefore, the characterization of the corresponding brain regions of ADHD patients in magnetic resonance imaging will be explored in terms of the following imaging techniques.

4.1 Functional magnetic resonance imaging

Functional magnetic resonance imaging (fMRI) primarily uses magnetic fields to measure the blood oxygen level-dependent (BOLD) response in the cerebral cortex and subcortical regions. By gathering data from participants while they are at rest and in various task-design scenarios, fMRI can indirectly reflect how the brain functions.

The resting-state fMRI describes the low-frequency fluctuations that arise spontaneously during an MRI scan while the patient's body is at rest and not thinking. The resting-state network describes the multiple brain regions where the fMRI signals are correlated with each other in the resting state. The default mode network (DMN), a significant resting-state network, is made up of brain areas that, in healthy individuals, exhibit increased activity during waking rest and deactivation with increasing attentional demands (93, 94). However, this negative correlation between the default mode network and attention will be diminished or nonexistent in ADHD patients, which could account for the reduced sustained attention brought on by default mode network-mediated attention deficiencies (95–98).

Moreover, Sun et al. (99) demonstrated that children with ADHD had more fragmented resting-state network connection patterns and delayed functional network development. Research employing resting-state fMRI has demonstrated dysfunctional connectivity in the brain regions of the dorsal anterior cingulate cortex and posterior cingulate cortex and aberrant developmental patterns in the interaction between the dorsal anterior cingulate cortex and DMN in patients with ADHD (99). Furthermore, TIAN et al. (100) discovered that children with ADHD had significantly improved functional connectivity in the dorsal anterior cingulate cortex as well as bilateral thalamus, bilateral cerebellum, and bilateral insula. Additionally, children diagnosed with ADHD exhibited reduced functional connectivity in the areas of the thalamus and basal ganglia (96).

fMRI combines many task paradigms to represent the various cognitive processes occurring in the brain. Studies on ADHD patients have revealed impairments in cognitive abilities such as working memory, sustained attention, and inhibitory function (101). Research has demonstrated (102) that when engaged in working memory tasks, individuals with ADHD exhibit decreased activity in bilateral frontal lobes, frontal-to-parietal areas and the insulae. Likewise, in comparison to normal controls, working memory-related brain regions consistently and repetitively exhibit underactivation (103, 104). Children with ADHD have also been observed to show under-activation of brain regions associated with inhibitory control in inhibitory function tasks (103, 104).

Furthermore, Christakou et al. (105) used magnetic resonance imaging to demonstrate that patients with ADHD exhibited significantly higher activation in precuneus regions but significantly lower activation in the left dorsolateral prefrontal cortex, superior parietal gyrus, and striatal-thalamic regions in an alertness task involving sustained attention. Additionally, children with ADHD mostly exhibit decreased activation of the right dorsolateral frontal-basal ganglia-thalamic-parietal network when doing tasks that target attentional processes (103, 106). Reduced frontal-striatal loop activation has also been seen in children with ADHD during sustained attention activities (107, 108).

4.2 Functional near-infrared spectroscopy

Functional near-infrared spectroscopy (fNIRS) utilizes near-infrared light to track variations in oxygen and deoxyhemoglobin concentrations over time. Notably, it has been used extensively in studies because it is less sensitive to motion artifacts than fMRI, safe, inexpensive, and requires less body immobilization. fNIRS is a useful tool for measuring brain activity during resting and task states. Blood flow and volume rise when brain areas are activated in response to stimuli, and this can be measured by determining the concentration of local hemoglobin (HbO), deoxyhemoglobin (HbR), or total hemoglobin (HbT). Thus, fNIRS is a valuable assessment instrument for neurodevelopmental research, particularly in analyzing the effects of interventions on children with ADHD (109, 110).

Researchers have demonstrated that resting-state fNIRS is repeatable in terms of functional connectivity and network topological characteristics (111–114). According to research conducted in 2020 by Wang et al. (115), children with ADHD had significantly lower functional connectivity and global efficiency of brain networks during the resting state when using fNIRS. Concurrently, each network node in the brain experienced corresponding changes in efficiency. The results may indicate deficiencies in reaction inhibition and information overload in vision and attention in children with ADHD, according to the dual pathway hypothesis. It was further established that functional connection networks and symptoms of ADHD are related. Besides, a negative correlation was identified between the reduced efficiency of the right somatomotor network nodes and the symptoms of hyperactivity and impulsivity. In 2021, based on a multiscale entropy study, Hu et al. found (116) that children with ADHD had lower brain signal variability in several functional brain networks (such as the default mode, frontoparietal network, attentional network, and visual network) than did healthy children, aligning with Wang's et al. (115) findings.

When examining the potential connection between alterations in brain activation and executive function in ADHD patients, fNIRS is a highly effective tool (117, 118). Meanwhile, a task-based investigation of dynamic functional connectivity in children with ADHD was carried out by Sutoko et al. (119). The frontal-cingulate-striatal-thalamic and frontal-parietal-cerebellar networks, which control working memory, attention, and inhibitory function, exhibit complicated multisystem deficits in ADHD patients.

In inhibitory control tasks, adolescents with ADHD have inferior connectivity within the inhibitory network (120) Sutoko et al. (121) discovered that children with ADHD tend to show a decreased likelihood of an advantageous connectivity state and an increased likelihood of other connectivity states in an inhibitory control task. In a 2023 study, Hou et al. (122) demonstrated that activation areas inhibiting cognitive interference ability were concentrated in the bilateral prefrontal cortex, whereas activation areas inhibiting control skills were broadly distributed in the bilateral prefrontal cortex, parietal and frontal regions, the left temporal and superior temporal cortex, the right inferior frontal gyrus, and the middle frontal gyrus. According to Inoue et al. (123), children with ADHD showed decreased prefrontal activation during a go/no-go task. Children with ADHD showed lower levels of brain activity in the left prefrontal cortex during go/no-go task, according to a 2017 study (124). Furthermore, Wu et al. (125) discovered that during a go/no-go task, children with ADHD had decreased levels of oxyhemoglobin concentration in the prefrontal brain. Prior research utilizing fMRI has also revealed that when children with ADHD do an inhibitory task, there is a significant bilateral decrease in cerebral blood flow in the prefrontal cortex region (126, 127).

In working memory tasks, the activation areas of verbal working memory in healthy individuals were primarily located in the right prefrontal cortex (PFC), particularly in the right ventral lateral prefrontal cortex (VLPFC) and dorsal lateral prefrontal cortex (DLPFC), and the activation areas of visuospatial working memory were found in the right prefrontal cortex, the frontal pole, and the left superior frontal cortex. However, the activation areas of patients with ADHD were less significant than those of healthy individuals, and the corresponding brain regions of working memory were either non-activated or weakly activated (122). The well-known working memory paradigm known as the n-back task has been used in functional neuroimaging studies of ADHD (128). Using fNIRS during the n-back task, Gu et al. (129) discovered that prefrontal complexity was lower in ADHD patients than in healthy controls. Two recent fNIRS investigations have demonstrated that when working on working memory tasks, the left DLPFC is more active in patients with ADHD (130, 131).

5 Future research directions

Future research on ADHD will focus on the following areas. Firstly, to more precisely clinically phenotype ADHD, it might be possible to synthesize genetic GWAS big data analysis with findings from ADHD cognitive science, brain connectivity mapping, and neuroimaging; in the future, and it might be possible to phenotype the ADHD phenotype in terms of functional impairment dimensions. Secondly, objective markers from genetics, epigenetics, and environmental factors that are strongly linked to the development of ADHD will be identified and utilized to facilitate early screening and support early diagnosis. Thirdly, neuroimaging studies of ADHD will gradually transition from MRI or near-infrared spectroscopic studies of ADHD to comprehensive studies integrating ADHD risk genes, specific cell types, developmental age-related brain networks, and neural network connectivity related to specific brain functions (cognition, emotion regulation, etc.). Additionally, they will map ADHD brain functions related to the age of onset of ADHD and its phenotypes, providing a powerful adjunct to the diagnosis of ADHD, as well as to typing, intervention and evaluation of therapeutic efficacy.

Furthermore, given the research on the mechanism of ADHD psychology and cognitive deficits, a digital, multi-scenario cognitive training system suitable for ADHD children of different ages will be developed, an accurate ADHD assessment system based on cognitive, behavioral, and emotional analyses as well as a digital cognitive and psychological intervention system will be established, and an intervention on ADHD cognitive deficits will be carried out with ADHD data-based prescriptions.

Besides, we will integrate ADHD neurological examination, cognitive and behavioral assessment, and brain network connection image analysis (resting state and task state) to assess ADHD children in all aspects, formulate individualized intervention plans, carry out related neuromodulation including repetitive transcranial magnetic stimulation, electroencephalographic biofeedback, magnetic resonance biofeedback, and transcranial direct current (DC)/alternating current (AC) stimulation, and observe the changes in the neuromodulation technology on the neural network connection and neural function, and establish reasonable and feasible neuromodulation therapeutic guidelines.

Finally, the pharmacological personalized treatment approach is a new direction for future ADHD treatment, aiming to identify biomarkers that can predict treatment response and guide personalized intervention. Based on genomics, neuroimaging and other neurological techniques to reveal the underlying biological mechanisms of ADHD, new interventional drugs can be developed to combat ADHD, which will help to target the treatment of different phenotypes of ADHD.

6 Conclusions

In summary, ADHD is a critically important neurodevelopmental condition in children. Through genetic GWAS analysis, epigenetic and neuroimaging studies in children with ADHD, researchers have discovered genome-wide significant loci associated with the development of ADHD, as well as thinning of gray matter thickness throughout the entire cerebral cortex, abnormalities in brain structure and function, and delayed development of neural networks in children with ADHD. This review offers potential uses in the investigation of the brain underpinnings of development, aging, and neurological illnesses.

Author contributions

FS: Writing – original draft. HZ: Writing – review & editing.

Funding

The authors declare that no financial support was received for the research, authorship, and/or publication of this article.

Conflict of interest

The authors declare that the research was conducted in the absence of any commercial or financial relationships that could be construed as a potential conflict of interest.

Publisher's note

References

1. Sayal K, Prasad V, Daley D, Ford T, Coghill D. ADHD in children and young people: prevalence, care pathways, and service provision. *Lancet Psychiatry*. (2018) 5 (2):175–86. doi: 10.1016/S2215-0366(17)30167-0

2. Wolraich ML, Hagan JF Jr, Allan C, Chan E, Davison D, Earls M, et al. Clinical practice guideline for the diagnosis, evaluation, and treatment of attention-deficit/hyperactivity disorder in children and adolescents. *Pediatrics*. (2019) 144(4). doi: 10.1542/peds.2019-2528

3. Li F, Cui Y, Li Y, Guo L, Ke X, Liu J, et al. Prevalence of mental disorders in school children and adolescents in China: diagnostic data from detailed clinical assessments of 17,524 individuals. *J Child Psychol Psychiatry*. (2022) 63(1):34–46. doi: 10.1111/jcpp.13445

4. Prieto AT. Attention-deficit/hyperactivity disorder and substance abuse. Scientific evidence. *Medicina*. (2020) 80(Suppl. 2):76–9.

5. Shi X, Ji Y, Cai S, Wu Y, Zhang L, Shen L, et al. Comorbidities and functional impairments in children with attention deficit hyperactivity disorder in China: a hospital-based retrospective cross-sectional study. *BMJ Open*. (2021) 11(3):e042196. doi: 10.1136/bmjopen-2020-042196

6. Cortese S. The neurobiology and genetics of attention-deficit/hyperactivity disorder (ADHD): what every clinician should know. *Eur J Paediatr Neurol*. (2012) 16(5):422–33. doi: 10.1016/j.ejpn.2012.01.009

7. Faraone SV, Banaschewski T, Coghill D, Zheng Y, Biederman J, Bellgrove MA, et al. The world federation of ADHD international consensus statement: 208 evidence-based conclusions about the disorder. *Neurosci Biobehav Rev*. (2021) 128:789–818. doi: 10.1016/j.neubiorev.2021.01.022

8. Barkley RA. Behavioral inhibition, sustained attention, and executive functions: constructing a unifying theory of ADHD. *Psychol Bull*. (1997) 121(1):65–94. doi: 10.1037/0033-2909.121.1.65

9. Uchida M, DiSalvo M, Walsh D, Biederman J. The heritability of ADHD in children of ADHD parents: a post-hoc analysis of longitudinal data. *J Atten Disord*. (2023) 27(3):250–7. doi: 10.1177/10870547221136251

10. Faraone SV, Larsson H. Genetics of attention deficit hyperactivity disorder. *Mol Psychiatry*. (2019) 24(4):562–75. doi: 10.1038/s41380-018-0070-0

11. Demontis D, Walters RK, Martin J, Mattheisen M, Als TD, Agerbo E, et al. Discovery of the first genome-wide significant risk loci for attention deficit/hyperactivity disorder. *Nat Genet*. (2019) 51(1):63–75. doi: 10.1038/s41588-018-0269-7

12. Demontis D, Walters GB, Athanasiadis G, Walters R, Therrien K, Nielsen TT, et al. Genome-wide analyses of ADHD identify 27 risk loci, refine the genetic architecture and implicate several cognitive domains. *Nat Genet*. (2023) 55 (2):198–208. doi: 10.1038/s41588-022-01285-8

13. Warikoo N, Faraone SV. Background, clinical features and treatment of attention deficit hyperactivity disorder in children. *Expert Opin Pharmacother*. (2013) 14 (14):1885–906. doi: 10.1517/14656566.2013.818977

14. Chang CH, Yu CJ, Du JC, Chiou HC, Chen HC, Yang W, et al. The interactions among organophosphate pesticide exposure, oxidative stress, and genetic polymorphisms of dopamine receptor D4 increase the risk of attention deficit/hyperactivity disorder in children. *Environ Res*. (2018) 160:339–46. doi: 10.1016/j.envres.2017.10.011

15. Tong JH, Cummins TD, Johnson BP, McKinley LA, Pickering HE, Fanning P, et al. An association between a dopamine transporter gene (*SLC6A3*) haplotype and ADHD symptom measures in nonclinical adults. *Am J Med Genet B Neuropsychiatr Genet*. (2015) 168b(2):89–96. doi: 10.1002/ajmg.b.32283

16. Pineau G, Villemonteix T, Slama H, Kavec M, Balériaux D, Metens T, et al. Dopamine transporter genotype modulates brain activity during a working memory task in children with ADHD. *Res Dev Disabil*. (2019) 92:103430. doi: 10.1016/j.ridd.2019.103430

17. Hong JH, Hwang IW, Lim MH, Kwon HJ, Jin HJ. Genetic associations between ADHD and dopaminergic genes (DAT1 and DRD4) VNTRs in Korean children. *Genes Genomics*. (2018) 40(12):1309–17. doi: 10.1007/s13258-018-0726-9

18. Gharaibeh MY, Batayneh S, Khabour OF, Daoud A. Association between polymorphisms of the DBH and DAT1 genes and attention deficit hyperactivity disorder in children from Jordan. *Exp Ther Med*. (2010) 1(4):701–5. doi: 10.3892/etm_00000108

19. Guney E, Işeri E, Ergun SG, Percin EF, Ergun MA, Yalcin O, et al. The correlation of attention deficit hyperactivity disorder with DRD4 gene polymorphism in Turkey. *Int J Hum Genet*. (2013) 13:145–52. doi: 10.1080/09723757.2013.11886210

20. Qian Q, Wang Y, Zhou R, Yang L, Faraone SV. Family-based and case-control association studies of DRD4 and DAT1 polymorphisms in Chinese attention deficit hyperactivity disorder patients suggest long repeats contribute to genetic risk for the disorder. *Am J Med Genet B Neuropsychiatr Genet*. (2004) 128b(1):84–9. doi: 10.1002/ajmg.b.30079

21. Banoei MM, Majidizadeh T, Shirazi E, Moghimi N, Ghadiri M, Najmabadi H, et al. No association between the DAT1 10-repeat allele and ADHD in the Iranian population. *Am J Med Genet B Neuropsychiatr Genet*. (2008) 147b(1):110–1. doi: 10.1002/ajmg.b.30578

22. Simsek M, Al-Sharbati M, Al-Adawi S, Ganguly SS, Lawatia K. Association of the risk allele of dopamine transporter gene (DAT1*10) in Omani male children with attention-deficit hyperactivity disorder. *Clin Biochem*. (2005) 38(8):739–42. doi: 10.1016/j.clinbiochem.2005.04.016

23. Thursina C, Nurputra DK, Harahap ISK, Harahap NIF, Sa'adah N, Wibowo S, et al. Determining the association between polymorphisms of the DAT1 and DRD4 genes with attention deficit hyperactivity disorder in children from Java Island. *Neurol Int*. (2020) 12(1):8292. doi: 10.4081/ni.2020.8292

24. Kuc K, Bielecki M, Racicka-Pawlukiewicz E, Czerwinski MB, Cybulska-Klosowicz A. The *SLC6A3* gene polymorphism is related to the development of attentional functions but not to ADHD. *Sci Rep*. (2020) 10(1):6176. doi: 10.1038/s41598-020-63296-x

25. Cifariello A, Pompili A, Gasbarri A. 5-HT(7) receptors in the modulation of cognitive processes. *Behav Brain Res*. (2008) 195(1):171–9. doi: 10.1016/j.bbr.2007.12.012

26. Albert PR, Le François B, Vahid-Ansari F. Genetic, epigenetic and posttranscriptional mechanisms for treatment of major depression: the 5-HT1A receptor gene as a paradigm. *J Psychiatry Neurosci*. (2019) 44(3):164–76. doi: 10.1503/jpn.180209

27. Kautzky A, Vanicek T, Philippe C, Kranz GS, Wadsak W, Mitterhauser M, et al. Machine learning classification of ADHD and HC by multimodal serotonergic data. *Transl Psychiatry*. (2020) 10(1):104. doi: 10.1038/s41398-020-0781-2

28. Chatterjee M, Saha S, Sinha S, Mukhopadhyay K. A three-pronged analysis confirms the association of the serotoninergic system with attention deficit hyperactivity disorder. *World J Pediatr*. (2022) 18(12):825–34. doi: 10.1007/s12519-022-00614-5

29. Shang CY, Lin HY, Gau SS. The norepinephrine transporter gene modulates intrinsic brain activity, visual memory, and visual attention in children with attention-deficit/hyperactivity disorder. *Mol Psychiatry*. (2021) 26(8):4026–35. doi: 10.1038/s41380-019-0545-7

30. Shirama A, Takeda T, Ohta H, Iwanami A, Toda S, Kato N. Atypical alert state control in adult patients with ADHD: a pupillometry study. *PLoS ONE*. (2020) 15(12): e0244662. doi: 10.1371/journal.pone.0244662

31. Hawi Z, Matthews N, Barry E, Kirley A, Wagner J, Wallace RH, et al. A high density linkage disequilibrium mapping in 14 noradrenergic genes: evidence of association between SLC6A2, ADRA1B and ADHD. *Psychopharmacology*. (2013) 225(4):895–902. doi: 10.1007/s00213-012-2875-x

32. Wang Y, Wang T, Du Y, Hu D, Zhang Y, Li H, et al. Polygenic risk of genes involved in the catecholamine and serotonin pathways for ADHD in children. *Neurosci Lett*. (2021) 760:136086. doi: 10.1016/j.neulet.2021.136086

33. Peterson BS, Rauh VA, Bansal R, Hao X, Toth Z, Nati G, et al. Effects of prenatal exposure to air pollutants (polycyclic aromatic hydrocarbons) on the development of brain white matter, cognition, and behavior in later childhood. *JAMA psychiatry*. (2015) 72(6):531–40. doi: 10.1001/jamapsychiatry.2015.57

34. He Y, Chen J, Zhu LH, Hua LL, Ke FF. Maternal smoking during pregnancy and ADHD: results from a systematic review and meta-analysis of prospective cohort studies. *J Atten Disord*. (2020) 24(12):1637–47. doi: 10.1177/1087054717696766

35. Wetherill L, Foroud T, Goodlett C. Meta-analyses of externalizing disorders: genetics or prenatal alcohol exposure? *Alcohol Clin Exp Res*. (2018) 42(1):162–72. doi: 10.1111/acer.13535

36. Li DK, Chen H, Ferber JR, Hirst AK, Odouli R. Association between maternal exposure to magnetic field nonionizing radiation during pregnancy and risk of attention-deficit/hyperactivity disorder in offspring in a longitudinal birth cohort. *JAMA Netw Open*. (2020) 3(3):e201417. doi: 10.1001/jamanetworkopen.2020.1417

37. Gou X, Wang Y, Tang Y, Qu Y, Tang J, Shi J, et al. Association of maternal prenatal acetaminophen use with the risk of attention deficit/hyperactivity disorder in offspring: a meta-analysis. *Aust N Z J Psychiatry*. (2019) 53(3):195–206. doi: 10.1177/0004867418823276

38. Rodriguez A. Maternal pre-pregnancy obesity and risk for inattention and negative emotionality in children. *J Child Psychol Psychiatry*. (2010) 51(2):134–43. doi: 10.1111/j.1469-7610.2009.02133.x

39. Fuemmeler BF, Zucker N, Sheng Y, Sanchez CE, Maguire R, Murphy SK, et al. Pre-pregnancy weight and symptoms of attention deficit hyperactivity disorder and executive functioning behaviors in preschool children. *Int J Environ Res Public Health*. (2019) 16(4):669. doi: 10.3390/ijerph16040667

40. McCoy BM, Rickert ME, Class QA, Larsson H, Lichtenstein P, D'Onofrio BM. Mediators of the association between parental severe mental illness and offspring neurodevelopmental problems. *Ann Epidemiol*. (2014) 24(9):629–34.e1. doi: 10.1016/j.annepidem.2014.05.010

41. Modesto T, Tiemeier H, Peeters RP, Jaddoe VW, Hofman A, Verhulst FC, et al. Maternal mild thyroid hormone insufficiency in early pregnancy and attention-deficit/hyperactivity disorder symptoms in children. *JAMA Pediatr*. (2015) 169(9):838–45. doi: 10.1001/jamapediatrics.2015.0498

42. Wolford E, Lahti M, Tuovinen S, Lahti J, Lipsanen J, Savolainen K, et al. Maternal depressive symptoms during and after pregnancy are associated with attention-deficit/hyperactivity disorder symptoms in their 3- to 6-year-old children. *PLoS ONE*. (2017) 12(12):e0190248. doi: 10.1371/journal.pone.0190248

43. Nomura Y, Marks DJ, Grossman B, Yoon M, Loudon H, Stone J, et al. Exposure to gestational diabetes mellitus and low socioeconomic status: effects on neurocognitive development and risk of attention-deficit/hyperactivity disorder in offspring. *Arch Pediatr Adolesc Med*. (2012) 166(4):337–43. doi: 10.1001/archpediatrics.2011.784

44. Nilsen FM, Tulve NS. A systematic review and meta-analysis examining the interrelationships between chemical and non-chemical stressors and inherent characteristics in children with ADHD. *Environ Res*. (2020) 180:108884. doi: 10.1016/j.envres.2019.108884

45. Ren Y, Fang X, Fang H, Pang G, Cai J, Wang S, et al. Predicting the adult clinical and academic outcomes in boys with ADHD: a 7- to 10-year follow-up study in China. *Front Pediatr*. (2021) 9:634633. doi: 10.3389/fped.2021.634633

46. Claussen AH, Holbrook JR, Hutchins HJ, Robinson LR, Bloomfield J, Meng L, et al. All in the family? A systematic review and meta-analysis of parenting and family environment as risk factors for attention-deficit/hyperactivity disorder (ADHD) in children. *Prev Sci*. (2022):1–23. doi: 10.1007/s11121-022-01358-4

47. Duh-Leong C, Fuller A, Brown NM. Associations between family and community protective factors and attention-deficit/hyperactivity disorder outcomes among US children. *J Dev Behav Pediatr*. (2020) 41(1):1–8. doi: 10.1097/DBP.0000000000000720

48. Durukan İ, Kara K, Almbaideen M, Karaman D, Gül H. Alexithymia, depression and anxiety in parents of children with neurodevelopmental disorder: comparative study of autistic disorder, pervasive developmental disorder not otherwise specified and attention deficit-hyperactivity disorder. *Pediatr Int*. (2018) 60(3):247–53. doi: 10.1111/ped.13510

49. Bublitz MH, Stroud LR. Maternal smoking during pregnancy and offspring brain structure and function: review and agenda for future research. *Nicotine Tob Res*. (2012) 14(4):388–97. doi: 10.1093/ntr/ntr191

50. Lebel C, Roussotte F, Sowell ER. Imaging the impact of prenatal alcohol exposure on the structure of the developing human brain. *Neuropsychol Rev*. (2011) 21 (2):102–18. doi: 10.1007/s11065-011-9163-0

51. Paolozza A, Rasmussen C, Pei J, Hanlon-Dearman A, Nikkel SM, Andrew G, et al. Deficits in response inhibition correlate with oculomotor control in children with fetal alcohol spectrum disorder and prenatal alcohol exposure. *Behav Brain Res*. (2014) 259:97–105. doi: 10.1016/j.bbr.2013.10.040

52. Blecharz-Klin K, Piechal A, Pyrzanowska J, Joniec-Maciejak I, Kiliszek P, Widy-Tyszkiewicz E. Paracetamol–the outcome on neurotransmission and spatial learning in rats. *Behav Brain Res*. (2013) 253:157–64. doi: 10.1016/j.bbr.2013.07.008

53. Short SJ, Lubach GR, Karasin AI, Olsen CW, Styner M, Knickmeyer RC, et al. Maternal influenza infection during pregnancy impacts postnatal brain development in the rhesus monkey. *Biol Psychiatry*. (2010) 67(10):965–73. doi: 10.1016/j.biopsych.2009.11.026

54. Willette AA, Lubach GR, Knickmeyer RC, Short SJ, Styner M, Gilmore JH, et al. Brain enlargement and increased behavioral and cytokine reactivity in infant monkeys following acute prenatal endotoxemia. *Behav Brain Res*. (2011) 219(1):108–15. doi: 10.1016/j.bbr.2010.12.023

55. Sullivan EL, Nousen EK, Chamlou KA. Maternal high fat diet consumption during the perinatal period programs offspring behavior. *Physiol Behav*. (2014) 123:236–42. doi: 10.1016/j.physbeh.2012.07.014

56. Kang SS, Kurti A, Fair DA, Fryer JD. Dietary intervention rescues maternal obesity induced behavior deficits and neuroinflammation in offspring. *J Neuroinflammation*. (2014) 11:156. doi: 10.1186/s12974-014-0156-9

57. Van Dam JM, Garrett AJ, Schneider LA, Hodyl NA, Goldsworthy MR, Coat S, et al. Reduced cortical excitability, neuroplasticity, and salivary cortisol in 11–13-year-old children born to women with gestational diabetes Mellitus. *EBioMedicine*. (2018) 31:143–9. doi: 10.1016/j.ebiom.2018.04.011

58. Xuan DS, Zhao X, Liu YC, Xing QN, Shang HL, Zhu PY, et al. Brain development in infants of mothers with gestational diabetes mellitus: a diffusion tensor imaging study. *J Comput Assist Tomogr*. (2020) 44(6):947–52. doi: 10.1097/RCT.0000000000001110

59. Lynch KM, Alves JM, Chow T, Clark KA, Luo S, Toga AW, et al. Selective morphological and volumetric alterations in the hippocampus of children exposed in utero to gestational diabetes mellitus. *Hum Brain Mapp*. (2021) 42(8):2583–92. doi: 10.1002/hbm.25390

60. Ahmed S, Cano M, Sánchez M, Hu N, Ibañez G. Effect of exposure to maternal diabetes during pregnancy on offspring's brain cortical thickness and neurocognitive functioning. *Child Neuropsychol*. (2023) 29(4):588–606. doi: 10.1080/09297049.2022.2103105

61. Wang KC, Chang HY. Epigenomics: technologies and applications. *Circ Res*. (2018) 122(9):1191–9. doi: 10.1161/CIRCRESAHA.118.310998

62. Xu Y, Chen XT, Luo M, Tang Y, Zhang G, Wu D, et al. Multiple epigenetic factors predict the attention deficit/hyperactivity disorder among the Chinese Han children. *J Psychiatr Res*. (2015) 64:40–50. doi: 10.1016/j.jpsychires.2015.03.006

63. van Mil NH, Steegers-Theunissen RP, Bouwland-Both MI, Verbiest MM, Rijlaarsdam J, Hofman A, et al. DNA methylation profiles at birth and child ADHD symptoms. *J Psychiatr Res*. (2014) 49:51–9. doi: 10.1016/j.jpsychires.2013.10.017

64. Wilmot B, Fry R, Smeester L, Musser ED, Mill J, Nigg JT. Methylomic analysis of salivary DNA in childhood ADHD identifies altered DNA methylation in VIPR2. *J Child Psychol Psychiatry*. (2016) 57(2):152–60. doi: 10.1111/jcpp.12457

65. Walton E, Pingault JB, Cecil CA, Gaunt TR, Relton CL, Mill J, et al. Epigenetic profiling of ADHD symptoms trajectories: a prospective, methylome-wide study. *Mol Psychiatry*. (2017) 22(2):250–6. doi: 10.1038/mp.2016.85

66. Chen YC, Sudre G, Sharp W, Donovan F, Chandrasekharappa SC, Hansen N, et al. Neuroanatomic, epigenetic and genetic differences in monozygotic twins discordant for attention deficit hyperactivity disorder. *Mol Psychiatry*. (2018) 23 (3):683–90. doi: 10.1038/mp.2017.45

67. Bannister AJ, Kouzarides T. Regulation of chromatin by histone modifications. *Cell Res*. (2011) 21(3):381–95. doi: 10.1038/cr.2011.22

68. Bartel DP. MicroRNAs: target recognition and regulatory functions. *Cell*. (2009) 136(2):215–33. doi: 10.1016/j.cell.2009.01.002

69. Srivastav S, Walitza S, Grünblatt E. Emerging role of miRNA in attention deficit hyperactivity disorder: a systematic review. *Atten Defic Hyperact Disord*. (2018) 10 (1):49–63. doi: 10.1007/s12402-017-0232-y

70. Dypås LB, Duale N, Olsen AK, Bustamante M, Maitre L, Escaramis G, et al. Blood miRNA levels associated with ADHD traits in children across six European birth cohorts. *BMC psychiatry*. (2023) 23(1):696. doi: 10.1186/s12888-023-05199-5

71. Kessler RC, Adler LA, Berglund P, Green JG, McLaughlin KA, Fayyad J, et al. The effects of temporally secondary co-morbid mental disorders on the associations of DSM-IV ADHD with adverse outcomes in the US national comorbidity survey replication adolescent supplement (NCS-A). *Psychol Med*. (2014) 44(8):1779–92. doi: 10.1017/S0033291713002419

72. Muskens JB, Velders FP, Staal WG. Medical comorbidities in children and adolescents with autism spectrum disorders and attention deficit hyperactivity disorders: a systematic review. *Eur Child Adolesc Psychiatry.* (2017) 26(9):1093–103. doi: 10.1007/s00787-017-1020-0

73. Merikangas KR, Calkins ME, Burstein M, He JP, Chiavacci R, Lateef T, et al. Comorbidity of physical and mental disorders in the neurodevelopmental genomics cohort study. *Pediatrics.* (2015) 135(4):e927–38. doi: 10.1542/peds.2014-1444

74. Demontis D, Walters GB, Athanasiadis G, Walters R, Therrien K, Nielsen TT, et al. Author correction: genome-wide analyses of ADHD identify 27 risk loci, refine the genetic architecture and implicate several cognitive domains. *Nat Genet.* (2023) 55(4):730. doi: 10.1038/s41588-023-01350-w

75. Noordermeer SDS, Luman M, Buitelaar JK, Hartman CA, Hoekstra PJ, Franke B, et al. Neurocognitive deficits in attention-deficit/hyperactivity disorder with and without comorbid oppositional defiant disorder. *J Atten Disord.* (2020) 24 (9):1317–29. doi: 10.1177/1087054715606216

76. Tistarelli N, Fagnani C, Troianiello M, Stazi MA, Adriani W. The nature and nurture of ADHD and its comorbidities: a narrative review on twin studies. *Neurosci Biobehav Rev.* (2020) 109:63–77. doi: 10.1016/j.neubiorev.2019.12.017

77. Hartman CA, Rommelse N, van der Klugt CL, Wanders RBK, Timmerman ME. Stress exposure and the course of ADHD from childhood to young adulthood: comorbid severe emotion dysregulation or mood and anxiety problems. *J Clin Med.* (2019) 8(11):1824. doi: 10.3390/jcm8111824

78. Rychik N, Fassett-Carman A, Snyder HR. Dependent stress mediates the relation between ADHD symptoms and depression. *J Atten Disord.* (2021) 25(12):1676–86. doi: 10.1177/1087054720925900

79. Zendarski N, Guo S, Sciberras E, Efron D, Quach J, Winter L, et al. Examining the educational gap for children with ADHD and subthreshold ADHD. *J Atten Disord.* (2022) 26(2):282–95. doi: 10.1177/1087054720972790

80. Fraporti TT, Contini V, Tovo-Rodrigues L, Recamonde-Mendoza M, Rovaris DL, Rohde LA, et al. Synergistic effects between ADORA2A and DRD2 genes on anxiety disorders in children with ADHD. *Prog Neuro-Psychopharmacol Biol Psychiatry.* (2019) 93:214–20. doi: 10.1016/j.pnpbp.2019.03.021

81. Park KJ, Kim MJ, Yum MS, Ko TS, Kim HW. Clinical and neuropsychological characteristics of children with epilepsy and attention-deficit/hyperactivity disorder. *Seizure.* (2021) 91:325–31. doi: 10.1016/j.seizure.2021.06.022

82. Wiggs KK, Chang Z, Quinn PD, Hur K, Gibbons R, Dunn D, et al. Attention-deficit/hyperactivity disorder medication and seizures. *Neurology.* (2018) 90(13): e1104–10. doi: 10.1212/WNL.0000000000005213

83. Karalok ZS, Öztürk Z, Gunes A. Cortical thinning in benign epilepsy with centrotemporal spikes (BECTS) with or without attention-deficit/hyperactivity (ADHD). *J Clin Neurosci.* (2019) 68:123–7. doi: 10.1016/j.jocn.2019.07.014

84. Brikell I, Ghirardi L, D'Onofrio BM, Dunn DW, Almqvist C, Dalsgaard S, et al. Familial liability to epilepsy and attention-deficit/hyperactivity disorder: a nationwide cohort study. *Biol Psychiatry.* (2018) 83(2):173–80. doi: 10.1016/j.biopsych.2017.08.006

85. Moey C, Hinze SJ, Brueton L, Morton J, McMullan DJ, Kamien B, et al. Xp11.2 microduplications including IQSEC2, TSPYL2 and KDM5C genes in patients with neurodevelopmental disorders. *Eur J Hum Genet.* (2016) 24(3):373–80. doi: 10.1038/ejhg.2015.123

86. Poliquin S, Hughes I, Shen W, Mermer F, Wang J, Mack T, et al. Genetic mosaicism, intrafamilial phenotypic heterogeneity, and molecular defects of a novel missense SLC6A1 mutation associated with epilepsy and ADHD. *Exp Neurol.* (2021) 342:113723. doi: 10.1016/j.expneurol.2021.113723

87. Xi XJ, Tang JH, Zhang BB, Xiao X, Hu XY, Wan Y, et al. Dlg4 and Vamp2 are involved in comorbid epilepsy and attention-deficit hyperactivity disorder: a microarray data study. *Epilepsy & Behav.* (2020) 110:107192. doi: 10.1016/j.yebeh.2020.107192

88. Shaw P, Eckstrand K, Sharp W, Blumenthal J, Lerch JP, Greenstein D, et al. Attention-deficit/hyperactivity disorder is characterized by a delay in cortical maturation. *Proc Natl Acad Sci USA.* (2007) 104(49):19649–54. doi: 10.1073/pnas.0707741104

89. Qian Y, Shuai L, Chan RC, Qian QJ, Wang Y. The developmental trajectories of executive function of children and adolescents with attention deficit hyperactivity disorder. *Res Dev Disabil.* (2013) 34(5):1434–45. doi: 10.1016/j.ridd.2013.01.033

90. Castellanos FX, Tannock R. Neuroscience of attention-deficit/hyperactivity disorder: the search for endophenotypes. *Nat Rev Neurosci.* (2002) 3(8):617–28. doi: 10.1038/nrn896

91. Ambrosino S, de Zeeuw P, Wierenga LM, van Dijk S, Durston S. What can cortical development in attention-deficit/hyperactivity disorder teach us about the early developmental mechanisms involved? *Cereb Cortex.* (2017) 27(9):4624–34. doi: 10.1093/cercor/bhx182

92. Shaw P, Sudre G. Adolescent attention-deficit/hyperactivity disorder: understanding teenage symptom trajectories. *Biol Psychiatry.* (2021) 89(2):152–61. doi: 10.1016/j.biopsych.2020.06.004

93. Buckner RL, Andrews-Hanna JR, Schacter DL. The brain's default network: anatomy, function, and relevance to disease. *Ann N Y Acad Sci.* (2008) 1124:1–38. doi: 10.1196/annals.1440.011

94. Raichle ME, Snyder AZ. A default mode of brain function: a brief history of an evolving idea. *NeuroImage.* (2007) 37(4):1083–90; discussion 97–9. doi: 10.1016/j.neuroimage.2007.02.041

95. Posner J, Park C, Wang Z. Connecting the dots: a review of resting connectivity MRI studies in attention-deficit/hyperactivity disorder. *Neuropsychol Rev.* (2014) 24 (1):3–15. doi: 10.1007/s11065-014-9251-z

96. Cao X, Cao Q, Long X, Sun L, Sui M, Zhu C, et al. Abnormal resting-state functional connectivity patterns of the putamen in medication-naïve children with attention deficit hyperactivity disorder. *Brain Res.* (2009) 1303:195–206. doi: 10.1016/j.brainres.2009.08.029

97. Castellanos FX, Margulies DS, Kelly C, Uddin LQ, Ghaffari M, Kirsch A, et al. Cingulate-precuneus interactions: a new locus of dysfunction in adult attention-deficit/hyperactivity disorder. *Biol Psychiatry.* (2008) 63(3):332–7. doi: 10.1016/j.biopsych.2007.06.025

98. Bos DJ, Oranje B, Achterberg M, Vlaskamp C, Ambrosino S, de Reus MA, et al. Structural and functional connectivity in children and adolescents with and without attention deficit/hyperactivity disorder. *J Child Psychol Psychiatry.* (2017) 58 (7):810–8. doi: 10.1111/jcpp.12712

99. Sun L, Cao Q, Long X, Sui M, Cao X, Zhu C, et al. Abnormal functional connectivity between the anterior cingulate and the default mode network in drug-naïve boys with attention deficit hyperactivity disorder. *Psychiatry Res.* (2012) 201 (2):120–7. doi: 10.1016/j.pscychresns.2011.07.001

100. Tian L, Jiang T, Wang Y, Zang Y, He Y, Liang M, et al. Altered resting-state functional connectivity patterns of anterior cingulate cortex in adolescents with attention deficit hyperactivity disorder. *Neurosci Lett.* (2006) 400(1–2):39–43. doi: 10.1016/j.neulet.2006.02.022

101. Lee S, Hill TR, Johnson B, Testa R, Priya V, Spencer-Smith M, et al. Can neurocognitive outcomes assist measurement-based care for children with attention-deficit/hyperactivity disorder? A systematic review and meta-analyses of the relationships among the changes in neurocognitive functions and clinical outcomes of attention-deficit/hyperactivity disorder in pharmacological and cognitive training interventions. *J Child Adolesc Psychopharmacol.* (2022) 32(5):250–77. doi: 10.1089/cap.2022.0028

102. Wu ZM, Bralten J, An L, Cao QJ, Cao XH, Sun L, et al. Verbal working memory-related functional connectivity alterations in boys with attention-deficit/hyperactivity disorder and the effects of methylphenidate. *J Psychopharmacol.* (2017) 31(8):1061–9. doi: 10.1177/0269881117715607

103. Hart H, Radua J, Nakao T, Mataix-Cols D, Rubia K. Meta-analysis of functional magnetic resonance imaging studies of inhibition and attention in attention-deficit/hyperactivity disorder: exploring task-specific, stimulant medication, and age effects. *JAMA psychiatry.* (2013) 70(2):185–98. doi: 10.1001/jamapsychiatry.2013.277

104. Samea F, Soluki S, Nejati V, Zarei M, Cortese S, Eickhoff SB, et al. Brain alterations in children/adolescents with ADHD revisited: a neuroimaging meta-analysis of 96 structural and functional studies. *Neurosci Biobehav Rev.* (2019) 100:1–8. doi: 10.1016/j.neubiorev.2019.02.011

105. Christakou A, Murphy CM, Chantiluke K, Cubillo AI, Smith AB, Giampietro V, et al. Disorder-specific functional abnormalities during sustained attention in youth with attention deficit hyperactivity disorder (ADHD) and with autism. *Mol Psychiatry.* (2013) 18(2):236–44. doi: 10.1038/mp.2011.185

106. Dickstein SG, Bannon K, Castellanos FX, Milham MP. The neural correlates of attention deficit hyperactivity disorder: an ALE meta-analysis. *J Child Psychol Psychiatry.* (2006) 47(10):1051–62. doi: 10.1111/j.1469-7610.2006.01671.x

107. Lukito S, Norman L, Carlisi C, Radua J, Hart H, Simonoff E, et al. Comparative meta-analyses of brain structural and functional abnormalities during cognitive control in attention-deficit/hyperactivity disorder and autism spectrum disorder. *Psychol Med.* (2020) 50(6):894–919. doi: 10.1017/S0033291720000574

108. Norman LJ, Carlisi C, Lukito S, Hart H, Mataix-Cols D, Radua J, et al. Structural and functional brain abnormalities in attention-deficit/hyperactivity disorder and obsessive-compulsive disorder: a comparative meta-analysis. *JAMA psychiatry.* (2016) 73(8):815–25. doi: 10.1001/jamapsychiatry.2016.0700

109. Chen WL, Wagner J, Heugel N, Sugar J, Lee YW, Conant L, et al. Functional near-infrared spectroscopy and its clinical application in the field of neuroscience: advances and future directions. *Front Neurosci.* (2020) 14:724. doi: 10.3389/fnins.2020.00724

110. Grazioli S, Mauri M, Crippa A, Maggioni E, Molteni M, Brambilla P, et al. Light up ADHD: II. Neuropharmacological effects measured by near infrared spectroscopy: is there a biomarker? *J Affect Disord.* (2019) 244:100–6. doi: 10.1016/j.jad.2018.10.100

111. Niu H, Wang J, Zhao T, Shu N, He Y. Revealing topological organization of human brain functional networks with resting-state functional near infrared spectroscopy. *PLoS ONE.* (2012) 7(9):e45771. doi: 10.1371/journal.pone.0045771

112. Niu H, Li Z, Liao X, Wang J, Zhao T, Shu N, et al. Test-retest reliability of graph metrics in functional brain networks: a resting-state fNIRS study. *PLoS ONE.* (2013) 8 (9):e72425. doi: 10.1371/journal.pone.0072425

113. Wang M, Yuan Z, Niu H. Reliability evaluation on weighted graph metrics of fNIRS brain networks. *Quant Imaging Med Surg*. (2019) 9(5):832–41. doi: 10.21037/qims.2019.05.08

114. Niu H, Khadka S, Tian F, Lin ZJ, Lu C, Zhu C, et al. Resting-state functional connectivity assessed with two diffuse optical tomographic systems. *J Biomed Opt*. (2011) 16(4):046006. doi: 10.1117/1.3561687

115. Wang M, Hu Z, Liu L, Li H, Qian Q, Niu H. Disrupted functional brain connectivity networks in children with attention-deficit/hyperactivity disorder: evidence from resting-state functional near-infrared spectroscopy. *Neurophotonics*. (2020) 7(1):015012. doi: 10.1117/1.NPh.7.1.015012

116. Hu Z, Liu L, Wang M, Jia G, Li H, Si F, et al. Disrupted signal variability of spontaneous neural activity in children with attention-deficit/hyperactivity disorder. *Biomed Opt Express*. (2021) 12(5):3037–49. doi: 10.1364/BOE.418921

117. Cui X, Bray S, Bryant DM, Glover GH, Reiss AL. A quantitative comparison of NIRS and fMRI across multiple cognitive tasks. *NeuroImage*. (2011) 54(4):2808–21. doi: 10.1016/j.neuroimage.2010.10.069

118. Boas DA, Elwell CE, Ferrari M, Taga G. Twenty years of functional near-infrared spectroscopy: introduction for the special issue. *NeuroImage*. (2014) 85(Pt 1):1–5. doi: 10.1016/j.neuroimage.2013.11.033

119. Sutoko S, Monden Y, Tokuda T, Ikeda T, Nagashima M, Funane T, et al. Exploring attentive task-based connectivity for screening attention deficit/hyperactivity disorder children: a functional near-infrared spectroscopy study. *Neurophotonics*. (2019) 6(4):045013. doi: 10.1117/1.NPh.6.4.045013

120. van Rooij D, Hartman CA, Mennes M, Oosterlaan J, Franke B, Rommelse N, et al. Altered neural connectivity during response inhibition in adolescents with attention-deficit/hyperactivity disorder and their unaffected siblings. *NeuroImage Clin*. (2015) 7:325–35. doi: 10.1016/j.nicl.2015.01.004

121. Sutoko S, Monden Y, Tokuda T, Ikeda T, Nagashima M, Funane T, et al. Atypical dynamic-connectivity recruitment in attention-deficit/hyperactivity disorder children: an insight into task-based dynamic connectivity through an fNIRS study. *Front Hum Neurosci*. (2020) 14:3. doi: 10.3389/fnhum.2020.00003

122. Hou L, Yang J, Xu L, Peng J, Joyce Law CY, Chen T. Activation of brain regions associated with working memory and inhibitory control in patients with attention-deficit/hyperactivity disorder in functional near-infrared spectroscopy: a systematic review. *Curr Med Imaging*. (2023) 19(8):865–73. doi: 10.2174/1573405618666220822101019

123. Inoue Y, Sakihara K, Gunji A, Ozawa H, Kimiya S, Shinoda H, et al. Reduced prefrontal hemodynamic response in children with ADHD during the go/NoGo task: a NIRS study. *Neuroreport*. (2012) 23(2):55–60. doi: 10.1097/WNR.0b013e32834e664c

124. Miao S, Han J, Gu Y, Wang X, Song W, Li D, et al. Reduced prefrontal cortex activation in children with attention-deficit/hyperactivity disorder during go/no-go task: a functional near-infrared spectroscopy study. *Front Neurosci*. (2017) 11:367. doi: 10.3389/fnins.2017.00367

125. Wu T, Liu X, Cheng F, Wang S, Li C, Zhou D, et al. Dorsolateral prefrontal cortex dysfunction caused by a go/no-go task in children with attention-deficit hyperactivity disorder: a functional near-infrared spectroscopy study. *Front Neurosci*. (2023) 17:1145485. doi: 10.3389/fnins.2023.1145485

126. Passarotti AM, Sweeney JA, Pavuluri MN. Neural correlates of response inhibition in pediatric bipolar disorder and attention deficit hyperactivity disorder. *Psychiatry Res*. (2010) 181(1):36–43. doi: 10.1016/j.pscychresns.2009.07.002

127. Rubia K, Cubillo A, Smith AB, Woolley J, Heyman I, Brammer MJ. Disorder-specific dysfunction in right inferior prefrontal cortex during two inhibition tasks in boys with attention-deficit hyperactivity disorder compared to boys with obsessive-compulsive disorder. *Hum Brain Mapp*. (2010) 31(2):287–99. doi: 10.1002/hbm.20864

128. Gu Y, Miao S, Han J, Liang Z, Ouyang G, Yang J, et al. Identifying ADHD children using hemodynamic responses during a working memory task measured by functional near-infrared spectroscopy. *J Neural Eng*. (2018) 15(3):035005. doi: 10.1088/1741-2552/aa9ee9

129. Gu Y, Miao S, Han J, Zeng K, Ouyang G, Yang J, et al. Complexity analysis of fNIRS signals in ADHD children during working memory task. *Sci Rep*. (2017) 7(1):829. doi: 10.1038/s41598-017-00965-4

130. Jang S, Choi J, Oh J, Yeom J, Hong N, Lee N, et al. Use of virtual reality working memory task and functional near-infrared spectroscopy to assess brain hemodynamic responses to methylphenidate in ADHD children. *Front Psychiatry*. (2020) 11:564618. doi: 10.3389/fpsyt.2020.564618

131. Calub CA, Rapport MD, Irurita C, Eckrich SJ, Bohil C. Attention control in children with ADHD: an investigation using functional near infrared spectroscopy (fNIRS). *Child Neuropsychol*. (2022) 28(8):1072–96. doi: 10.1080/09297049.2022.2047913

frontiers | Frontiers in Radiology

TYPE Original Research
PUBLISHED 28 June 2024
DOI 10.3389/fradi.2024.1416672

Check for updates

OPEN ACCESS

EDITED BY
Yunzhi Huang,
Nanjing University of Information Science and Technology, China

REVIEWED BY
Alfonso Mastropietro,
National Research Council (CNR), Italy
Joseph Yuan-Mou Yang,
Murdoch Childrens Research Institute, Royal Children's Hospital, Australia

*CORRESPONDENCE
Anouk S. Verschuur
✉ a.s.verschuur@alumnus.utwente.nl

RECEIVED 12 April 2024
ACCEPTED 10 June 2024
PUBLISHED 28 June 2024

CITATION
Verschuur AS, Tax CMW, Boomsma MF, Carlson HL, van Wezel-Meijler G, King R, Leemans A and Leijser LM (2024) Feasibility study to unveil the potential: considerations of constrained spherical deconvolution tractography with unsedated neonatal diffusion brain MRI data.
Front. Radiol. 4:1416672.
doi: 10.3389/fradi.2024.1416672

Feasibility study to unveil the potential: considerations of constrained spherical deconvolution tractography with unsedated neonatal diffusion brain MRI data

Anouk S. Verschuur[1,2,3]*, Chantal M. W. Tax[2,4], Martijn F. Boomsma[1,5], Helen L. Carlson[6], Gerda van Wezel-Meijler[7], Regan King[3], Alexander Leemans[2] and Lara M. Leijser[3]

[1]Department of Radiology, Isala Hospital, Zwolle, Netherlands, [2]Image Sciences Institute, University Medical Center Utrecht, Utrecht, Netherlands, [3]Department of Pediatrics, Section of Newborn Critical Care, University of Calgary, Calgary, AB, Canada, [4]CUBRIC, School of Physics and Astronomy, Cardiff University, Cardiff, United Kingdom, [5]Division of Imaging and Oncology, University Medical Center Utrecht, Utrecht, Netherlands, [6]Department of Pediatrics, Cumming School of Medicine, University of Calgary, Calgary, AB, Canada, [7]Department of Neonatology, Isala Women and Children's Hospital, Zwolle, Netherlands

Purpose: The study aimed to (1) assess the feasibility constrained spherical deconvolution (CSD) tractography to reconstruct crossing fiber bundles with unsedated neonatal diffusion MRI (dMRI), and (2) demonstrate the impact of spatial and angular resolution and processing settings on tractography and derived quantitative measures.

Methods: For the purpose of this study, the term-equivalent dMRIs (single-shell b800, and b2000, both 5 b0, and 45 gradient directions) of two moderate-late preterm infants (with and without motion artifacts) from a local cohort [Brain Imaging in Moderate-late Preterm infants (BIMP) study; Calgary, Canada] and one infant from the developing human connectome project with high-quality dMRI (using the b2600 shell, comprising 20 b0 and 128 gradient directions, from the multi-shell dataset) were selected. Diffusion tensor imaging (DTI) and CSD tractography were compared on b800 and b2000 dMRI. Varying image resolution modifications, (pre-)processing and tractography settings were tested to assess their impact on tractography. Each experiment involved visualizing local modeling and tractography for the corpus callosum and corticospinal tracts, and assessment of morphological and diffusion measures.

Results: Contrary to DTI, CSD enabled reconstruction of crossing fibers. Tractography was susceptible to image resolution, (pre-) processing and tractography settings. In addition to visual variations, settings were found to affect streamline count, length, and diffusion measures (fractional anisotropy and mean diffusivity). Diffusion measures exhibited variations of up to 23%.

Conclusion: Reconstruction of crossing fiber bundles using CSD tractography with unsedated neonatal dMRI data is feasible. Tractography settings affected streamline reconstruction, warranting careful documentation of methods for reproducibility and comparison of cohorts.

KEYWORDS
diffusion tensor imaging, constrained spherical deconvolution, diffusion MRI, tractography, neonatal

1 Introduction

Understanding the early stages of human brain development holds significant clinical importance, as many neurological and neurobehavioral disorders have their origins in the perinatal period (1). Unraveling the intricate processes of normal and abnormal brain development may contribute to identification of increased risk for developmental problems as early as in the neonatal period. Ultimately, this may lead to individualized treatment plans and improved monitoring to promote healthy brain development and outcomes. To date, conventional MRI techniques have fallen short in elucidating subtle developmental variances (2). Diffusion MRI (dMRI) is a dedicated method to study the microscopic brain tissue architecture and thus subtle developmental variances (3).

A recent review by our group[1] showed that 66% of the dMRI studies on infants aged 0–2 years use diffusion tensor imaging (DTI) to study white matter tracts. DTI allows for reconstruction of only one white matter fiber direction per voxel, while an estimated 90% of the adult brain consists of crossing fiber configurations at commonly used spatial resolutions (4). Advanced tractography techniques, such as constrained spherical deconvolution (CSD), that allow for reconstruction of multiple streamline[2] directions per voxel may thus more accurately reflect the organizational complexity of the brain's white matter (see Figure 1A) (5). While widely applied in the adult brain, adopting the more advanced techniques to the neonatal brain poses practical and technical challenges.[1]

Lengthy and complex dMRI sequences as used in adults and state-of-the-art research imaging protocols are not feasible on neonates, because of the use of the feed and sleep method (6) for performing neonatal brain MRI in the clinical as well as research setting. Although the feed and sleep method eliminates the need for sedation and associated risks, it often limits the duration of scanning to minimize infant waking and motion. As a result, most available neonatal dMRI datasets use relatively low b-values (<b2000), single-shell data, and low angular resolution (<40 directions).[1] In addition, the small brain and relatively large and often anisotropic voxels affect scan quality with increased partial volume effects and lower signal-to-noise ratios, which in turn considerably affects the quality of streamline reconstructions.[1]

Toselli et al. (7) conducted a comparison of density maps and fiber bundle reconstructions of the corticospinal tract (CST), corticopontocerebellar tract and cerebellar-thalamic tract using DTI and CSD on dMRI data from unsedated neonates. They emphasized the advantages of CSD tractography, particularly its ability to reconstruct crossing fibers in adult data (7). The authors scored the fiber bundle reconstructions on presence of potential false positive streamlines, false negative streamlines, and anatomical accuracy (7). However, while the study addressed the performance of CSD in reconstructing fiber bundles, it did not specifically investigate the feasibility of reconstructing crossing streamlines. The findings primarily focused on tract appearance in relation to their volume, without visualizing fiber orientation distribution functions (fODF) or intersection of two crossing fiber bundles. Given the complexity involved in reconstructing crossing fibers, the study did not provide conclusive evidence regarding the feasibility of reconstructing crossing fiber bundles using CSD with unsedated neonatal dMRI data.

Therefore, our study aimed to assess the feasibility of utilizing CSD tractography to reconstruct crossing fiber bundles on unsedated neonatal dMRI data with low b-values, single-shell data and low angular resolution. Specifically, we aimed to visualize differences between CSD and DTI tractography and demonstrate the impact of image resolution and processing settings on dMRI tractography and derived diffusion measures for downstream tract-analysis. The potential of CSD to reconstruct crossing fibers from unsedated neonatal dMRI may stimulate a shift towards employing advanced tractography techniques in neonates, ultimately resulting in more reliable and detailed assessment of the developing brain white matter. Such a shift may prove invaluable for identifying disparities in normal and abnormal brain maturation in young infants to advance neuroprotective care and outcomes.

2 Methods

As part of the "Brain Imaging in Moderate-late Preterm infants" (BIMP) study (ethics approval: REB19-1194), a cohort of

---

[1] Verschuur AS, King R, Tax CMW, Boomsma MF, van Wezel-Meijler G, Leemans A, et al.. Methodological considerations on diffusion MRI tractography in infants aged 0-2 years: a scoping review. Under review.

[2] For a comprehensive explanation of the tractography terms used in this paper, readers are encouraged to refer to Jeurissen, B et al. Diffusion MRI fiber tractography of the brain. NMR in biomedicine, 2019;32(4), https://doi.org/10.1002/nbm.3785. This paper provides detailed definitions and explanations that may aid in understanding the terminology employed in the current paper.

moderate-late preterm infants (32^{+0}–35^{+6} weeks' gestation) was prospectively recruited between November 2020 and March 2023 from the neonatal intensive care units at Rockyview General Hospital and Peter Lougheed Centre, Calgary, Canada. Infants with congenital malformations of the central nervous system, chromosomal disorders, inborn errors of metabolism, congenital infections, central nervous system infections, brain injury acquired after the neonatal period, or with parents unable to provide written informed consent in English were excluded. Parents of infants have provided signed informed consent for participation in the BIMP-study.

As for the explorative nature of the study, two subjects without visual brain injury on term-equivalent MRI or serial cranial ultrasound, one with and one without visual motion artifacts on the dMRI scans, were randomly selected. The motion scan contained outlier slices as a result of motion-induced signal dropouts. A single preprocessed dMRI scan with low motion scores from the developing human connectome project (dHCP)[3] was additionally selected. We opted for the inclusion of only three MRI scans as they represent a diverse range of scan types, ensuring clarity in our experiments while maintaining comprehensiveness.

2.1 MRI acquisition

Imaging was performed at the Alberta Children's Hospital on a research-dedicated 3 Tesla General Electric MR750W system (manufacturer), managed by the Child and Adolescent Imaging Research (CAIR) program. Infants underwent MRI around term equivalent age (TEA; 40–44 weeks postmenstrual age) without sedation; natural sleep was induced with the feed and sleep technique. A vacuum bag immobilizer was used to further immobilize the infant. Earmuffs and headphones provided hearing protection.

T2-weighted imaging [axial fast spin echo, repetition time = 4,400 ms, echo time = 120 ms, flip angle = 111°, acquisition matrix = 320 × 320, reconstruction matrix = 512 × 512, field of view = 19.2 cm, pixel spacing = 0.375 × 0.375 mm, slice thickness = 3 mm (0.4 mm gap)] and dMRI scans were used for this study. dMRI scans were acquired with pulsed-gradient spin echo echo planar imaging (PGSE EPI) with the following parameters: repetition time (b800/b2000) = 7000 ms/10000 ms, echo time (b800/b2000) = 81.4 ms/97.9 ms, 49 slices, acquisition matrix = 100 × 100, reconstruction matrix = 256 × 256, acquired voxel size = 2 × 2 × 2 mm, reconstructed (8) voxel size = 0.78 × 0.78 × 2 mm, b-value b800 and b2000 acquired separately (i.e., single shell), 45 non-collinear gradient directions and 5 b0 images per dMRI scan.

The dHCP data acquisition has been previously described (9). In short, dMRI data were acquired on a 3 Tesla Philips Achieva scanner (manufacturer), also using a PGSE EPI sequence. The parameters included: multiband factor 4, repetition time = 3,800 ms, echo time = 90 ms, 64 interleaved slices with 3 mm step and 1.5 mm overlap, 1.5 × 1.5 × 1.5 mm reconstructed voxel size, *b*-values 400, 1,000 and 2,600 with 64, 88 and 128 gradient directions, respectively, and 20 b0 images per dMRI scan, totaling 300 volumes.

2.2 MRI processing

T2-weighted MRI scans were skull stripped using the brain extraction tool (BET) from the FMRIB Software Library (FSL; version 6.0.3, Oxford University, UK) (10). Results were visually checked and manually corrected when extra-cerebral tissue was still present after performing BET. dMRI scans were preprocessed using MRtrix3 (version 3.0.2) and Advanced Normalization Tools (ANTs; version 2.3.5) (11, 12). Both b800 and b2000 scans underwent preprocessing encompassing denoising (patch size = 7) (13), Gibbs ringing correction (default settings) (14), motion correction (no reverse phase encoding, with slice-to-volume misalignment correction (15) and outlier handling (16); eddy options were: slm = linear, mporder = 6, s2v_niter = 5, s2v_lambda = 1 s2v_interp = trilinear), eddy induced distortion correction (17), and bias correction (default settings) (18) using MRtrix3 (19). Echo planar imaging (EPI) distortions were corrected by rigid registration of the T2-weighted MRI to the mean b0-image, followed by anterior-posterior affine registration (BSplineSyN) of the mean b0-image to the registered T2-weighted MRI using ANTs registration. The b0 transformation parameters were then applied to the full 4-dimensional dMRI volume. White matter masks were created by segmenting the mean b0 image of each scan using the dHCP structural pipeline (20) and combining the resulting tissue masks into a single mask, this included white matter, hippocampus, cerebellum and brain stem masks. Preprocessed images were used for tractography.

The dHCP scan was processed with the automated dHCP neonatal dMRI processing pipeline as described by Bastiani et al. (21).

2.3 Baseline tractography settings

MRtrix3 was used for all local modeling and tractography. For DTI tractography, the diffusion tensor was fitted with weighted linear least squares and eigenvectors and eigenvalues extracted, followed by fiber assigned by continuous tracking (FACT), a deterministic algorithm, for whole brain tractography (22). Initial CSD tractography was performed with response function estimation using the Tournier algorithm (23), followed by CSD fiber orientation distribution function (fODF) estimation (23), fODF intensity and inhomogeneity normalization (24), and deterministic streamline tractography based on spherical deconvolution (SD_STREAM) for whole brain tractography (25).

Baseline streamline settings for both DTI and CSD tractography were as follows: 10 million streamlines, step size = 0.5 mm, angle 40°, minimum length = 30 mm, no maximum length, fODF or fractional anisotropy (FA) cutoff = 0.1, white matter masking (consisting of white matter, cerebellum and

---

[3] https://www.developingconnectome.org/project/

brainstem), and only for CSD 4th-order Runge-Kutta integration (26) to eliminate curvature overshoot. Variations to these settings to evaluate differences in output are described in Part A, B and C below. A schematic summary of these settings is provided in Figure 1.

Regions of interest (ROI) were manually drawn for fiber bundle segmentation (see Figure 2). A body section of the corpus callosum (CC) at the level of the CST was segmented with bilateral sagittal ROIs, placed 6 slices lateral to the mid-sagittal plane. The CST was segmented with one axial ROI in the superior-anterior region of the pons and one axial ROI at the level of the base of the CC. Association fibers (superior longitudinal fasciculus) were segmented with two coronal ROIs in the dorsal part of the frontal lobe and dorsal part of the parietal lobe. After initial bundle segmentation, exclusion ROIs were applied to avoid inclusion of secondary bundles (e.g., cerebellar or CC streamlines in the CST). Exclusion ROIs were placed as follows (see Figure 2): for the CC—(1) axial plane, elongated oval-shaped ROI in the mid-brain and between the temporal lobes at the base of the lateral ventricles, (2) axial plane, directly below the body of the CC, to exclude fornix streamlines, (3) coronal plane, directly in front of inclusion ROIs to exclude cingulum streamlines; for the CST—(1) sagittal plane, mid-sagittal slice, (2) coronal plane, crossing the cerebellar peduncles; for the association fibers—sagittal plane, mid-sagittal slice (same as CST).

2.4 Testing tractography settings

2.4.1 Part A—foundational choices

DTI and CSD tractography were performed on both the b800 and b2000 dMRI scans from the BIMP subject whose scans were without motion artifacts, using baseline streamline settings. After part A, tractography was exclusively conducted utilizing CSD.

2.4.2 Part B—image resolution and processing

The impact of spatial and angular resolution on streamline reconstruction was assessed by resampling the b2000 BIMP MRI data and the dHCP MRI data. BIMP data was (1) resampled to 2 mm and 1 mm isotropic voxels, and (2) using original voxel size, the number of gradient directions was decreased from 45 to 32. Thirty-two gradient directions were chosen to match the 30–32 gradient directions commonly applied in neonatal dMRI tractography. Downsampling was performed by in-/excluding volumes to a ratio 2/1 (the last 6 volumes were all included). dHCP data was processed as single shell data with $b = 2{,}600$ s/mm^2 and 128 gradient directions. In addition, the number of gradient directions was decreased to 45 (by selecting the first 53 volumes, including 8 b0 volumes, an equal distribution was preserved) for the dHCP data to simulate BIMP data quality. fODF estimation, streamline reconstruction and bundle segmentation were performed using baseline settings.

The BIMP scan with motion artifacts was preprocessed twice, once with and once without outlier replacement using the FSL repol function (16). fODF estimation, streamline reconstruction and bundle segmentation were performed using baseline settings.

Three response function estimation algorithms were applied to the original preprocessed b2000 BIMP data, including the Tournier (23), FA (27) and Tax (tailored to MRtrix3) (28) algorithms. The following steps, including streamline reconstruction and bundle segmentation, were performed using baseline settings.

2.4.3 Part C—tractography settings

Effects of three key settings on streamline reconstruction were tested, including fODF threshold (0.05, 0.1, 0.2, 0.3, 0.4, 0.5, 0.6, 0.7), angle threshold (30°, 40°, 50°, 60°), and step size (0.39 mm [=1/2 in-plane voxel size], 0.78 mm [=in-plane voxel size], 1 mm and 2 mm). fODF estimation was done using baseline settings. In case the step size was larger than the ROI thickness, the algorithm stepped over the ROI (Supplementary Figure S1). The ROI thickness (0.78 mm in coronal and sagittal plane and 2 mm in axial plane) was then increased to three slices in the coronal and sagittal plane and to two slices in the axial plane for reconstructions with step size 1 mm and 2 mm.

2.5 Visualization and quantification of local modeling and tractography

Visualization comprised of a combination of (1) histograms to assess the number of peaks per white matter voxel (fODF threshold 0.2), (2) local modeling of centrum semiovale, and (3) streamline reconstructions of the CC and CST for all experiments. Motion correction visualization additionally comprised (1) dMRI volumes to demonstrate the effect of outlier replacement, (2) tractography from a randomly placed single voxel in the posterior limb of the internal capsule (Figure 2) to visualize differences between tract reconstruction from the same voxel in a scan with and without motion correction, and (3) local modeling (scaling 2) and tractography differences between results with and without outlier replacement.

Streamline and diffusion measures, including streamline count, average streamline length [standard deviation (SD)], fractional anisotropy (FA; percentage change relative to baseline settings) and mean diffusion (MD; percentage change relative to baseline settings) were calculated for each reconstructed fiber bundle. Calculations were performed with MRTrix3 (tcksample with -stat_tck option or tckstats) and averaged in python 3 where appropriate. Streamline count and mean streamline length (SD) are included in the figures. Diffusion measures are summarized in tables.

3 Results

3.1 Subject characteristics

The dMRI data of two infants from the BIMP study (with a total of 138 infants recruited) and one infant from dHCP were selected for this study (see images of raw data in Supplementary Figure S2). The BIMP infants were born late preterm (35 weeks gestation) and the dHCP infant was born full term (39 weeks gestation); see Table 1 for neonatal and TEA infant characteristics.

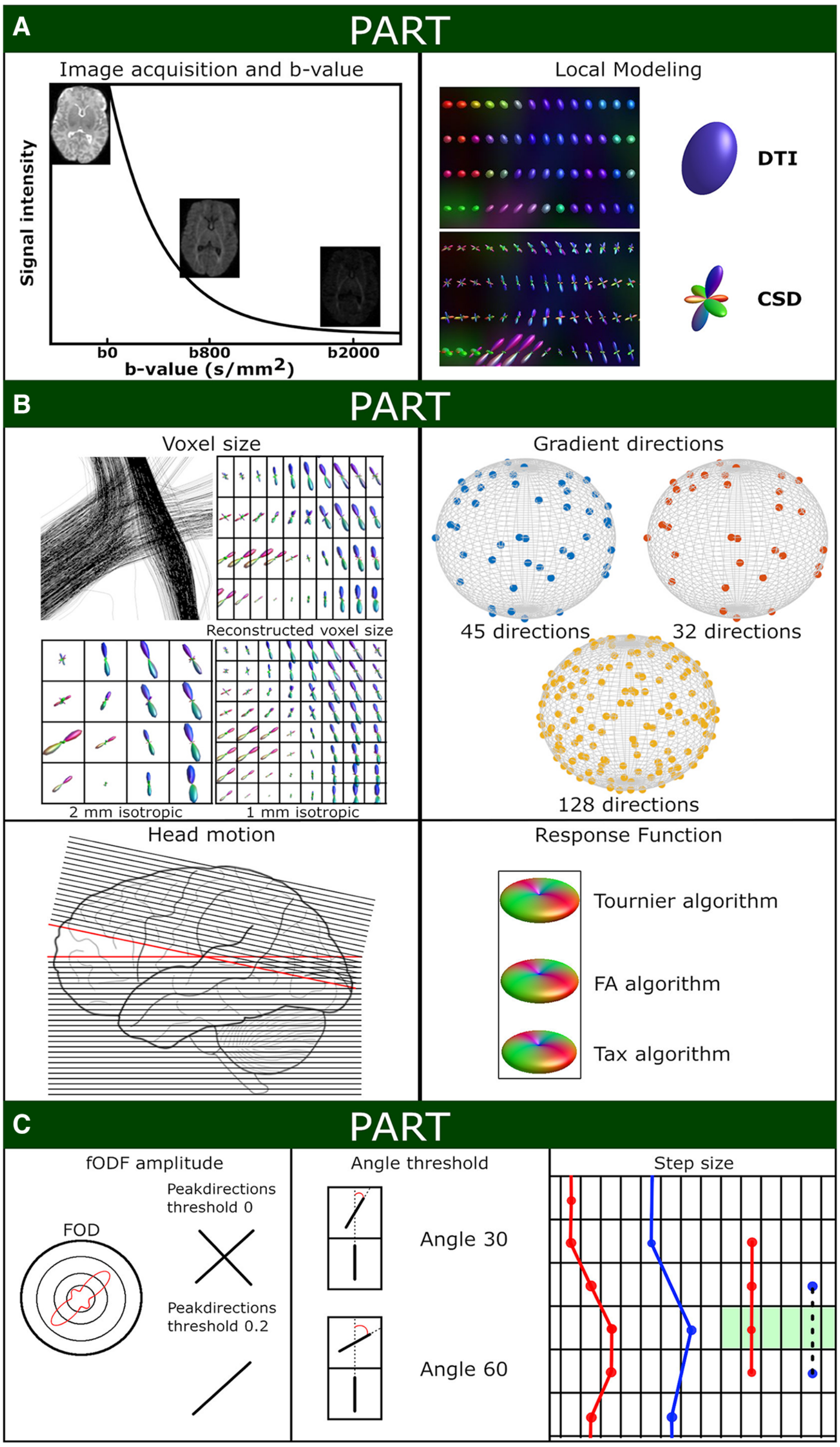

FIGURE 1
Schematic overview of experiment settings. (A) Shows the signal intensity relative to the applied b-values (with screenshots of the non-motion BIMP scan) and a local modeling reconstruction using diffusion tensor imaging (DTI) and constrained spherical deconvolution (CSD). (B) Displays the spatial and angular resolution and processing settings. Top left panel: The voxel size section shows a coronal snapshot of streamline reconstructions and the corresponding local modeling reconstructions for different voxel sizes with a grid overlay. Top right panel: Gradient directions were plotted on a sphere for BIMP-data (45 and 32 gradient directions) and dHCP-data (128 gradient directions). Bottom left panel: Head motion can result in signal dropout. As shown in this figure, tilting the head forward mid scanning (scanning caudal to cranial; red lines) results in double scanning of the posterior area (overlapping lines) and missing data of the frontal area (gap). Bottom right panel: Response function estimation with three algorithms results in minor differences, mainly in the amplitude of the response function. (C) Displays the tractography settings. The impact of fODF threshold 0 or 0.2 for displayed (2-dimensional) fODF, angle threshold for angle 30 of 60 and step size are show. A step size larger than the voxel size (blue dots) may result in streamlines being missed (black dashed line) by the region of interest (green area).

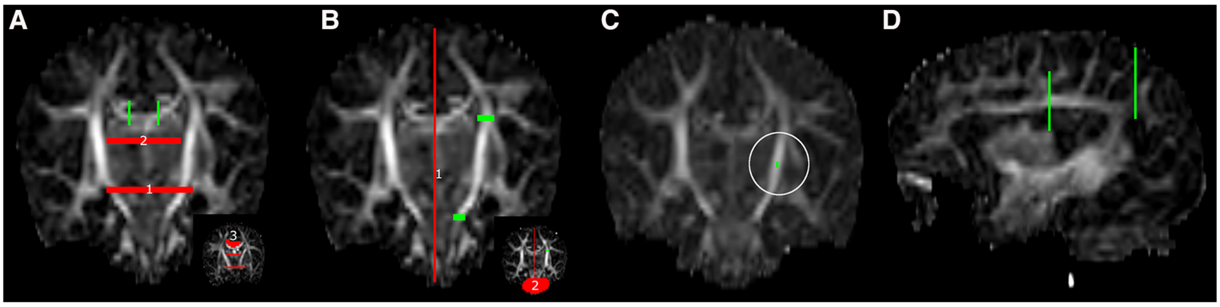

FIGURE 2
ROI placement for fiber bundle tractography, (A) corpus callosum, (B) left corticospinal tract, (C) single voxel tractography from a random ROI in the left posterior limb of internal capsule (white circle) and (D) left association fibers. Green: inclusion ROIs; red: exclusion ROIs.

TABLE 1 Infant characteristics.

	BIMP	BIMP motion	dHCP
Neonatal period			
Gestational age in weeks^{+days}	35^{+2}	35^{+6}	39^{+4}
Birth weight in grams	1,790	2,595	3,100
Head circumference in cm	31	33	Not registered
Gender	Female	Female	Female
Plurity	Twin	Singleton	Singleton
Admission to neonatal intensive care unit	Yes	Yes	Unknown
At TEA MRI			
PMA in weeks^{+days}	42^{+3}	41^{+4}	39^{+5}
Weight in grams	2,850	3,610	Unknown
Head circumference in cm	35.7 (T1 MRI)	35.8 (T1 MRI)	35

Head circumference was measured from axial T1 MRI (29).

3.2 Part A: foundational choices

The difference between single-direction tensor estimation with DTI and multi-direction fODF estimation with CSD is visualized in Figure 3. Where DTI local modeling was not designed to reveal potential crossing fibers, CSD based local modeling allowed for tracing of crossing fibers. Fiber bundle reconstructions of the CC, CST and association fibers were visibly different between DTI, with clean and clearly separated bundles, and CSD, with more branched and intersected or crossing bundles (see Figure 3 inserts). The difference between b800 and b2000 scans can best be seen on reconstructions with CSD, where streamlines projected more laterally [CC (red), CST (blue) and association fibers (green)] in b2000 scans compared to the b800 scans (Figure 3). CSD on b2000 scans resulted in most reconstructed streamlines and longest average streamline length for the superior longitudinal fasciculus bundle.

3.3 Part B: image resolution and processing

Compared to the reconstructed anisotropic voxel size (0.78 × 0.78 × 2 mm), 2 mm isotropic voxels showed a lower percentage of voxels with 3 peaks (Figure 4). Visually, the 2 mm isotropic voxels resulted in less evident crossing of CC streamlines with those of the CST in the local modeling reconstructions (highlighted by the yellow circle in Figure 4) than the reconstructed anisotropic voxel size. The local modeling differences were reflected in the streamline reconstructions; a branch of the CC was not reconstructed (yellow arrow Figure 4) and less branching was visible in general (red circle Figure 4). In contrast, the 1 mm isotropic voxels showed higher fODF density and was visually more apparent where bundles cross, but only minor effects on streamline reconstructions were seen. Downsampling the number of gradient directions influenced the direction of the fODFs, which was reflected in a missing branch of the CC (white arrow Figure 4).

Downsampling the angular resolution of high-quality research data to 45 directions led to increased amplitudes (in all directions) of fODFs in voxels exhibiting equal fODF amplitude across multiple directions (Figure 5). Tractography was most affected at branches in more peripheral regions of the brain. Comparing the original BIMP data and down-sampled dHCP data, considerable differences in tract reconstruction and branching were observed.

The number of gradient directions and the voxel size affected streamline count and length. Notably, resolution and number of gradient directions had an inverse effect on streamline count and length of the CC and CST. The inverse effect was best seen in the 32-gradient scan (Figure 4), where the CC had a higher streamline count and length compared to the 45-gradient scan, while the CST had a lower count and length. Down sampling from 128 to 45 gradient directions had a different effect on streamline reconstruction and resulted in a higher count and lower length for both the CC and CST (Figure 5).

Motion artifacts decreased image quality and affected angularity and amplitude of local modeling (Figure 6). Tractography of the CC and CST was visibly affected by motion artifacts (yellow circles Figure 6). Notably, distinct tracts were reconstructed from seeding in a single voxel in the posterior limb of internal capsule (Figure 6). Failure to perform motion correction resulted in a decreased streamline count and shorter mean streamline length in the single voxel reconstruction, but CST streamline count and length were only marginally affected.

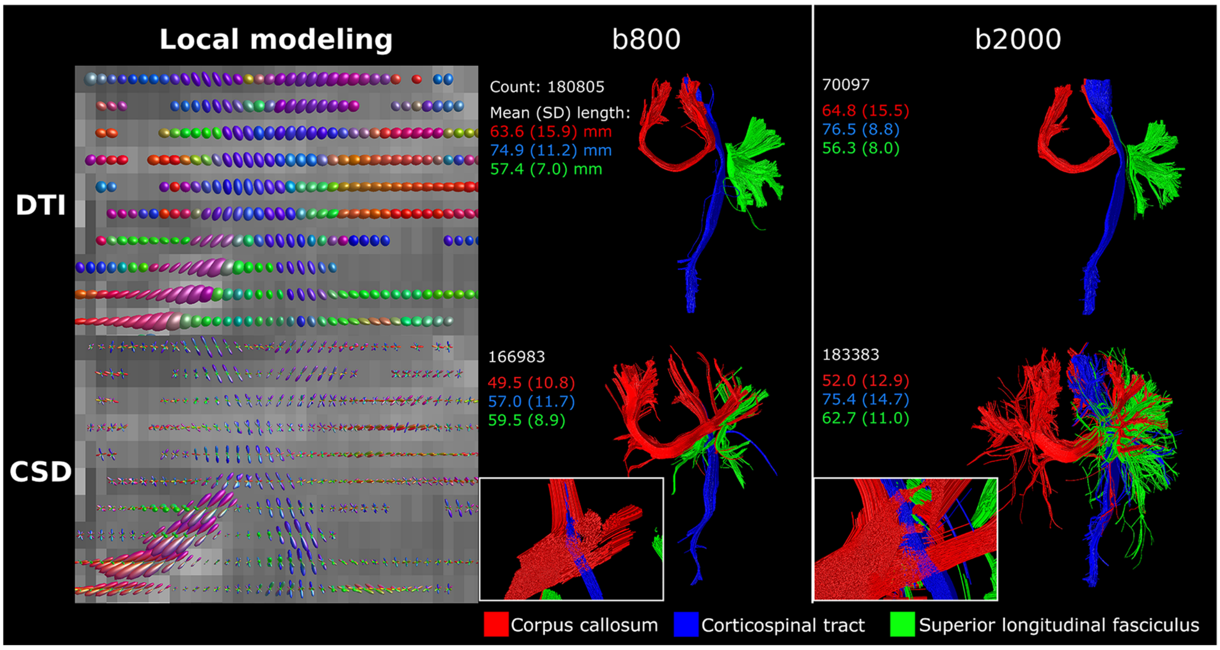

FIGURE 3
DTI vs. CSD tractography using single-shell b800 and b2000 neonatal dMRI data with low angular resolution (45 directions). DTI resulted in clean and separated bundle reconstructions, while CSD resulted in more branched and intersected bundle reconstructions. Reconstructions were acquired from the BIMP scan without motion.

The application of three different response functions did not result in major differences in fODF directionality, but fODF amplitude was notably different, predominantly for the primary fiber direction (Figure 7). The amplitude was smallest for the Tournier algorithm and largest for the Tax algorithm. The amplitude shift was most evident in the branching of the CC. Specifically, the Tournier algorithm yielded more peripheral branching compared to the FA algorithm, while in the Tax algorithm, one branch was absent in the CC (white arrow Figure 7). Furthermore, the higher amplitude coincided with a reduction in voxels exhibiting three peaks, and an increase in streamline count and length for CC reconstructions but not for CST reconstructions.

3.4 Part C: tractography settings

The fODF threshold mostly affected the complexity and branching of the fiber bundles (Figure 8). Higher fODF thresholds resulted in a shift from mostly three peak directions per white matter voxel (threshold 0.05) towards mostly one peak direction per white matter voxel (threshold 0.4 and higher; Figure 8). The degree of branching vastly decreased with increasing fODF threshold. For threshold 0.6 and higher, no streamlines could be generated for the CC and therefore not visualized in Figure 8.

An increasing angle threshold increased bundle complexity and branching (Figure 9). Best seen in the CST, bundle diameter visually increased with increasing angle (Figure 9).

Step size primarily affected tract reconstruction when the step size was larger than the voxel size (Figure 10). Step size 0.39 mm (1/2× voxel size) and 0.78 mm (1× voxel size) only showed minor variance in tract reconstruction. However, 1 mm and 2 mm step size resulted in the reconstruction of new branches, with 2 mm step size showing the most noticeable differences (yellow circles Figure 10).

Streamline count and length were substantially affected by tractography settings, with effects varying for the CC and CST.

3.5 Diffusion measures

Spatial and angular resolution, (pre-)processing and tractography settings affected diffusion measures, such as FA and MD. Variation of up to 23% (CSD b2000 vs. CSD b800 superior longitudinal fasciculus) in diffusion measure were seen (see Tables 2–4). Fundamental settings from part A had the most impact on diffusion measures, and response function and step size from part B and C had the least impact on diffusion measures (all <5% change).

4 Discussion

The search for optimal white matter tract reconstruction in adult data has been ongoing since the inception of dMRI brain tractography. Surprisingly, there has been a notable scarcity of research in optimizing tractography in the neonatal brain. While the techniques employed are not novel and results align with expectations based on adult data, this study was, to the best of

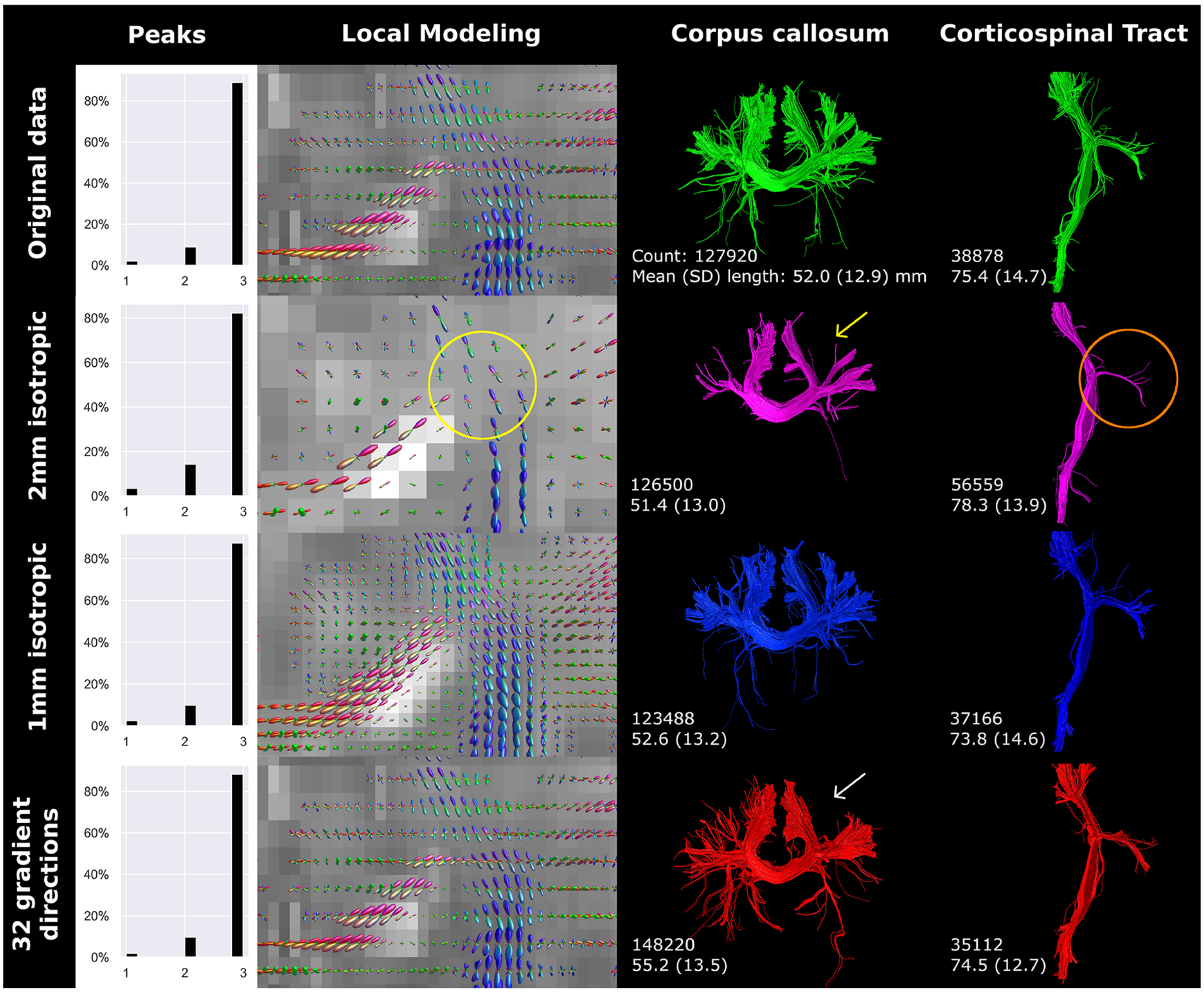

FIGURE 4
Spatial and angular resolution of unsedated neonatal diffusion MRI, including voxel (an)isotropy, voxel size and number of gradient directions affected streamline reconstructions. Crossing of corpus callosum streamlines with corticospinal tract streamlines were less apparent in the 2 mm isotropic scan (yellow circle) and different image resolution affected the reconstruction of a branch of the corpus callosum (white arrows). Tractography settings, such as step size (set to 0.5 mm), were not adapted to resolution. Reconstructions were acquired from the BIMP scan without motion.

our knowledge, the first to extensively investigate the feasibility of reconstructing crossing fiber bundles using unsedated neonatal dMRI data. Our findings confirmed feasibility and highlighted notable tract reconstruction differences between CSD and DTI tractography techniques. We additionally assessed the performance of CSD tractography, which was found to be susceptible to technical and practical choices made during dMRI acquisition, image preprocessing, local modeling, and fiber tracking. This susceptibility was evident both visually (local modeling and tractography) and quantitatively (morphological and diffusion measures), emphasizing the necessity of careful consideration and optimization of technical and practical factors in neonatal dMRI studies using CSD.

Our results suggest CSD to be a feasible and effective method for reconstructing white matter tracts with unsedated neonatal dMRI data and confirmed CSD's superiority (30) over DTI in handling crossing fiber regions (31). To the best of our knowledge, only one study has previously compared (deterministic) DTI and (probabilistic) CSD tractography with unsedated neonatal dMRI data. Toselli et al. qualitatively assessed three white matter tracts based on the presence of false-positive and false-negative tracts and anatomical accuracy of the reconstructed bundles as rated by two neuroradiologists (7). Although the authors state that CSD allows for reconstruction of white matter tracts more completely than DTI, CSD's ability to reconstruct crossing fiber bundles could not be deducted from the presented results (7). Also, observed differences may not only be attributed to local modeling technique, but also fiber tracking technique since deterministic tractography was used for DTI and probabilistic tractography was used for CSD (7). The distinct characteristics of these fiber tracking techniques—such as deterministic tracking yielding a single fiber per seed voxel and probabilistic tracking generating a multitude of potential trajectories per seed voxel—significantly influences the visual appearance of reconstructed bundles (32).

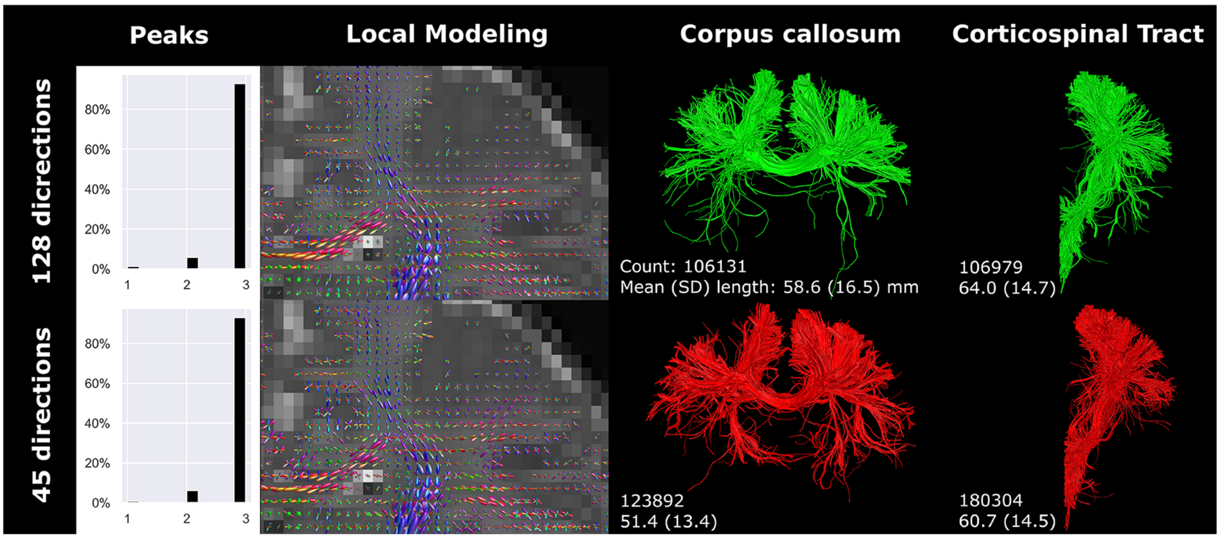

FIGURE 5
High-quality diffusion MRI data from the developing human connectome project was down sampled from 128 (single-shell; upper row) to 45 (lower row) gradient directions. Branching/fanning of the corpus callosum was visibly affected by down sampling. Reconstructions were acquired from the dHCP scan.

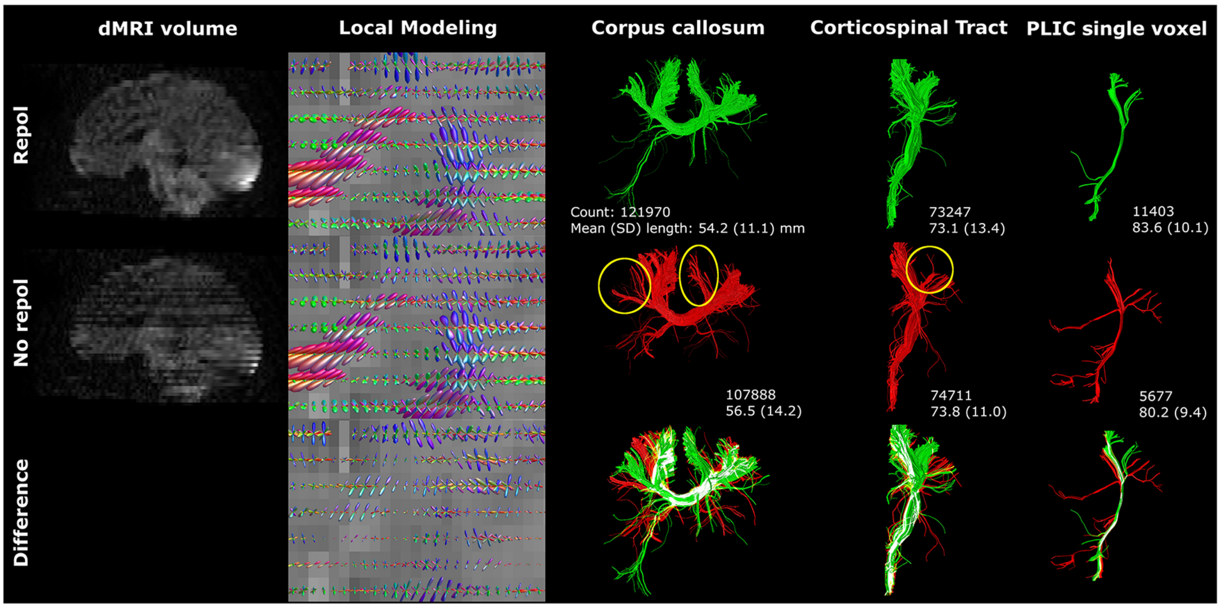

FIGURE 6
Motion artifacts (reflected in signal dropout) affected tractography. The single voxel posterior limb of internal capsule reconstruction was severely affected by axial slice dropout, resulting in less and shorter tracts. However, these findings were not reflected in the CST reconstructions. Reconstructions were acquired from the BIMP scan with motion. The lower row visualizes differences between repol and no repol with overlapping streamlines visualized in white.

Further testing of methodological settings along the dMRI processing pipeline illustrated the influence of spatial and angular resolution, and preprocessing settings on tractography. Generally, an isotropic voxel size is preferred over an anisotropic voxel size due to its advantages in uniform resolution, equal sampling, and reduced partial volume effects (33). The 1 mm isotropic resolution is visually favored over the 2 mm (Figure 3), but it either requires longer scan times during high-resolution acquisition or necessitates data resampling. The voxel size resampling utilized in this study involves data interpolation, which may affect data quality. Consequently, differences observed in local modeling and tract reconstruction may not solely arise

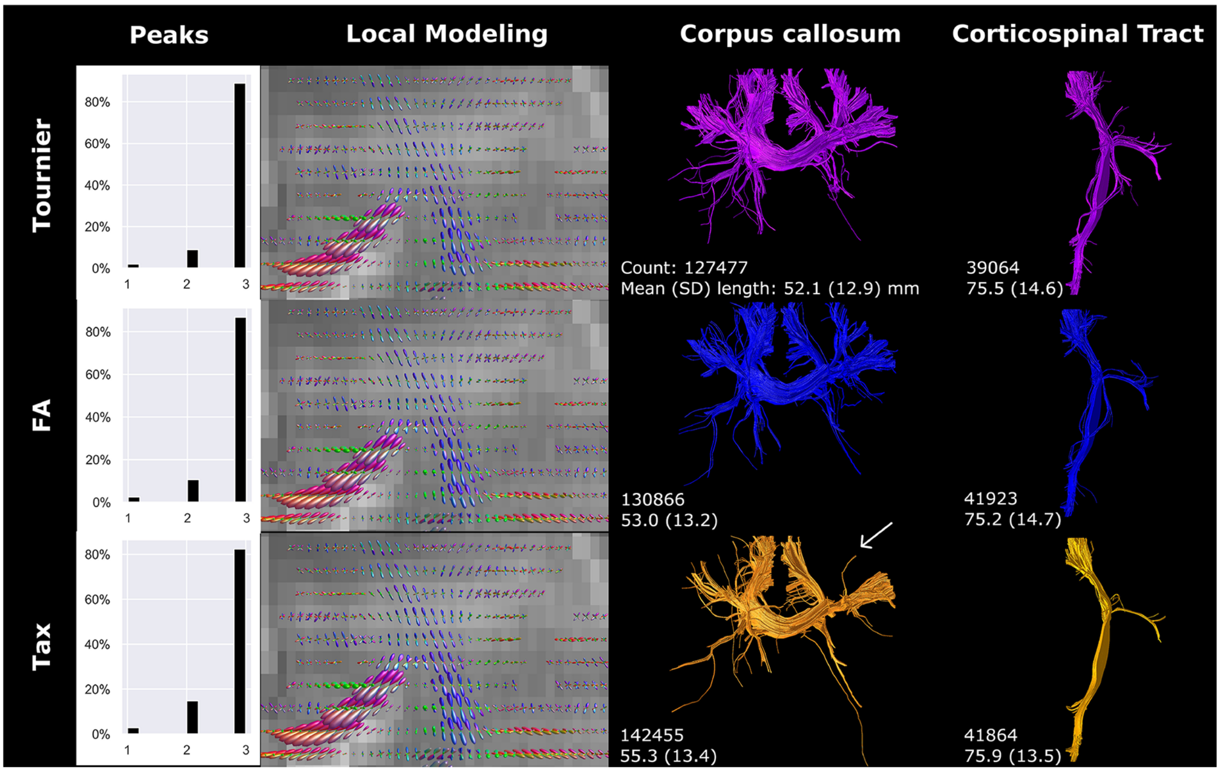

FIGURE 7
Response function method affected local modeling and tractography reconstructions. A higher fODF amplitude was found for FA, compared to Tournier, and for Tax, compared to FA. Reconstructions were acquired from the BIMP scan without motion.

from variations in voxel size. It is important to note, however, that the reconstructed voxel size of images used in this study differed from the acquired voxel size, also introducing uncertainties due to interpolation (8).

Reducing the number of gradient directions reduces angular information and leads to greater uncertainty in fODF estimations (31). The transition from 45 to 32 directions (BIMP data) in this study exerted a more pronounced visual impact on streamline reconstruction than the shift from 128 to 45 directions (dHCP data). According to a study by Tournier et al., a minimum of 45 gradient directions is recommended for intermediate b-values (approximately $b = 3{,}000$ s/mm^2), with preferably higher angularity to boost overall signal-to-noise ratio (34). Consequently, 32 directions may prove insufficient, resulting in elevated uncertainty values and reconstruction errors. An added complexity for the current study is that the dHCP-subject was born full term (39^{+4}) while the BIMP-subject was born late preterm (35^{+2}). Moderate-late preterm infants typically exhibit less brain maturation compared to full-term infants at TEA, thereby potentially influencing the visualized differences in angular resolution.

The practice of scanning infants without sedation offers benefits by avoiding sedation-related risks, but also increases the likelihood of infants waking during the scan, introducing motion artifacts. dMRI scans are particularly sensitive to infant motion due to the complexity, duration, and loudness of noises associated with the sequences (35). Our results show that omitting signal dropout correction (FSL repol) severely affects white matter tract reconstructions (Figure 5). Moreover, signal dropout represents just one of the effects of motion (other effects include slice-to-volume or volume-to-volume misalignment) and motion is not the only common artifact in dMRI. Other artifacts can be induced by factors such as Gibbs ringing, eddy and EPI distortions, and signal inhomogeneity. Therefore, thorough quality assessment and artifact correction before tractography are crucial, as failing to address these issues leads to heightened uncertainty in streamline output. An overview of dMRI-related artifacts and how to approach correction was previously described by Tax et al. (36).

The influence of response function estimation algorithm selection seems to be limited in our images. Nevertheless, variations such as the missing branch in the CC reconstruction with the Tax algorithm were observed. The recursive calibration parameters (relative magnitude between main and second peak, and anisotropy of the initial response function) for this algorithm were set to accommodate typical adult scans at higher *b*-values and may have to be adjusted for infant data. While providing further technical explanations for these techniques falls beyond the scope of this paper, the experiment underscores how conscious or unconscious choices in data processing can influence tractography outcomes.

Although tractography settings frequently vary between studies,[1] they exert a significant influence on tractography outcomes. For

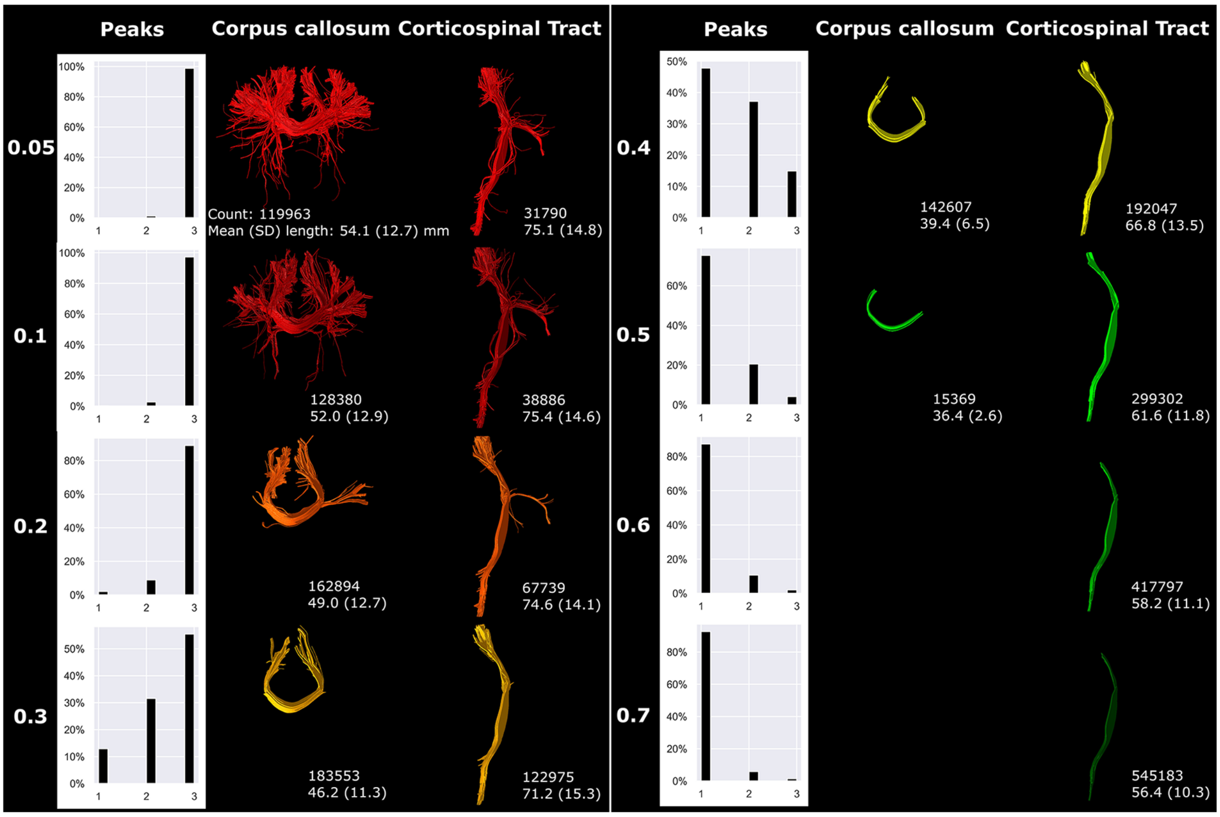

FIGURE 8
fODF thresholding (indicated on the left) mostly affected more peripheral sections of fiber bundles. Reconstructions were acquired from the BIMP scan without motion.

example, the effects of varying the FOD threshold visually adheres to a logical pattern, resulting in shorter and less branching tracts as the FOD increases. However, in contradiction, the streamline count increases with an increasing FOD threshold. This discrepancy can be attributed to the tractography settings, where the streamline count for whole brain tractography was set to 10 million. The algorithm continues to seed until this threshold has been reached, while increasing the FOD threshold decreases the number of potential seeding locations.

A small step size (smaller than the voxel size) is generally advised for fiber tracking, as larger step size may result in the algorithm stepping over the ROIs, potentially missing eligible streamlines (stepping over inclusion ROI) or potentially reconstructing too many streamlines (stepping over exclusion ROI). Therefore, for step sizes larger than the voxel size, ROI-thickness was increased, see Supplementary Figure S1.

Visual reconstructions, as well as streamline count and length, were affected by most of the setting adjustments. Importantly, effects varied between the CC and CST fiber bundles in some of the experiments. This indicates that different fiber bundles are impacted differently by methodological choices. Furthermore, diffusion measures experienced variation of up to 23%, exceeding the typical percentage change observed when comparing diffusion measures between populations (5%–10% change). In contrast, only minimal FA variations were found for the CST. CST reconstructions were mostly affected at the peripheral parts of the tracts, while the majority of the tract with relatively high FA values is the main, dense branch. Variations in peripheral reconstructions may therefore not severely affect the CST FA values. The results emphasize the significance of testing settings on the available dataset and carefully observing their effects on tract reconstruction, in order to identify the optimal setting combination for the specific dataset and tracts prior to analyzing large datasets (37). Subsequently, accurate and comprehensive reporting of processing and tractography settings to facilitate reproducibility of studies is essential.

Since the first introduction of tractography for analysis of neonatal data, the preferred method has remained DTI.[1] In adult data, CSD tractography has been studied on a larger scale, including comparisons of DTI and CSD tractography on dMRI data of lower quality (generally single-shell, b-value <2,000 s/mm^2 and <40 gradient directions) (38–41). Although none of these studies have primarily focused on assessing feasibility of reconstructing crossing fiber bundles—such as zooming in on the fODFs and tract reconstructions at regions where fibers cross—the presented images of fiber tract reconstructions for visual comparison of DTI and CSD provide insight into the appearance of tracts and the preferred use of CSD over DTI (38–41).

The implementation of CSD tractography for neonatal data brings forth concerns regarding potential false positive and false

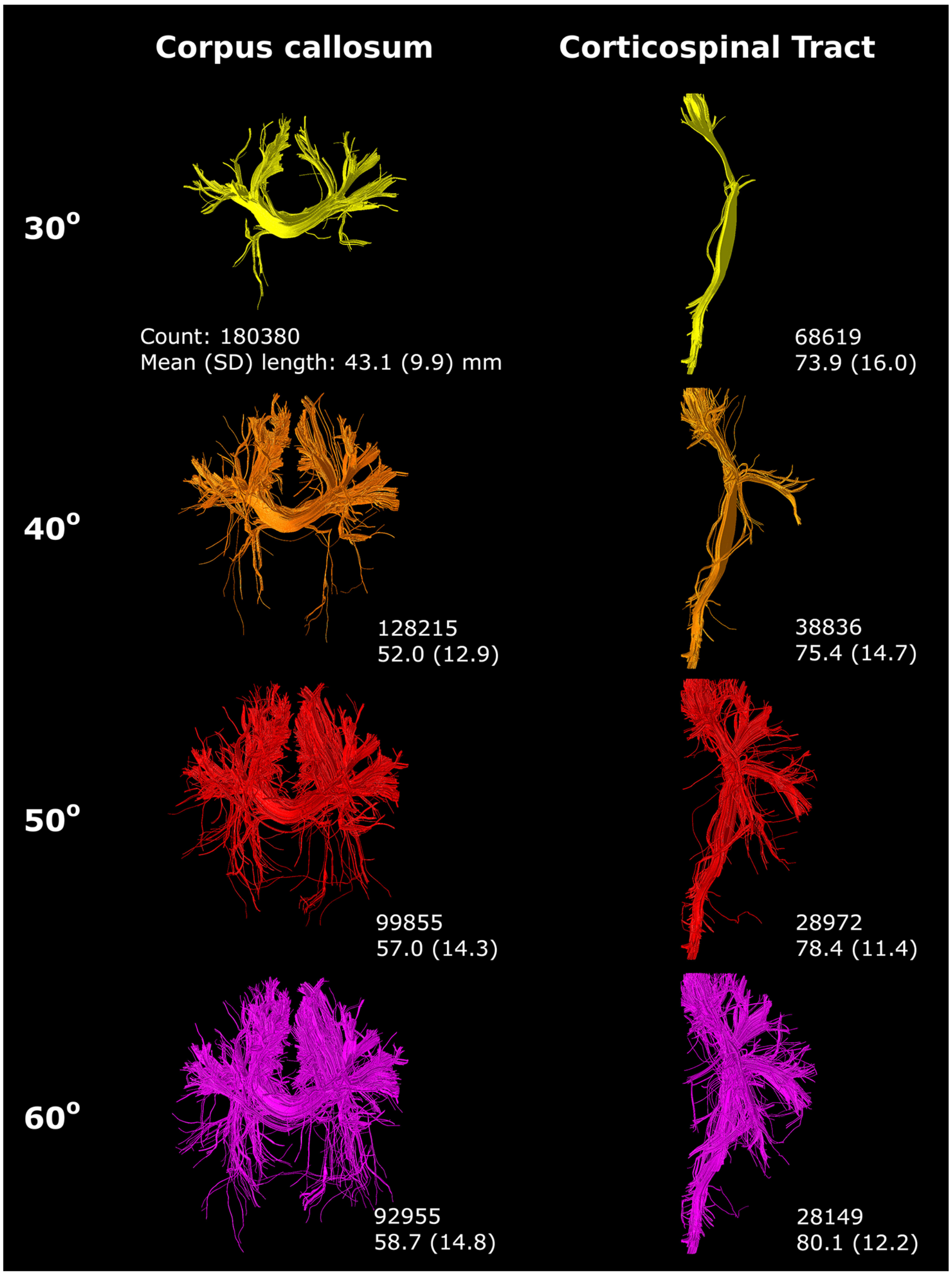

FIGURE 9
An increasing angle threshold (indicated on the left) resulted in more branching of streamlines and a visually increased bundle diameter. Reconstructions were acquired from the BIMP scan without motion.

negative streamlines (4). For instance, the streamlines that project inferiorly in the reconstruction of the CC (see Figure 8 with high angle threshold) may be considered false positive tracts, as their existence has not been anatomically confirmed. However, such reconstructions are not uncommon and are also reported in adult data (4). Nevertheless, evaluating anatomical accuracy poses challenges, as numerous factors influence tractography reconstruction. In two studies in which research groups were tasked with performing tractography on a raw adult dataset (4) or segmenting white matter tracts from an adult whole brain tractography (42), significant variations in tract reconstruction were observed. Schilling et al. even noted that bundle segmentation from a provided whole brain tractogram was a greater source of variability in the virtual dissection process than imaging protocols and variability across subjects (42). Therefore, while assessing anatomical accuracy is crucial, addressing the challenges associated with variability in tractography reconstruction and bundle segmentation may be necessary beforehand.

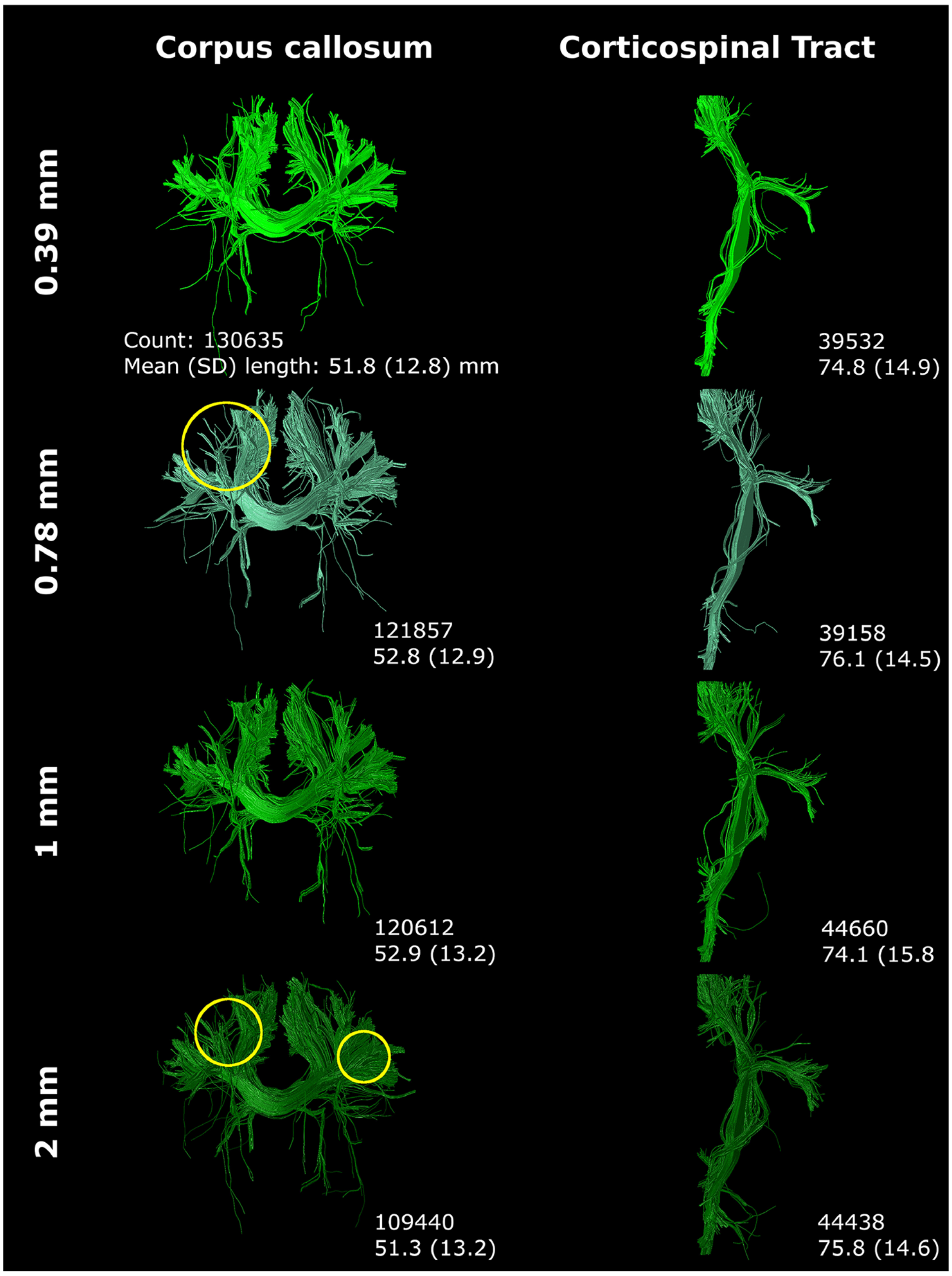

FIGURE 10
Step size (listed on left) mostly affected tract reconstruction with a step size larger than the voxel size (with increased region of interest thickness). Differences were highlighted with yellow circles. Reconstructions were acquired from the BIMP scan without motion.

4.1 Strengths and limitations

To the best of our knowledge, this study is the first to demonstrate the feasibility of CSD with unsedated neonatal dMRI data, considering its capacity to reconstruct crossing fiber bundles and visualize local modeling in regions with crossing fibers. We systematically explored the implications of imaging and image processing choices across all stages of acquisition, preprocessing, and tractography on streamline reconstructions, with a focus on visualizing local modeling and two major fiber bundles. However, some limitations should be acknowledged. We limited our assessment to two fiber bundles crossing in the centrum semiovale, acknowledging that effects on streamline reconstruction and crossing fiber bundles may vary in other brain regions. In addition, anatomical accuracy was not assessed. We recognize the importance, and intend to address this in future studies. Furthermore, while executing this study, multiple tractography approaches were tested on the available data. Processing the multi-shell dHCP was preferably done using the multi-shell multi-tissue algorithm from Dhollander (43).

TABLE 2 Diffusion measures for experiments as indicated under part A for each reconstructed fiber bundle.

Experiment description		Fiber bundle	Mean FA	%-change	Mean MD	%-change
DTI	b800	CC	0.342		0.00132	
	b2000	CC	0.346	1.23	0.00118	**−10.60**
CSD	b800	CC	0.304	**−11.31**	0.00137	3.84
	b2000	CC	0.312	**−8.70**	0.00122	**−7.19**
DTI	b800	CST	0.407		0.00106	
	b2000	CST	0.420	3.40	0.00098	**−7.68**
CSD	b800	CST	0.404	−0.59	0.00103	−2.88
	b2000	CST	0.408	0.41	0.00097	**−8.53**
DTI	b800	SLF	0.261		0.00125	
	b2000	SLF	0.266	1.87	0.00122	−2.62
CSD	b800	SLF	0.219	**−16.09**	0.00155	**23.76**
	b2000	SLF	0.247	**−5.31**	0.00123	−2.02

Mean fractional anisotropy and mean diffusivity values were derived from a single fiber bundle. Percentage-change was calculated with respect to DTI on a b800 scan. Bold values highlight experiments with >5% change in diffusion measure.
DTI, diffusion tensor imaging; CSD, constrained spherical deconvolution; FA, fractional anisotropy; MD, mean diffusivity; fODF, fiber orientation distribution function; CC, corpus callosum; CST, corticospinal tract; SLF, superior longitudinal fasciculus; PLIC, posterior limb of internal capsule.

TABLE 3 Diffusion measures for experiments as indicated under part B for each reconstructed fiber bundle.

Experiment description		Fiber bundle	Mean FA	%-change	Mean MD	%-change
BIMP	Reconstructed	CC	0.312		0.00122	
	2 mm	CC	0.289	**−7.57**	0.00121	−1.48
	1 mm	CC	0.302	−3.49	0.00121	−1.29
	32 directions	CC	0.310	−0.85	0.00122	−0.58
	Reconstructed	CST	0.408		0.00097	
	2 mm	CST	0.414	1.51	0.00097	0.11
	1 mm	CST	0.346	**−15.30**	0.00098	1.12
	32 directions	CST	0.398	−2.46	0.00097	−0.28
dHCP	128 directions	CC	0.380		0.00114	
	45 directions	CC	0.387	1.88	0.00105	**−8.40**
	128 directions	CST	0.413		0.00106	
	45 directions	CST	0.440	**6.62**	0.00094	**−11.79**
Response function	Tournier	CC	0.312		0.00122	
	FA	CC	0.313	0.10	0.00122	−0.21
	Tax	CC	0.314	0.36	0.00122	−0.49
	Tournier	CST	0.408		0.00097	
	FA	CST	0.411	0.81	0.00097	−0.14
	Tax	CST	0.412	1.08	0.00097	0.04
Motion correction	Repol	CC	0.274		0.00117	
	No repol	CC	0.280	2.40	0.00118	0.25
	Repol	CST	0.372		0.000972	
	No repol	CST	0.362	−2.85	0.000970	−0.15
	Repol	PLIC	0.392		0.00097	
	No repol	PLIC	0.360	**−8.15**	0.00098	0.72

Mean fractional anisotropy and mean diffusivity values were derived from a single fiber bundle. Percentage-change was calculated with respect to (1) reconstructed anisotropic voxels with 45 directions for BIMP data, (2) 128 directions for dHCP data, (3) Tournier algorithm, and (4) motion correction with repol option. Bold values highlight experiments with >5% change in diffusion measure. FA, fractional anisotropy; MD, mean diffusivity; fODF, fiber orientation distribution function; CC, corpus callosum; CST, corticospinal tract; SLF, superior longitudinal fasciculus; PLIC, posterior limb of internal capsule.

However, when testing this algorithm on the dHCP data, it failed to model white matter, grey matter and cerebrospinal fluid-like signal contributions properly. Similar results were previously reported by Dhollander et al. (44). Improving multi-shell multi-tissue algorithms for neonatal data is needed to also allow for full utilization of the high-quality data. Moreover, this study only assessed deterministic CSD compared to deterministic DTI tractography, other local modeling approaches and probabilistic algorithms were not assessed. Furthermore, we selected a focused sub-set of processing and tractography settings anticipated to have a strong impact on streamline reconstruction. While acknowledged that additional settings, such as streamline count, seeding method, choice of software toolbox employing different algorithms, various imaging acquisition settings, and MR system may also influence tractography outputs, the scope of these factors is too large to include them all. Nonetheless, the

TABLE 4 Diffusion measures for experiments as indicated under part C for each reconstructed fiber bundle.

Experiment description		Fiber bundle	Mean FA	%-change	Mean MD	%-change
fODF threshold	0.05	CC	0.309	−1.23	0.00122	−0.20
	0.1	CC	0.312		0.00122	
	0.2	CC	0.324	3.70	0.00121	−0.88
	0.3	CC	0.338	**8.09**	0.00119	−2.37
	0.4	CC	0.346	**10.75**	0.00118	−3.53
	0.5	CC	0.349	**11.74**	0.00114	**−6.53**
	0.05	CST	0.408	−0.11	0.000970	0.03
	0.1	CST	0.408		0.000970	
	0.2	CST	0.412	0.90	0.000966	−0.36
	0.3	CST	0.422	3.38	0.000960	−1.07
	0.4	CST	0.441	**7.95**	0.000949	−2.11
	0.5	CST	0.457	**11.95**	0.000938	−3.24
	0.6	CST	0.468	**14.62**	0.000931	−3.99
	0.7	CST	0.476	**16.60**	0.000929	−4.19
Angle threshold	30	CC	0.324		0.00125	
	40	CC	0.313	−3.57	0.00122	−1.84
	50	CC	0.306	**−5.58**	0.00121	−2.75
	60	CC	0.304	**−6.09**	0.00121	−3.01
	30	CST	0.415		0.000964	
	40	CST	0.408	−1.61	0.000970	0.65
	50	CST	0.399	−3.74	0.000979	1.60
	60	CST	0.397	−4.33	0.000983	1.97
Step size	0.39	CC	0.313		0.00122	
	0.78	CC	0.312	−0.43	0.00122	−0.09
	1	CC	0.311	−0.66	0.00123	0.07
	2	CC	0.312	−0.30	0.00122	−0.06
	0.39	CST	0.409		0.000970	
	0.78	CST	0.407	−0.54	0.000971	0.14
	1	CST	0.405	−1.06	0.000969	−0.02
	2	CST	0.406	−0.68	0.000971	0.12

Mean fractional anisotropy and mean diffusivity values were derived from a single fiber bundle. Percentage-change was calculated with respect to (1) fODF threshold 0.1, (2) angle 30 and (3) step-size 0.39 mm. Bold values highlight experiments with >5% change in diffusion measure.

DTI, diffusion tensor imaging; CSD, constrained spherical deconvolution; FA, fractional anisotropy; MD, mean diffusivity; fODF, fiber orientation distribution function; CC, corpus callosum; CST, corticospinal tract; SLF, superior longitudinal fasciculus; PLIC, posterior limb of internal capsule.

selected factors offer valuable insights into the implications of decision-making processes on settings and their effect on tractography outcomes.

4.2 Recommendations/future directions

In the field of neonatal dMRI tractography with CSD, studies should focus on refining multi-shell multi-tissue models for neonatal data to better characterize tissue microstructure and utilize the full potential of multi-shell data acquired from neonates. Secondly, exploring global modeling techniques could offer valuable insights by incorporating information from larger brain regions simultaneously (instead of focusing on a single voxel with current techniques), potentially enhancing the accuracy and robustness of streamline reconstructions. Thirdly, leveraging deep learning methods, such as TractSeg (45), holds promise for improving efficiency, accuracy and reproducibility in streamline reconstruction, but applicability on neonatal data should be assessed first. Finally, we encourage researchers to experiment with settings in multiple study subjects and thoroughly document the final settings to enhance reproducibility and comparability of multi-center data. While experimenting, it is crucial to bear in mind that cleaner tracts, more fiber crossings, a higher streamline count, or longer streamlines do not inherently equate to more accurate results or “higher connectivity” (46). Jones et al. published a comprehensive overview on basic insights, limitations, pitfalls, misunderstandings, misconceptions and misinterpretation of dMRI, highlighting common misconceptions of dMRI tractography (46).

5 Conclusion

Tractography with unsedated neonatal diffusion MRI data using CSD is feasible and has advantages over using DTI for this type of data. CSD is valuable for reconstructing crossing fiber bundles, resulting in more peripherally projecting fiber branches of the corpus callosum and corticospinal tracts.

We take caution with defining specific methods or combinations of settings for researchers in the field of neonatal dMRI, as these settings may yield different effects on datasets distinct from those used in our study. Instead, we aimed to demonstrate the feasibility of CSD tractography with unsedated neonatal dMRI data and illustrate the impact of processing choices on tractography outcomes. This study sheds light on the technical and practical decisions involved in neonatal dMRI tractography, highlighting that variations in settings from acquisition to tractography have a substantial effect on output, within and across datasets. From acquisition to tractography analysis, settings should be carefully deliberated before initiating a study and notable distinctions between adult and neonatal applications should be kept in mind during this process.

Data availability statement

The datasets presented in this article are not readily available because the dataset utilized in this study is subject to restrictions preventing its sharing or public distribution. As such, we are unable to provide access to the dataset. Requests to access the datasets should be directed to Lara Leijser, lara.leijser@ucalgary.ca.

Ethics statement

The studies involving humans were approved by Health Research Ethics Board of Alberta. The studies were conducted in accordance with the local legislation and institutional requirements. Written informed consent for participation in this study was provided by the participants' legal guardians/next of kin.

Author contributions

AV: Conceptualization, Data curation, Formal Analysis, Funding acquisition, Investigation, Methodology, Project administration, Software, Validation, Visualization, Writing – original draft, Writing – review & editing. CT: Conceptualization, Formal Analysis, Methodology, Software, Supervision, Validation, Writing – review & editing. MB: Conceptualization, Funding acquisition, Methodology, Supervision, Writing – review & editing. HC: Conceptualization, Methodology, Validation, Writing – review & editing. GW-M: Conceptualization, Funding acquisition, Methodology, Supervision, Writing – review & editing. RK: Investigation, Writing – review & editing. AL: Conceptualization, Methodology, Supervision, Validation, Writing – review & editing. LL: Conceptualization, Formal Analysis, Funding acquisition, Methodology, Resources, Supervision, Validation, Writing – review & editing.

Funding

The author(s) declare financial support was received for the research, authorship, and/or publication of this article.

AV is jointly supported by the Royal Netherlands Academy of Arts and Sciences (KNAW, Amsterdam, The Netherlands), ter Meulen Fund [KNAWWF/1327/TMB202126], Isala Science and Innovation Fund (Zwolle, the Netherlands), Science Fund Medical Specialist Isala (Zwolle, the Netherlands) and the Newborn Brain Society Early Career Award 2024. LL's research program is jointly supported by the Alberta Children's Hospital Foundation, Alberta Children's Hospital Research Institute and the Calgary Health Foundation (Calgary, Canada). CT is supported by the Wellcome Trust [215944/Z/19/Z] and a Veni grant (17331) from the Dutch Research Council (NWO). The sponsors had no role in the design and conduct of the study, the collection, management, analysis and interpretation of the data, the preparation, review and approval of the manuscript, or the decision to submit the manuscript for publication. For the purpose of open access, the author has applied a CC BY public copyright license to any Author Accepted Manuscript version arising from this submission.

Acknowledgments

These results were partially obtained using data made available from the *Developing Human Connectome Project* funded by the European Research Council under the European Union's Seventh Framework Programme (FP/2007-2013)/ERC Grant Agreement no. [319456].

Conflict of interest

The authors declare that the research was conducted in the absence of any commercial or financial relationships that could be construed as a potential conflict of interest.

Publisher's note

Supplementary material

The Supplementary Material for this article can be found online at: https://www.frontiersin.org/articles/10.3389/fradi.2024.1416672/full#supplementary-material

References

1. Hüppi PS, Dubois J. Diffusion tensor imaging of brain development. *Semin Fetal Neonatal Med*. (2006) 11(6):489–97. doi: 10.1016/j.siny.2006.07.006

2. Boswinkel V, Verschuur AS, Nijholt IM, van Osch JAC, Nijboer-Oosterveld J, Beare RJ, et al. Mild brain lesions do not affect brain volumes in moderate-late preterm infants. *Eur J Paediatr Neurol*. (2021) 34:91–8. doi: 10.1016/j.ejpn.2021.08.003

3. Emsell L, Van Hecke W, Tournier J. Introduction to diffusion tensor imaging. In: Van Hecke W, editor. *Diffusion Tensor Imaging*. New York, NY: Springer (2016). p. 7–19. doi: 10.1007/978-1-4939-3118-7_2

4. Maier-Hein KH, Neher PF, Houde J, Côté M, Garyfallidis E, Zhong J, et al. The challenge of mapping the human connectome based on diffusion tractography. *Nat Commun*. (2017) 8(1):1349. doi: 10.1038/s41467-017-01285-x

5. Farquharson S, Tournier J. High angular resolution diffusion imaging. In: Van Hecke W, editor. *Diffusion Tensor Imaging*. New York, NY: Springer (2016). p. 383–418. doi: 10.1007/978-1-4939-3118-7_20

6. Antonov NK, Ruzal-Shapiro CB, Morel KD, Millar WS, Kashyap S, Lauren CT, et al. Feed and wrap MRI technique in infants. *Clin Pediatr (Phila)*. (2016) 56 (12):1095. doi: 10.1177/0009922816677806

7. Toselli B, Tortora D, Severino M, Arnulfo G, Canessa A, Morana G, et al. Improvement in white matter tract reconstruction with constrained spherical deconvolution and track density mapping in low angular resolution data: a pediatric study and literature review. *Front Pediatr*. (2017) 5(182):1–15. doi: 10.3389/fped.2017.00182

8. Dyrby TB, Lundell H, Burke MW, Reislev NL, Paulson OB, Ptito M, et al. Interpolation of diffusion weighted imaging datasets. *NeuroImage*. (2014) 103:202. doi: 10.1016/j.neuroimage.2014.09.005

9. Hutter J, Tournier JD, Price AN, Cordero-Grande L, Hughes EJ, Malik S, et al. Time-efficient and flexible design of optimized multishell HARDI diffusion. *Magn Reson Med*. (2017) 79(3):1276. doi: 10.1002/mrm.26765

10. Smith SM. Fast robust automated brain extraction. *Hum Brain Mapp*. (2002) 17 (3):143. doi: 10.1002/hbm.10062

11. Tournier J, Smith R, Raffelt D, Tabbara R, Dhollander T, Pietsch M, et al. MRtrix3: a fast, flexible and open software framework for medical image processing and visualisation. *NeuroImage*. (2019) 202:116137. doi: 10.1016/j.neuroimage.2019.116137

12. Avants BB, Tustison N, July HJ. Advanced Normalization Tools (ANTS). (2014).

13. Veraart J, Novikov DS, Christiaens D, Ades-Aron B, Sijbers J, Fieremans E. Denoising of diffusion MRI using random matrix theory. *NeuroImage*. (2017) 142:394. doi: 10.1016/j.neuroimage.2016.08.016

14. Kellner E, Dhital B, Kiselev VG, Reisert M. Gibbs-ringing artifact removal based on local subvoxel-shifts. *Magn Reson Med*. (2015) 76(5):1574. doi: 10.1002/mrm.26054

15. Andersson JLR, Graham MS, Drobnjak I, Zhang H, Filippini N, Bastiani M. Towards a comprehensive framework for movement and distortion correction of diffusion MR images: within volume movement. *NeuroImage*. (2017) 152:450. doi: 10.1016/j.neuroimage.2017.02.085

16. Andersson JLR, Graham MS, Zsoldos E, Sotiropoulos SN. Incorporating outlier detection and replacement into a non-parametric framework for movement and distortion correction of diffusion MR images. *NeuroImage*. (2016) 141:556. doi: 10.1016/j.neuroimage.2016.06.058

17. Andersson JLR, Sotiropoulos SN. An integrated approach to correction for off-resonance effects and subject movement in diffusion MR imaging. *NeuroImage*. (2015) 125:1063. doi: 10.1016/j.neuroimage.2015.10.019

18. Zhang Y, Brady M, Smith S. Segmentation of brain MR images through a hidden markov random field model and the expectation-maximization algorithm. *IEEE Trans Med Imaging*. (2001) 20(1):45–57. doi: 10.1109/42.906424

19. Smith SM, Jenkinson M, Woolrich MW, Beckmann CF, Behrens TEJ, Johansen-Berg H, et al. Advances in functional and structural MR image analysis and implementation as FSL. *NeuroImage*. (2004) 23:S208. doi: 10.1016/j.neuroimage.2004.07.051

20. Makropoulos A, Robinson EC, Schuh A, Wright R, Fitzgibbon S, Bozek J, et al. The developing human connectome project: a minimal processing pipeline for neonatal cortical surface reconstruction. *NeuroImage*. (2018) 173:88–112. doi: 10.1016/j.neuroimage.2018.01.054

21. Bastiani M, Andersson JLR, Cordero-Grande L, Murgasova M, Hutter J, Price AN, et al. Automated processing pipeline for neonatal diffusion MRI in the developing human connectome project. *NeuroImage*. (2018) 185:750. doi: 10.1016/j.neuroimage.2018.05.064

22. Mori S, Crain BJ, Chacko VP, Van Zijl PC. Three-dimensional tracking of axonal projections in the brain by magnetic resonance imaging. *Ann Neurol*. (1999) 45 (2):265. doi: 10.1002/1531-8249(199902)45:2<265::aid-ana21>3.0.co;2-3

23. Tournier JD, Calamante F, Connelly A. Determination of the appropriate b value and number of gradient directions for high-angular-resolution diffusion-weighted imaging. *NMR Biomed*. (2013) 26(12):1775–86. doi: 10.1002/nbm.3017

24. Raffelt D, Dhollander T, Tournier J, Tabbara R, Smith RE, Pierre E, et al. *Bias field correction and intensity normalisation for quantitative analysis of apparent fibre density*. (2017).

25. Tournier JD, Calamante F, Connelly A. MRtrix: diffusion tractography in crossing fiber regions. *Int J Imaging Syst Tech*. (2012) 22(1):53–66. doi: 10.1002/ima.22005

26. Basser PJ, Pajevic S, Pierpaoli C, Duda J, Aldroubi A. In vivo fiber tractography using DT-MRI data. *Magn Reson Med*. (2000) 44(4):625. doi: 10.1002/1522-2594(200010)44:4<625::aid-mrm17>3.0.co;2-o

27. Tournier JD, Calamante F, Gadian DG, Connelly A. Direct estimation of the fiber orientation density function from diffusion-weighted MRI data using spherical deconvolution. *NeuroImage*. (2004) 23(3):1176–85. doi: 10.1016/j.neuroimage.2004.07.037

28. Tax CMW, Jeurissen B, Vos SB, Viergever MA, Leemans A. Recursive calibration of the fiber response function for spherical deconvolution of diffusion MRI data. *NeuroImage*. (2013) 86:67. doi: 10.1016/j.neuroimage.2013.07.067

29. Rau A, Demerath T, Kremers N, Eckenweiler M, Von Der Warth R, Urbach H. Measuring the head circumference on MRI in children: an interrater study. *Clin Neuroradiol*. (2021) 31(4):1021. doi: 10.1007/s00062-021-01019-z

30. Farquharson S, Tournier JD, Calamante F, Fabinyi G, Schneider-Kolsky M, Jackson GD, et al. White matter fiber tractography: why we need to move beyond DTI. *J Neurosurg*. (2013) 118(6):1363–6. doi: 10.3171/2013.2.JNS121294

31. Van Hecke W, Emsell L, Sunaert S. *Diffusion Tensor Imaging*. 1st ed. New York, NY: Springer (2016).

32. Jeurissen B, Descoteaux M, Mori S, Leemans A. Diffusion MRI fiber tractography of the brain. *NMR Biomed*. (2019) 32(4):1–22. doi: 10.1002/nbm.3785

33. Caan MWA. DTI Analysis methods: fibre tracking and connectivity. In: Van Hecke W, editor. *Diffusion Tensor Imaging*. New York, NY: Springer (2016). p. 205–28. doi: 10.1007/978-1-4939-3118-7_11

34. Tournier J, Calamante F, Connelly A. *How many diffusion gradient directions are required for HARDI?* (2009). p. 358.

35. Tax CMW, Vos SB, Leemans A. Checking and correcting DTI data. In: Van Hecke W, editor. *Diffusion Tensor Imaging: A Practical Handbook*. New York, NY: Springer (2016). p. 127–50. doi: 10.1007/978-1-4939-3118-7_7

36. Tax CMW, Bastiani M, Veraart J, Garyfallidis E, Okan Irfanoglu M. What's new and what's next in diffusion MRI preprocessing. *NeuroImage*. (2022) 249:118830. doi: 10.1016/j.neuroimage.2021.118830

37. Chamberland M, Whittingstall K, Fortin D, Mathieu D, Descoteaux M. Real-time multi-peak tractography for instantaneous connectivity display. *Front Neuroinform*. (2014) 8:59. doi: 10.3389/fninf.2014.00059

38. Calamuneri A, Arrigo A, Mormina E, Milardi D, Cacciola A, Chillemi G, et al. White matter tissue quantification at low b-values within constrained spherical deconvolution framework. *Front Neurol*. (2018) 9(716):1–14. doi: 10.3389/fneur.2018.00716

39. Tallus J, Mohammadian M, Kurki T, Roine T, Posti JP, Tenovuo O. A comparison of diffusion tensor imaging tractography and constrained spherical deconvolution with automatic segmentation in traumatic brain injury. *NeuroImage Clin*. (2022) 37:103284. doi: 10.1016/j.nicl.2022.103284

40. Mormina E, Arrigo A, Calamuneri A, Alafaci C, Tomasello F, Morabito R, et al. Optic radiations evaluation in patients affected by high-grade gliomas: a side-by-side constrained spherical deconvolution and diffusion tensor imaging study. *Neuroradiology*. (2016) 58(11):1067. doi: 10.1007/s00234-016-1732-8

41. Auriat AM, Borich MR, Snow NJ, Wadden KP, Boyd LA. Comparing a diffusion tensor and non-tensor approach to white matter fiber tractography in chronic stroke. *NeuroImage Clin*. (2015) 7:771. doi: 10.1016/j.nicl.2015.03.007

42. Schilling KG, Rheault F, Petit L, Hansen CB, Nath V, Yeh F, et al. Tractography dissection variability: what happens when 42 groups dissect 14 white matter bundles on the same dataset? *NeuroImage*. (2021) 243:118502. doi: 10.1016/j.neuroimage.2021.118502

43. Dhollander T, Raffelt D, Connelly A. *Unsupervised 3-tissue response function estimation from single-shell or multi-shell diffusion MR data without a co-registered T1 image*. (2016).

44. Dhollander T, Mito R, Connelly A. *Single-shell 3-tissue CSD (SS3T-CSD) modelling of developing HCP (dHCP) diffusion MRI data*. (2019).

45. Wasserthal J, Neher P, Maier-Hein K. TractSeg-fast and accurate white matter tract segmentation. *Neuroimage*. (2018) 183:239–53. doi: 10.1016/j.neuroimage.2018.07.070

46. Jones DK, Knösche TR, Turner R. White matter integrity, fiber count, and other fallacies: the do's and don'ts of diffusion MRI. *NeuroImage*. (2012) 73:239. doi: 10.1016/j.neuroimage.2012.06.081

frontiers | Frontiers in Neurology

TYPE Original Research
PUBLISHED 14 August 2024
DOI 10.3389/fneur.2024.1427273

EDITED BY
Ye Wu,
Nanjing University of Science and Technology, China

REVIEWED BY
Jiaolong Qin,
Nanjing University of Science and Technology, China
Yoonmi Hong,
University of North Carolina at Chapel Hill, United States
Jianzhong He,
Zhejiang University of Technology, China

*CORRESPONDENCE
Emiliano Trimarco
✉ emiliano.trimarco@inibica.es

RECEIVED 03 May 2024
ACCEPTED 24 July 2024
PUBLISHED 14 August 2024

CITATION
Trimarco E, Jafrasteh B, Jiménez-Luque N, Marín Almagro Y, Román Ruiz M, Lubián Gutiérrez M, Ruiz González E, Segado Arenas A, Lubián-López SP and Benavente-Fernández I (2024) Thalamic volume in very preterm infants: associations with severe brain injury and neurodevelopmental outcome at two years. *Front. Neurol.* 15:1427273.
doi: 10.3389/fneur.2024.1427273

Thalamic volume in very preterm infants: associations with severe brain injury and neurodevelopmental outcome at two years

Emiliano Trimarco[1]*, Bahram Jafrasteh[1],
Natalia Jiménez-Luque[1], Yolanda Marín Almagro[1],
Macarena Román Ruiz[1], Manuel Lubián Gutiérrez[1,2],
Estefanía Ruiz González[1,2], Antonio Segado Arenas[1,2],
Simón Pedro Lubián-López[1,2] and
Isabel Benavente-Fernández[1,2,3]

[1]Biomedical Research and Innovation Institute of Cádiz (INiBICA) Research Unit, Puerta del Mar University Hospital, Cádiz, Spain, [2]Division of Neonatology, Department of Paediatrics, Puerta del Mar University Hospital, Cádiz, Spain, [3]Area of Paediatrics, Department of Child and Mother Health and Radiology, Medical School, University of Cádiz, Cádiz, Spain

Introduction: Several studies demonstrate the relationship between preterm birth and a reduced thalamus volume at term-equivalent age. In contrast, this study aims to investigate the link between the thalamic growth trajectory during the early postnatal period and neurodevelopment at two years of age.

Methods: Thalamic volume was extracted from 84 early MRI scans at postmenstrual age of 32.33 (± 2.63) weeks and 93 term-equivalent age MRI scans at postmenstrual age of 42.05 (± 3.33) weeks of 116 very preterm infants (56% male) with gestational age at birth of 29.32 (± 2.28) weeks and a birth weight of 1158.92 (± 348.59) grams. Cognitive, motor, and language outcomes at two years of age were assessed with Bayley Scales of Infant and Toddler Development Third Edition. Bivariate analysis was used to describe the clinical variables according to neurodevelopmental outcomes and multilevel linear regression models were used to examine the impact of these variables on thalamic volume and its relationship with neurodevelopmental outcomes.

Results: The results suggest an association between severe brain injury and thalamic growth trajectory (β coef $= -0.611$; $p < 0.001$). Moreover, thalamic growth trajectory during early postnatal life was associated with the three subscale scores of the neurodevelopmental assessment (cognitive: β coef $= 6.297$; $p = 0.004$; motor: β coef $= 7.283$; $p = 0.001$; language: β coeficient $= 9.053$; $p = 0.002$).

Discussion: These findings highlight (i) the impact of severe brain injury on thalamic growth trajectory during early extrauterine life after preterm birth and (ii) the relationship of thalamic growth trajectory with cognitive, motor, and language outcomes.

KEYWORDS

thalamus, preterm infants, neurodevelopment, brain injury, MRI

1 Introduction

Very preterm infants (VPI), those born at or before 32 weeks of gestational age (GA), have a higher risk of mortality and adverse neurodevelopmental outcome (1–3). Despite improvements in survival rates over the past few decades including for extremely preterm infants (4–6), preterm birth continues to impact negatively on long-term neurodevelopmental outcomes (7–10). Crucial brain development events that take place in the third trimester of pregnancy may be disrupted and modified by preterm birth with subsequent risk of neurological injury (11–13). Preterm delivery and its consequences can impact specific aspects of cerebral development, such as the thalamocortical system (14–17), affecting thalamic volume and white matter maturation even in the absence of brain injury (18). Thus, thalamic volume in premature newborns has been associated with the type of nutrition (19), the presence of white matter injury (20–23), exposure to painful procedures (24), parenting (25). Recent research by our group demonstrated the potential to cluster magnetic resonance images (MRI) deemed pathological according to Kidokoro's score (26) using only morphological thalamus variables extracted from term-equivalent age (TEA) T1-weighted scans (27). Abnormalities in thalamocortical connectivity and reduced thalamic volume have been linked to adverse neurodevelopmental outcomes (28–30) and lower cognitive performance in adulthood (31, 32) in very preterm population. Furthermore, abnormalities in thalamocortical connectivity explored with functional MRI have been associated with Autism Spectrum Disorder (33, 34). While numerous studies have explored various aspects of early (35, 36) and TEA (14, 28, 29) brain scans, there is a notable lack of research investigating the combination of these scans using volume growth trajectory analysis. Our study aims to address this gap by providing insights into the neurodevelopmental processes from early to TEA, thereby contributing to a deeper understanding of brain development during this critical period. Using a trajectory instead of just a point provides a dynamic and comprehensive measure of brain development by capturing changes in thalamic volume over time, as opposed to a single static measurement. This approach allows for the identification of growth patterns, offering valuable insights into developmental processes and potential abnormalities that might be missed with a single volume measure.Therefore, our hypothesis seeks to investigate the relationship between clinical complications, such as brain injury, and the thalamic volume growth trajectory measured at two distinct time points. Additionally, we aim to explore the potential of utilizing the thalamic volume growth trajectory as a predictive marker for neurodevelopmental outcomes at two years of age in a population of VPI. This investigation involves a comprehensive analysis of thalamic volume changes over time, considering various clinical factors that may influence neurodevelopmental outcomes.

2 Material and methods

2.1 Participants

This longitudinal study included VPI, with GA at birth ≤ 32 weeks, admitted to the Hospital Puerta del Mar, Cádiz, Spain, from January 2018 to September 2021. The exclusion criteria were defined as the presence of congenital or chromosomal anomalies, metabolic disorders, and central nervous system infections. This study was approved by the Research and Ethics Committee, and all parents or guardians of the participants provided informed consent. The data used in this study were collected and managed using Research Electronic Data Capture (REDCap) software (37, 38). The initial cohort included 194 eligible infants, of which 152 had at least one MRI. We excluded 36 patients who did not complete neurodevelopmental assessment at 2 years, with a final sample size of 116 preterm infants with at least one MRI and 2-year neurodevelopmental assessment (Figure 1A). VPI not included in the final study sample (n= 78) did not differ significantly in GA, birth weight, and sex from those included, as reported in Table 1. We included 177 brain MRIs: 84 (47.5%) were early scans at a mean PMA of 32.33 (± 2.63) weeks, and 93 (52.5%) TEA scans were performed at a mean PMA of 42.05 (± 3.33) weeks. Remarkably, 61 of 116 infants (52.6%) had both early and TEA scans (Figure 1B). Our final study sample included 116 VPI (56% male) with a mean GA at birth of 29.32 (± 2.28) weeks and a mean birth weight of 1158.92 (± 348.59) grams.

2.2 MRI acquisition and analysis

MRI scans were performed at 2 chronological points: in the first weeks of life and at the TEA. MRI scans were performed using a 1.5 T scanner Magneton Symphony (Siemens Health Care, Erlangen, Germany) located in the radiology unit. T1w images were obtained using a three-dimensional spoiled gradient [repetition time 1,660 (RT)/echo time 5.16(ET)]. The acquisition parameters were as follows: spacing in x, y and z direction: 0.54, 0.54, 1.09; echo time=3.67 ms; flip angle=15° and repetition time=1910.0 ms. The obtained T1w MRI has been converted to equal spacing of 0.9 for study purpose. MRI preprocessing included automatic brain extraction followed by manual correction, N4 bias field correction, and image enhancement and it was performed using MELAGE (39). The results were verified by experts and manually corrected if needed. The thalamus segmentation was performed using an approach from our previous work (27) and was further refined by experts in the group. Specifically, we employed a multi-atlas approach using the Melbourne Children's Regional Infant Brain (M-CRIB 2.0) atlas (40). We first registered the MRI images to the neonatal atlas and then transferred the atlas labels to the MRI images. Finally, we used a local atlas weighting to assign a label to the thalamus, similar to the neonatal pipeline proposed by (41, 42). Figure 2 illustrates an example of early and TEA MRI images with overlaid segmentation. From left to right, we can see coronal, sagittal, and axial views, respectively. After the left and right thalamic volume segmentions, we tested the correlation between them. The Pearson correlation coefficient was very high (r = 0.98), indicating a very strong linear relationship and suggesting that the two volumes are almost identical in our study population. Therefore, the sum of left and right volumes was used in the statistical analysis as a more robust measure of overall thalamic volume.

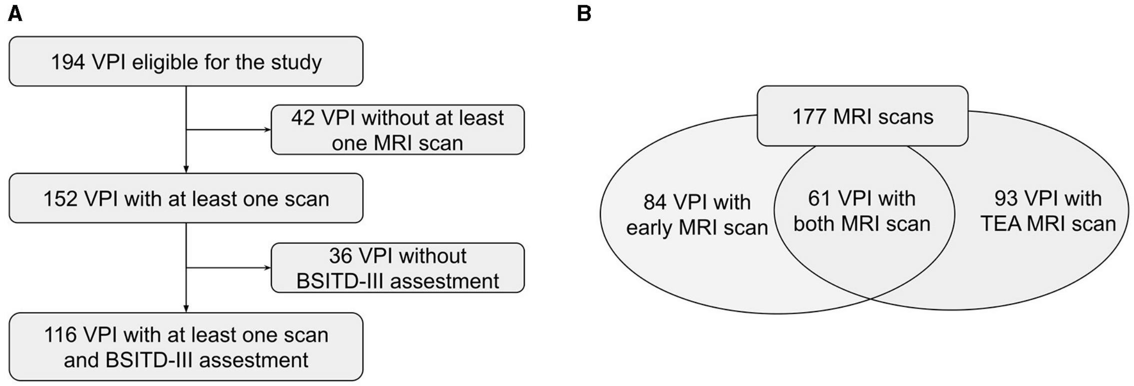

FIGURE 1
(A, B) Flow diagram of the study population. VPI, Very Preterm Infants; MRI, Magnetic Resonance Image; BSITD-III, Bayley Scales of Infant and Toddler Development, Third Edition; TEA, Term-Equivalent Age.

TABLE 1 **Comparison between very preterm infants included in the study and ones excluded.**

	VPI included (*n* = 116)	VPI excluded (*n* = 78)	*p*
GA (weeks)	29.3 ± 2.3	28.2 ± 2.8	0.621
Sex (Male)	65 (56.0 %)	39 (50.0 %)	0.409
Weight (grams)	1,159 ± 349	1,036 ± 383	0.594

VPI, very preterm infants; GA, gestational age. Continuous variables are presented as mean ± standard deviation; Binary variables are shown as an absolute and relative frequency (percentage).

2.3 Clinical variables

Perinatal and postnatal variables were prospectively collected, including sex, weight at birth, GA, and postmenstrual age (PMA) at the time of the scan. VPI born with a weight below the 10th percentile for the gestational age are defined as small for gestational age (SGA) (43). The comorbidities were grouped in a scale based on other composite medical risk scales (44, 45), including: significant patent ductus arteriosus (PDA) (patent requiring surgical or pharmacological closure), severe retinopathy of prematurity (ROP) (stage 3 or higher), moderate to severe bronchopulmonary dysplasia (BPD) (oxygen requirements at 36 weeks PMA), late-onset sepsis (LOS) (systemic signs of infection and isolation of a bacterial pathogen in blood culture after 5 days of life) and necrotising enterocolitis (NEC) (Bell stage II or higher). The presence of at least one comorbidity was scored with 1, and absence was scored with 0. Severe brain injury was considered in the presence of grade 3 germinal matrix-intraventricular hemorrhage (GM-IVH 3) and/or parenchymal hemorrhagic infarction (PHI), and/or moderate to severe white matter injury (WMI) (46). Maternal years of education were considered an approximation to socioeconomic status (47, 48).

2.4 Neurodevelopmental outcomes

At two years of corrected age, assessments were performed using the Bayley Scales of Infant and Toddler Development, Third Edition (BSITD-III) (49). The cognitive, motor, and language scale scores are standardized to a mean of 100 and a standard deviation of 15. In our study sample, the mean scores obtained were 100.26 (± 14.74) for cognitive, 98.80 (± 14.20) for motor and 96.48 (± 17.25) for language scales. The three scores were considered both quantitative measurements and qualitative ones, considering a favorable outcome as a score $\geq$ 85, while an adverse outcome was considered for a score $<$ 85. Among the VPI included in the study, 16 (13.8%) showed an adverse cognitive outcome, 19 (16.4%) an adverse motor outcome and 22 (19.0%) an adverse language outcome.

2.5 Statistical analysis

The initial phase involves a descriptive analysis of the clinical variables of VPI, comparing those exhibiting favorable outcomes to those with adverse outcomes for each BSITD-III subscale. Variables were described as frequency and percentage if they were categorical variables. If continuous, they were expressed as mean and standard deviation or median and interquartile range after testing for normality. Bivariate analysis was performed using Pearson's chi-squared test or Fisher's exact test for categorical variables and Student t-test or Mann-Whitney U test for continuous variables. The second step concerns a multilevel linear regression model to study the association between clinical variables and thalamic volume, accounting for repeated measurements and time. In the third stage, multilevel linear regression models were used to investigate the relationship between thalamic volume and clinical variables with each BSITD-III subscale score, accounting for repeated measurements and time. The included variables

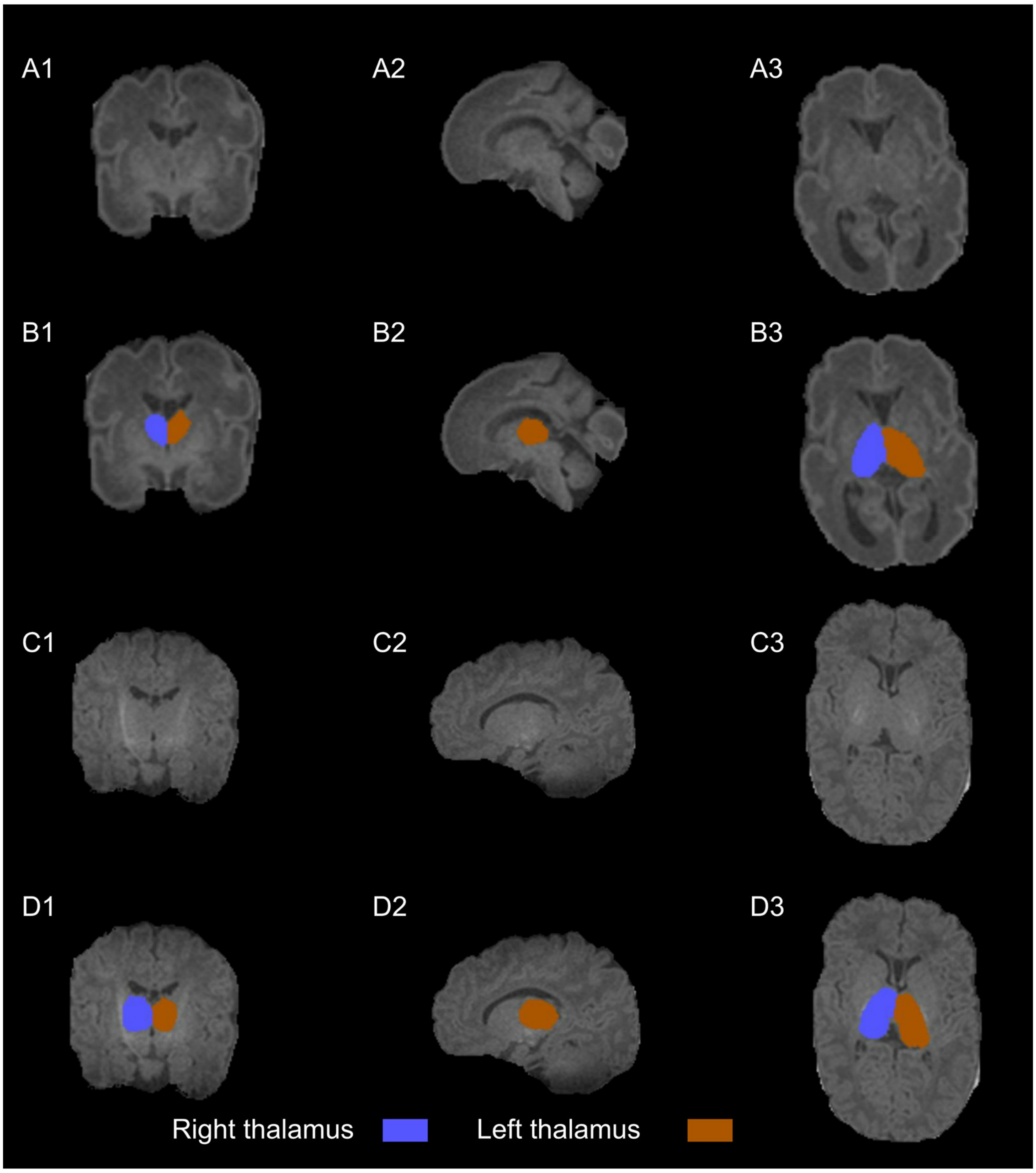

FIGURE 2
T1w images **(A–C)** with thalamus segmentation **(B–D)** into coronal (1), sagittal (2), and axial planes (3). The scans are from a healthy very preterm infant of 29.14 weeks of gestational age. The early scan **(A, B)** shows a right thalamus volume (blue) of 1.75 cm^3 and a left thalamus volume (orange) of 1.80 cm^3 at 27.57 weeks of postmenstrual age while the TEA scan **(C, D)** shows a right thalamus volume (blue) of 4.45 cm^3 and a left thalamus volume (orange) of 4.47 cm^3 at 43.14 weeks of postmenstrual age.

were selected based on the theoretical background and with a backward stepwise approach to exclude the non-significant variables if not considered variables for which an adjustment was needed. All models are adjusted for GA, PMA at the scan and total brain volume. Statistical analysis was conducted using Stata 17.0 (Stata Statistical Software: Release 17, College Station, TX: StataCorp LP). The results were considered statistically significant at $p \geq 0.05$.

3 Results

3.1 Clinical variables and 2-year neurodevelopmental outcome

Adverse cognitive outcome was related to sex, with a higher proportion of males having adverse cognitive outcome compared to good outcome (14 (87.5%) vs. 51 (51.0%); p=0.006), significant

TABLE 2 **Clinical variables of VPI with and without adverse outcome.**

	Cognitive outcome			Motor outcome			Language outcome			
	Adverse (*n* = 16)	Favorable (*n* = 100)	*p*	Adverse (*n* = 19)	Favorable (*n* = 97)	*p*	Adverse (*n* = 22)	Favorable (*n* = 94)	*p*	Total (n = 116)
Sex (male)	14 (87.5%)	51 (51.0%)	0.006*	14 (73.7%)	51 (52.6%)	0.129	18 (81.8%)	47 (50%)	0.008*	65 (56.0 %)
Weight (grams)	1,075 ± 409	1,172 ± 338	0.150	1,142 ± 336	1,162 ± 353	0.407	1,051 ± 396	1,184 ± 334	0.053	1,159 ± 349
SGA	3 (18.7%)	15 (15.0%)	0.713	3 (15.8%)	15 (15.5%)	1.000	6 (27.3%)	12 (12.8%)	0.107	18 (15.5%)
GA (weeks)	28.3 ± 2.7	29.5 ± 2.2	0.066	29.0 ± 2.4	29.4 ± 2.3	0.395	28.7 ± 2.6	29.4 ± 2.2	0.241	29.3 ± 2.3
Significant PDA	5 (31.2%)	9 (9.0%)	0.025*	5 (26.3%)	9 (9.3%)	0.053	5 (22.7%)	9 (9.6%)	0.138	14 (12.1%)
ROP	3 (18.7%)	4 (4.0%)	0.054	4 (21.0%)	3 (3.1%)	0.013*	4 (18.2%)	3 (3.2%)	0.024*	7 (6.0%)
BPD	7 (43.75%)	15 (15.0%)	0.006*	9 (47.4%)	13 (13.4%)	0.001*	10 (45.4%)	12 (12.8%)	0.001*	22 (19.0%)
LOS	5 (31.2%)	22 (22.0%)	0.524	6 (31.6%)	21 (21.6%)	0.349	6 (27.3%)	21 (22.3%)	0.622	27 (23.3%)
NEC	0 (0.0%)	1 (1.0%)	1.000	0 (0.0%)	1 (1.0%)	1.000	1 (4.5%)	0 (0.0%)	0.190	1 (0.9%)
Comorbidity index	11 (68.7%)	34 (34.0%)	0.012*	12 (63.2%)	33 (34.0%)	0.017*	12 (54.5%)	33 (35.1%)	0.092	45 (38.8%)
GM-IVH 3 and/or PHI	6 (37.5%)	6 (6.0%)	0.001*	5 (26.3%)	7 (7.2%)	0.012*	5 (22.7%)	7 (7.4%)	0.034*	12 (10.3%)
WMI	2 (12.5%)	2 (2.0%)	0.091	3 (18.7%)	1 (1.0%)	0.014*	3 (13.6%)	1 (1.0%)	0.021*	4 (3.4%)
Severe brain injury	7 (43.7%)	8 (8.0%)	0.001*	7 (36.8%)	8 (8.2%)	0.001*	7 (31.8%)	8 (8.5%)	0.003*	15 (12.9%)
Maternal education (years)	13.2 ± 4.2	14.8 ± 3.8	0.067	13.3 ± 4.4	14.9 ± 3.8	0.050*	13.2 ± 3.6	14.9 ± 3.9	0.028*	14.9 ± 3.9

SGA, small for gestational age; GA, gestational age; PDA, patent ductus arteriosus; ROP, retinopathy of prematurity; BPD, bronchopulmonary dysplasia; LOS, late-onset sepsis; NEC, necrotising enterocolitis; GM-IVH 3, germinal matrix-intraventricular hemorrhage of grade 3; PHI, parenchymal hemorrhagic infarction; WMI, white matter injury. Continuous variables are presented as mean ± standard deviation; Binary variables are shown as an absolute and relative frequency (percentage). $^*p < 0.05$.

TABLE 3 Results of the multilevel linear regression model based clinical variables in relation to thalamic volume.

Thalamic volume: Wald chi^2=2666.86, *p*-model <0.0001		
	Coef β	*p*
Const	5.694	<0.001*
GA	0.028	0.212
Sex (Male)	-0.035	0.694
PMA at scan	0.013	0.499
Comorbidity index	-0.056	0.598
Severe brain injury	-0.611	<0.001*
Maternal education (years)	0.008	0.536
Total brain volume	0.015	<0.001*

GA, gestational age; PMA, postmenstrual age. $^*p < 0.05$.

PDA (5 (31.2%) vs. 9 (9.0%); *p*=0.025), moderate to severe BPD (7 (43.75%) vs. 15 (15.0%); *p*=0.006), grade 3 GM-IVH and/or PHI (6 (37.5%) vs. 6 (6.0%); *p*=0.001) and severe brain injury (7 (43.7%) vs. 8 (8.0%); *p*=0.001). Regarding the motor score, adverse outcome was related to severe ROP (4 (21.0%) vs. 3 (3.1%); *p*=0.013), moderate to severe BPD (9 (47.4%) vs. 13 (13.4%); *p*=0.001), GM-IVH 3 and/or PHI (5 (26.3%) vs. 7 (7.2%); *p*=0.012), moderate to severe WMI (3 (18.7%) vs. 1 (1.0%); *p*=0.014) and severe brain injury (7 (36.8%) vs. 8 (8.2%); *p*=0.001). We also found fewer years of maternal education were associated with adverse motor outcome (13.3 ± 4.4 vs 14.9 ± 3.8; *p*=0.050). Finally, adverse language outcome was associated with being male (18 (81.8%) vs. 47 (50.0%); *p*=0.008), severe ROP (4 (18.2%) vs 3 (3.2%); *p*=0.024), moderate to severe BPD (10 (45.4%) vs 12 (12.8%); *p*=0.001), GM-IVH 3 and/or PHI (5 (22.7%) vs. 7 (7.4%); *p*=0.034), moderate to severe WMI (3 (13.6%) vs. 1 (1.0%); *p*=0.021) and severe brain injury (7 (31.8%) vs. 8 (8.5%); *p*=0.003). In addition, fewer years of maternal education (13.2 ± 3.6 vs. 14.9 ± 3.9; *p*=0.028) were also associated with adverse language outcome. A detailed description of the clinical variables related to the 2-year neurodevelopmental outcome is present in Table 2.

3.2 Clinical variables and thalamic volume

When studying the association of thalamic volume with perinatal variable, we found that severe brain injury was significantly related to thalamic volume (β coef=-0.611; *p*=<0.001). Table 3 summarizes the results of the multilevel regression model and Figure 3 shows the thalamic growth trajectory in VPI with severe brain injury and those without it.

3.3 Thalamus volume related to 2-year neurodevelopmental outcome

We studied the relationship of thalamic volume, total brain volume, and perinatal variables with the 2-year neurodevelopmental outcome accounting for repeated measurement and time. Table 4 shows the multilevel model for each BSITD-III subscale. Thalamic growth trajectory during early life was significantly related to cognitive (β coef=6.297; *p*=0.004), motor (β coef = 7.283; *p*=0.001) and language (β coef=9.053; *p*=0.002) outcomes at 2 years of age. Similarly, PMA at scan was related to cognitive (β coef=-1.468; *p*=0.005), motor (β coef=-1.839; *p*<0.001) and language (β coef=-1.541; *p*=0.004) outcomes. Moreover, years of maternal education were related to cognitive outcome (β coef=0.946; *p*=0.001) and sex (male) was related to language outcome (β coef=-9.091; *p*=0.002).

4 Discussion

Our findings align with previous studies that have demonstrated a significant relationship between the presence of severe brain injury and reduced thalamic volume in VPI (14, 50). Srinivasan et al. (14) reported significantly reduced thalamic and lentiform volumes in VPI at TEA compared to term-born controls, with the most marked reductions observed in those with brain injury. Similarly, Kersbergen et al. (50) reported a reduced volume of the thalamus in the TEA scan but not in the early ones of VPI with a specific type of white matter lesion, the cystic periventricular leukomalacia. In addition, some studies indicated a significant relationship between thalamic morphology and neurodevelopment (28, 51). Kline et al. (51) found that thalamic volume, together with temporal lobe curvature and insula curvature, were significant predictors of motor development by analyzing structural brain MRI data at TEA and relating it to BSITD-III motor scores at two years of age in a cohort of 75 VPI. In our study, which includes a larger sample size, we demonstrate a significant relationship between thalamic growth trajectory and various developmental outcomes, including cognitive, motor, and language abilitiess. The study by Loh et al. (28) reported smaller volumes of basal ganglia and thalamic in very preterm compared to term-born infants at TEA. It also establishes a positive relationship between neonatal basal ganglia and thalamic volumes and 7-year neurodevelopmental outcomes, underlining the persistent effect among the lifespan of a reduced thalamic volume at birth. Regarding early scan, Pagnozzi et al. (35) identified cortical gray matter volumes, cortical thickness, and sulcal depth as early predictors of the cognitive and motor outcome at 2 years of age through a prospective cohort of 181 infants with MRI data acquired between 29-35 weeks of PMA. Analogously, Moeskops et al. (36) examined the predictive capacity of automatic quantitative brain MRI descriptors for identifying preterm infants at risk of low cognitive and motor outcomes at 2-3 years of age utilizing MRI scans from 173 VPI acquired between 30 and 40 weeks of PMA. Both early scan studies didn't consider the volume of the thalamus in isolation, but rather, it is grouped with other regions of deep gray matter.

Notably, most studies focusing on morphological MRI analyses often concentrate on scans acquired at TEA, whereas only a few studies consider early scans, and none examine both early scans and TEA scans together. Our work underscores the advantage of studying MRI data from different time points in early extrauterine life and offers insights into thalamic growth trajectory and its

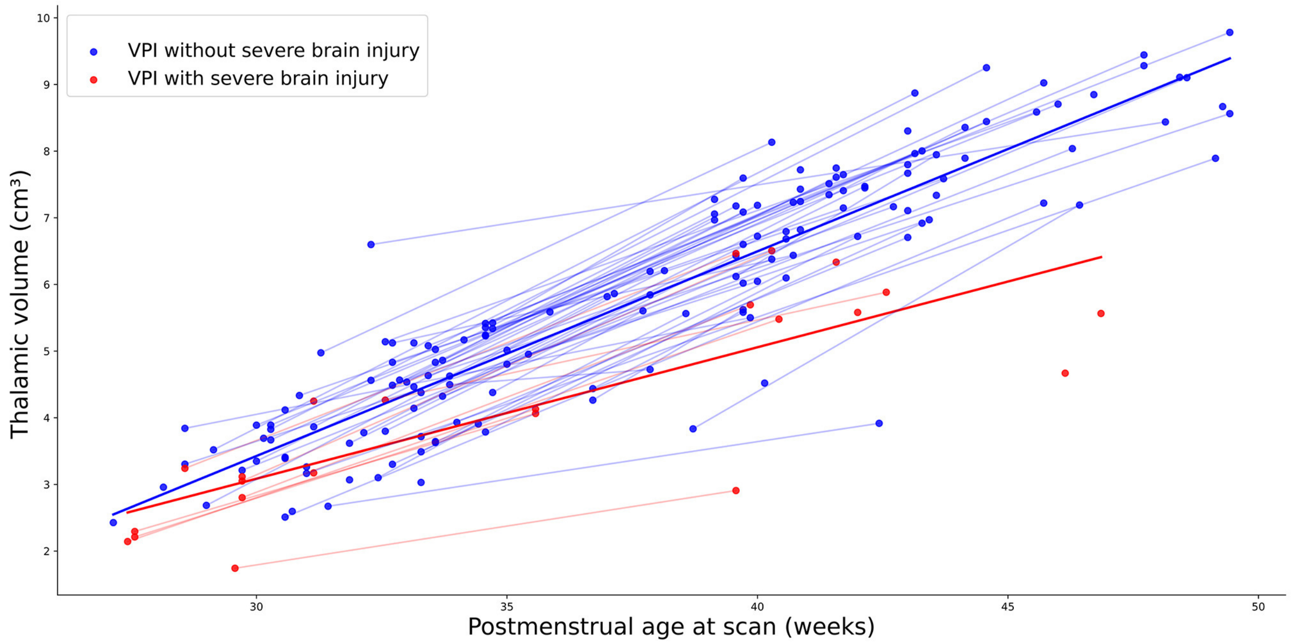

FIGURE 3
Thalamic growth trajectory in VPI with severe brain injury (red points) and those without severe brain injury (blue points).

TABLE 4 **Thalamic volume and clinical variables related to 2-year neurodevelopment outcomes.**

	Cognitive		Motor		Language	
	Coef β	p	Coef β	p	Coef β	p
Const	102.646	<0.001*	103.768	<0.001*	102.487	<0.001*
GA	0.494	0.376	0.296	0.564	0.535	0.453
Sex (male)	-3.320	0.164	-4.209	0.063	-9.091	0.002*
PMA at scan	-1.468	0.005*	-1.839	<0.001*	-1.541	0.004*
Comorbidity index	0.171	0.950	-4.206	0.099	0.647	0.862
Severe brain injury	-6.098	0.102	-5.254	0.161	-4.787	0.330
Maternal education (years)	0.946	0.001*	0.521	0.103	0.743	0.080
Total brain volume	-0.023	0.530	-0.026	0.477	-0.065	0.169
Thalamic volume	6.297	0.004*	7.283	0.001*	9.053	0.002*

GA, gestational age; PMA, postmenstrual age. $^{*}p < 0.05$.

impact on neurodevelopment in preterm infants. While some studies adjust their analyses for socioeconomic factors like the mother's educational level, few incorporate potential comorbidities commonly affecting VPI into their analyses. Incorporating such comorbidities into analyses can provide a more comprehensive understanding of the factors influencing outcomes in the preterm population.

This study has several limitations that should be considered: the sample size was relatively small, and future studies with larger cohorts are warranted to validate and generalize the findings. The study focused on thalamic volume, and it would be valuable to consider other brain regions and their interactions in future investigations. Our analyses do not account for potential other confounding factors, such as pain procedures during the early extrauterine life, which has been related to regionally-specific alterations in the thalamus (24) and later adverse neurodevelopment outcome (52).

Moving forward, our research aims to expand in several directions to enhance the depth and scope of our findings. Firstly, we plan to increase the sample size to improve the statistical power and generalizability of our results. Additionally, we intend to extend our investigation beyond infancy and include assessments of neurodevelopmental outcomes during preschool and school-age years. This longitudinal approach will allow us to examine the long-term impact of thalamic growth trajectory in early extrauterine life. Furthermore, we plan to integrate data from other MRI sequences to gain a more comprehensive understanding of brain structure and function. By incorporating information from different imaging modalities, such as diffusion tensor imaging, we can explore additional aspects of brain maturation and connectivity that may contribute to neurodevelopmental outcomes.

5 Conclusion

The present work shows the impact of severe brain injury on thalamic growth trajectory during early extrauterine life after preterm birth and the relationship with 2-year cognitive, motor, and language outcomes. Our study highlights how a reduced thalamic volume may reflect atypical brain development, which in turn seems to impact long-term neurodevelopmental outcome. These findings warrant further research, which could lead to tailoring interventions and strategies starting during early postnatal life to promote optimal neurodevelopment.

Data availability statement

The raw data supporting the conclusions of this article will be made available by the authors, without undue reservation.

Ethics statement

The studies involving humans were approved by Comité Coordinador de Ética de la Investigación Biomédica de Andalucía. The studies were conducted in accordance with the local legislation and institutional requirements. Written informed consent for participation in this study was provided by the participants' legal guardians/next of kin.

Author contributions

ET: Conceptualization, Data curation, Formal analysis, Investigation, Methodology, Visualization, Writing – original draft, Writing – review & editing. BJ: Conceptualization, Data curation, Formal analysis, Methodology, Software, Writing – review & editing. NJ-L: Data curation, Writing – review & editing. YM: Data curation, Writing – review & editing. MR: Data curation, Writing – review & editing. ML: Data curation, Writing – review & editing. ER: Data curation, Writing – review & editing. AS: Data curation, Writing – review & editing. SL-L: Conceptualization, Methodology, Supervision, Writing – review & editing. IB-F: Conceptualization, Methodology, Supervision, Writing – review & editing.

Funding

The author(s) declare financial support was received for the research, authorship, and/or publication of this article. This study was funded by the PARENT project from the European Union's Horizon 2020 research and innovation program under the Marie Sklodowska-Curie Innovative Training Network 2020. Grant Agreement N 956394.

Conflict of interest

Publisher's note

References

1. Agarwal PK, Shi L, Rajadurai VS, Zheng Q, Yang PH, Khoo PC, et al. Factors affecting neurodevelopmental outcome at 2 years in very preterm infants below 1250 grams: a prospective study. *J. Perinatol.* (2018) 38:1093–100. doi: 10.1038/s41372-018-0138-3

2. Delnord M, Zeitlin J. Epidemiology of late preterm and early term births-An international perspective. In: *Seminars in Fetal and Neonatal Medicine*. Amsterdam: Elsevier (2019). p. 3–10.

3. Darmstadt GL, Al Jaifi NH, Arif S, Bahl R, Blennow M, Cavallera V, et al. New World Health Organization recommendations for care of preterm or low birth weight infants: health policy. *EClinicalMed.* (2023) 63:102155. doi: 10.1016/j.eclinm.2023.102155

4. Cao Y, Jiang S, Sun J, Hei M, Wang L, Zhang H, et al. Assessment of neonatal intensive care unit practices, morbidity, and mortality among very preterm infants in China. *JAMA Netw Open.* (2021) 4:e2118904–e2118904. doi: 10.1001/jamanetworkopen.2021.18904

5. Bell EF, Hintz SR, Hansen NI, Bann CM, Wyckoff MH, DeMauro SB, et al. Mortality, in-hospital morbidity, care practices, and 2-year outcomes for extremely preterm infants in the US, 2013-2018. *JAMA.* (2022) 327:248–63. doi: 10.1001/jama.2021.23580

6. Lundgren P, Morsing E. Háard AL, Rakow A, Hellström-Westas L, Jacobson L, et al. National cohort of infants born before 24 gestational weeks showed increased survival rates but no improvement in neonatal morbidity. *Acta Paediatrica.* (2022) 111:1515–25. doi: 10.1111/apa.16354

7. Pascal A, Govaert P, Oostra A, Naulaers G, Ortibus E, Van den Broeck C. Neurodevelopmental outcome in very preterm and very-low-birthweight infants born over the past decade: a meta-analytic review. *Dev Med Child Neurol.* (2018) 60:342–55. doi: 10.1111/dmcn.13675

8. O'Reilly H, Johnson S, Ni Y, Wolke D, Marlow N. Neuropsychological outcomes at 19 years of age following extremely preterm birth. *Pediatrics.* (2020) 145:2087. doi: 10.1542/peds.2019-2087

9. Doyle LW, Spittle A, Anderson PJ, Cheong JLY. School-aged neurodevelopmental outcomes for children born extremely preterm. *Arch Dis Child.* (2021) 106:834–8. doi: 10.1136/archdischild-2021-321668

10. Vanes LD, Murray RM, Nosarti C. Adult outcome of preterm birth: Implications for neurodevelopmental theories of psychosis. *Schizophr Res*. (2022) 247:41–54. doi: 10.1016/j.schres.2021.04.007

11. Duerden EG, Halani S, Ng K, Guo T, Foong J, Glass TJ, et al. White matter injury predicts disrupted functional connectivity and microstructure in very preterm born neonates. *NeuroImage: Clinical*. (2019) 21:101596. doi: 10.1016/j.nicl.2018.11.006

12. Srivastava R, Mailo J, Dunbar M. Perinatal stroke in fetuses, preterm and term infants. In: *Seminars in Pediatric Neurology*. Amsterdam: Elsevier (2022). p. 100988. doi: 10.1016/j.spen.2022.100988

13. Inder TE, Volpe JJ, Anderson PJ. Defining the neurologic consequences of preterm birth. *New Engl J Med*. (2023) 389:441–53. doi: 10.1056/NEJMra2303347

14. Srinivasan L, Dutta R, Counsell SJ, Allsop JM, Boardman JP, Rutherford MA, et al. Quantification of deep gray matter in preterm infants at term-equivalent age using manual volumetry of 3-tesla magnetic resonance images. *Pediatrics*. (2007) 119:759–65. doi: 10.1542/peds.2006-2508

15. Ball G, Boardman JP, Rueckert D, Aljabar P, Arichi T, Merchant N, et al. The effect of preterm birth on thalamic and cortical development. *Cereb Cortex*. (2012) 22:1016–24. doi: 10.1093/cercor/bhr176

16. Ball G, Boardman JP, Aljabar P, Pandit A, Arichi T, Merchant N, et al. The influence of preterm birth on the developing thalamocortical connectome. *Cortex*. (2013) 49:1711–21. doi: 10.1016/j.cortex.2012.07.006

17. Zubiaurre-Elorza L, Soria-Pastor S, Junque C, Fernandez-Espejo D, Segarra D, Bargallo N, et al. Thalamic changes in a preterm sample with periventricular leukomalacia: correlation with white-matter integrity and cognitive outcome at school age. *Pediatr Res*. (2012) 71:354–60. doi: 10.1038/pr.2011.70

18. Wisnowski JL, Ceschin RC, Choi SY, Schmithorst VJ, Painter MJ, Nelson MD, et al. Reduced thalamic volume in preterm infants is associated with abnormal white matter metabolism independent of injury. *Neuroradiology*. (2015) 57:515–25. doi: 10.1007/s00234-015-1495-7

19. Coviello C, Keunen K, Kersbergen KJ, Groenendaal F, Leemans A, Peels B, et al. Effects of early nutrition and growth on brain volumes, white matter microstructure, and neurodevelopmental outcome in preterm newborns. *Pediatr Res*. (2018) 83:102–10. doi: 10.1038/pr.2017.227

20. Volpe JJ. Brain injury in premature infants: a complex amalgam of destructive and developmental disturbances. *Lancet Neurol*. (2009) 8:110–24. doi: 10.1016/S1474-4422(08)70294-1

21. Ligam P, Haynes RL, Folkerth RD, Liu L, Yang M, Volpe JJ, et al. Thalamic damage in periventricular leukomalacia: novel pathologic observations relevant to cognitive deficits in survivors of prematurity. *Pediatr Res*. (2009) 65:524–9. doi: 10.1203/PDR.0b013e3181998baf

22. Nagasunder A, Kinney H. Blüml S, Tavaré C, Rosser T, Gilles F, et al. Abnormal microstructure of the atrophic thalamus in preterm survivors with periventricular leukomalacia. *Am J Neuroradiol*. (2011) 32:185–91. doi: 10.3174/ajnr.A2243

23. Cayam-Rand D, Guo T, Synnes A, Chau V, Mabbott C. Benavente-Fernández I, et al. Interaction between preterm white matter injury and childhood thalamic growth. *Ann Neurol*. (2021) 90:584–94. doi: 10.1002/ana.26201

24. Duerden EG, Grunau RE, Guo T, Foong J, Pearson A, Au-Young S, et al. Early procedural pain is associated with regionally-specific alterations in thalamic development in preterm neonates. *J Neurosci*. (2018) 38:878–86. doi: 10.1523/JNEUROSCI.0867-17.2017

25. Treyvaud K, Thompson DK, Kelly CE, Loh WY, Inder TE, Cheong JL, et al. Early parenting is associated with the developing brains of children born very preterm. *Clin Neuropsychol*. (2021) 35:885–903. doi: 10.1080/13854046.2020.1811895

26. Kidokoro H, Neil JJ, Inder TE. New MR imaging assessment tool to define brain abnormalities in very preterm infants at term. *Am J Neuroradiol*. (2013) 34:2208–14. doi: 10.3174/ajnr.A3521

27. Trimarco E, Jafrasteh B. Lubián-Lopez SP, Benavente-Fernández I. Thalamic features extraction and analysis in magnetic resonance imaging of preterm infants. *Determined*. (2022) 3363:167–78. Available at: https://ceur-ws.org/Vol-3363/paper13.pdf

28. Loh WY, Anderson PJ, Cheong JL, Spittle AJ, Chen J, Lee KJ, et al. Neonatal basal ganglia and thalamic volumes: very preterm birth and 7-year neurodevelopmental outcomes. *Pediatr Res*. (2017) 82:970–8. doi: 10.1038/pr.2017.161

29. Nunes AS, Kozhemiako N, Hutcheon E, Chau C, Ribary U, Grunau RE, et al. Atypical neuromagnetic resting activity associated with thalamic volume and cognitive outcome in very preterm children. *NeuroImage: Clinical*. (2020) 27:102275. doi: 10.1016/j.nicl.2020.102275

30. Jakab A, Natalucci G, Koller B, Tuura R. Rüegger C, Hagmann C. Mental development is associated with cortical connectivity of the ventral and nonspecific thalamus of preterm newborns. *Brain Behav*. (2020) 10:e01786. doi: 10.1002/brb3.1786

31. Menegaux A, Meng C. Bäuml JG, Berndt MT, Hedderich DM, Schmitz-Koep B, et al. Aberrant cortico-thalamic structural connectivity in premature-born adults. *Cortex*. (2021) 141:347–62. doi: 10.1016/j.cortex.2021.04.009

32. Thalhammer M, Nimpal M, Schulz J, Meedt V, Menegaux A, Schmitz-Koep B, et al. Consistently lower volumes across thalamus nuclei in very premature-born adults. *Neuroimage*. (2024) 297:120732. doi: 10.1016/j.neuroimage.2024.120732

33. Nair A, Carper RA, Abbott AE, Chen CP, Solders S, Nakutin S, et al. Regional specificity of aberrant thalamocortical connectivity in autism. *Hum Brain Mapp*. (2015) 36:4497–511. doi: 10.1002/hbm.22938

34. Linke AC, Keehn RJJ, Pueschel EB, Fishman I. Müller RA. Children with ASD show links between aberrant sound processing, social symptoms, and atypical auditory interhemispheric and thalamocortical functional connectivity. *Dev Cognit Neurosci*(2018) 29:117–26. doi: 10.1016/j.dcn.2017.01.007

35. Pagnozzi AM, van Eijk L, Pannek K, Boyd RN, Saha S, George J, et al. Early brain morphometrics from neonatal MRI predict motor and cognitive outcomes at 2-years corrected age in very preterm infants. *Neuroimage*. (2023) 267:119815. doi: 10.1016/j.neuroimage.2022.119815

36. Moeskops P. Iv́sgum I, Keunen K, Claessens NH, van Haastert IC, Groenendaal F, et al. Prediction of cognitive and motor outcome of preterm infants based on automatic quantitative descriptors from neonatal MR brain images. *Scient Rep*. (2017) 7:2163. doi: 10.1038/s41598-017-02307-w

37. Harris PA, Taylor R, Thielke R, Payne J, Gonzalez N, Conde JG. Research electronic data capture (redcap)–a metadata-driven methodology and workflow process for providing translational research informatics support. *J Biomed Inform*. (2009) 42:377–81. doi: 10.1016/j.jbi.2008.08.010

38. Harris PA, Taylor R, Minor BL, Elliott V, Fernandez M, O'Neal L, et al. The REDCap consortium: building an international community of software platform partners. *J Biomed Inform*. (2019) 95:103208. doi: 10.1016/j.jbi.2019.103208

39. Jafrasteh B, López SPL, Fernández IB. MELAGE: a purely python based neuroimaging software (Neonatal). *arXiv [Preprint]*. arXiv:230907175. (2023). doi: 10.48550/arXiv.2309.07175

40. Alexander B, Loh WY, Matthews LG, Murray AL, Adamson C, Beare R, et al. Desikan-Killiany-Tourville atlas compatible Version of M-CRIB neonatal parcellated whole brain atlas: the M-CRIB 2.0. *Front Neurosci*. (2019) 13:34. doi: 10.3389/fnins.2019.00034

41. Makropoulos A, Gousias IS, Ledig C, Aljabar P, Serag A, Hajnal JV, et al. Automatic whole brain MRI segmentation of the developing neonatal brain. *IEEE Trans Med Imag*. (2014) 33:1818–31. doi: 10.1109/TMI.2014.2322280

42. Makropoulos A, Robinson EC, Schuh A, Wright R, Fitzgibbon S, Bozek J, et al. The developing human connectome project: a minimal processing pipeline for neonatal cortical surface reconstruction. *Neuroimage*. (2018) 173:88–112. doi: 10.1016/j.neuroimage.2018.01.054

43. Schlaudecker EP, Munoz FM, BardajíA, Boghossian NS, Khalil A, Mousa H, et al. Small for gestational age: case definition & guidelines for data collection, analysis, and presentation of maternal immunisation safety data. *Vaccine*. (2017) 35:6518. doi: 10.1016/j.vaccine.2017.01.040

44. Lundequist A. Böhm B, Smedler AC. Individual neuropsychological profiles at age 51/2 years in children born preterm in relation to medical risk factors. *Child Neuropsychology*. (2013) 19:313–31. doi: 10.1080/09297049.2011.653331

45. Yaari M, Treyvaud K, Lee KJ, Doyle LW, Anderson PJ. Preterm birth and maternal mental health: longitudinal trajectories and predictors. *J Pediatr Psychol*. (2019) 44:736–47. doi: 10.1093/jpepsy/jsz019

46. Agut T, Alarcon A. Caba nas F, Bartocci M, Martinez-Biarge M, Horsch S. Preterm white matter injury: ultrasound diagnosis and classification. *Pediat Res*. (2020) 87:37–49. doi: 10.1038/s41390-020-0781-1

47. Patra K, Greene MM, Patel AL, Meier P. Maternal education level predicts cognitive, language, and motor outcome in preterm infants in the second year of life. *Am J Perinatol*. (2016) 33:738–44. doi: 10.1055/s-0036-1572532

48. ElHassan NO, Bai S, Gibson N, Holland G, Robbins JM, Kaiser JR. The impact of prematurity and maternal socioeconomic status and education level on achievement-test scores up to 8th grade. *PLoS ONE*. (2018) 13:e0198083. doi: 10.1371/journal.pone.0198083

49. Bayley N. *Bayley Scales of Infant and Toddler Development*. San Antonio, TX: PsycTESTS Dataset. (2005).

50. Kersbergen KJ, De Vries LS, Groenendaal F, Van Haastert IC, Chew AT, Makropoulos A, et al. Corticospinal tract injury precedes thalamic volume reduction in preterm infants with cystic periventricular leukomalacia. *J Pediatr*. (2015) 167:260–8. doi: 10.1016/j.jpeds.2015.05.013

51. Kline JE, Illapani VSP, He L, Parikh NA. Automated brain morphometric biomarkers from MRI at term predict motor development in very preterm infants. *NeuroImage: Clinical*. (2020) 28:102475. doi: 10.1016/j.nicl.2020.102475

52. Cook KM, De Asis-Cruz J, Kim JH, Basu SK, Andescavage N, Murnick J, et al. Experience of early-life pain in premature infants is associated with atypical cerebellar development and later neurodevelopmental deficits. *BMC Med*. (2023) 21:435. doi: 10.1186/s12916-023-03141-w

frontiers | Frontiers in Pediatrics

TYPE Review
PUBLISHED 10 September 2024
DOI 10.3389/fped.2024.1451688

OPEN ACCESS

EDITED BY
Ye Wu,
Nanjing University of Science and Technology, China

REVIEWED BY
Zan Chen,
Zhejiang University of Technology, China
Liwei Hu,
Shanghai Children's Medical Center, China

*CORRESPONDENCE
Xiao Fan
✉ fanxiao@cqmu.edu.cn

[†]These authors have contributed equally to this work and share first authorship

RECEIVED 19 June 2024
ACCEPTED 28 August 2024
PUBLISHED 10 September 2024

CITATION
Zhang L, Feng C, He L, Huang S-Y, Liu X-Y and Fan X (2024) MOG-antibody-associated transverse myelitis with the H-sign and unusual MRI enhancement: a case report and literature review.
Front. Pediatr. 12:1451688.
doi: 10.3389/fped.2024.1451688

MOG-antibody-associated transverse myelitis with the H-sign and unusual MRI enhancement: a case report and literature review

Lu Zhang[†], Chuan Feng[†], Ling He, Shi-Yu Huang,
Xin-Yin Liu and Xiao Fan*

Department of Radiology, National Clinical Research Center for Child Health and Disorders, Ministry of Education Key Laboratory of Child Development and Disorders, Children's Hospital of Chongqing Medical University, Chongqing, China

Transverse myelitis is the second most common symptoms in myelin oligodendrocyte antibody-associated diseases (MOGAD), causing obvious clinical manifestation. T2-hyperintense lesions mainly restricted to the gray matter in the spinal cord on axial magnetic resonance imaging, produce the H-sign, which is thought to be the typical finding of MOGAD. Contrast enhancement can be observed in some cases of myelin oligodendrocyte antibody-associated transverse myelitis (MOG-TM). However, reports on the enhancement pattern associated with the H-sign are rarely seen. In this report, we describe a case of pediatric MOG-TM in which the H-sign was observed without enhancement, while the surrounding white matter exhibited enhancement. This pattern contradicts the previously observed gray matter involvement. Then we reviewed the literatures of myelin oligodendrocyte antibody-positive myelitis to focus on the neuroimaging features and discuss the implications of our finding.

KEYWORDS

myelin oligodendrocyte glycoprotein, antibody, myelitis, magnetic resonance imaging, H-sign

Introduction

Myelin oligodendrocyte antibody-associated disease (MOGAD) is a central nervous system (CNS) demyelinating disease that has been identified in recent years. Transverse myelitis (TM) is the second most common presentation, occurring in approximately 26% of MOGAD (1). TM is characterized clinically by an acute or subacute onset of motor, sensory, and autonomic symptoms and signs attributable to cord dysfunction (2). The severity of the attack varies, typically moderate to severe with expanded disability status scale (EDSS) scores >4 in about half of patients with up to one-third

---

Abbreviations
ADEM, acute disseminated encephalomyelitis; AQP-4, aquaporin-4; BBB, blood-brain barrier; CNS, central nervous system; CSF, cerebrospinal fluid; EDSS, expanded disability status scale; LETM, longitudinally extensive transverse myelitis; MOG, myelin oligodendrocyte glycoprotein; MOGAD, myelin oligodendrocyte antibody-associated diseases; MOG-TM, myelin oligodendrocyte antibody-associated transverse myelitis; MRI, magnetic resonance imaging; MS, multiple sclerosis; NMOSD, neuromyelitis optica spectrum disorder; SETM, short transverse myelitis; T1W, T1-weighted; T2W, T2-weighted; TM, transverse myelitis.

being non-ambulatory at the nadir of acute myelitis attack (3, 4), and many requiring bladder catheterization (5). Magnetic resonance imaging (MRI) is incorporated into the diagnostic criteria for MOGAD as the sole imaging modality capable of visualizing spinal cord lesions.

According to the latest diagnosis criteria of MOGAD (2023) (6), acute T2-hyperintense lesions restricted to the gray matter in the spinal cord on axial imaging, produce the H-sign (as seen in 30%–50% of patients), which is thought to be the typical finding of myelin oligodendrocyte antibody-associated transverse myelitis (MOG-TM) (6). This finding challenges the prevailing notion that demyelinating diseases primarily affect white matter in the central nervous system. Contrast enhancement is seen in approximately 50% of patients with MOG-TM, and cauda equina and pial enhancement have been reported (3, 7–9). Reports on the enhancement pattern associated with the H-sign are rarely seen.

MOG-TM can also be involved in children, who may be observed the H-sign on MRI. In this study, we presented one pediatric patient diagnosed with MOG-TM, observed a characteristic H-sign on axial MRI. Interestingly, only the white matter surrounding the H-sign exhibited enhancement.

Case presentation

An 11-year-old boy exhibited progressive numbness and weakness in both lower extremities for 2 days after experiencing an unexplained fall 6 days prior to hospitalization (February 8, 2018). Within 2 days of admission, he experienced quadriplegia, in addition to sensory and motor deficits below the nipples bilaterally, as well as dysfunction of bowel and bladder control. Neurological and physical examinations demonstrated reduced muscle strength in the lower limbs, as well as the absence of knee, abdominal wall and cremasteric reflexes. His medical and family history were found to be unremarkable. Upon admission, the blood analysis showed an increase in white blood cell count (15.92×10^9/L), an elevated percentage of neutrophils (93%), and an elevated level of C-reactive protein (11 mg/L). The following day, there was an increase in the total cellular count in the cerebrospinal fluid (CSF) (550×10^9/L) and an increase in nucleated cells (420×10^6/L). Serum and CSF samples were examined for demyelinating and autoimmune antibodies using a cell-based assay with full-length human antigenic substrates at the China branch of Euroimmun Medical Diagnostic Laboratory (EUROIMMUN AG, Lübeck, Germany). The results showed a positive titer of MOG-antibody at 1:100 in the serum and 1:1 in the CSF. However, other demyelinating antibodies such as aquaporin-4 (AQP-4) and autoimmune antibodies in both the blood and CSF tested negative.

Six days after admission, a spinal MRI scan showed significant signal changes in the entire cervical and thoracic spinal cord segments on T1-weighted (T1W) and T2-weighted (T2W) sequences. These changes were consistent with a diagnosis of longitudinally extensive transverse myelitis (LETM) and short transverse myelitis (SETM) (Figure 1A), with the C2-T6 segment primarily affected in the gray matter and displaying the characteristic “H-sign” (Figures 1B,C). The white matter exhibited pronounced enhancement following the injection of contrast agent, particularly in the posterior funiculus, depicting primarily patchy enhancement. However, no enhancement was detected in the H-sign (Figures 1D,E). After performing a cranial MRI scan, multiple lesions were observed in the bilateral cerebral hemispheres, right basal ganglia, pons, and medulla, without any enhancement (Figures 1F,G).

Therefore, the diagnosis of MOGAD was confirmed, and first-line immunotherapy, including intravenous methylprednisolone and immunoglobulin, was commenced promptly. After 2 months of consistent treatment, there was a marked improvement in symptoms, with only residual symptoms remaining, such as mild bladder dysfunction and motor dysfunction in both lower limbs. The oral steroid dosage was taken for about 40 days and subsequently tapered gradually with outpatient monitoring. After 41 days since the initial scan, a follow-up MRI revealed obvious absorption of the previously abnormal signals in the spinal cord without any noticeable enhancement, consistent with the clinical presentation (Figure 1H). During the latest telephone follow-up on April 8, 2024, his family reported no recurrence of symptoms.

Literature review on neuroimaging

We then performed a review of current literatures, using “myelin oligodendrocyte glycoprotein” or “MOG” as the search terms, to identify research studies performed on myelin oligodendrocyte antibody-positive myelitis focusing on the description of the “H-sign” and enhancement pattern. Studies lacking MRI original data were excluded. Data of 237 patients were collected from eight publications and Table 1 summarizes 135 cases of MOG-TM with the H-sign, accounting for 29.4%–83.3% of the incidence rate. The proportion of lesion enhancement also varied, ranging from 25.0% to 60.0%. The enhancement pattern were typically patchy and faint or nodular. Moreover, leptomeningeal or subpial enhancement and spinal nerve roots enhancement were not uncommon. In three pediatric cohorts (total $n = 77$), the H-sign were observed in 51 out of 77 cases (66.2%). 50.0% (26/52) lesion enhancement were found in children with MOG-antibody-positive myelitis, which is the most common. This is then followed by the enhancement of leptomeninges and nerve roots, making up 38.5% (20/52) and 30.8% (16/52) respectively. Unfortunately, there was insufficient information available regarding the enhancement of lesions displaying the H-sign.

Discussion

Studies from multiple countries support MOGAD as a global disease affecting people of all ages. The incidence of MOGAD is 1.6–3.4 per million people per year, and the prevalence is estimated at 20 per million (95% CI 11–34) (15, 16). Myelin oligodendrocyte glycoprotein (MOG) is expressed on the surface

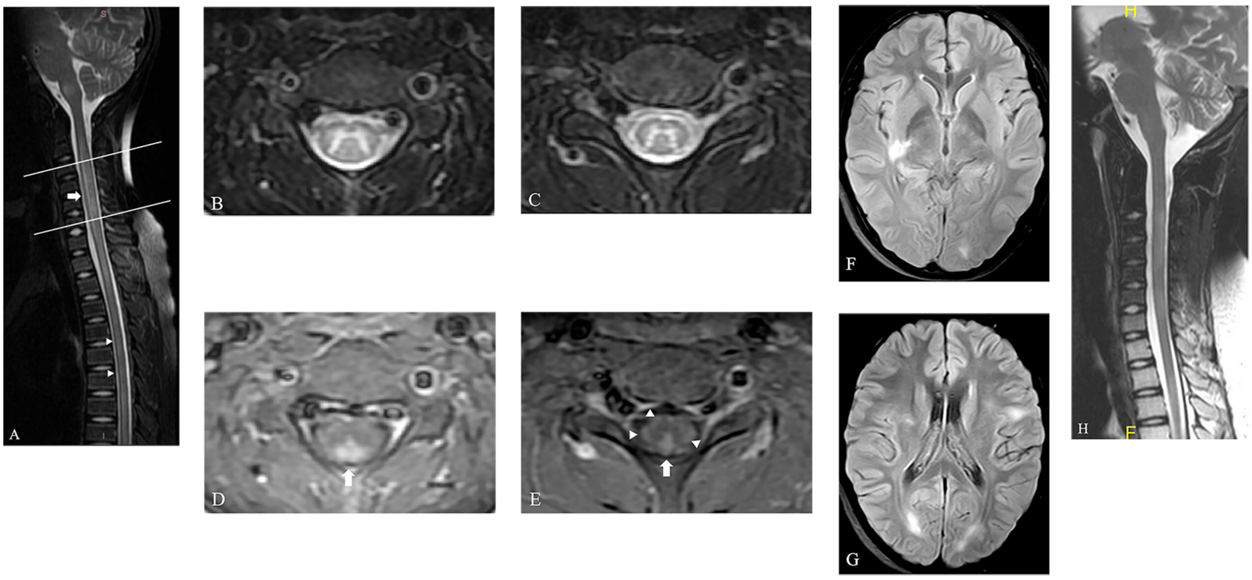

FIGURE 1
The spinal MRI of this patient. **(A)** The sagittal T2W image of spine shows LETM ranging from C2 to T1 segments (arrow) and SETM in thoracic spinal cord (arrow head). **(B,C)** Axial T2W images of spine show hyperintensity primarily located in the gray matter and displaying the characteristic "H-sign" in the level of C3 (the upper line in a) and C6 (the lower line in a). **(D,E)** This hyperintensity displays no enhancement, but the bilateral posterior funiculus was obviously enhanced on axial T1W images (arrow). The bilateral lateral funiculus and right anterior funiculus were also found moderate enhancement (arrow head). **(F,G)** Axial fluid-attenuated inversion recovery images of brain show multiple lesions located in the right basal ganglia and bilateral cerebral hemispheres, with no enhancement (not shown). **(H)** A follow-up MRI scan of spine shows obvious absorption of the previously abnormal signals in the spinal cord.

of the myelin sheath, mainly in CNS neurons, and accounts for about 0.5% of myelin components (17, 18). Thus, MOGAD is generally considered to have a favorable prognosis compared to other CNS demyelinating diseases such as AQP-4 positive neuromyelitis optica spectrum disorder (NMOSD) and multiple sclerosis (MS). Nevertheless, MOGAD have garnered significant interest among neurologists due to its tendency to relapse.

TM, which is one of the main symptoms of MOGAD, has an incidence of roughly 20%–30%, a male-to-female ratio of roughly 1:1, and a peak age of onset at 20–40 years old (10). Younger children usually present as a component of acute disseminated encephalomyelitis (ADEM), while older children may be concurrent with optic neuritis (12). Most patients experience good to excellent motor recovery (3, 7, 19), but permanent bladder, bowel or sexual dysfunction can occur (3, 7, 20). Early detection of lesions, especially the typical findings of MOG-TM on MRI, facilitates early immune intervention. According to the latest criteria proposed by the International MOGAD Panel, the presence of H-sign on MRI is considered a supportive feature for the diagnosis of MOGAD in cases of myelitis (6).

We report a pediatric patient diagnosed with MOGAD who had the characteristic H-sign on spinal MRI. It is widely accepted that the enhancement of lesions in MOGAD on MRI is thought to be due to the disruption of the blood-brain barrier (BBB) resulting from inflammation. Circulating cytokines may increase the BBB's permeability and promote inflammatory infiltration into the CNS (21, 22). In this case, the T2 hyperintensity was identified in the gray matter (referred to as the H-sign) without any enhancement. In contrast, the surrounding white matter displayed significant enhancement. This suggests that the BBB in the white matter may have been compromised due to inflammation, despite the absence of hyperintensity on T2W images. Therefore, the pathological alterations may not be restricted solely to the gray matter exhibiting T2 hyperintensity, but also involve the white matter with potentially more severe effects. Our results did not align with previous studies suggesting that the presence of the H-sign on MRI indicated exclusive or primary gray matter involvement in MOG-TM (2–4, 23).

Due to the important role of the H-sign in diagnosis, a review of literatures of MOG-TM cases with the H-sign from the last decade was undertaken to gain insight into its etiology. A total of 135 patients of MOG-TM displaying the H-sign were collected from eight studies, in which only three were pediatric cohort, the other five were mixed cohort. The most common clinical manifestations reported in these eight studies were weakness, sensory disturbances and bowel/bladder dysfunction. Although some patients with MOG-TM experienced severe symptoms (EDSS ≥ 7) at onset, the majority of patients had complete resolution of symptoms during follow-up, with residual sphincter dysfunction in some cases. These results are generally in accordance with mild myelin damage observed in the pathology of MOGAD (24). Simultaneously, we further summarize the enhancement characteristics of these cases. The H-sign was reported ranging from 29.4% to 83.3% and was also common in pediatrics accounting for approximately 66.2%. In terms of enhancement, there were lesions with enhancement (typically

TABLE 1 A review of patients of MOGAD with H sign published in the last 10 years.

No. /Total no. (%)	No. 1 mixed cohort	No. 2 mixed cohort	No. 3 mixed cohort	No. 4 pediatric cohort	No. 5 mixed cohort	No. 6 mixed corhort	No. 7 pediatric corhort	No. 8 pediatric corhort
Research	Dubey et al. (3)	Zhang Bao et al. (10)	Fadda et al. (9)	Tantsis et al. (2)	Kitley et al. (11)	Netravathi et al. (12)	El Naggar et al. (13)	Ren et al. (14)
Demographics (*n*=)	54	38	40	10	9	19	33	34
Typical age at first myelitis (year)	3–73 (median: 25)	7–57 (mean: 28.13 ± 12.74)	3.80–11.48 (median: 6.71)	6.0–14.8 (median:11.0)	mean: 32.29	1–66 (median:21)^d	5–10 (median: 7)	0.5–13.1 (7)
Sex (F:M)	24:30	62:68	23:17	6:4	4:5	13:6	14:19	16:18
Follow-up time	2–120 months (median: 24)	NA	4.14–8.30 years (median: 5.96)	NA	22–38.5 months (median: 18)	median: 1 year	NA	8–109 months (median: 28)
Clinical features								
Antecedent	31 (57%)	23/55^a (41.8%)	NA	NA	NA	40/93 (43.0%)	NA	3/35^a (8.6%)
Infection/ immunization	33 (61%)	3/55^a (5.5%)	NA	NA	NA	0	NA	1/35^a (2.7%)
Disease course (monophasic or relapsing)	Relapsing (32/54, 59.3%）	Relapsing (75/130, 57.7%）	NA	NA	Monophasic	Relapsing (3/19, 15.8%)	NA	Relapsing (6/34, 17.7%）
Myelitis symptoms								
Weakness	45/54 (83.3)	29/38 (76.3)	NA	10/10 (100.0)	NA	NA	NA	32/35 (91.4)
Sensory disturbances	48/54 (88.9)	33/38 (86.8)	NA	8/10 (80.0)	NA	NA	NA	16/35 (45.7)
Bowel/bladder dysfunction	45/54 (83.3)	26/38 (68.4)	NA	9/10 (90.0)	33%	NA	NA	22/35 (62.9)
Erectile dysfunction in men	13/24 (54.2)	NA	NA	NA	NA	NA	NA	NA
EDSS ≥ 7 at myelitis nadir	18/54 (33.3)	NA	NA	NA	Median 6.0 (range: 4–8.5)	NA	NA	16/35 (45.7)
Recovery from myelitis attacks	Median mRS was 1 (range: 0–4)	Median EDSS was 1 (range, 0–7.5)	Median EDSS was 1 (range, 0–1.5) in 22 patients	NA	The median EDSS was 0 (range, 0–2.5)	NA	NA	Median EDSS was 0 (range, 0–2)
Need for gait aid long term	3/54 (5.6）	NA	0/22^b	NA	0	NA	NA	0
Extra spine manifestations								
Optic neuritis	NA	11/27 (40.7)	2/40 (5.0)	NA	4/9 (44.4)	NA	7/33 (21.2)	NA
Encephalopathy	✓		17/40 (42.5)	NA	2/9 (22.2)	NA	14/33 (42.4)	15/35 (42.9)
Non-specific symptoms	NA	NA	6/40 (15.0)	NA	NA	NA	NA	NA
CSF findings acutely								
Oligoclonal bands	1/38 (2.6)	NA	NA	0/8	4/9 (44.4)	3 (15.8%)	4/32 (12.5)	11/35 (31.4)
White cell count >5/μl	30/42 (71.4)	NA	NA	NA	>10/ul: 5（55.6%)	8 (42.1%)	NA	22/35 (62.9)
White cell count >50/μl	22/42 (52.4)	NA	NA	NA	NA		NA	NA

(*Continued*)

patchy and faint or nodular), leptomeningeal or subpial enhancement and spinal nerve root enhancement. Approximately half of the pediatric patients displayed focal enhancement of the lesion, however, the specific details of the enhancement in relation to the H-sign were not clarified.

The findings from prior studies have confirmed that a large proportion of individuals diagnosed with MOG-TM demonstrate a positive outcome, regardless of the severity of symptoms present at the disease onset (25). This may be attributed to the lesser impact of the disease on gray matter, which is a crucial organ housing neurons, and is not the primary site of damage in demyelinating diseases. Therefore, in conjunction with our case, we propose that although the gray matter exhibits hyperintensity on T2W images (appearing as the H-sign) and seems to be the most severely affected area, the lesions may primarily consist of edema and the BBB remains intact. Once the inflammation resolves, the edema would decrease soon and the clinical manifestations would vanish. However, the white matter, which did not display obvious hyperintensity adjacent to the gray matter on T2W images, showed enhancement, indicating a disruption of the BBB. Nevertheless, the demyelination process of the white matter appeared to be more amenable to repair than the gray matter damage. The difference of enhancement pattern between the gray and white matter might be a possible reason to explain the positive outcome of MOG-TM.

As previously stated, most of MOG-TM lesions tend to resolve effectively, leading to a limited number of spinal cord biopsies available to substantiate our findings. According to a recent animal study on MOG-IgG experimental autoimmune encephalomyelitis (EAE), inflammation was found to initiate primarily in the white matter region during both acute and chronic stages of the disease (26). The infiltration and activation of inflammatory cells such as macrophages and T-cells mainly existed in the white matter with a small amount in the gray matter. The rate of spinal demyelinating lesions in these model mice was relatively high, particularly in the posterior funiculus, where it exceeded 60% at the acute stage (26). Thus, we speculate that the possible cause of the enhancement of the posterior funiculus, located opposite to the H-sign area in our case, may be attributed to the accumulation of MOG antibodies or a significant presence of inflammatory cells in the white matter. In the acute stage of MOGAD, there should be inflammatory edema present in both white and gray matter, leading to increased T2W signals in both areas. This is consistent with MOG-TM lacking the characteristic H-sign. However, the high levels of MOG antigen in the white matter region (27), may lead to a concentration of MOG antibody or inflammatory cells, potentially reducing the T2W signal in the white matter and eventually causing the formation of the H-sign. The elevated cellularity or high concentration deposition of protein may lead to a decrease in the T2W signal within the lesion area, as demonstrated in various other medical conditions (28–30). Additional animal experiments and clinical studies are necessary to validate the relationship between the H sign and the levels of MOG antibodies in MOGAD. Nevertheless, our findings indicate that it is imperative to not only prioritize gray matter lesions in

TABLE 1 Continued

No. /Total no. (%)	No. 1 mixed cohort	No. 2 mixed cohort	No. 3 mixed cohort	No. 4 pediatric cohort	No. 5 mixed cohort	No. 6 mixed corhort	No. 7 pediatric corhort	No. 8 pediatric corhort
Spinal MRI findings at onset								
Negative	3	NA	1	NA	0	NA	0	NA
Positive (T2 hyper intensity)	51	NA	39	NA	9	41	33/33	NA
Axial H sign	15/51 (29.4)	26/52 (50.0)	22/35 (62.9)	5/10 (50.0)	5/6 (83.3)	16[c]	24/33 (72.7)	22/35 (62.9)
Enhancement pattern	14/54 (25.9%) lesion enhancement, patchy and faint	NA	Nodular 8/32 (25.0%), leptomeningeal enhancement 22/32 (68.8%), spinal roots 11/32 (34.4%)	Lesion enhancement 2/8 (25.0%), ventral nerve root enhancement 2/8 (25.0%), dorsal nerve root enhancement 2/8 (25.0%)	2/6 (33.3%) lesion enhancement, details NA	Lesion enhancement ($n = 19$) and subpial enhancement ($n = 5$, 12.2%)	Lesion enhancement 18/30 (60.0%), leptomeningeal enhancement 16/30 (53.3%), Nerve root enhancement 4/30 (13.3%)	Lesion enhancement 6/14 patients (42.9%), typically patchy and faint. leptomeningeal enhancement 4/14 (28.6%), spinal roots enhancement 8/14 (57.1%)

[a] Total numbers of myelitis attacks.
[b] 22 cases had EDSS scores.
[c] Total of lesions was not available.
[d] Total numbers of MOGAD, not myelitis.

MOG-TM due to the presence of the H sign, but also to consider the possibility of more severe lesions in the white matter.

There are several limitations to our study. First, our sample size utilized was limited, and studies with larger sample is needed to clarify the enhancement pattern of the H-sign. Second, pathological biopsy evidence was lacking and only animal experiments were conducted to support the findings. Third, prospective experiments are required to investigate the correlation between the H-sign and serum antibody titers.

This study presents a pediatric case of MOG-TM, who exhibited a distinct H-sign and an unusual enhancement pattern. It is important to highlight that the H-sign, indicative of gray matter involvement, may not represent the critical anatomical region associated with MOG-TM. Furthermore, we recommend the use of enhanced MRI for patients suspected of having MOG-TM.

Author contributions

LZ: Investigation, Writing – original draft, Writing – review & editing. CF: Conceptualization, Data curation, Formal Analysis, Investigation, Methodology, Project administration, Validation, Writing – original draft, Writing – review & editing. LH: Data curation, Project administration, Writing – review & editing. S-YH: Investigation, Writing – original draft. X-YL: Investigation, Writing – original draft. XF: Data curation, Formal Analysis, Investigation, Methodology, Project administration, Supervision, Validation, Writing – original draft, Writing – review & editing.

Funding

The author(s) declare that no financial support was received for the research, authorship, and/or publication of this article.

Conflict of interest

Publisher's note

References

1. Longbrake E. Myelin oligodendrocyte glycoprotein-associated disorders. *Contin Lifelong Learn Neurol.* (2022) 28:1171–93. doi: 10.1212/CON.0000000000001127

2. Tantsis EM, Prelog K, Alper G, Benson L, Gorman M, Lim M, et al. Magnetic resonance imaging in enterovirus-71, myelin oligodendrocyte glycoprotein antibody, aquaporin-4 antibody, and multiple sclerosis-associated myelitis in children. *Dev Med Child Neurol.* (2019) 61(9):1108–16. doi: 10.1111/dmcn.14114

3. Dubey D, Pittock SJ, Krecke KN, Morris PP, Sechi E, Zalewski NL, et al. Clinical, radiologic, and prognostic features of myelitis associated with myelin oligodendrocyte glycoprotein autoantibody. *JAMA Neurol.* (2019) 76(3):301–9. doi: 10.1001/jamaneurol.2018.4053

4. Mariano R, Messina S, Roca-Fernandez A, Leite MI, Kong Y, Palace JA. Quantitative spinal cord MRI in MOG-antibody disease, neuromyelitis optica and multiple sclerosis. *Brain.* (2021) 144(1):198–212. doi: 10.1093/brain/awaa347

5. Sechi E, Cacciaguerra L, Chen JJ, Mariotto S, Fadda G, Dinoto A, et al. Myelin oligodendrocyte glycoprotein antibody-associated disease (MOGAD): a review of clinical and MRI features, diagnosis, and management. *Front Neurol.* (2022) 13 (885218). doi: 10.3389/fneur.2022.885218

6. Banwell B, Bennett JL, Marignier R, Kim HJ, Brilot F, Flanagan EP, et al. Diagnosis of myelin oligodendrocyte glycoprotein antibody-associated disease: international MOGAD panel proposed criteria. *Lancet Neurol.* (2023) 22(3):268–82. doi: 10.1016/S1474-4422(22)00431-8

7. Mariano R, Messina S, Kumar K, Kuker W, Leite MI, Palace J. Comparison of clinical outcomes of transverse myelitis among adults with myelin oligodendrocyte glycoprotein antibody vs aquaporin-4 antibody disease. *JAMA Netw Open.* (2019) 2 (10):e1912732. doi: 10.1001/jamaneurol.2018.4053

8. Rinaldi S, Davies A, Fehmi J, Beadnall HN, Wang J, Hardy TA, et al. Overlapping central and peripheral nervous system syndromes in MOG antibody-associated disorders. *Neurol Neuroimmunol Neuroinflamm.* (2020) 8(1):e924. doi: 10.1212/NXI.0000000000000924

9. Fadda G, Alves CA, O'Mahony J, Castro DA, Yeh EA, Marrie RA, et al. Comparison of spinal cord magnetic resonance imaging features among children with acquired demyelinating syndromes. *JAMA Netw Open.* (2021) 4(10):e2128871. doi: 10.1001/jamanetworkopen.2021.28871

10. ZhangBao J, Huang W, Zhou L, Wang L, Chang X, Lu C, et al. Myelitis in inflammatory disorders associated with myelin oligodendrocyte glycoprotein antibody and aquaporin-4 antibody: a comparative study in Chinese Han patients. *Eur J Neurol* (2021) 28(4):1308–15. doi: 10.1111/ene.14654

11. Kitley J, Waters P, Woodhall M, Leite MI, Murchison A, George J, et al. Neuromyelitis optica spectrum disorders with aquaporin-4 and myelin-oligodendrocyte glycoprotein antibodies: a comparative study. *JAMA Neurol.* (2014) 71(3):276–83. doi: 10.1001/jamaneurol.2013.5857

12. Netravathi M, Holla VV, Nalini A, Yadav R, Vengalil S, Oommen AT, et al. Myelin oligodendrocyte glycoprotein-antibody-associated disorder: a new inflammatory CNS demyelinating disorder. *J Neurol.* (2021) 268(4):1419–33. doi: 10.1007/s00415-020-10300-z

13. Naggar IE, Cleaveland R, Wendel EM, Bertolini A, Schanda K, Karenfort M, et al. MR imaging in children with transverse myelitis and acquired demyelinating syndromes. *Mult Scler Relat Disord.* (2022) 67(104068). doi: 10.1016/j.msard.2022.104068

14. Ren C, Zhang W, Zhou A, Zhou J, Cheng H, Tang X, et al. Clinical and radiologic features among children with myelin oligodendrocyte glycoprotein antibody-associated myelitis. *Pediatr Neurol.* (2023) 143:96–9. doi: 10.1016/j.pediatrneurol.2023.02.019

15. de Mol CL, Wong Y, van Pelt ED, Wokke B, Siepman T, Neuteboom RF, et al. The clinical spectrum and incidence of anti-MOG-associated acquired demyelinating syndromes in children and adults. *Mult Scler.* (2020) 26(7):806–14. doi: 10.1177/1352458519845112

16. O'Connell K, Hamilton-Shield A, Woodhall M, Messina S, Mariano R, Waters P, et al. Prevalence and incidence of neuromyelitis optica spectrum disorder, aquaporin-4 antibody-positive NMOSD and MOG antibody-positive disease in Oxfordshire, UK. *J Neurol Neurosurg Psychiatry.* (2020) 91(10):1126–8. doi: 10.1136/jnnp-2020-323158

17. Reindl M, Waters P. Myelin oligodendrocyte glycoprotein antibodies in neurological disease. *Nat Rev Neurol.* (2019) 15(2):89–102. doi: 10.1038/s41582-018-0112-x

18. Pham-Dinh D, Mattei MG, Nussbaum JL, Roussel G, Pontarotti P, Roeckel N, et al. Myelin/oligodendrocyte glycoprotein is a member of a subset of the immunoglobulin superfamily encoded within the major histocompatibility complex. *Proc Natl Acad Sci U S A.* (1993) 90(17):7990–4. doi: 10.1073/pnas.90.17.7990

19. Ciron J, Cobo-Calvo A, Audoin B, Bourre B, Brassat D, Cohen M, et al. Frequency and characteristics of short versus longitudinally extensive myelitis in

adults with MOG antibodies: a retrospective multicentric study. *Mult Scler*. (2020) 26 (8):936–44. doi: 10.1177/1352458519849511

20. Jurynczyk M, Messina S, Woodhall MR, Raza N, Everett R, Roca-Fernandez A, et al. Clinical presentation and prognosis in MOG-antibody disease: a UK study. *Brain*. (2017) 140(12):3128–38. doi: 10.1093/brain/awx276

21. Corbali O, Chitnis T. Pathophysiology of myelin oligodendrocyte glycoprotein antibody disease. *Front Neurol*. (2023) 14(1137998). doi: 10.3389/fneur.2023.1137998

22. McCusker RH, Kelley KW. Immune-neural connections: how the immune system's response to infectious agents influences behavior. *J Exp Biol*. (2013) 216(Pt 1):84–98. doi: 10.1242/jeb.073411

23. Mishal B, Divate P. 'H' sign in a case of MOG myelitis. *Neurol India*. (2022) 70 (4):1682–3. doi: 10.4103/0028-3886.355180

24. Takai Y, Misu T, Fujihara K, Aoki M. Pathology of myelin oligodendrocyte glycoprotein antibody-associated disease: a comparison with multiple sclerosis and aquaporin 4 antibody-positive neuromyelitis optica spectrum disorders. *Front Neurol*. (2023) 14(1209749). doi: 10.3389/fneur.2023.1209749

25. Jarius S, Ruprecht K, Kleiter I, Borisow N, Asgari N, Pitarokoili K, et al. MOG-IgG in NMO and related disorders: a multicenter study of 50 patients. Part 2: epidemiology, clinical presentation, radiological and laboratory features, treatment responses, and long-term outcome. *J Neuroinflammation*. (2016) 13(1):280. doi: 10.1186/s12974-016-0718-0

26. Remlinger J, Bagnoud M, Meli I, Massy M, Linington C, Chan A, et al. Modelling MOG antibody-associated disorder and neuromyelitis optica spectrum disorder in animal models: spinal cord manifestations. *Mult Scler Relat Disord*. (2023) 78(104892). doi: 10.1016/j.msard.2023.104892

27. Mills JD, Kavanagh T, Kim WS, Chen BJ, Kawahara Y, Halliday GM, et al. Unique transcriptome patterns of the white and grey matter corroborate structural and functional heterogeneity in the human frontal lobe. *PLoS One*. (2013) 8(10): e78480. doi: 10.1371/journal.pone.0078480

28. Fujita A, Sakai O, Chapman MN, Sugimoto H. IgG4-related disease of the head and neck: CT and MR imaging manifestations. *Radiographics*. (2012) 32(7):1945–58. doi: 10.1148/rg.327125032

29. Baur A, Stäbler A, Lamerz R, Bartl R, Reiser M. Light chain deposition disease in multiple myeloma: MR imaging features correlated with histopathological findings. *Skeletal Radiol*. (1998) 27(3):173–6. doi: 10.1007/s002560050360

30. Wang Q, Takashima S, Fukuda H, Takayama F, Kobayashi S, Sone S. Detection of medullary thyroid carcinoma and regional lymph node metastases by magnetic resonance imaging. *Arch Otolaryngol Head Neck Surg*. (1999) 125(8):842–8. doi: 10.1001/archotol.125.8.842

frontiers | Frontiers in Neurology

TYPE Original Research
PUBLISHED 18 October 2024
DOI 10.3389/fneur.2024.1465440

OPEN ACCESS

EDITED BY
Yunzhi Huang,
Nanjing University of Information Science and Technology, China

REVIEWED BY
Baolai Liu,
Shanxi Provincial People's Hospital, China
Vassilios Tsitouras,
Aristotle's University, Greece

*CORRESPONDENCE
Renée Lampe
✉ renee.lampe@tum.de

RECEIVED 16 July 2024
ACCEPTED 26 September 2024
PUBLISHED 18 October 2024

CITATION
Sidorenko I, Brodkorb S, Felderhoff-Müser U, Rieger-Fackeldey E, Krüger M, Feddahi N, Kovtanyuk A, Lück E and Lampe R (2024) Assessment of intraventricular hemorrhage risk in preterm infants using mathematically simulated cerebral blood flow.
Front. Neurol. 15:1465440.
doi: 10.3389/fneur.2024.1465440

Assessment of intraventricular hemorrhage risk in preterm infants using mathematically simulated cerebral blood flow

Irina Sidorenko[1], Silke Brodkorb[2], Ursula Felderhoff-Müser[3], Esther Rieger-Fackeldey[4], Marcus Krüger[2], Nadia Feddahi[3], Andrey Kovtanyuk[1], Eva Lück[1] and Renée Lampe[1,5]*

[1]Department of Clinical Medicine, Center for Digital Health and Technology, Orthopedic Department, Research Unit for Pediatric Neuroorthopedics and Cerebral Palsy of the Buhl-Strohmaier Foundation, Klinikum rechts der Isar, School of Medicine and Health, Technical University of Munich, Munich, Germany, [2]Clinic for Neonatology, Munich Clinic Harlaching & Schwabing, Munich, Germany, [3]Department of Pediatrics I, Neonatology, Paediatric Intensive Care, Paediatric Infectious Diseases, Paediatric Neurology, Centre for Translational Neuro-and Behavioural Sciences, University Hospital Essen, Faculty of Medicine, University of Duisburg-Essen, Essen, Germany, [4]Clinic and Policlinic for Neonatology, Klinikum rechts der Isar, School of Medicine and Health, Technical University of Munich, Munich, Germany, [5]Markus Würth Professorship, Technical University of Munich, Munich, Germany

Intraventricular hemorrhage (IVH)4 is one of the most threatening neurological complications associated with preterm birth which can lead to long-term sequela such as cerebral palsy. Early recognition of IVH risk may prevent its occurrence and/or reduce its severity. Using multivariate logistic regression analysis, risk factors significantly associated with IVH were identified and integrated into risk scales. A special aspect of this study was the inclusion of mathematically calculated cerebral blood flow (CBF) as an independent predictive variable in the risk score. Statistical analysis was based on clinical data from 254 preterm infants with gestational age between 23 and 30 weeks of pregnancy. Several risk scores were developed for different clinical situations. Their efficacy was tested using ROC analysis, and validation of the best scores was performed on an independent cohort of 63 preterm infants with equivalent gestational age. The inclusion of routinely measured clinical parameters significantly improved IVH prediction compared to models that included only obstetric parameters and medical diagnoses. In addition, risk assessment with numerically calculated CBF demonstrated higher predictive power than risk assessments based on standard clinical parameters alone. The best performance in the validation cohort (with AUC = 0.85 and TPR = 0.94 for severe IVH, AUC = 0.79 and TPR = 0.75 for all IVH grades and FPR = 0.48 for cases without IVH) was demonstrated by the risk score based on the MAP, pH, CRP, CBF and leukocytes count.

KEYWORDS

preterm birth, immature brain, intraventricular hemorrhage, cerebral blood flow, multivariate logistic regression analysis, risk score, prognostic accuracy, ROC analysis

1 Introduction

Advances in obstetric and neonatal care in recent decades have resulted in a significant reduction in perinatal mortality. However, the incidence of intraventricular hemorrhage (IVH) in preterm infants with gestational age (GA) less than 32 weeks of pregnancy or body weight at birth (BW) less than 1,500 g remains still very high. It reaches 40% (1) for preterm infants and increases for lower gestational age, reaching 52% for very preterm infants born before 28 weeks gestation (WG) (2). IVH is one of the most threatening complications of preterm birth, which may lead to death or long term severe neurological disorders, such as motor, sensor and/or cognitive disabilities. It is caused by rupture of the fragile vascular vessels within the germinal matrix, a highly vascularised layer located above the caudate nucleus and composed of glial and neuronal progenitor cells (3). The prediction of IVH and development of prevention strategies are among the most important tasks of modern neonatal care.

The underlying cause of cerebral hemorrhage in preterm infants is multifactorial. Risk factors can be divided into several groups. The first group includes pregnancy pathologies that are usually known before delivery. The second group consists of birth characteristics, including Apgar score, which are known already in the first minutes of life. The most recognized risk factors associated with IVH are low gestational age, low birth weight and low Apgar scores (2, 3). The third group contains medical diseases, among which the perinatal infection and early sepsis are the most dangerous (1, 2). This parameters can be included in risk models as soon as diseases have been diagnosed. The fourth group consists of medical parameters that are determined through routine laboratory tests, blood gas analysis and regular observations. These measurements are usually performed several times a day as part of the standard monitoring of preterm infants. Due to the regularity of the investigations, these parameters provide valuable information about the patient's current status.

Another risk factor associated with the low gestational age is immaturity of the cerebral vascular system. The presence of germinal matrix before 32 WG plays a crucial role in the development of IVH (3). The weakness of the cytoskeletal structure exposes the delicate vasculature of the germinal matrix to an increased risk of rupture. Another anatomical feature of germinal matrix vessels is that capillaries are larger in diameter and the muscular layer of the vessels is poorly developed or absent. Thus, these anatomic features make the vessels susceptible to rupture and increase the risk of cerebral hemorrhage in early childhood. In addition, autoregulation of immature cerebral vessels is underdeveloped (4), resulting in an inadequate response to cerebral blood flow (CBF) fluctuations. Thus, critical CBF values are additional risk factors for IVH (3, 4), and taking them into account could potentially improve prognostic models.

Since gestational age, birth weight and Apgar score are often not sufficient to determine the health condition of preterm neonates, several multidimensional scales have been developed to assess risks for mortality or survival (5). The most popular scores, such as CRIB (clinical risk index for babies), CRIB-II (6, 7), SNAP (score for neonatal acute physiology), SNAP-II (8, 9), SNAPPE (score for neonatal acute physiology with perinatal extension) (10), PREM (prematurity risk evaluation measure) (11), were initially validated as predictors of mortality and morbidity, however they also have been shown to predict severe IVH more accurately than BW or GA alone (12). While low GA and BW alone are definitely important predictors for IVH, several other score systems for predicting early risk for severe hemorrhage based on various medical parameters have been developed (1, 13, 14).

All of the above mentioned methods have primarily included prenatal and perinatal variables, neonatal diseases and clinical parameters available within the first hours of life, arguing that the vast majority of IVH occurs within the first 48 h. Although numerous perinatal, obstetric and neonatal risk factors associated with IVH may be identified early after birth (15), recent studies have revealed a significant association between IVH and some routinely recorded clinical parameters such as systolic and diastolic arterial blood and respiratory data (16–18). Additionally, it was demonstrated that fluctuating CBF had a significant association with IVH (19, 20). Furthermore, CBF was an important variable in machine learning models for differentiation between preterm infants with and without IVH (18).

Despite existing non-invasive methods to measure CBF, such as xenon-133 (21), near-infrared spectroscopy (NIRS) (22), diffusion correlation spectroscopy (DCS) (23) and others, CBF is not yet a routinely measured parameter in monitoring preterm infants in the neonatal intensive care unit (NICU). The mathematical model for calculating CBF from standard clinical records of mean arterial pressure (MAP), partial pressure of carbon dioxide (pCO_2), partial pressure of oxygen (pO_2), and hematocrit (Ht) were in good agreement with experimental measurements (19, 24) and can therefore be used to analyze IVH risk factors instead of measured values.

The main aim of this study was to develop predictive models for different clinical situations to identify preterm infants at increased risk of IVH using standard pre/postnatal and birth parameters, medical diagnoses and routinely measured parameters. We also investigated a possibility to enhance a prognostic accuracy of the IVH risk scores by including numerically calculated CBF as independent predictive variable.

2 Materials and methods

2.1 Study population and data collection

The present work is a retrospective study based on clinical data of two cohorts of preterm infants with gestational age 23–30 WG born in four German hospitals with the highest level of care according to the German regulations. The study was approved by the ethic committee of School of Medicine Klinikum rechts der Isar, Technical University of Munich (Ref. 364/15), and Ethic Committee of University Hospital Essen, University Duisburg-Essen (Ref. 16-7284-BO).

The derivation cohort used for construction of IVH risk scores included 254 preterm infants born between 2006 and 2016. The prediction accuracy of the developed risk scores was validated on more recent population of 63 preterm infants (validation cohort) born between 2017 and 2019.

In all four settings, occurrence of IVH was diagnosed by cranial ultrasound performed routinely on day 1, 3, 7, 14 of life and more frequently (up to daily) in case of suspected hemorrhage. The severity of IVH was divided into four grades according to Papile classification (25). In the study, groups of patients with and without IVH diagnosis are referred to as the affected and control groups.

In both cohorts, the following clinical data were collected:

I. Pregnancy pathologies: (1) EPH-gestosis/pre-eclampsia, (2) preterm premature rupture of membranes (PPROM), (3) chorioamnionitis/intra-amniotic infection syndrome, (4) intrauterine growth restriction (IUGR), (5) *in vitro* fertilization (IVF), (6) feto-fetal transfusion syndrome (FFTS).

II. Birth parameters: (1) delivery mode (spontaneous or by cesarean section), (2) sex, (3) birth weight, (4) gestational age, (5) singleton/multiple births, (6) Apgar at 1 min, (7) Apgar at 5 min, (8) Apgar at 10 min.

III. Medical diagnoses: (1) respiratory distress syndrome (RDS), (2) sepsis, (3) pulmonary hemorrhage, (4) erythrocyte transfusion, (5) acidosis (metabolic and/or respiratory), (6) focal/spontaneous intestinal perforation (FIP/SIP), (7) thrombocytopenia, (8) necrotizing enterocolitis (NEC), (9) cholestasis, (10) cardiopulmonary adaptation disorder.

IV. Routinely measured parameters (this group of parameters consists of measurements provided by routine laboratory tests, blood gas analyses and regular observations, which are usually carried out several times a day as part of the standard monitoring of premature babies): (1) pH, (2) pCO_2, (3) pO_2, (4) MAP, (5) Ht, (6) leukocyte count, (7) thrombocyte count, (8) C-reactive protein (CRP).

V. Additionally, within the framework of this study, the CBF and CBF-CBF_{mean} are calculated for each set of measurements of MAP, pCO_2, pO_2 and Ht and treated as independent parameters in the statistical analyses.

The six pregnancy pathologies and eight birth parameters were recorded shortly after birth, further 10 infant diagnoses were recorded during postnatal care. In addition, eight routinely measured clinical parameters were systematically recorded during 7 days before and 3 days after IVH diagnose, or 10 days after birth for preterm infants without IVH diagnosis.

2.2 Calculation of the cerebral blood flow

In the present study we calculate CBF from the 6 medical parameters, namely WG, BW, MAP, pCO_2, pO_2 and Ht using the hierarchical cerebral vascular model that was initially proposed for adult brain (26) and then adjusted to the peculiarities of the immature brain (19, 27). In the model, the cerebral vascular system is represented by 19 serially connected levels, each containing parallel connected vessels of a certain size. At each level, the number of vessels and their length and diameter are scaled according to the patient's gestational age and the brain weight estimated from the birth weight (28). At the capillary level, an additional area is added as a parallel circuit with the number of vessels corresponding to the relative volume of the germinal matrix at a given gestational age (29). Furthermore, the effect of Ht on blood viscosity is included in the calculation of vascular resistance (30, 31) and autoregulation activity of the brain vessels (vasoconstriction and vasodilation) is accounted by increasing and decreasing of vessel's diameter according to the measured values of MAP, pCO_2 and pO_2 (19, 24, 27).

The calculated CBF value was included in the statistical analyses as an independent parameter. In addition, the mean value of CBF for the group of infants without IVH was calculated for each WG. The obtained CBF_{mean} value was used as a reference value of the optimal CBF at each WG and the CBF-CBF_{mean} value was included as a further predictive variable in the statistical analyses.

2.3 Statistical methods

To build a risk score, multivariable stepwise logistic regression analysis was applied (1, 13). In our study, IVH diagnosis plays a role of response variable y, which has a binary type. The predictive variables (predictors) x_j are medical characteristics, which have either continuous or binary type. The selection of potential variables for scoring system started with the analysis of parameters related to IVH. To detect IVH risk factors, a univariate analysis was performed using two-sided Wilcoxon's rank-sum test for continuous and Fisher's exact test for categorical parameters (32). A 5% significance level, which corresponds to p-value = 0.05, was taken as the threshold value for including each parameter as a candidate variable in the multivariate prediction model.

The parameters found to be associated with IVH were then ranked in respect to the response variable according to the p-values of chi-square test with null hypothesis that predictor and response variable are independent. The p-value <0.05 means that the predictor and response variable are significantly associated with each other. Predictors with larger values $-\log(p)$ were ranked higher and the value $-\log(0.05) = 3$ was taken as the threshold for including them into the score model.

Incorporation of independent predictors into risk scores was performed using a generalized linear regression with logit link function as follows:

$$y = \frac{\exp\left(b_0 + \sum_{j=1}^{N}\left(x_j b_j\right)\right)}{1 + \exp\left(b_0 + \sum_{j=1}^{N}\left(x_j b_j\right)\right)}$$

In order to prevent overfitting, we implemented stepwise predictors selection. We started with a single variable model ($N = 1$) using the highest ranked predictor and added lower ranking predictors after running the chi-squared test with the null hypothesis that deviance of old and new regression models are equal. A p-value <0.05 rejects the null hypothesis and means that new predictor significantly improves the fitting model and should be included in the score. Only predictors with statistically significant coefficients b_j were included in the model, and only models that were statistically significantly different from the constant model were used further for construction of risk scores.

The coefficients b_j obtained by the linear regression analyses were then integrated in a risk score as follows:

$$S(t) = b_0 + \sum_{j=1}^{N} x_j(t) b_j$$

Here x_j (t) is the value of the predictor j averaged over all measurements up to time t. For early IVH prediction, as long as the measured clinical parameters are not available, only the parameters of groups I–III were considered in the regression model. For the prediction of IVH on the second day, the clinical parameters were averaged over the first day of life (measurements of preterms with IVH on the first day are then excluded), and for the later prediction of IVH, parameters were averaged over all days before IVH.

To evaluate the effectiveness of the risk scores constructed, the receiver operating characteristic (ROC) method for classification between the control and affected groups was applied (33, 34). For each patient from control and affected groups score value was calculated, then true positive rate (TPR) and false positive rate (FPR) (Table 1) were computed for different threshold values. The ROC curves were constructed by plotting TPR against FPR, and the area under the ROC curve (AUC) was estimated (35). The later provides a quantitative measure of predictive power of the score: perfect predictor has $AUC = 1$, which corresponds to $TPR = 1$ and $FPR = 0$, and predictor with $AUC = 0.5$ is equivalent to random choice. The threshold for optimal performance was chosen at the point on the ROC curve with the smallest distance to the upper left corner of the unit square (36) and used further for the normalization of the regression coefficient b_0, so that the threshold for IVH risk was equal to 0 for all risk scores. The validation of the resulting IVH risk scores was performed by calculating the TPR and FPR using independent data from the validation cohort.

Statistical analyses was carried out using standard library of MATLAB2024a. Observations with missing values were not used in analyses, medical parameters that were measured less often than others were extended until the next regular measurement. For calculation of CBF, missing parameter values were replaced with the latest measured value.

3 Results

3.1 Identification of risk parameters of IVH

Basic clinical characteristics of the derivation and validation cohorts are presented in Table 2. Here, continuous variables are expressed as mean and standard deviation, while binary variables are presented as the number of cases and percentages.

To create a risk score, the data from the derivation cohort of 254 patients (136 with and 118 without diagnosis of IVH) was used. During data collection, the affected and control groups were matched according to gestational age and birth weight. Thus, these parameters had statistically equal (p-value >0.05) mean values (Table 3) and, therefore, were not used in this study as predictor variables for risk assessment.

TABLE 1 Variables of ROC analyses.

Variable	Definition
P	The total number of patients with IVH
N	The total number of patients without IVH
TP	True positive (the number of correctly detected patients with IVH)
TN	True negative (the number of correctly detected patients without IVH)
FP	False positive (the number of patients without IVH detected as with IVH)
FN	False negative (the number of patients with IVH detected as without IVH)
$TPR = TP/P$	True positive rate
$FPR = FP/N$	False positive rate

The statistical comparison of pregnancy pathologies, birth parameters and infant diagnoses in the affected and control groups of the derivation cohort is presented in Table 4. The table is sorted according to the p-value: the most significant parameters, i.e., those with the smallest p-value, are at the top. Seven parameters (EPH-gestosis/pre-eclampsia, PPROM, cardiopulmonary adaptation disorder, IUGR, IVF, RDS and FFTS) demonstrated inverse relationship with the development of IVH, i.e., the percentage of preterm infants with these diagnoses in the affected group was lower than in the control group. This can be explained by the effects of the medical treatment provided, which is out of scope of this study. Therefore, these parameters were not considered as predictor variables in the following risk assessment. Another seven parameters (sepsis, delivery mode, erythrocyte transfusion, chorioamnionitis, thrombocytopenia, NEC and multiple birth) had no significant association with IVH (i.e., p-value >0.5). Significant association with IVH (i.e., p-value <0.5) was revealed for the following 8 parameters: Apgar at 1 min, Apgar at 5 min, Apgar at 10 min, FIP/SIP, cholestasis, acidosis, male sex and pulmonary hemorrhage. The parameters found to be associated with IVH were further used as predictive variables in the logistic regression analyses.

3.2 Construction of IVH risk scores

We started the construction of risk scores with the ranking of the predictive variables (Figure 1), which were then included stepwise in the multivariable regression analyses according to their significance. For different clinical situations, several scores were designed (Table 5). The performance of the resulting scores was evaluated using the ROC analysis. We determined the optimal threshold from the ROC curve for patients with all grades of IVH and then calculated the TPR and FPR for patients with all (I–IV) and severe (III–IV) grades of IVH (the example of ROC curve with optimal threshold and corresponding scatter plot is shown in Figure 2).

For the initial prediction of IVH risk, we constructed the score S1 based only on pregnancy pathologies, birth parameters and infant diagnoses, which are usually known before measured parameters are available (Figure 1 left). Although eight parameters were significantly associated with IVH, two of them, namely Apgar at 1 min and Apgar at 5 min, were absent in the score due to their high correlation with Apgar at 10 min (Pearson correlation 0.61 and 0.77, respectively). The score S1 demonstrated only moderate performance ($AUC = 0.74$) and included several statistically insignificant coefficients, suggesting that this group of medical parameters was insufficient for effective IVH prediction.

The improvement of IVH prediction can be achieved by including routinely measured parameters in the regression model. In the first day of life, the availability of measurements is usually limited. To determine risk scores for first and second days of life, we averaged routinely measured parameters over the first day (patients with IVH on the first day are excluded from consideration at this stage). Thus, only pH and leukocyte count demonstrated significant association with IVH (Figure 1 middle). Two other parameters, CBF-CBF_{min} and pCO_2, were close to the limit of significance. It is important to note, that mathematically calculated parameter CBF-CBF_{min} had stronger association with IVH than each of the parameters used for its calculation (Figure 1 middle). The integration of the significant

TABLE 2 Clinical characteristics of the study cohorts.

Clinical characteristic	Derivation cohort *n* = 254 (100%)			Validation cohort *n* = 63 (100%)		
	Min	Max	Mean ± Stdev	Min	Max	Mean ± Stdev
Gestational age [WG + days]	23	30 + 6	26.45 ± 2.11	23 + 1	30 + 6	26.39 ± 2.17
Birth weight [g]	335	1580	864.06 ± 279.1	490	1590	905.16 ± 279.65
Male sex	122 (48%)			39 (61.90%)		
Multiple birth	95 (37.4%)			25 (39.68%)		
Vaginal delivery	22 (8.66%)			7 (11.11%)		
IVH	136 (53.54%)			37 (58.73%)		
EPH-gestosis/pre-eclampsia	25 (9.84%)			2 (3.17%)		
PPROM	73 (28.74%)			32 (50.79%)		
Chorioamnionitis	117 (46.06%)			43 (68.25%)		
IUGR	14 (5.51%)			0		
IVF	32 (12.59%)			8 (12.69%)		
FFTS	8 (3.15%)			1 (1.59%)		
RDS	84 (33.07%)			14 (22.22%)		
Sepsis	120 (47.24%)			20 (31.75%)		
Pulmonary hemorrhage	21 (8.27%)			8 (12.69%)		
Erythrocyte transfusion	164 (64.57%)			39 (61.90%)		
Acidosis (metabolic and/or respiratory)	38 (14.96%)			10 (15.87%)		
FIP/SIP	23 (9.06%)			3 (4.76%)		
Thrombocytopenia	21 (8.27%)			4 (6.35%)		
NEC	20 (7.87%)			10 (15.87%)		
Cholestasis	12 (4.72%)			0		
Cardiopulmonary adaptation disorder	19 (7.48%)			18 (28.57%)		

TABLE 3 Comparison of gestational age and birth weight of affected and control groups.

Parameter	With IVH *n* = 136	No IVH *n* = 118	*p*-value
Gestational age	26.25 ± 2.05	26.68 ± 2.17	0.12
Birth weight	875.66 ± 300.5	850.68 ± 252.81	0.70

measured parameters averaged over the first day of life (Figure 1 middle) in the regression procedure resulted in the risk models with 4 and 3 parameters (score S2 and S3 in Table 5), which both had only significant regression coefficients and much better performance in ROC analyses than S1 (Table 5).

To construct a risk score for prediction of IVH when the values of all measured parameters are already available, we averaged them for all days before IVH and added averaged values to the regression analysis according to their significance (Figure 1 right). In this case, the calculated CBF was ranked fourth among statistically significant parameters and had a stronger association with IVH than pCO_2, pO_2, and Ht, which are used for its calculation. Inclusion of the measured parameters averaged over all days before IVH improved the resulting risk scores (scores S4 and S5 in Table 5). Further improvement in risk score was achieved by adding the calculated CBF to the regression model (scores S6 and S7 in Table 5). The performance of the risk score S7 is illustrated on the Figure 2 (left: ROC curve with optimal threshold value; middle: scatter plot of score values of individual patient).

In order to demonstrate the advantage of including the calculated CBF in the risk model, we constructed a risk score without CBF but with all clinical parameters used in the mathematical model to calculate CBF. The performance of the resulting risk score ($S = pH + Leukocytes + pO_2 + pCO_2 + MAD + Ht$, not in Table 5) with $AUC = 0.88$ appeared to be worse than $AUC = 0.94$ of the risk score S7 which includes CBF. This result indicates that the mathematical model for CBF calculation provides complementary information that improves the prediction of IVH risk.

3.3 Validation of the constructed IVH risk scores

Clinical characteristics of the validation cohort of 63 preterm infants are presented in Table 2. For each patient in the validation cohort, score values with coefficients presented in Table 5 were calculated (Figure 2 right) and used to determine FPR for control group and TPR for all and severe grades of IVH (Table 6). The best performance was achieved by the scores, which included routinely measured parameters and calculated CBF (scores S5, S6 and S7). For this scores, correct identification of patients with IVH (TPR)

TABLE 4 Pregnancy pathologies, birth parameters and infant diagnoses in the derivation cohort.

Parameter	With IVH $n = 136$ (100%)	No IVH $n = 118$ (100%)	p-value
Apgar at 1 min	**5.19 ± 2.25**	**6.21 ± 2.02**	**<0.001**
Apgar at 5 min	**6.80 ± 1.82**	**7.52 ± 1.41**	**<0.001**
Apgar at 10 min	**7.73 ± 1.37**	**8.37 ± 0.97**	**<0.001**
FIP/SIP	**20 (14.7%)**	**3 (2.54%)**	**<0.001**
Cholestasis	**11 (8.09%)**	**1 (0.85%)**	**0.01**
Acidosis	**27 (19.85%)**	**11 (9.32%)**	**0.02**
Sex (male)	**74 (54.4%)**	**48 (40.68%)**	**0.03**
Pulmonary hemorrhage	**16 (11.76%)**	**5 (4.24%)**	**0.04**
EPH-gestosis/pre-eclampsia	7 (5.18%)	18 (15.25%)	0.01
Sepsis	70 (51.47%)	50 (42.37%)	0.17
PPROM	34 (25.00%)	39 (33.05%)	0.17
Delivery mode (spontaneous birth)	15 (11.02%)	7 (5.93%)	0.18
Erythrocyte transfusion	93 (68.38%)	71 (60.17%)	0.19
Chorioamnionitis	67 (49.26%)	50 (42.37%)	0.31
Cardiopulmonary adaptation disorder	8 (5.88%)	11 (9.32%)	0.34
IUGR	6 (4.41%)	8 (6.78%)	0.43
IVF	15 (11.03%)	17 (14.41%)	0.45
Thrombocytopenia	13 (9.56%)	8 (6.78)	0.49
RDS	42 (30.88%)	42 (35.59%)	0.50
NEC	12 (8.82%)	8 (6.78%)	0.64
Multiple birth	52 (38.24%)	43 (36.44%)	0.79
FFTS	4 (2.94%)	4 (3.39)	1

Key information in the table is highlighted in bold.

in the validation cohort remained at the same level as in the derivation cohort. False identification of healthy patients to be at risk of IVH (FPR) in validation cohort was higher than in the derivation cohort. However, increase of FPR was smaller for risk scores with fewer parameters, which were derived only from measured parameters (scores S5 and S7 in Table 6). The overestimation demonstrated by the scores with medical diagnoses can be explained by the fact that all medical diagnoses are in fact already characterized by the measured parameters. The moderate FPR value reflected the fact that the control group did not consist of absolute healthy individuals. All patients without IVH who had high score values (Figure 2 right), had also elevated CRP level (greater than 10 mg/L) indicating an inflammation. In this case, although they did not have IVH, they could not be regarded as healthy patients either.

4 Discussion

IVH is one of the most dangerous pathologies of preterm birth leading to serious lifelong disabilities. The origin and progression of IVH has a multifactorial background. The present study focused on statistical analysis of various medical factors associated with IVH which then were used for construction of a scoring system for prediction of IVH risk. Using a stepwise multivariable logistic regression analysis, several risk scores were constructed for different clinical situations. A particular novelty of the present research was the inclusion of mathematically calculated CBF as an independent predictor variable in the construction of IVH risk scores.

The IVH risk score based only on prenatal and birth parameters, Apgar values and medical diagnoses (S1) has demonstrated only moderate performance, indicating that they are insufficient for effective IVH prediction. A considerable improvement in the prediction of IVH was achieved by including the measured parameters into the logistic regression model. As a result, risk

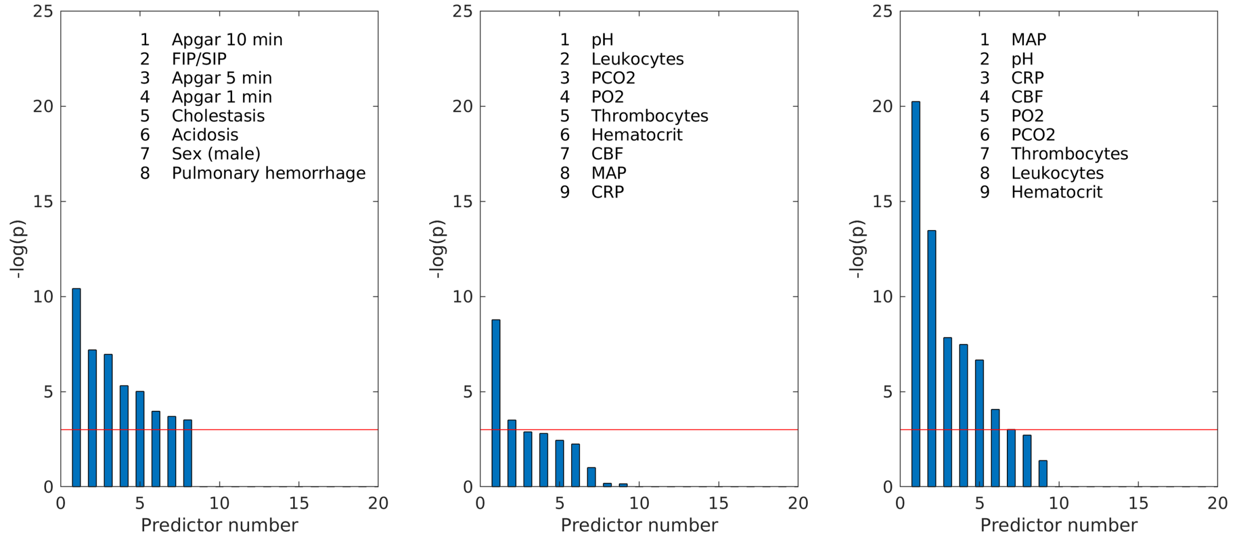

FIGURE 1
Ranking of the predictive variables according to their p-values of chi-square test: (left) medical parameters from Table 4 significantly associated with IVH; (middle) routinely measured parameters averaged over the first day of life; (right) routinely measured parameters averaged over all days before IVH in the affected groups and over 10 days of life in the control group. The red line corresponds to the significance threshold $-\log(p) = 3$, which corresponds to the p-value = 0.05.

TABLE 5 **Performance of the constructed IVH risk scores on the derivation cohort.**

Score $b_{0\,\ldots\,6}$ $p\_value_{0\,\ldots\,6}$	AUC		TPR		FPR
	IVH grades		IVH grades		
	I–IV	III–IV	I–IV	III–IV	
S1 = Apgar at 10 min + FIP/SIP + cholestasis + acidosis + male sex + pulmonary hemorrhage $b_{0\,\ldots\,6}$ = [1.8967; −0.3255; 1.8685; 2.0971; 0.7245; 0.7077; 1.0828] p-value$_{0\,\ldots\,6}$ = [0.0570; 0.0111; 0.0047; 0.0523; 0.0755; 0.0109; 0.0492]	0.74	0.78	0.55	0.64	0.17
S2 = Apgar at 10 min + pH + FIP/SIP + Leukocytes $b_{0\,\ldots\,4}$ = [102.4143; −0.3403; −13.5181; 2.0952; −0.0993] p-value$_{0\,\ldots\,4}$ = [<0.0001; 0.0360; <0.0001; 0.0234; <0.0001]	0.81	0.88	0.75	0.87	0.25
S3 = Apgar at 10 min + pH + Leukocytes $b_{0\,\ldots\,3}$ = [101.9569; −0.3345; −13.4425; −0.0970] p-value$_{0\,\ldots\,3}$ = [<0.0001; 0.0385; <0.0001; 0.0001]	0.79	0.86	0.78	0.90	0.29
S4 = MAP + pH + CRP + FIP/SIP + male sex + Leukocytes $b_{0\,\ldots\,6}$ = [108.5723; −0.1105; 14.3532; 0.4666; 2.2413; 0.7966; −0.0704] p-value$_{0\,\ldots\,6}$ = [0.0013; 0.0020; 0.0021; 0.0091; 0.0107; 0.0365; 0.0055]	0.84	0.94	0.77	0.91	0.19
S5 = MAP + pH + CRP + Leukocytes $b_{0\,\ldots\,4}$ = [117.5718; −0.0969; −15.5920; 0.5566; −0.06549] p-value$_{0\,\ldots\,4}$ = [0.0004; 0.0042; 0.0007; 0.0018; 0.0034]	0.82	0.93	0.72	0.88	0.21
S6 = MAP + pH + CRP + CBF + FIP/SIP + Leukocytes $b_{0\,\ldots\,6}$ = [85.6357; −0.1753; −10.9974; 0.4205; 0.1264; 2.0791; −0.0677] p-value$_{0\,\ldots\,6}$ = [0.0172; 0.0004; 0.0270; 0.0346; 0.0161; 0.0195; 0.0042]	0.85	0.94	0.79	0.91	0.23
S7 = MAP + pH + CRP + CBF + Leukocytes $b_{0\,\ldots\,5}$ = [85.9253; −0.1780; −11.0513; 0.4525; 0.1268; −0.0581] p-value$_{0\,\ldots\,5}$ = [0.0152; 0.0003, 0.0243; 0.0225; 0.0150; 0.0070]	0.84	0.94	0.77	0.91	0.22

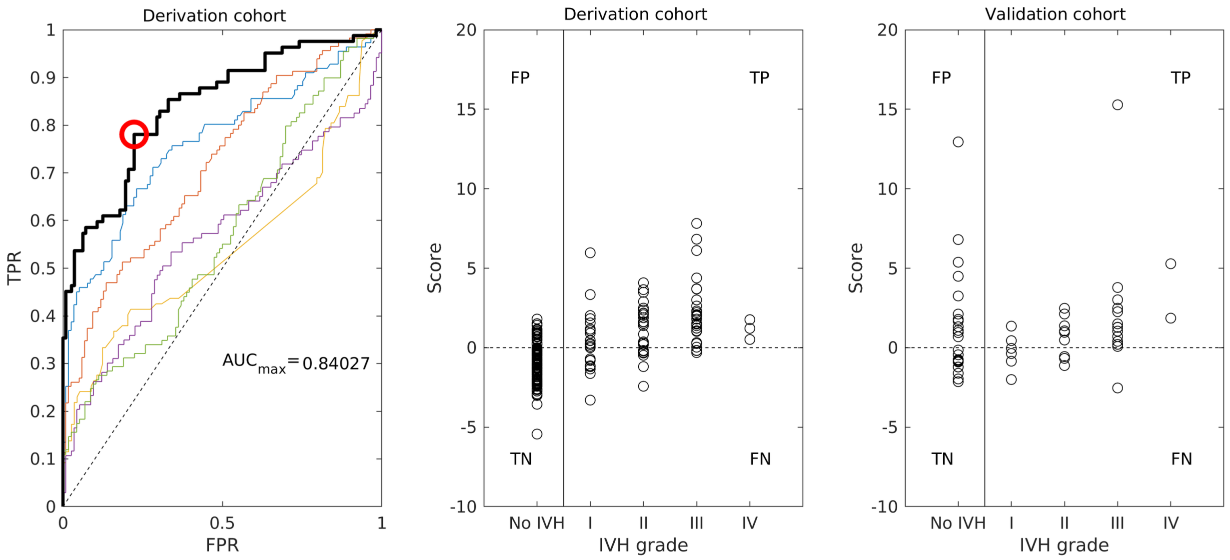

FIGURE 2
Performance of the IVH risk score S7 (see Tables 5, 6): ROC curve (left) and scatter plot (middle) for the derivation cohort; scatter plot for the validation cohort (right).

scores constructed using parameters averaged over the first day of life (S2 and S3) and over all days before IVH (S4–S7) demonstrated TPR = 0.9 for severe IVH both in the derivation and validation cohorts.

The best performance in the validation cohort with AUC = 0.85 and TPR = 0.94 for severe IVH, AUC = 0.79 and TPR = 0.75 for all IVH grades, and FPR = 0.48 for cases without IVH was demonstrated by the risk score S7 which included CBF. The advantages of CBF as an

TABLE 6 Performance of the constructed IVH risk scores on the validation cohort.

Score	AUC		TPR		FPR
	IVH grades		IVH grades		
	I–IV	III–IV	I–IV	III–IV	
S1	0.64	0.69	0.51	0.61	0.42
S2	0.57	0.67	0.77	0.86	0.72
S3	0.58	0.67	0.80	0.86	0.64
S4	0.79	0.85	0.72	0.88	0.64
S5	0.79	0.85	0.72	0.94	0.48
S6	0.79	0.85	0.75	0.88	0.52
S7	**0.79**	**0.85**	**0.75**	**0.94**	**0.48**

Key information in the table is highlighted in bold.

independent predictive variable were confirmed by several statistical methods. Thus, the calculated CBF was ranked fourth among statistically significant parameters and had a stronger association with IVH than pCO_2, pO_2 and Ht, which were used for its calculation. Furthermore, the superiority of the risk score with CBF as an independent parameter was also demonstrated by comparison with a risk score constructed without CBF but taking into account all clinical parameters used in the mathematical model to calculate CBF. The better performance of risk assessment using CBF was evidenced by a higher AUC value compared with the AUC for risk assessment without CBF (0.94 vs. 0.86), which proves that the mathematical model for calculating CBF provides additional information that improves IVH risk prediction.

The moderate FPR value reflects the fact that the control group did not consist of completely healthy patients. For example, all patients without IVH but with high scores had elevated CRP levels indicating inflammation. Thus, constructed risk scores may reveal additional morbidity risks for the preterm infant. Since the main purpose of the constructed scores is to identify patients at risk, the obtained FPR values are acceptable for this situation. The absence of medical diagnoses in the best score can be explained by the argument that all medical diagnoses are in fact characterized by the measured parameters.

The focus of the present work was on the role of routinely measured clinical parameters and calculated CBF in the development of a risk scores for IVH prediction. The importance of measured parameters in the early detection of IVH risk in low birth weight newborns (<1,500 g) was also demonstrated in Huvanandana et al. (16) by scoring models derived using time series analyses of blood pressure and respiratory data. In our study, the developed IVH risk scales demonstrated in both the derivation and validation cohorts the high performance, which is comparable to data published in the literature. In Chien et al. (12), the standard SNAP II mortality risk score (9) combined with GA and Apgar at 5 min demonstrated an AUC = 0.8 for IVH prediction in a cohort of 4,226 infants with GA < 32 weeks. Heuchan et al. (37) developed a novel prognostic model for IVH prediction based on five predictive variables (GA, antenatal corticosteroids, transfer after birth, Apgar at 1 min < 4, male gender) that demonstrated AUC = 0.76 for severe IVH and AUC = 0.67 for any grade of IVH on a cohort of 5,712 infants with gestation of 24–30 weeks. In Vogtmann et al. (1), in cohort of 1,782 neonates with GA < 32 completed weeks of gestation or BW < 1,500 g, severe IVH could be predicted with an accuracy of 87.7% on the basis of five variables (GA, pathological Doppler result, Apgar at 1 min < 6, perinatal infection, and delivery mode). A scoring system including only three factors (low GA, low Apgar at 5 min, and presence of bleeding diathesis within the 7 days of life) developed by Coskun et al. (14) could predicted IVH in preterm infants with GA between 24 and 34 weeks with AUC = 0.85 for a derivation cohort with 144 preterm infants and AUC = 0.81 for a validation cohort with 89 preterm infants.

In the present study, several risk scores based on routinely measured parameters and calculated CBF were developed. They have demonstrated better performance compared to risk models based only on once-measured parameters (like Apgar) and medical diagnoses. In addition, the developed IVH risk scores provide dynamic information about the patient's condition, which can vary from hour to hour. This indicates the need for further investigation of possible prognostic variables among clinical parameters. Also, medical treatment may be considered in the further development of the risk models.

At present, many researchers are investigating neonatal cerebral hemodynamics using modern techniques such as transcranial Doppler (TCD) ultrasound and NIRS monitoring to predict periventricular-intraventricular hemorrhage in preterm infants (38, 39). Although a strong association between IVH and low superior vena cava flow (SVCF) and high Anterior cerebral artery resistive index (ACA-RI) has been revealed (38) the absolute values of global CBF cannot be recalculated from measurements because it is difficult to determine the diameter of intracranial vessels (38, 40). In this case, the mathematical calculation of CBF provides an opportunity to obtain additional information that may improve the prediction of IVH in preterm infants. The developed mathematical model for CBF calculation was previously validated against NIRS, Doppler and Xenon-133 clearance measurements and demonstrated good agreement with published experimental results (19). Furthermore, the current study showed that the inclusion of calculated CBF in IVH risk models resulted in improved performance of prognostic scores. Therefore, in the future, when CBF measurement becomes a routine procedure in neonatal healthcare, the developed risk scores can be used with the measured data.

Nowadays, numerous data and parameters are collected and centrally managed on admission to the NICU. This already allows for automated computerized data analysis (41). Existing health monitoring methods can be further advanced with new strategies, such as the mathematical model for calculating CBF and the IVH risk scores presented in this paper. The good performance of the developed scores allows their use in clinical practice as a complementary tool to other clinical scores and measurement methods to identify preterm infants at high risk of severe IVH, which may lead to a more effective therapeutic approach for these children.

Data availability statement

The data analyzed in this study is subject to the following licenses/restrictions: raw data supporting the conclusions of this manuscript will be made available to any qualified researcher upon request to the corresponding author. Requests to access these datasets should be directed to renee.lampe@tum.de.

Ethics statement

The studies involving humans were approved by the Ethic Committee of School of Medicine Klinikum rechts der Isar, Technical University of Munich (Ref. 364/15), and Ethic Committee of University Hospital Essen, University Duisburg-Essen (Ref. 16-7284-BO). The studies were conducted in accordance with the local legislation and institutional requirements. Written informed consent for participation was not required from the participants or the participants' legal guardians/next of kin because this was a retrospective study with anonymized, routinely collected data; no special data was collected for the study; no declaration of consent required according to the Ethics Committee.

Author contributions

IS: Conceptualization, Data curation, Formal analysis, Investigation, Methodology, Software, Validation, Visualization, Writing – original draft, Writing – review & editing. SB: Data curation, Validation, Writing – review & editing. UF-M: Conceptualization, Data curation, Validation, Writing – review & editing. ER-F: Data curation, Writing – review & editing. MK: Data curation, Validation, Writing – review & editing. NF: Data curation, Software, Writing – review & editing. AK: Investigation, Software, Writing – review & editing. EL: Investigation, Writing – review & editing. RL: Conceptualization, Funding acquisition, Project administration, Resources, Supervision, Validation, Writing – original draft, Writing – review & editing.

Funding

The author(s) declare that financial support was received for the research, authorship, and/or publication of this article. The study was performed under the financial support of the Klaus Tschira Foundation, Würth Foundation, and Buhl-Strohmaier-Foundation.

Acknowledgments

The authors acknowledge the support of the Klaus Tschira Foundation, Würth Foundation, and Buhl-Strohmaier-Foundation.

Conflict of interest

The authors declare that the research was conducted in the absence of any commercial or financial relationships that could be construed as a potential conflict of interest.

Publisher's note

References

1. Vogtmann C, Koch R, Gmyrek D, Kaiser A, Friedrich A. Risk-adjusted intraventricular hemorrhage rates in very premature infants: towards quality assurance between neonatal units. *Dtsch Arztebl Int*. (2012) 109:527–33. doi: 10.3238/arztebl.2012.0527

2. Siffel C, Kistler KD, Sarda SP. Global incidence of intraventricular hemorrhage among extremely preterm infants: a systematic literature review. *J Perinat Med*. (2021) 49:1017–26. doi: 10.1515/jpm-2020-0331

3. Ballabh P. Intraventricular hemorrhage in premature infants: mechanism of disease. *Pediatr Res*. (2010) 67:1–8. doi: 10.1203/PDR.0b013e3181c1b176

4. Rhee CJ, da Costa CS, Austin T, Brady KM, Czosnyka M, Lee JK. Neonatal cerebrovascular autoregulation. *Pediatr Res*. (2018) 84:602–10. doi: 10.1038/s41390-018-0141-6

5. McLeod JS, Menon A, Matusko N, Weiner GM, Gadepalli SK, Barks J, et al. Comparing mortality risk models in VLBW and preterm infants: systematic review and meta-analysis. *J Perinatol*. (2020) 40:695–703. doi: 10.1038/s41372-020-0650-0

6. Rautonen J, Mäkelä A, Boyd H, Apajasalo M, Pohjavuon M. CRIB and SNAP: assessing the risk of death for preterm neonates. *Lancet*. (1994) 343:1272–3. doi: 10.1016/s0140-6736(94)92158-x

7. Parry G, Tucker J, Tarnow-Mordi W. CRIB II: an update of the clinical risk index for babies score. *Lancet*. (2003) 361:1789–91. doi: 10.1016/S0140-6736(03)13397-1

8. Richardson DK, Gray JE, McCormick MC, Workman K, Goldmann DA. Score for neonatal acute physiology: a physiologic severity index for neonatal intensive care. *Pediatrics*. (1993) 91:617–23. doi: 10.1542/peds.91.3.617

9. Richardson DK, Corcoran JD, Escobar GJ, Lee SK. SNAP-II and SNAPPE-II: simplified newborn illness severity and mortality risk scores. *J Pediatr*. (2001) 138:92–100. doi: 10.1067/mpd.2001.109608

10. Dammann O, Shah B, Naples M, Bednarek F, Zupancic J, Allred EN, et al. SNAP-II and SNAPPE-II as predictors of death among infants born before the 28th week of gestation. Inter-institutional variations. *Pediatrics*. (2009) 124:e1001:–e1006. doi: 10.1542/peds.2008-3233

11. Cole TJ, Hey EN, Richmond S. The PREM score: a graphical tool for predicting survival in very preterm births. *Arch Dis Child Fetal Neonatal Ed*. (2010) 95:F14–9. doi: 10.1136/adc.2009.164533

12. Chien LY, Whyte R, Thiessen P, Walker R, Brabyn D, Lee SK. Snap-II predicts severe intraventricular hemorrhage and chronic lung disease in the neonatal intensive care unit. *J Perinatol*. (2002) 22:26–30. doi: 10.1038/sj.jp.7210585

13. Luque MJ, Tapia JL, Villarroel L, Marshall G, Musante G, Carlo W, et al. A risk prediction model for severe intraventricular hemorrhage in very low birth weight infants and the effect of prophylactic indomethacin. *J Perinatol*. (2014) 34:43–8. doi: 10.1038/jp.2013.127

14. Coskun Y, Isik S, Bayram T, Urgun K, Sakarya S, Akman I. A clinical scoring system to predict the development of intraventricular hemorrhage (IVH) in premature infants. *Childs Nerv Syst*. (2018) 34:129–36. doi: 10.1007/s00381-017-3610-z

15. Lago P, Freato F, Bettiol T, Chiandetti L, Vianello A, Zaramella P. Is the CRIB score (clinical risk index for babies) a valid tool in predicting neurodevelopmental outcome in extremely low birth weight infants? *Biol Neonate*. (1999) 76:220–7. doi: 10.1159/000014162

16. Huvanandana J, Nguyen C, Thamrin C, Tracy M, Hinder M, McEwan AL. Prediction of intraventricular haemorrhage in preterm infants using time series analysis of blood pressure and respiratory signals. *Sci Rep*. (2017) 7:46538. doi: 10.1038/srep46538

17. Lampe R, Turova V, Botkin N, Eckardt L, Felderhoff-Müser U, Rieger-Fackeldey E, et al. Postnatal paraclinical parameters associated to occurrence of intracerebral hemorrhage in preterm infants. *Neuropediatrics*. (2019) 50:103–10. doi: 10.1055/s-0038-1677515

18. Turova V, Sidorenko I, Eckardt L, Rieger-Fackeldey E, Felderhoff-Müser U, Alves-Pinto A, et al. Machine learning models for identifying preterm infants at risk of cerebral hemorrhage. *PloS One*. (2020) 15:e0227419. doi: 10.1371/journal.pone.0227419

19. Sidorenko I, Turova V, Botkin N, Eckardt L, Alves-Pinto A, Felderhoff-Müser U, et al. Modeling cerebral blood flow dependence on carbon dioxide and mean arterial blood pressure in the immature brain with accounting for the germinal matrix. *Front Neurol*. (2018) 9:812. doi: 10.3389/fneur.2018.00812

20. Lampe R, Rieger-Fackeldey E, Sidorenko I, Turova V, Botkin N, Eckardt L, et al. Assessing key clinical parameters before and after intraventricular hemorrhage in very preterm infants. *Eur J Pediatr*. (2020) 179:929–37. doi: 10.1007/s00431-020-03585-9

21. Jayasinghe D, Gill AB, Levene MI. CBF reactivity in hypotensive and normotensive preterm infants. *Pediatr Res*. (2003) 54:848–53. doi: 10.1203/01.PDR.0000088071.30873.DA

22. Wally D, Velik-Salchner C. Nahinfrarotspektroskopie unter kardiopulmonaler REANIMATION und mechanischer Kreislaufunterstützung. *Med Klin Intensivmed Notfmed*. (2015) 110:621–30. doi: 10.1007/s00063-015-0012-4

23. Diop M, Kishimoto J, Toronov V, Lee DS, Lawrence KS. Development of a combined broadband near-infrared and diffusion correlation system for monitoring cerebra blood flow and oxidative metabolism in preterm infants. *Biomed Opt Express*. (2015) 6:3907–18. doi: 10.1364/BOE.6.003907

24. Sidorenko I, Turova V, Botkin N, Kovtanyuk A, Eckardt L, Alves-Pinto A, et al. Assessing haemorrhage-critical values of cerebral blood flow by modelling biomechanical stresses on capillaries in the immature brain. *Sci Rep*. (2020) 10:14196–10. doi: 10.1038/s41598-020-71087-7

25. Papile L, Burstein J, Burstein R, Koffler H, Koops B. Relationship of intravenous sodium bicarbonate infusions and cerebral intraventricular hemorrhage. *J Pediatr*. (1978) 93:834–6. doi: 10.1016/s0022-3476(78)81096-8

26. Piechnik SK, Chiarelli PA, Jezzard P. Modelling vascular reactivity to investigate the basis of the relationship between cerebral blood volume and flow under CO_2 manipulation. *NeuroImage*. (2008) 39:107–18. doi: 10.1016/j.neuroimage.2007.08.022

27. Lampe R, Botkin N, Turova V, Blumenstein T, Alves-Pinto A. Mathematical modelling of cerebral blood circulation and cerebral autoregulation: towards preventing intracranial hemorrhages in preterm newborns. *Comput Math Methods Med*. (2014) 2014:965275. doi: 10.1155/2014/965275

28. Guihard-Costa AM, Larroche JC. Differential growth between the fetal brain and its infratentorial part. *Early Hum Dev*. (1990) 23:27–40. doi: 10.1016/0378-3782(90)90126-4

29. Kinoshita Y, Okudera T, Tsuru E, Yokota A. Volumetric analysis of the germinal matrix and lateral ventricles performed using MR images of postmortem fetuses. *AJNR Am J Neuroradiol*. (2001) 22:382–8.

30. Botkin ND, Kovtanyuk AE, Turova VL, Sidorenko IN, Lampe R. Accounting for tube hematocrit in modeling of blood flow in cerebral capillary networks. *Comput Math Methods Med*. (2019) 2019:4235937. doi: 10.1155/2019/4235937

31. Sidorenko I, Turova V, Rieger-Fackeldey E, Felderhoff-Müser U, Kovtanyuk A, Brodkorb S, et al. Mathematical modeling of the hematocrit influence on cerebral blood flow in preterm infants. *PloS One*. (2021) 16:e0261819. doi: 10.1371/journal.pone.0261819

32. Gursoy T, Hayran M, Derin H, Ovali F. A clinical scoring system to predict the development of bronchopulmonary dysplasia. *Am J Perinatol*. (2015) 32:659–66. doi: 10.1055/s-0034-1393935

33. Hanley JA, McNeil BJ. The meaning and use of the area under a receiver operating characteristic (ROC) curve. *Radiology*. (1982) 143:29–36. doi: 10.1148/radiology.143.1.7063747

34. Hanley JA, McNeil BJ. A method of comparing the areas under receiver operating characteristics curves derived from the same cases. *Radiology*. (1983) 148:839–43. doi: 10.1148/radiology.148.3.6878708

35. Hajian-Tilaki K. Receiver operating characteristic (ROC) curve analysis for medical diagnostic test evaluation. *Caspian J Intern Med*. (2013) 4:627.

36. DeLong ER, DeLong DM, Clarke-Pearson DL. Comparing the areas under two or more correlated receiver operating characteristic curves: a nonparametric approach. *Biometrics*. (1988) 44:837–45. doi: 10.2307/2531595

37. Heuchan AM, Evans N, Smart DH, Simpson JM. Perinatal risk factors for major intraventricular haemorrhage in the Australian and New Zealand neonatal network, 1995–97. *Arch Dis Child Fetal Neonatal Ed*. (2002) 86:86F–890F. doi: 10.1136/fn.86.2.f86

38. Farag MM, Gouda MH, Almohsen AM, Khalifa MA. Intraventricular hemorrhage prediction in premature neonates in the era of hemodynamics monitoring: a prospective cohort study. *Eur J Pediatr*. (2022) 181:4067–77. doi: 10.1007/s00431-022-04630-5

39. Zhang Y, Liu D, Mao Y, Gao Q, Xiong T. Cerebral near-infrared spectroscopy monitoring to predict periventricular-intraventricular haemorrhage and neurodevelopmental outcomes in preterm infants: a protocol for a systematic review and meta-analysis. *BMJ Paediatr Open*. (2023) 7:e001859–5. doi: 10.1136/bmjpo-2023-001859

40. Kehrer M, Blumenstock G, Ehehalt S, Goelz R, Poets C, Schöning M. Development of cerebral blood flow volume in preterm neonates during the first two weeks of life. *Pediatr Res*. (2005) 58:927–30. doi: 10.1203/01.PDR.0000182579.52820.C3

41. Variane GF, Camargo JP, Rodrigues DP, Magalhães M, Mimica MJ. Current status and future directions of neuromonitoring with emerging technologies in neonatal care. *Front Pediatr*. (2022) 9:755144. doi: 10.3389/fped.2021.755144

frontiers | Frontiers in Pediatrics

TYPE Original Research
PUBLISHED 20 November 2024
DOI 10.3389/fped.2024.1471080

Check for updates

OPEN ACCESS

EDITED BY
Sahar Ahmad,
University of North Carolina at Chapel Hill,
United States

REVIEWED BY
Alena Uus,
King's College London, United Kingdom
Samson Nivins,
Karolinska Institutet (KI), Sweden

*CORRESPONDENCE
Paolo Brambilla
✉ paolo.brambilla1@unimi.it

RECEIVED 26 July 2024
ACCEPTED 30 October 2024
PUBLISHED 20 November 2024

CITATION
Ciceri T, Squarcina L, Bertoldo A, Brambilla P, Melzi S and Peruzzo D (2024) Fetal gestational age prediction via shape descriptors of cortical development.
Front. Pediatr. 12:1471080.
doi: 10.3389/fped.2024.1471080

Fetal gestational age prediction via shape descriptors of cortical development

Tommaso Ciceri[1,2], Letizia Squarcina[3], Alessandra Bertoldo[2,4], Paolo Brambilla[3,5]*, Simone Melzi[6] and Denis Peruzzo[1]

[1]NeuroImaging Lab, Scientific Institute IRCCS Eugenio Medea, Bosisio Parini, Italy, [2]Department of Information Engineering, University of Padua, Padua, Italy, [3]Department of Pathophysiology and Transplantation, University of Milan, Milan, Italy, [4]Neuroscience Center, University of Padua, Padua, Italy, [5]Department of Neurosciences and Mental Health, Fondazione IRCCS Ca' Granda Ospedale Maggiore Policlinico, Milan, Italy, [6]Department of Informatics, Systems and Communication (DISCo), University of Milano-Bicocca, Milan, Italy

Introduction: Gyrification is the intricate process through which the mammalian cerebral cortex develops its characteristic pattern of sulci and gyri. Monitoring gyrification provides valuable insights into brain development and identifies potential abnormalities at an early stage. This study analyzes the cortical structure in neurotypical and pathological (spina bifida) fetuses using various shape descriptors to shed light on the gyrification process during pregnancy.
Methods: We compare morphometric properties encoded by commonly used scalar point-wise curvature-based signatures—such as mean curvature (H), Gaussian curvature (K), shape index (SI), and curvedness (C)—with multidimensional point-wise shape signatures, including spectral geometry processing methods like the Heat Kernel Signature (HKS) and Wave Kernel Signature (WKS), as well as the Signature of Histograms of Orientations (SHOT), which combines histogram and signature techniques. These latter signatures originate from computer graphics techniques and are rarely applied in the medical field. We propose a novel technique to derive a global descriptor from a given point-wise signature, obtaining GHKS, GWKS, and GSHOT. The extracted signatures are then evaluated using Support Vector Regression (SVR)-based algorithms to predict fetal gestational age (GA).
Results: GSHOT better encodes the GA to other global multidimensional point-wise shape signatures (GHKS, GWKS) and commonly used scalar point-wise curvature-based signatures (C, H, K, SI, FI), achieving a prediction R^2 of 0.89 and a mean absolute error of 6 days in neurotypical fetuses, and a R^2 of 0.64 and a mean absolute error of 10 days in pathological fetuses.
Conclusion: GSHOT provides researchers with an advanced tool to capture more nuanced aspects of fetal brain development and, specifically, of the gyrification process.

KEYWORDS

fetal brain, gestational age prediction, shape descriptors, cortical surface, MRI

Abbreviations
MRI, magnetic resonance imaging; GA, gestational age; HKS, Heat Kernel Signature; WKS, Wave Kernel Signature; SHOT, Signature of Histograms of OrienTations; H, mean curvature; K, Gaussian curvature; SI, shape index; FI, folding index; C, curvedness; SVR, Support Vector Regression; T2w, T2-weighted; PCA, Principal Component Analysis.

1 Introduction

Magnetic resonance imaging (MRI) has become a pivotal tool for the study of brain morphology and understanding structural alterations associated with various pathological conditions. Various geometric quantities can be exploited to summarize the morphometric information, providing valuable insights into population-based studies, contributing to our understanding of brain-related disorders, and paving the way for more personalized approaches to diagnosis and treatment. Advanced shape analysis techniques allow us to explore new dimensions of brain morphology beyond traditional measures (e.g., brain volumes and surface areas). Some of these techniques utilize spectral (1) and local extrinsic geometric (2) properties to gain deeper insights into brain shape characteristics. Spectral shape analysis techniques involve analyzing the shape of an object based on its spectral properties, and this is typically accomplished by encoding the shape through a differential operator and computing its eigendecomposition. On the other hand, local geometric properties focus on analyzing the shape at a more localized and detailed level, typically involving specific quantities such as curvature, surface normals, or deformations at specific points or regions of the shape. In this fashion, shapes can be compared by measuring similarities between these features. Thus, the efficacy of shape descriptors can be assessed in terms of discriminativeness and robustness against shape variations due to noise or deformations (3).

In this work, we analyze the fetal brain cortical structure using different shape descriptors to enhance our comprehension of the fetal brain gyrification process, i.e., the formation of gyri and sulci. The gyrification process plays a crucial role in brain development, contributing significantly to overall growth, organization, and functionality. Just like fetal ultrasound provides an estimate of gestational age (GA) by measuring basic morphometric features (such as skull size or femur length), tools linking brain morphological MR images to the central nervous system development can be a valuable resource for monitoring pregnancy and detecting fetal diseases in their initial stages. Here, we estimate the fetus GA in weeks, comparing the cortical structure morphometric properties encoded with the commonly used scalar point-wise curvature-based descriptors to those derived via multidimensional point-wise shape signatures which are widely used in computer graphics analysis. We examine several scalar point-wise signatures based on curvature: mean curvature (H), which measures extrinsic curvature or folding; Gaussian curvature (K), which measures intrinsic curvature or distortion; shape index (SI) and folding index (FI), indicators of shape and folding patterns (4). Moreover, we consider the curvedness (C), a signature incorporating information from both H and K, a valuable measure of the gyrification process (5, 6). On the other hand, we examine three different multidimensional point-wise shape signatures that are rarely applied in the medical field: the Heat Kernel Signature [HKS, (7)], the Wave Kernel Signature [WKS, (8)], and the Signature of Histograms of OrienTations [SHOT, (2)]. HKS is derived from the heat equation, a partial differential equation that describes the heat diffusion across the surface over time. Similarly, WKS is derived from the solution of another partial differential equation, the wave equation, which describes the evolution of waves across the surface over time. SHOT is computed by dividing the neighborhood around each point into multiple cells and calculating histograms of relative orientations of the normals in each cell. These histograms are then concatenated to obtain the final signature, which results in a compact representation of the local geometric properties of the shape. In the last years, several studies have been proposed to analyze fetal brain gyrification by extracting cortical surface morphometric properties. In this context, scalar point-wise curvature-based measures are the gold standard for assessment of neurodevelopment (5, 6, 9–14). Other novel techniques based on sulcal pattern analysis can be employed to observe geometric and topological patterning of early sulcal folds, including 3D positions, sulcal basin surface area, and depth (4, 15–17).

Furthermore, we define a novel procedure to extract a global encoding framework from these multidimensional point-wise shape signatures, leading to their global version. We namely refer to the global descriptors produced through our pipeline as Global plus the name of the input pointwise descriptor we use, Global Heat Kernel Signature (GHKS), Global Wave Kernel Signature (GWKS), and Global Signature of Histograms of OrienTations (GSHOT). The global descriptor has several excellent advantages such as it allows for shape comparisons using minimal shape preprocessing, it is robust to noise since it implicitly employs surface smoothing by neglecting higher frequencies of the shape, and finally, it encodes isometric invariance properties of the shape, which are crucial to deal with shape deformations.

We tested our *descriptors* in the context of the fetal brain gyrification process. A linear Support Vector Regression (SVR)-based approach (18) was employed to predict the fetus GA from the cortical structure morphometric properties encoded by descriptors. Experiments on a public dataset of 80 fetuses ($n = 31$ neurotypical and $n = 49$ pathological (19), and two public atlases of 18 and 16 fetuses (20, 21) showed promising prediction results in distinguishing the fetal brain gyrification process.

2 Methods

The proposed approach comprises five main steps: data gathering, cortical structure reconstruction, computation of shape descriptors, and GA prediction.

2.1 Data

We included data from different sources in this study. In particular, we used two publicly available fetal brain atlases (20, 21) and one publicly available fetal brain dataset (19). For each source, we used all the provided data without assessing the quality of the fetal brain high-resolution reconstruction and tissue segmentation. A brain atlas is a digital representation of

TABLE 1 Summary of the publicly available fetal brain MRI atlases and dataset used in our study.

Data	MRI contrast	Tissue labels	GA range	Cohort	Public link
CRL atlas	T2w	124	21–38 weeks	18	http://crl.med.harvard.edu/research/fetal_brain_atlas
dHCP fetal atlas	T2w	19	21–36 weeks	16	https://gin.g-node.org/kcl_cdb/fetal_brain_mri_atlas
FeTA dataset	T2w	7	20–35 weeks	80 (31 neurotypical 49 pathological)	https://www.synapse.org/#!Synapse:syn25649159/wiki/610007

the human brain population, which highlights common structural features and provides a reference point for researchers and clinicians to compare and analyze specific brain regions. On the other hand, a brain dataset refers to a collection of brain images of real fetuses, thus characterized by unique variations.

The fetal brain atlas introduced by Gholipour et al. (20) (hereafter, "CRL atlas") is defined at the GA range of 21–38 weeks. It consists of an age-specific T2-weighted (T2w) template and label images of 124 brain tissues, including gray matter (GM) and white matter (WM). The fetal brain atlas introduced by Uus et al. (21) (hereafter, "dHCP fetal atlas") is defined at 21–36 weeks. It includes age-specific T2w templates and 19 brain tissue labels, separate for each hemisphere.

On the other hand, the fetal brain dataset introduced initially by Payette et al. (22) and later updated (19) (hereafter, "FeTA dataset") consists of MRI-reconstructed images of 80 fetuses ($n = 49$ pathological and $n = 31$ neurotypical) defined in the GA range of 20–35 weeks. Each subject was released with a T2w template brain reconstruction (reconstructed with either NiftyMIC[1], MIALSRTK[2], or Simple IRTK[3]) with the corresponding seven brain tissue label images. Pathological subjects included fetuses with spina bifida either before or after fetal spinal lesion repair surgery, as these were the only publicly available pathological datasets (23). A summary of the available cohort of fetuses is reported in Table 1.

2.2 Cortical structure reconstruction

Our study focused on the cortical structure of the fetal brain, which is defined as the external layer of the parenchymal tissue and will become the cortical GM in the mature brain (Figure 1). During embryonic development, the brain is surrounded by a thin layer (darker than other tissues in the T2w images) called the cortical plate (CP). In the beginning, the CP is a flat and smoothed structure; as the brain grows and enlarges, it thickens and differentiates into different cortical layers. Visually, this results in folds, or gyri, and grooves, or sulci, that give the brain its characteristic wrinkled appearance. By the end of fetal development, the differentiated CP becomes the outermost layer of the brain, known as the cortical GM.

The CP folding process can be monitored using its boundary surfaces, i.e., the external and internal surfaces. The external surface separates the parenchyma from the cerebrospinal fluid. On the other hand, the inner surface divides the CP and the WM structure. We decided to focus on the inner cortical surface since the interface between WM and cortex is more stable and less prone to segmentation errors due to partial volume effects than the cortex-cerebrospinal fluid interface (15).

For each data set, we generated the inner cortical volume by merging the already validated tissue segmentation labels, which encompass the WM to the inner structures of the brain. Although the different datasets were generated using different segmentation protocols (19–21), they all include the inner cortical surface as boundary between structures, enabling consistent identification in each dataset used. Consequently, the volume obtained for each fetus was binarized and underwent manual refinement to remove any erroneous segmented components (i.e., voxel connected to the main WM mask by a single vertex). Subsequently, we extracted (MATLAB *isosurface* function) a triangular mesh representing the boundary of the binary image, i.e., the inner surface of the CP. Furthermore, we employed Freesurfer (surfer.nmr.mgh.harvard.edu) to geometrically smooth the resulting mesh, removing noise and minor geometric alterations. Figure 2 shows an example of the fetal brain's inner cortical surfaces across different gestational weeks.

2.3 Shape descriptors

To capture the most informative intrinsic geometric properties of the inner cortical surface shape, we computed both scalar point-wise curvature-based signatures (C, H, K, SI, FI) and multidimensional point-wise shape signatures (HKS, WKS, SHOT).

Scalar point-wise curvature-based signatures are computed for each vertex of the surface mesh using the FreeSurfer function *mris_curvature_stats* (10). Subsequently, we derived a global description of the derived signature by computing the frequency over a 100 bins discretization (MATLAB *histcounts* function), and we normalized the derived distribution for the number of associated vertices, which is an intrinsic characteristic of each fetus (24).

Multidimensional point-wise shape signatures are computed accordingly. In detail, the HKS and WKS descriptors are implemented with an in-house MATLAB code. Here, we used k

---

[1] https://github.com/gift-surg/NiftyMIC

[2] https://github.com/Medical-Image-Analysis-Laboratory/mialsuperresolutiontoolkit

[3] https://gitlab.com/mariadeprez/irtk-simple

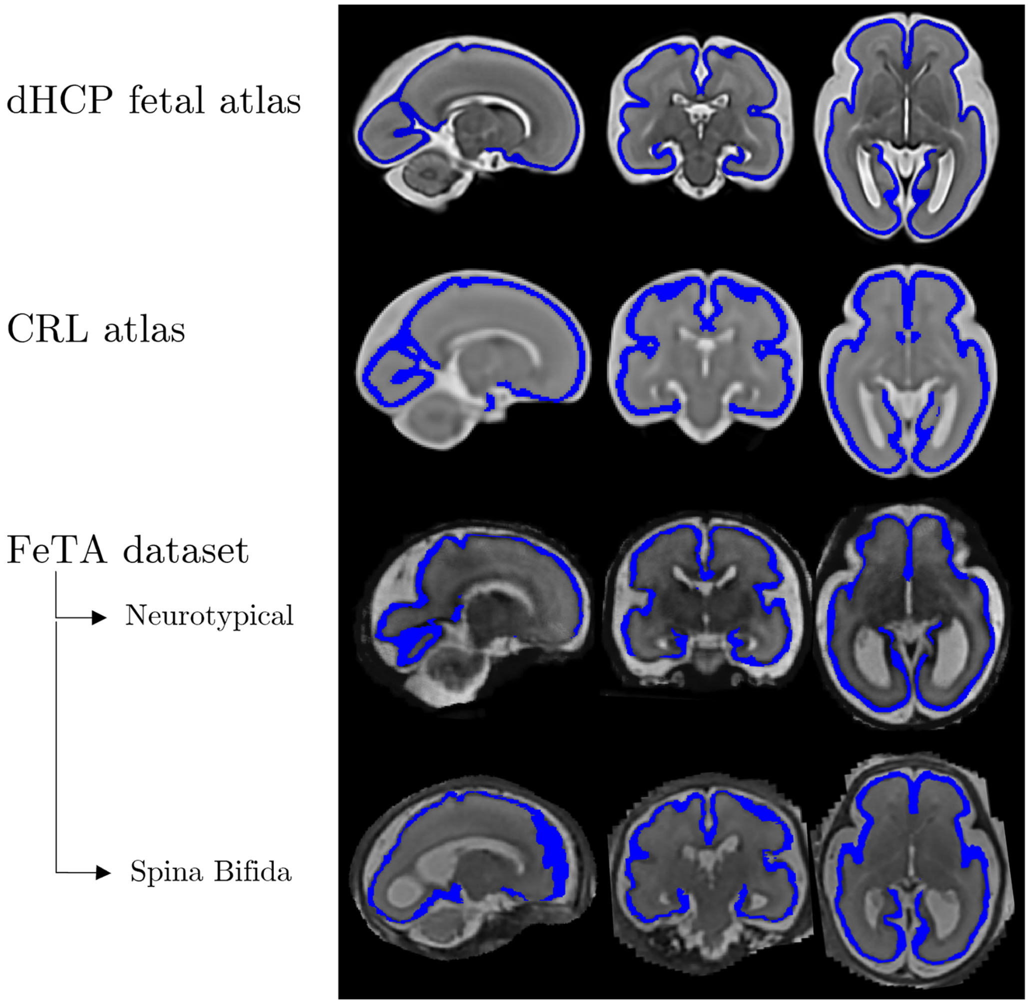

FIGURE 1
Examples of brain images and corresponding cortical plate segmentations in various atlases (20, 21) and datasets (19) for a 28-week gestational age fetus. Structural anatomical (grayscale) and cortical plate segmentation (blue) overlaid. From left to right, the fetal brains are displayed in three different orientations - sagittal, coronal, and axial.

= 100 eigenvalues and scaled the temporal domain logarithmically in $n = 10$ time values, as suggested by Sun et al. (7). On the other hand, the SHOT descriptor is implemented in Pyshot, a Python library publicly available on GitHub (https://github.com/uhlmanngroup/pyshot). As for the point-wise curvature-based signatures, we derived a global description from HKS, WKS, and SHOT features, computing their distribution on a 100 bins discretization, and we normalized the derived distribution for the number of associated vertices. Finally, we concatenated the obtained distributions for each time point to derive its global signature similar to what was proposed in (3). A schematic example of the proposed global HKS is presented in Figure 3. This schema is adopted for each multidimensional signature investigated to obtain its global version.

To aid in the data visualization of the signatures extracted by each descriptor, we performed a Principal Component Analysis (PCA). We derived a 2D scatter plot representing each descriptor's first and second principal components. These components contain the most relevant variations shown in the dataset, proving its capability to encode the changes in shape.

2.4 Gestational age prediction

We implemented a ML experiment to investigate whether and which derived signatures include the information associated with CP development, and if they can be used to predict a subject's GA.

We used a SVR algorithm to predict the GA in weeks for each image sample from the features extracted with the shape descriptor from the inner cortical surface mesh. SVR is one of the most powerful supervised machine learning approaches used for regression tasks (25), which aims to find a hyperplane maximizing the margin while minimizing errors in a high-dimensional feature space. It is an extension of the support vector machine classification algorithm but it predicts continuous output values instead of class labels. In the present study, only

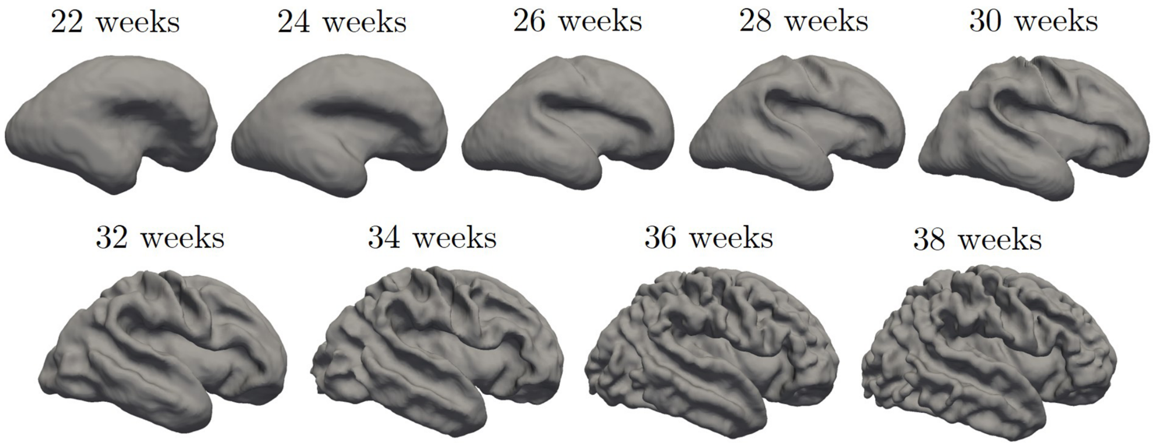

FIGURE 2
Inner cortical surface of the fetal brain from 28 to 38 gestational weeks. The surfaces depicted in the figure are generated from the previously quoted Gholipour et al. (20) atlas.

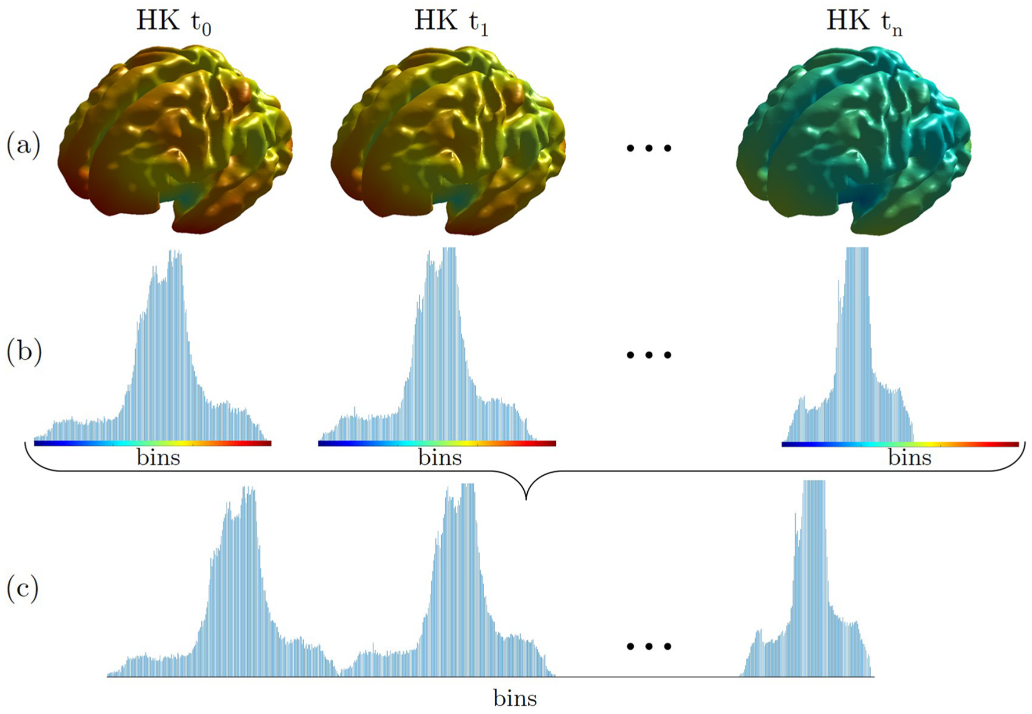

FIGURE 3
An example of a global descriptor construction for the HKS signature (GHKS). **(a)** Each point of the inner cortical shape of the brain is colored according to the heat kernel (HK) value at time t_i. **(b)** These values are then gathered into histograms for each scale t_i. **(c)** The histograms are concatenated, leading to the global signature. The brain's surfaces shown in the figure are generated from a 33-week fetus of the previously quoted Gholipour et al. (20) atlas.

linear kernels were employed since nonlinear methods may require sample sizes that are too large to generalize well (26). Furthermore, we decided to use the z-score method to normalize the data, estimating the mean and the standard deviation on the training set and applying them to normalize the test set. We trained each SVR model on the signatures extracted from the atlases (20, 21) and tested it on the signatures extracted from the FeTA dataset (19). We evaluated the goodness-of-fit of the SVR models by measuring the mean absolute error (MAE), the root mean square error (RMSE), which is more sensitive to outliers than MAE, and the coefficient of determination (R^2), which denotes the amount of variation in potential new observations. The concordance between predicted and true GA was determined using Lin's concordance correlation coefficient, with strength of agreement assessed by McBride's criteria as follows: poor, <0.90; moderate, 0.90–0.95; substantial, 0.95–0.99; almost perfect >0.99 (27, 28).

3 Results

The proposed GA prediction method was employed for the characterization of the fetal brain gyrification process occuring during pregnancy. A dataset of 114 images ($n = 31$ neurotypical and $n = 49$ pathological from public dataset, and $n = 34$ neurotypical from online available atlases) has been evaluated. After the surface construction, the scalar point-wise curvature-based signatures (C, H, K, SI, FI) and the global multidimensional point-wise shape signatures (GHKS, GWKS, and GSHOT) were computed and normalized by the z-score technique. The GA prediction procedure is employed as described in Section 2.4. Notably, each linear-based kernel SVR algorithm was trained on the shape signatures extracted from the inner cortical surface of fetuses included in atlases (20, 21) and tested on the fetuses included in the public dataset (19), differentiating between neurotypical and pathological fetuses. Table 2 shows the performance of the individual SVR models in predicting GA for neurotypical fetuses. GSHOT outperforms other shape descriptors, both the scalar point-wise curvature-based signatures and the global multidimensional point-wise shape signatures, achieving a prediction R^2 of 0.89 and a corresponding MAE of 6.3 days. FI is the best scalar point-wise curvature-based descriptor, achieving prediction performance comparable to GSHOT. Notably, it achieved a prediction R^2 of 0.75 and a MAE of 9.9 days. According to Lin's concordance correlation coefficient, the GSHOT model demonstrated *substantial* agreement between descriptor-based GA predictions and GA ground truths (ρc = 0.95, 95% CI = 0.89–0.97), whereas the FI model showed *poor* agreement (ρc = 0.84, 95% CI = 0.72–0.91).

Table 3 shows the GA prediction performance of the considered individual SVR models tested on the pathological subset of the FeTA dataset. The results highlight a larger prediction error compared to the neurotypical subset of the FeTA dataset. Similarly, GSHOT outperforms other descriptors, achieving a prediction R^2 of 0.64 and a corresponding MAE of 10.1 days. However, the agreement between predictions and ground truths for this model was *poor* based on Lin's concordance correlation coefficient (ρc = 0.80, $^{95\%}$CI = 0.70–0.87).

In Figure 4, the GA prediction obtained with the best global multidimensional point-wise shape signature (GSHOT) and with the best scalar point-wise curvature-based signature (FI) is visualized in the true vs. predicted response plot (top row), and the prediction model is evaluated using the residual plot (bottom row). All the GSHOT points are close to the diagonal line, suggesting an excellent estimation of the SVR model. Moreover, the points of FI are more dispersed than those of GSHOT. Finally, the residuals obtained in the GA prediction from the pathological population are much larger than those obtained from the neurotypical population. An exhaustive visualization of the results obtained from each descriptor is reported in the Supplementary Figures S1, S2, which shows larger prediction errors and a similar trend for both neurotypical and pathological populations.

PCA analysis shows that shape descriptors codify the largest part of the relevant information about the inner surface of the CP in the first few components. Among all the shape descriptors, GSHOT and FI provide the best performances. Their combined first two components explain 98.8% of the variability in the FeTA neurotypical fetuses and more than 95% in the FeTA

TABLE 2 Gestational age prediction in neurotypical fetuses, expressed in weeks.

Performance metric [weeks]	Scalar point-wise curvature-based signatures					Global multidimensional point-wise shape signatures		
	C	H	K	SI	FI	GHKS	GWKS	GSHOT
RMSE	2.81	4.81	4.11	3.87	1.76	2.04	2.36	**1.18**
MAE	2.40	4.32	3.52	3.53	1.41	1.63	1.65	**0.91**
R^2	0.36	−0.86	−0.36	−0.20	0.75	0.67	0.55	**0.89**

The goodness-of-fit of the individual linear-SVR models is evaluated by measuring the mean absolute error (MAE), the root mean square error (RMSE), and the coefficient of determination (R^2). The scalar point-wise curvature-based signatures (C, H, K, SI, FI) and the global multidimensional point-wise shape signatures (GHKS, GWKS, GSHOT) are compared.
The best-performing metrics are shown in bold.

TABLE 3 Gestational age prediction in pathological (spina bifida) fetuses, expressed in weeks.

Performance metric [weeks]	Scalar point-wise curvature-based signatures					Global multidimensional point-wise shape signatures		
	C	H	K	SI	FI	GHKS	GWKS	GSHOT
RMSE	2.96	8.50	6.25	6.04	3.27	3.31	3.53	**1.87**
MAE	2.62	8.10	5.75	5.55	2.47	2.84	2.71	**1.44**
R^2	0.10	−6.46	−3.03	−2.77	−0.10	−0.13	−0.28	**0.64**

The goodness-of-fit of the individual linear-SVR models is evaluated by measuring the mean absolute error (MAE), the root mean square error (RMSE), and the coefficient of determination (R^2). The scalar point-wise curvature-based signatures (C, H, K, SI, FI) and the global multidimensional point-wise shape signatures (GHKS, GWKS, GSHOT) are compared.
The best-performing metrics are shown in bold.

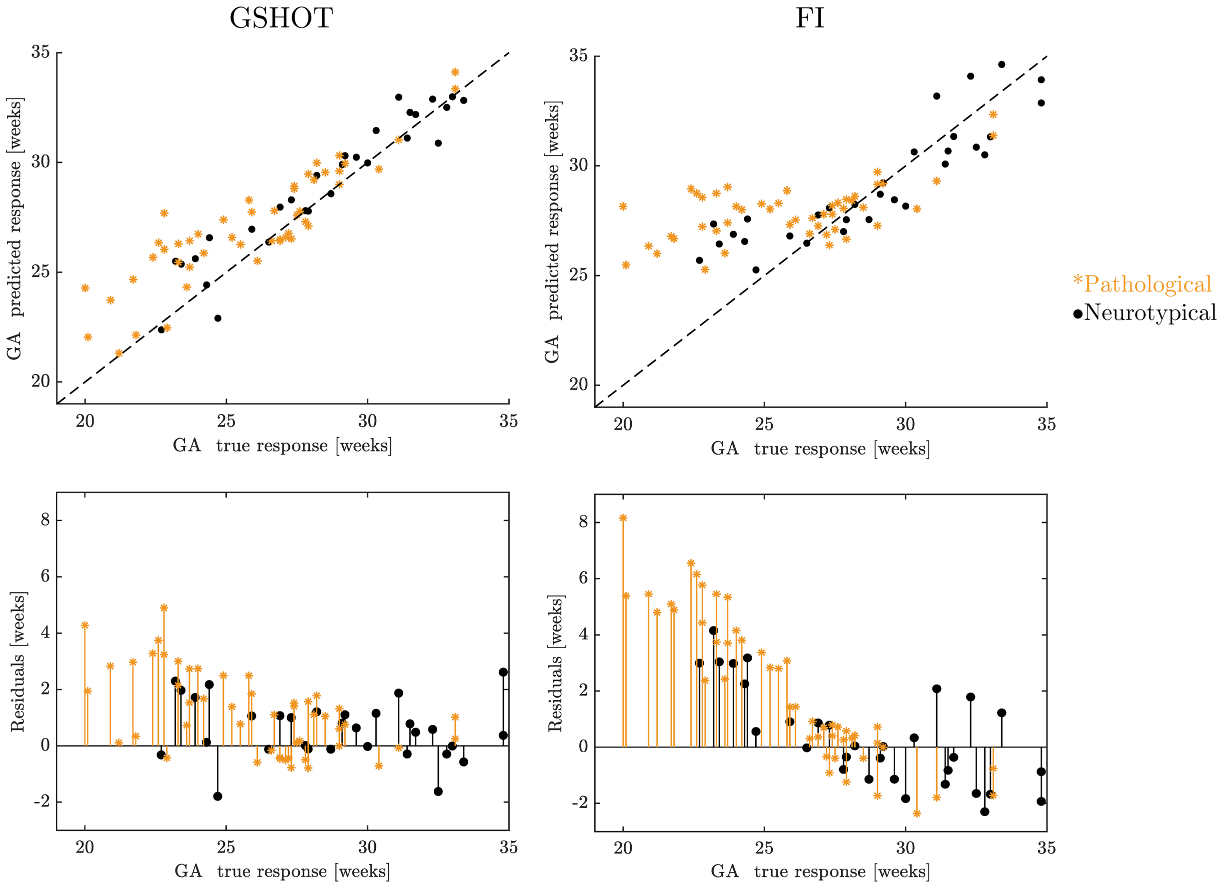

FIGURE 4
A visualization of the results in GA prediction using GSHOT and FI. The figure displays the true vs. predicted response plots at the top and the residual plots at the bottom. Black points represent neurotypical fetuses, while pathological (spina bifida) fetuses are described by blue stars. The FeTA dataset was used for GA prediction (19).

pathological fetuses (Supplementary Table S1). Figure 5 shows that GSHOT provides a clear graphical representation of the fetal evolution. The different GA samples are distributed in a distinct “U” shape, with an increase from right to left on the first component (x-axis). The GA ranges behave symmetrically on the second component (y-axis), growing downwards on the negative axis values and upwards on the positive axis values. This geometric behavior interpretation cannot be inferred from FI results as it revealed lower discretization ability.

The other descriptors have a graphical representation worse than FI (see Supplementary Figure S3).

4 Discussion

Gyrification in the human fetus occurs from the 10th gestational week and continues hierarchically almost up until the last weeks of pregnancy (29). During gyrification, the smooth surface of the fetal brain develops folds and wrinkles, increasing the surface area of the cerebral cortex. This folding is essential for accommodating the large number of cortical neurons and connections within the limited space of the skull. However, disruptions or abnormalities during this process can lead to cortical malformations such as lissencephaly [smooth brain, (30)], or polymicrogyria [excessive folding, (31)]. These malformations are associated with various neurological disorders and cognitive impairments. Therefore, understanding its construction mechanism is crucial for studying brain development, function, and disorders (32).

Here, we introduced novel multidimensional point-wise shape signatures (HKS, WKS, SHOT) to analyze the inner cortical surface development in the fetal brain by an innovative procedure. These signatures are a well-established method in computer graphics to analyze the geometry of an object based on its spectral properties. However, they have rarely been applied in the medical field due to the intricate nature of medical data, the heavy workload and professional expertise required, and the need for thorough validation and approval processes to comply with regulatory standards (3, 33). We compared the shape properties of the brain’s cortical structure extracted from multidimensional point-wise shape signatures with those obtained from scalar point-wise curvature-based signatures (C, H, K, SI, FI). The results obtained from the GA prediction through shape properties indicate that GSHOT is the most reliable shape descriptor. GSHOT accurately captures the morphological

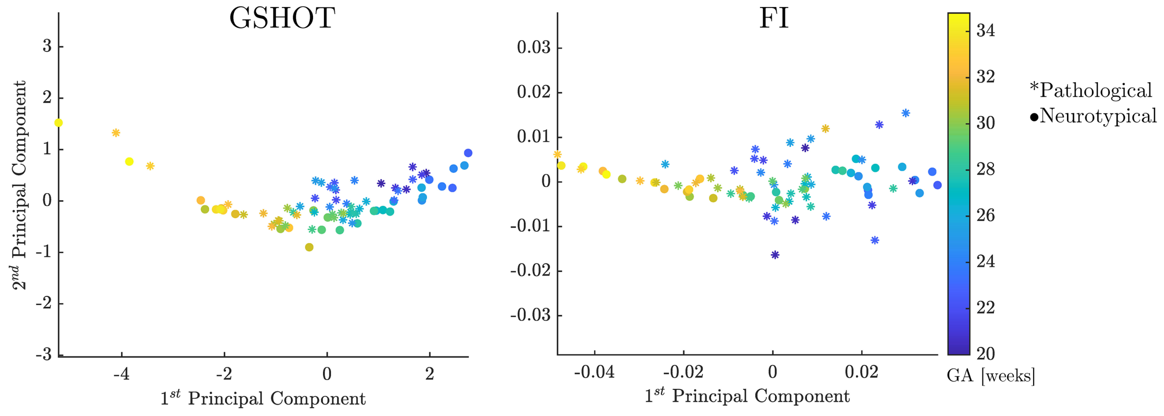

FIGURE 5
GSHOT and FI first and second principal components. Neurotypical fetuses are represented by points, while pathological (spina bifida) fetuses are represented by stars. The colorbar displays the color code used for the fetus GA ranges. These results are derived from Payette et al. (19) dataset.

changes during fetal neurodevelopment, with an estimated error of less than a week, outperforming all other descriptors investigated. Figure 4 shows that this error remains consistent during gestation. Furthermore, Figure 5 highlights that the first principal component explains a large portion (93.2%) of all variability, proving its capability to encode changes in morphological shape. Consequently, this principal component alone can be considered the best representative summary of the fetal gyrification process. The GA prediction in pathological subjects (i.e., fetuses with spina bifida) tends to be overestimated, particularly in the earlier gestational weeks where the fetuses have not yet undergone spinal lesion repair surgery. Therefore, the lack of cerebrospinal fluid circulation can lead to abnormal pressure dynamics in the brain. This, in turn, may result in more pronounced or abnormal cortical folding. The difference between the predicted GA and the actual GA can serve as an indicator of pathology, making it easier to understand compared to the output of geometric analysis. This approach is similar to clinical practices in ultrasound, where each biometric measurement of the fetal brain is compared to the physiological range associated with the specified GA to identify any discrepancies. We can state that the implemented linear-SVR method is reliable, independently of fetal brain reconstruction method used (NiftyMIC, MIALSRTK, or Simple IRTK) thanks to the inclusion of all reconstruction typologies in the dataset used for training.

This study presents some limitations. First, other measures related to cortical folding, such as the gyrification index (34) and sulcal depth, can be studied. Furthermore, given cortical folding alterations associated with several pathologies (e.g., ventriculomegaly), cortical thickness is another measure worth investigating, considering partial volume effects. Second, other regression models (e.g., relevance vector regression RVR and Gaussian process regression GPR) can be tested by applying different kernel functions (e.g., polynomial, radial basis) to achieve the highest prediction performances. Third, we identified a larger prediction error in the pathological subset of the FeTA dataset used as test set. Unfortunately, we were not able to establish if this was caused by the clinical condition or by a model error. On the other hand, spina bifida is characterized by several malformative aspects both in the neonatal and in fetal central nervous system, encompassing not only altered gyrifications, but also altered brain and infratentorial structures size, and corpus callosum hypoplasia or partial dysgenesis (35–37). It is therefore reasonable to assume that the implemented shape descriptors highlighted a different developmental pattern in the gyrification process, leading to an error in the estimated GA that can be used as an indicator of pathology. Future works will investigate the brain's structure surface development across its different regions by using GSHOT to uncover new insight into the neurodevelopment process. Moreover, the quality of the T2w brain reconstructions and relative tissue label maps were not investigated as it is out of the scope of this study and has been previously addressed (19–21).

5 Conclusion

In this work, global multidimensional point-wise shape signatures (GHKS, GWKS, and GSHOT) are exploited to improve the prediction of GA in neurotypical and pathological fetuses.

GSHOT outperforms other global multidimensional point-wise signatures and scalar point-wise curvature-based signatures (C, H, K, SI, FI), providing researchers with a more sophisticated tool to capture more nuanced aspects of shapes. This approach enhances the accuracy and effectiveness of shape analysis tasks such as classification, segmentation, or matching, potentially leading to new methods for early detection of fetal diseases. In addition, a novel exploration of the fetal brain based on this approach can potentially uncover new insight into the structures development of the brain.

Finally, this innovative procedure for extracting multidimensional global descriptors from a given point-wise signature can also be applied in different scenarios of shape analysis within computer graphics.

Data availability statement

Publicly available datasets were analyzed in this study. This data can be found here: http://crl.med.harvard.edu/research/fetal_brain_atlas; https://gin.g-node.org/kcl_cdb/fetal_brain_mri_atlas; https://www.synapse.org/#!Synapse:syn25649159/wiki/610007.

Author contributions

TC: Data curation, Formal Analysis, Methodology, Resources, Software, Validation, Visualization, Writing – original draft, Writing – review & editing. LS: Resources, Writing – review & editing. AB: Supervision, Writing – review & editing. PB: Funding acquisition, Project administration, Writing – review & editing. SM: Conceptualization, Funding acquisition, Resources, Supervision, Writing – review & editing. DP: Conceptualization, Funding acquisition, Resources, Supervision, Writing – review & editing.

Funding

The author(s) declare financial support was received for the research, authorship, and/or publication of this article. This work was partially supported by grants from the Italian Ministry of Health to Paolo Brambilla (RF-2019-12371349, “Ricerca corrente 2023” and “Ricerca corrente 2024”) and Denis Peruzzo (“Ricerca corrente 2023” and “Ricerca corrente 2024”), and by a grant from the Italian Ministry of University and Research to Simone Melzi (“Dipartimenti di Eccellenza 2023-2027”, Department of Informatics, Systems and Communication of the University of Milano-Bicocca).

Acknowledgments

We gratefully acknowledge the support of NVIDIA Corporation with the RTX A5000 GPUs granted to the University of Milano-Bicocca through the Academic Hardware Grant Program for the project “Learned representations for implicit binary operations on real-world 2D-3D data”.

Conflict of interest

The authors declare that the research was conducted in the absence of any commercial or financial relationships that could be construed as a potential conflict of interest.

Publisher’s note

Supplementary material

The Supplementary Material for this article can be found online at: https://www.frontiersin.org/articles/10.3389/fped.2024.1471080/full#supplementary-material

References

1. Lévy B, Zhang H. Spectral mesh processing. *ACM SIGGRAPH 2010 Courses* (2010). p. 1–312. doi: 10.1145/1837101.1837109

2. Salti S, Tombari F, Di Stefano L. SHOT: unique signatures of histograms for surface and texture description. *Comput Vis Image Underst.* (2014) 125:251–64. doi: 10.1016/j.cviu.2014.04.011

3. Castellani U, Mirtuono P, Murino V, Bellani M, Rambaldelli G, Tansella M, et al. A new shape diffusion descriptor for brain classification. *Med Image Comput Comput Assist Interv.* (2011) 14(Pt 2):426–33. doi: 10.1007/978-3-642-23629-7_52

4. Demirci N, Holland MA. Cortical thickness systematically varies with curvature and depth in healthy human brains. *Hum Brain Mapp.* (2022) 43(6):2064–84. doi: 10.1002/hbm.25776

5. Hu HH, Chen HY, Hung CI, Guo WY, Wu YT. Shape and curvedness analysis of brain morphology using human fetal magnetic resonance images in utero. *Brain Struct Funct.* (2013) 218(6):1451–62. doi: 10.1007/s00429-012-0469-3

6. Wu J, Awate SP, Licht DJ, Clouchoux C, du Plessis AJ, Avants BB, et al. Assessment of MRI-based automated fetal cerebral cortical folding measures in prediction of gestational age in the third trimester. *AJNR Am J Neuroradiol.* (2015) 36(7):1369–74. doi: 10.3174/ajnr.A4357

7. Sun J, Ovsjanikov M, Guibas L. A concise and provably informative multi-scale signature based on heat diffusion. *Comput Graph Forum.* (2009) 28(5):1383–92. doi: 10.1111/j.1467-8659.2009.01515.x

8. Aubry M, Schlickewei U, Cremers D. The wave kernel signature: a quantum mechanical approach to shape analysis. *2011 IEEE Iinternational Cconference on Ccomputer Vvision Wworkshops (ICCV Wworkshops).* IEEE (2011). p. 1626–33.

9. Batchelor PG, Castellano Smith AD, Hill DL, Hawkes DJ, Cox TC, Dean AF. Measures of folding applied to the development of the human fetal brain. *IEEE Trans Med Imaging.* (2002) 21(8):953–65. doi: 10.1109/TMI.2002.803108

10. Pienaar R, Fischl B, Caviness V, Makris N, Grant PE. A methodology for analyzing curvature in the developing brain from preterm to adult. *Int J Imaging Syst Technol.* (2008) 18(1):42–68. doi: 10.1002/ima.20138

11. Clouchoux C, Kudelski D, Gholipour A, Warfield SK, Viseur S, Bouyssi-Kobar M, et al. Quantitative *in vivo* MRI measurement of cortical development in the fetus. *Brain Struct Funct.* (2012) 217(1):127–39. doi: 10.1007/s00429-011-0325-x

12. Habas PA, Scott JA, Roosta A, Rajagopalan V, Kim K, Rousseau F, et al. Early folding patterns and asymmetries of the normal human brain detected from in utero MRI. *Cerebral Cortex.* (2012) 22(1):13–25. doi: 10.1093/cercor/bhr053

13. Shimony JS, Smyser CD, Wideman G, Alexopoulos D, Hill J, Harwell J, et al. Comparison of cortical folding measures for evaluation of developing human brain. *NeuroImage.* (2016) 125:780–90. doi: 10.1016/j.neuroimage.2015.11.001

14. Tarui T, Im K, Madan N, Madankumar R, Skotko BG, Schwartz A, et al. Quantitative MRI analyses of regional brain growth in living fetuses with down syndrome. *Cerebral Cortex.* (2020) 30(1):382–90. doi: 10.1093/cercor/bhz094

15. Benkarim OM, Hahner N, Piella G, Gratacos E, González Ballester MA, Eixarch E, et al. Cortical folding alterations in fetuses with isolated non-severe ventriculomegaly. *NeuroImage Clin.* (2018) 18:103–14. doi: 10.1016/j.nicl.2018.01.006

16. Tarui T, Madan N, Farhat N, Kitano R, Ceren Tanritanir A, Graham G, et al. Disorganized patterns of sulcal position in fetal brains with agenesis of corpus Callosum. *Cerebral Cortex.* (2018) 28(9):3192–203. doi: 10.1093/cercor/bhx191

17. Tarui T, Madan N, Graham G, Kitano R, Akiyama S, Takeoka E, et al. Comprehensive quantitative analyses of fetal magnetic resonance imaging in isolated cerebral ventriculomegaly. *NeuroImage Clin*. (2023) 37:103357. doi: 10.1016/j.nicl.2023.103357

18. Drucker H, Burges CJ, Kaufman L, Smola A, Vapnik V. Support vector regression machines. Advances in neural information processing systems 9 (1996).

19. Payette K, Li HB, de Dumast P, Licandro R, Ji H, Siddiquee MMR, et al. Fetal brain tissue annotation and segmentation challenge results. *Med Image Anal*. (2023) 88:102833. Advance online publication. doi: 10.1016/j.media.2023.102833

20. Gholipour A, Rollins CK, Velasco-Annis C, Ouaalam A, Akhondi-Asl A, Afacan O, et al. A normative spatiotemporal MRI atlas of the fetal brain for automatic segmentation and analysis of early brain growth. *Sci Rep*. (2017) 7(1):476. doi: 10.1038/s41598-017-00525-w

21. Uus A, Kyriakopoulou V, Cordero Grande L, Christiaens D, Pietsch M, Price A, et al. Multi-channel spatio-temporal MRI atlas of the normal fetal brain development from the developing human connectome project. *G-Node*. (2023). doi: 10.12751/g-node.ysgsy1

22. Payette K, de Dumast P, Kebiri H, Ezhov I, Paetzold JC, Shit S, et al. An automatic multi-tissue human fetal brain segmentation benchmark using the fetal tissue annotation dataset. *Sci Data*. (2021) 8(1):167. doi: 10.1038/s41597-021-00946-3

23. Ciceri T, Casartelli L, Montano F, Conte S, Squarcina L, Bertoldo A, et al. Fetal brain MRI atlases and datasets: a review. *NeuroImage*. (2024) 292:120603. doi: 10.1016/j.neuroimage.2024.120603

24. Rodriguez-Carranza CE, Mukherjee P, Vigneron D, Barkovich J, Studholme C. A framework for *in vivo* quantification of regional brain folding in premature neonates. *NeuroImage*. (2008) 41(2):462–78. doi: 10.1016/j.neuroimage.2008.01.008

25. Zhou W, Yan Z, Zhang L. A comparative study of 11 non-linear regression models highlighting autoencoder, DBN, and SVR, enhanced by SHAP importance analysis in soybean branching prediction. *Sci Rep*. (2024) 14(1):5905. doi: 10.1038/s41598-024-55243-x

26. Rasmussen PM, Madsen KH, Lund TE, Hansen LK. Visualization of nonlinear kernel models in neuroimaging by sensitivity maps. *NeuroImage*. (2011) 55(3):1120–31. doi: 10.1016/j.neuroimage.2010.12.035

27. Lawrence I, Lin K. A concordance correlation coefficient to evaluate reproducibility. *Biometrics*. (1989) 45(1):255–68. doi: 10.2307/2532051

28. McBride GB. (2005). NIWA client report: HAM2005-062, 45, 307-310. *A proposal for strength-of-agreement criteria for Lin's concordance correlation coefficient*.

29. Rajagopalan V, Scott J, Habas PA, Kim K, Corbett-Detig J, Rousseau F, et al. Local tissue growth patterns underlying normal fetal human brain gyrification quantified in utero. *J Neurosci*. (2011) 31(8):2878–87. doi: 10.1523/JNEUROSCI.5458-10.2011

30. Mochida GH. Genetics and biology of microcephaly and lissencephaly. *Semin Pediatr Neurol*. (2009) 16(3):120–6. doi: 10.1016/j.spen.2009.07.001

31. Squier W, Jansen A. Polymicrogyria: pathology, fetal origins and mechanisms. *Acta Neuropathol Commun*. (2014) 2:80. doi: 10.1186/s40478-014-0080-3

32. Fernández V, Llinares-Benadero C, Borrell V. Cerebral cortex expansion and folding: what have we learned? *EMBO J*. (2016) 35(10):1021–44. doi: 10.15252/embj.201593701

33. Dahdouh S, Limperopoulos C. Unsupervised fetal cortical surface parcellation. *Proc SPIE Int Soc Opt Eng*. (2016) 9784:97840J. doi: 10.1117/12.2212805

34. Zilles K, Armstrong E, Schleicher A, Kretschmann HJ. The human pattern of gyrification in the cerebral cortex. *Anat Embryol*. (1988) 179(2):173–9. doi: 10.1007/BF00304699

35. Mufti N, Aertsen M, Ebner M, Fidon L, Patel P, Rahman MBA, et al. Cortical spectral matching and shape and volume analysis of the fetal brain pre- and post-fetal surgery for spina bifida: a retrospective study. *Neuroradiology*. (2021) 63(10):1721–34. doi: 10.1007/s00234-021-02725-8

36. Mufti N, Sacco A, Aertsen M, Ushakov F, Ourselin S, Thomson D, et al. What brain abnormalities can magnetic resonance imaging detect in foetal and early neonatal spina bifida: a systematic review. *Neuroradiology*. (2022) 64(2):233–45. doi: 10.1007/s00234-021-02853-1

37. Mufti N, Chappell J, Aertsen M, Ebner M, Fidon L, Deprest J, et al. Assessment of longitudinal brain development using super-resolution magnetic resonance imaging following fetal surgery for open spina bifida. *Ultrasound Obstet Gynecol*. (2023) 62(5):707–20. doi: 10.1002/uog.26244

frontiers | Frontiers in Pediatrics

TYPE Case Report
PUBLISHED 27 February 2025
DOI 10.3389/fped.2025.1463314

OPEN ACCESS

EDITED BY
Ye Wu,
Nanjing University of Science and Technology, China

REVIEWED BY
Cristine Sortica da Costa,
Great Ormond Street Hospital for Children NHS Foundation Trust, United Kingdom
Yiang Pan,
Zhejiang University of Technology, China

*CORRESPONDENCE
Hemmen Sabir
✉ hemmen.sabir@ukbonn.de

RECEIVED 11 July 2024
ACCEPTED 13 February 2025
PUBLISHED 27 February 2025

CITATION
Groteklaes A, Dresbach T, Born M, Mueller A and Sabir H (2025) Case Report: Ultralow-field portable MRI improves the diagnosis of congenital hydrocephalus.
Front. Pediatr. 13:1463314.
doi: 10.3389/fped.2025.1463314

Case Report: Ultralow-field portable MRI improves the diagnosis of congenital hydrocephalus

Anne Groteklaes[1], Till Dresbach[1], Markus Born[2], Andreas Mueller[1] and Hemmen Sabir[1]*

[1]Department of Neonatology and Pediatric Intensive Care, Children's Hospital, University Hospital Bonn, Bonn, Germany, [2]Division of Pediatric Radiology, Department of Radiology, University Hospital Bonn, Bonn, Germany

Introduction: Congenital hydrocephalus is an increasing condition both in high as in low and middle income countries. Main causes include aqueductal stenosis, neonatal central nervous system infections, intracranial hemorrhage, malformations and tumors. Investigation of its etiology should include magnetic resonance imaging (MRI) to detect especially pathologies of the fossa cranii posterior. However, MRI is not available to every infant presenting with congenital hydrocephalus especially in those countries with the highest prevalence. New portable ultralow-field MRI (ULF) allows low resource and bedside imaging and thus widens the access to MRI for those infants. This study presents two cases of newborns with congenital hydrocephalus who underwent ULF scanning revealing a tumor of the fossa cranii posterior as cause of hydrocephalus. This study shows that ULF scanning allows to detect and characterize brain tumors as well as metastases.

Setting and patients: In this case report, we present two cases of newborns antenatally diagnosed with hydrocephalus with no further pathology detected in repeated cranial ultrasound and, in one case, fetal MRI. We performed ULF imaging using a portable 0.064T MRI during natural sleep and high-field 3T MRI to investigate the etiology of congenital hydrocephalus in these infants.

Main results: ULF imaging revealed a tumor of the fossa cranii posterior in both cases. MRI signalling detected in ULF imaging was specific for each tumor (ATRT, low grade glioma). In one case, ULF imaging also detected intracerebral metastasis.

Conclusions: We demonstrated that ULF imaging is able to detect tumors of the fossa cranii posterior that are not detected on ultrasound and shows their specific MR-signalling as well as detect metastasis. Additionally, compared to 3T MRI, ULF MRI was able to reveal significant findings while requiring fewer resources and being easier to perform. Therefore, we propose that children with congenital hydrocephalus not showing any abnormalities on cranial ultrasound should undergo ULF MRI. This imaging modality holds potential for monitoring neonatal tumors and detecting metastasis.

KEYWORDS
newborn, low-field portable MRI, tumor, hydrocephalus, aqueductal stenosis, metastasis, point-of-care

1 Introduction

Congenital hydrocephalus is the most common indication for neurosurgical interventions in neonates. Its incidence has significantly increased in low- and middle-income countries (LMIC), with an incidence of 123/100.000 live births (1–4). The most common causes of congenital hydrocephalus are aqueductal stenosis, neonatal central nervous system infections, intracranial hemorrhage, and malformations, such as neural tube defects or tumors (5). Fetal ventriculomegaly is one of the most commonly diagnosed abnormalities in prenatal ultrasound scanning (1–2/1,000 live births) (6).

While fetal ventriculomegaly is usually diagnosed with ultrasound, this technology has several limitations, as it is operator-dependent and the ability to penetrate the fetal calvarium is limited. In particular, pathologies in the fossa cranii posterior are often missed when performing only ultrasound imaging. Magnetic resonance imaging (MRI) can detect additional anomalies such as cerebellar tumors, anatomic abnormalities, cysts, and hemorrhages in 20%–50% of the cases with no additional findings on ultrasound, especially in corpus callosum pathologies, hemorrhage, folding abnormalities, and other brain abnormalities (7–9). However, not every infant presenting with congenital hydrocephalus receives MR-imaging, and especially in countries with the highest prevalence (LMIC), these resources are very limited (10–12). The reason for this is the high resource requirement characterized by high costs and the need for technical, spatial and personnel infrastructure such as reliable-continuous high-power electricity supply, liquid helium which maintains the superconductivity of the magnet, electromagnetic shielding, and a large fringe field safety exclusion radius (13).

Ultralow-field portable MR Imaging (ULF) is a new imaging tool that allows low-resource and bedside imaging. The portable 0.064-T MRI device currently available (Hyperfine, Gulford, CT) has a magnetic field formed by two horizontally oriented permanent magnets, while the receiver coil and radiofrequency transmit coils are on a platform inside the gantry (14). ULF imaging requires fewer resources owing to its lower cost and lower personnel and infrastructure requirements. Moreover, it reduces the risks, as patients do not need to be transported or sedated for imaging (15, 16). ULF MR-devices have already been trialed in both adult and pediatric settings (15–18, 19–21). Thus, ULF provides a new opportunity to provide MRI to infants with congenital hydrocephalus who would not otherwise receive an MRI, both in LMIC (due to limited resources) as well as in high-income countries, as not every infant presenting with congenital hydrocephalus receives an MRI (9).

Herein, we present two cases of newborns antenatally diagnosed with fetal hydrocephalus due to presumed aqueductal stenosis. As no other pathologies were found on initial postnatal cranial ultrasounds, both infants underwent ULF imaging to detect a possible cause of the hydrocephalus. In both infants, a tumor of the posterior fossa was found. This diagnosis makes a significant difference in the treatment and prognosis of these infants. Findings were missed in repeated cranial ultrasounds by experienced operators and could be clearly diagnosed using ULF imaging. Moreover, ULF imaging detected metastases in one infant that were not detected on cranial ultrasound.

2 Patient information

2.1 Case 1

A girl was born at 36 + 6 weeks of gestation (WOG) by cesarean section to a 35-year-old mother. Prenatal ultrasound performed in 32 WOG showed ventricular hydrocephalus due to assumed aqueduct stenosis.

2.2 Case 2

A boy was born at 37 + 6 WOG via cesarean section to a 36-year-old mother. Prenatal ultrasound performed at 23 WOG showed fetal hydrocephalus with mild dilatation of the third ventricle.

3 Diagnostic assessment

3.1 Ultralow-field and standard imaging

Infants underwent ULF scanning on a 0.064T (64mT) Swoop® (Hyperfine, Inc., Guilford, USA; hardware version: 1.7, software version 8.7 beta) utilizing the built-in radiofrequency interference rejection method, 29 single-channel transmit/eight-channel receiver adult head coil with additional Hyperfine Inc. Baby Nest, designed to facilitate the imaging of newborns by placing their head at the magnet isocentre. The setting during the ULF scan is shown in Figure 1.

After parental consent infants were scanned at their bedside, either just next to the mother bed at the delivery station, or at their cot in the neonatal ward. The local ethics committee approved the study to be performed at the Children's Hospital, University Hospital Bonn/Germany (Ethics Nr 167/22). Parents and infants could stay with each other during the entire scan, and parents could also touch their baby to not disturb the early time of parent-child interaction. The infants did not receive any sedation, and imaging took place during natural sleep. A pediatrician supervised the clinical care of all infants during the imaging. The sequences acquired were T1 (TI 500 ms, UNITY), T2 (axial and isotropic imaging, 2 mm linear scan), axial FLAIR, and axial DWI ($b = 0\ s/mm^2$ and $b = 900\ s/mm^2$). The scanning time was approximately 48 min. Images were reconstructed by the system using linear image reconstruction methods (including geometric distortion correction and receive coil sensitivity correction. Images were post-processed using Python (Dicom2niftie), FLIRT, and Fsllab. We acquired at least 2 T2-sequences which were then averaged using FSLlab. The only shielding utilised by the Hyperfine Swoop is radio frequency electromagnetic shielding, which is achieved by the use of a partial faraday cage. The entrance to the scanner is an opening in this cage, which the patient is placed through and the parent can reach

FIGURE 1
Setting of bedside ULF scanning. Infants were scanned on the Hyperfine Inc. Swoop system, equipped with the single channel transmit/eight channel receive adult head coil with additional Hyperfine Inc. Baby Nest which places the infant's head at the magnet isocentre. Parents could touch their infant during the ULF scan.

through to settle their child. There is no static magnetic field shielding employed, however the Gauss Guard indicates the extent of the 5 Gauss Line. Parents are screened for MRI safety using an MRI screening form before entering this zone, as are patients. ULF MRI was performed by a pediatrician. No other personnel was involved for the scan.

Standard MRI neuroimaging was performed using a 3T Philips Ingenia Elition scanner. The infants were imaged using an MR incubator and sedated by an experienced clinician. Personnel included involved: The neonatologist performing the sedation, a nurse attending a scan, another nurse helping for the transport of the infant from the neonatal ward to the radiologic department, a radiologist and a radiological technical assistant. The sequences acquired were T1, T2, SWI, DWI, and contrast-enhanced. The scanning time was ~90 min.

Cranial ultrasound was performed with a Philips AA26050 L ultrasound machine. Prenatal ultrasound was performed using a GE ultrasound machine by DEGUM III operators.

Fetal MRI was performed at a 1.5T Philips Ingenia scanner and at a 1.5T Siemens Solar scanner.

3.1.1 Case 1

Repeated fetal ultrasounds showed no further intracranial pathologies, and screening for congenital infectious diseases [cytomegalovirus (CMV), Toxoplasma gondii, and parvovirus B19] was negative. No fetal magnetic resonance imaging (MRI) was performed.

Postnatally, no additional findings were found on cranial ultrasonography. As the head circumference increased, surgery was planned on the 5th day of life. Prior to surgery, the infant underwent standard high-field 3 Tesla MR scanning, which revealed a tumor of the fossa cranii posterior (Figure 2A, arrows).

Shunt surgery was performed without taking any tissue samples, and 7 days later (on the 11th day of life), ULF imaging was performed confirming the pre-known tumor and detecting it had hemorrhaged since the time the HF-MRI was performed (Figure 2B, arrows). The mass in the tumor showed massive diffusion restriction and a cortex-isointense T2 signal (Figure 2B, arrows). In addition, the ULF scan detected new disseminated metastases supra- and infratentorially, showing a high T1 signal and diffusion restriction on DWI and a corresponding low T2

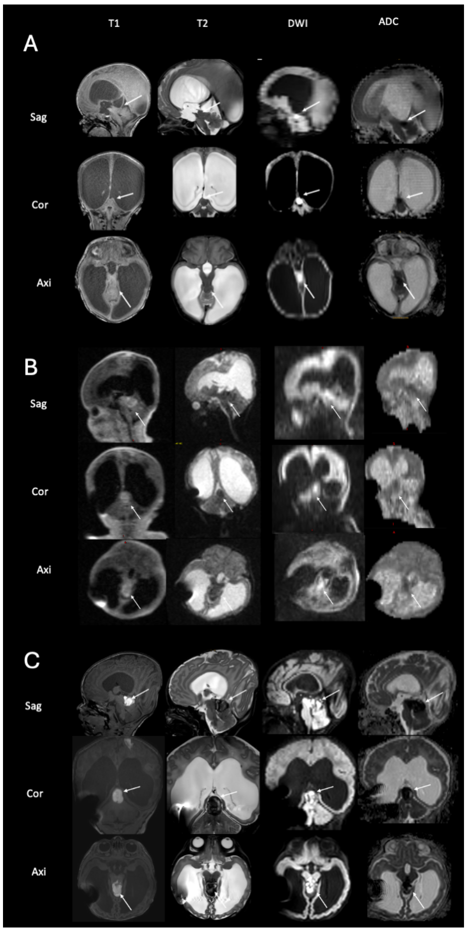

FIGURE 2
Imaging of the tumor in the fossa cranii posterior of case 1 with high-field imaging at 5th day of life (A), ultralow-field imaging at 11th day of life (B) and high-field imaging at 19th day of life (C) the scan at 5th day of life reveals a tumor of the fossa cranii posterior (arrows) with low T2 and cortexisointense T1-signalling and diffusion restriction (A) the ULF scan at 11th day of life (B) shows the tumor has hemorrhaged (visible in T1, arrows) and confirms the characteristical signalling of ATRT tumors with low T2 signal and diffusion restriction. Note the artifact by the implanted VP shunt. The high-field scan at 19th day of life (C), confirms the findings of the ULF scan (compare to B).

signal (Figures 3A,B,C, arrows). 3T MRI was performed on the 19th day of life and confirmed the findings of the ULF MRI (Figures 2C, 3C,D,F, arrows). In knowledge of the MR findings, we performed targeted cranial ultrasound by experienced operators, which also confirmed the findings of the ULF scan. Biopsy was taken at 21th day of life.

Taken together, ULF MRI showed a tumor of the fossa cranii posterior with low T2 and cortexisointense T1-signalling and diffusion restriction (Figure 2B, arrows). This is a characteristical signalling of atypical teratoid rhabdoid tumor (ATRT) with low T2 signal and diffusion restriction. Moreover, ULF MRI revealed parietal (Figure 3A, arrows), cerebellar (Figure 3B, arrows) and periventricular (Figure 3E, arrows) metastasis with a high T1 and low T2 signal and diffusion restriction.

Taken together, due to its typical radiologic features and rapid metastasis, a diagnosis of ATRT was suspected. The best supportive care was offered, and the infant went home with his parents.

3.1.2 Case 2

Repeated fetal ultrasound by DEGUM III operators showed a ruptured midline with no further intracranial pathologies, screening for CMV and Toxoplasma Gondii was negative, genomic testing including trisomy 13,18,21, and trio exome analysis from amniocentesis showed no pathologic findings. Fetal MRI was performed at 26 + 5 and 34 WOG, showing features of aqueduct stenosis.

Postnatally, no additional findings were found on cranial ultrasonography by several investigators.

The infant underwent ULF scanning on the 4th day of life, revealing a tumor of the fossa cranii posterior (1.1 × 1 × 0.8 cm) (Figure 4A, arrows). The tumor showed a high T2 signal and low T1 signal (Figure 4A, arrows). The tumor did not show any diffusion restriction (Figure 4A, arrows). These findings were confirmed by 3-T-MRI on the 5th day of life (Figure 4B, arrows) as well as by afterwards performed targeted cranial ultrasound by experienced operators in knowledge of the MR-findings. As the head circumference increased, surgery was planned on the 6th day of life.

Taken together, this tumor showed typical radiologic features of low-grade gliomas (high T2 signal, low T1 signal, no diffusion restriction as seen in Figure 4). To date, no biopsy has been performed. The infant then underwent active surveillance. A second MRI, performed in the 6th week of life, showed no progression.

4 Discussion

In this study, we present two neonates born with congenital hydrocephalus with no known additional pathologies on repeated ultrasound scans and, in one patient, two fetal MRIs. ULF scanning revealed tumors of the fossa cranii posterior as the underlying etiology for hydrocephalus and, therefore, made a huge change to therapeutic procedures as well as prognosis. Moreover, we showed that ULF can be used to detect metastasis in the neonatal brain. This is the first reported case of a neonatal tumor and metastasis detected using ULF scanning. Moreover, we showed that ULF scanning can not only detect brain tumors, but also show specific radiologic features of brain tumors (in this case shown for low-grade glioma and ATRT) and therefore has a high influence on the treatment of these children and even the decision to go for best supportive care.

The aqueductal stenosis is a common cause of congenital hydrocephalus (6). Its etiology can be due to an anatomic anomaly as well as a secondary change due to various pathologies, such as central nervous system infections (CMV, Toxoplasmosis) and subsequent adhesions, or external compression through tumors, cysts, or intracerebral hemorrhage as well as genetic reasons (5, 22, 23). Therefore, the diagnosis of fetal ventriculomegaly should be accompanied by testing for infections (CMV, Toxoplasmosis) as well as genetic testing (5, 24). Radiographic evaluation should include ultrasonography to further investigate the cause of hydrocephalus. Fetal MRI is used to provide information about the etiology of hydrocephalus and to identify additional anatomic anomalies, such as

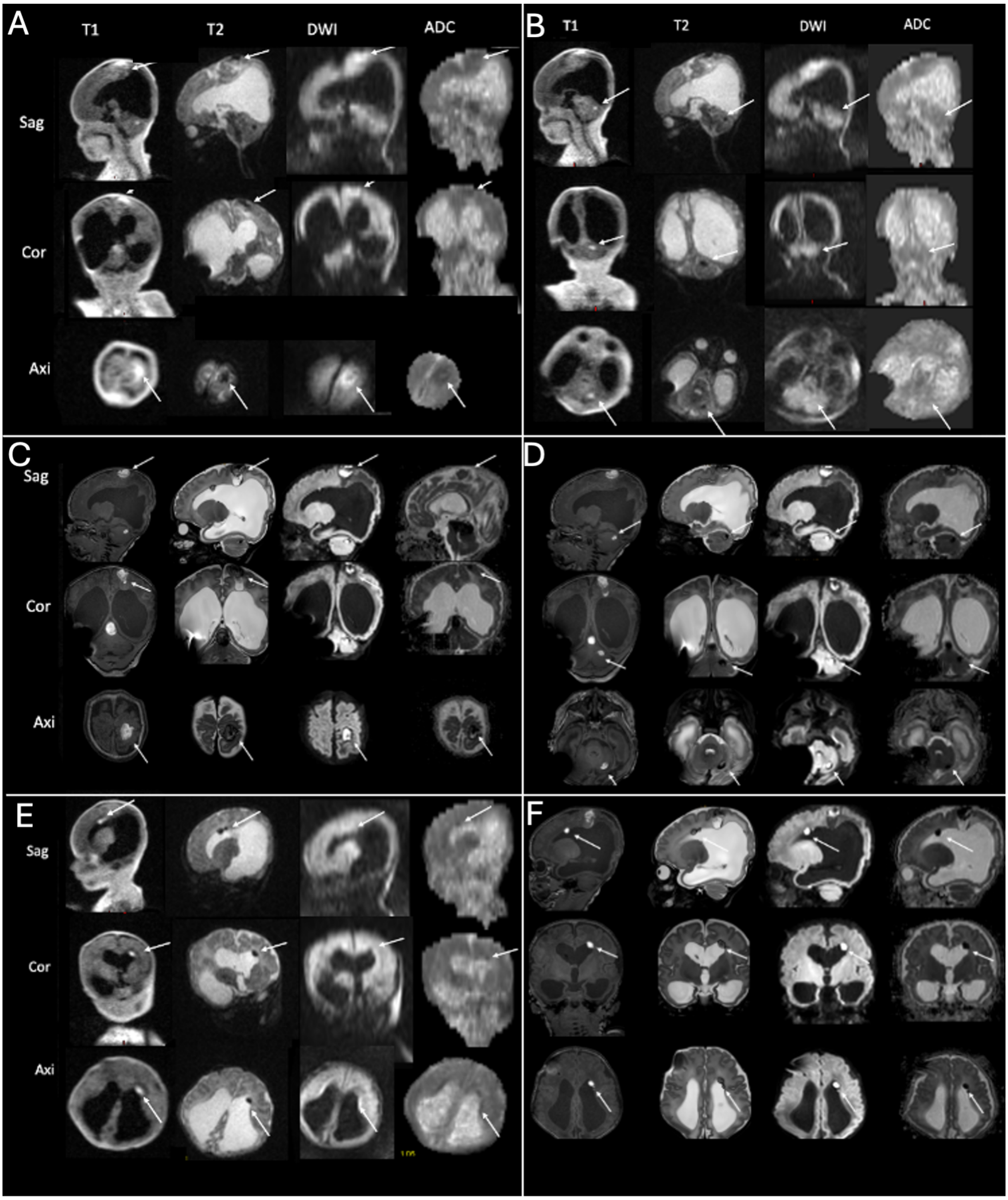

FIGURE 3
ULF (A,B,E) and high-field (C,D,F) imaging of case 1. The ULF scan at 11th day of life reveals parietal [(A) arrows], cerebellar [(B) arrows] and periventricular [(E) arrows] metastasis with a high T1 and low T2 signal and diffusion restriction. The high-field scan at 19th day of life confirms the findings of the parietal [(C) arrows], cerebellar [(D) arrows] and periventricular [(F) arrows] metastasis).

septo-orbic dysplasia and malformations of cortical development, leading to closer observation, monitoring, or further interventions (5–7, 24–26).

Postnatally, routine surveillance should include physical examination, serial head circumference measurements, and serial radiographic imaging (5). Radiographic examinations with cranial ultrasound should be performed to provide further information on the etiology and surveillance of infants (6). Postnatal MRI is required to investigate the etiology of hydrocephalus, as well as the appearance of the ventricular system, which may significantly change surgical strategies (5).

ULF portable MRI is a new technique that allows bedside imaging in both high- and low-resource settings. ULF imaging requires less

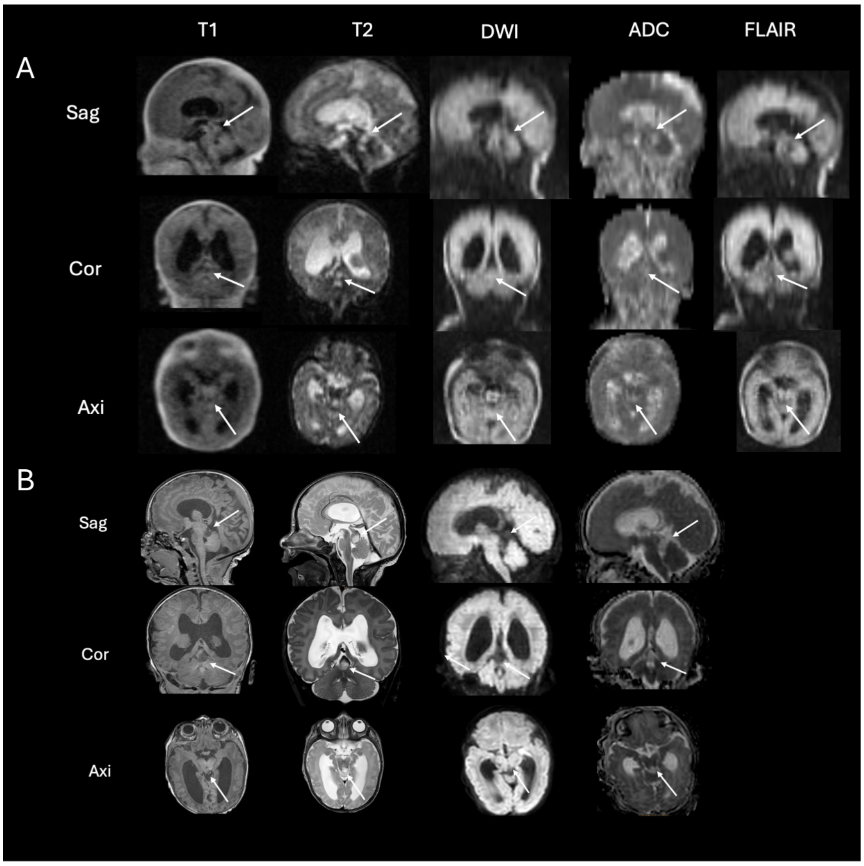

FIGURE 4
ULF (A) and high-field (B) scanning of case 2. The ULF scan at 4th day of life reveals a tumor of the fossa cranii posterior [(A) arrows] showing high T2 signal and low T1 signal without diffusion restriction. The high-field scan at 5th day of life (B) confirms the ULF finding from the previous day showing a tumor of the fossa cranii posterior (arrows) with low T1 and high T2 signal without diffusion restriction.

resources, due to its lower cost, and lower personnel and infrastructure requirements. Moreover, it reduces the risks as patients do not need to be transported or sedated for imaging (27). Thus, ULF MRI provides a new opportunity to provide MRI to infants with congenital hydrocephalus who would not receive an MRI otherwise, both in LMIC as well as in high-income countries. Moreover, ULF MRI could allow point-of-care imaging within high-resource environments. There is increasing evidence of using ULF MRI in diagnosing different diseases, so far primarly described in the adult population (11–17). For example, several studies have shown the possibility to detect and monitor strokes in adult patients (15, 28–30). There is limited evidence in children and neonates. However, it has been shown that ULF MRI can be used in ECMO patients (16), in neonates detecting hydrocephalus, hypoxia- ischemia and agenesia of the corpus callosum (15, 20) and in children detecting intracranial hemorrhage (31). In adults, detection of intracerebral tumor using ULF MRI has been described in few cases (10, 32–34); however, no detection of metastasis using ULF MRI has so far been reported in literature and this is the first description of diagnosis of metastasis and ATRT using ULF MRI.

In this study, we demonstrated that ULF MRI is safe and feasible in neonates with congenital hydrocephalus. We showed that ULF imaging can be performed without the use of sedation and without separating the parents from their children at the bedside in neonatal and delivery wards. We showed that there were no restrictions on medical care owing to ULF imaging. Moreover, in one case, we demonstrated that ULF imaging can be performed in children with a ventricular-peritoneal (VP) shunt and that shunting positions have not changed due to ULF MRI. Therefore, ULF MRI can be used as a safe diagnostic tool for infants with VP shunts.

We demonstrated that ULF scanning can detect intracerebral tumors that had not been detected on either fetal MRI or sequential pre- and postnatal cranial ultrasound. We showed that ULF MRI could detect intracerebral metastases. To the best of our knowledge, these are the first cases described in the literature with ULF scanning for the detection of neonatal tumors and metastasis. We demonstrated that ULF scanning can not only detect these findings but also show specific radiologic features of brain tumors (in this case, ATRT and low-grade glioma), and therefore lead to therapeutic decisions.

Comparing ULF imaging with conventional high-field imaging, high-field scanning has a higher resolution and shows a more detailed image of the brain. Moreover, contrast enhancement can be used on high-field MRI, which has so far not been trialed in ULF, and therefore provides more information about the tumor. Thus, there are limitations of the use of ULF MRI for the diagnosis of congenital hydrocephalus, as especially very small pathologies require higher resolution and higher image quality than ULF can so far provide. Nevertheless, even without contrast enhancement, ULF could detect metastasis and show radiologic features typical for specific brain tumors, which were then confirmed by high-field scanning.

As ULF scanning requires fewer resources and, due to its feasibility at the bedside, is less stressful to patients than high field scanning (13, 16), we suggest that all children with congenital hydrocephalus, especially those with aqueductal stenosis and no clear etiology on cranial ultrasound, should be examined with ULF. Moreover, it reduces stress to the parents, as they do not need to be separated from their child, and early parent-child interaction is not disturbed. Patients have not to move significantly, which also reduces stress to the patients as equipment and staff resources, and allows imaging in very unstable patients (15, 16). No extra monitoring is needed, which also contributes to minimizing stress and resources.

To conclude, ULF MRI widens the access of MRI to infants both in high- and low- and middle-income countries who would not otherwise receive an MRI.

We also demonstrated that the ULF characterizes intracerebral tumors and detect metastasis. As it is easy to perform and requires only low resources, it can be used as a serial imaging tool to image neonates with tumors to detect metastasis, progression, and hemorrhages. Furthermore, it is not dependent on the operator's skills and has this advance compared to cranial ultrasound, by which in these cases the findings were missed until knowledge of the tumor was aquired through ULF imaging. Moreover, as it shows specific findings for specific tumors, it helps to make a diagnosis and treatment decisions.

5 Patients perspective

Both ULF scans were attended by a pediatrician and both parents. Neither the pediatrician nor the parents noticed any signs of stress in the infants. The parents reported the ULF scan was less stressfull than the high field scan. Both families agreed that ULF scanning was a less invasive opportunity to examine their children.

6 Conclusions

Ultralow-field MRI can be instrumental in clarifying the etiology of congenital hydrocephalus, particularly in detecting tumors that may not be detected by fetal MRI and serial ultrasound, even when performed by highly skilled professionals. This is the first reported case of a neonatal tumor and metastasis detected using ULF scanning.

ULF MRI is capable of detecting intracerebral tumors, identifying specific tumor features, and thus aiding in more accurate diagnoses. It can also reveal metastasis, progression, and hemorrhage in neonatal tumors.

Additionally, compared to 3T MRI, ULF MRI was able to reveal significant findings while requiring fewer resources and being easier to perform. Therefore, we recommend that children with congenital hydrocephalus who show no abnormalities on cranial ultrasound should undergo ULF MRI. This imaging modality holds potential for monitoring neonatal tumors and detecting metastasis.

Future research and development are needed for ULF imaging, especially as imaging technologies are rapidly advancing and ULF imaging capabilities improve each year. This progress could make ULF MRI a viable screening and surveillance tool in high-income countries and extend MRI accessibility to low- and middle-income countries. Investigating contrast enhancement in ULF MRI is crucial for further characterizing intracranial tumors.

Data availability statement

The original contributions presented in the study are included in the article/Supplementary Material, further inquiries can be directed to the corresponding author.

Ethics statement

The studies involving humans were approved by University Hospital Bonn/Germany. The studies were conducted in accordance with the local legislation and institutional requirements. Written informed consent for participation in this study was provided by the participants' legal guardians/next of kin. Written informed consent was obtained from the individual(s), and minor (s)' legal guardian/next of kin, for the publication of any potentially identifiable images or data included in this article.

Author contributions

AG: Formal Analysis, Investigation, Visualization, Writing – original draft, Writing – review & editing. TD: Supervision, Validation, Writing – review & editing. MB: Resources, Writing – review & editing. AM: Funding acquisition, Resources, Writing – review & editing. HS: Conceptualization, Investigation, Project administration, Supervision, Validation, Writing – review & editing.

Funding

The author(s) declare financial support was received for the research, authorship, and/or publication of this article. This work is supported by the Bill and Melinda Gates Foundation (Ultralow field Neuroimaging In The Young: INV-005798).

Acknowledgments

We would like to thank the families of the two neonates in participating in our study. We thank all staff involved in neonatal scanning.

Conflict of interest

The authors declare that the research was conducted in the absence of any commercial or financial relationships that could be construed as a potential conflict of interest.

Publisher's note

References

1. Dewan MC, Rattani A, Mekary R, Glancz LJ, Yunusa I, Baticulon RE, et al. Global hydrocephalus epidemiology and incidence: systematic review and meta-analysis. *J Neurosurg.* (2019) 130(4):1065–79. doi: 10.3171/2017.10.JNS17439

2. Enslin JMN, Thango NS, Figaji A, Fieggen GA. Hydrocephalus in low and middle-income countries—progress and challenges. *Neurol India.* (2021) 69(Supplement):S292–7. doi: 10.4103/0028-3886.332285

3. Kheiri G, Naderian N, Karami S, Habibi Z, Nejat F. Prenatal ventriculomegaly: natural course, survival, and neurodevelopmental status. *J Neurosurg Pediatr.* (2021) 27(5):497–502. doi: 10.3171/2020.9.PEDS20612

4. Persson E-K, Anderson S, Wiklund L-M, Uvebrant P. Hydrocephalus in children born in 1999–2002: epidemiology, outcome and ophthalmological findings. *Childs Nerv Syst.* (2007) 23(10):1111–8. doi: 10.1007/s00381-007-0324-7

5. Pindrik J, Schulz L, Drapeau A. Diagnosis and surgical management of neonatal hydrocephalus. *Semin Pediatr Neurol.* (2022) 42:100969. doi: 10.1016/j.spen.2022.100969

6. McKechnie L, Vasudevan C, Levene M. Neonatal outcome of congenital ventriculomegaly. *Semin Fetal Neonatal Med.* (2012) 17(5):301–7. doi: 10.1016/j.siny.2012.06.001

7. Griffiths PD, Brackley K, Bradburn M, Connolly DJA, Gawne-Cain ML, Griffiths DI, et al. Anatomical subgroup analysis of the MERIDIAN cohort: ventriculomegaly. *Ultrasound Obstet Gynecol.* (2017) 50(6):736–44. doi: 10.1002/uog.17475

8. Griffiths PD, Reeves MJ, Morris JE, Mason G, Russell SA, Paley MNJ, et al. A prospective study of fetuses with isolated ventriculomegaly investigated by antenatal sonography and in utero MR imaging. *AJNR Am J Neuroradiol.* (2010) 31(1):106–11. doi: 10.3174/ajnr.A1767

9. Cardoen L, Catte L de, Demaerel P, Devlieger R, Lewi L, Deprest J, et al. The role of magnetic resonance imaging in the diagnostic work-up of fetal ventriculomegaly. *Facts Views Vis Obgyn.* (2011) 3(3):159–63.

10. Liu Y, Leong ATL, Zhao Y, Xiao L, Mak HKF, Tsang ACO, et al. A low-cost and shielding-free ultra-low-field brain MRI scanner. *Nat Commun.* (2021) 12(1):7238. doi: 10.1038/s41467-021-27317-1

11. OECD. *Magnetic Resonance Imaging (MRI) Units (indicator).* Paris: OECD (2024). Available online at: https://data.oecd.org/healthqt/magnetic-resonance-imaging-mri-units.htm (Cited May 23, 2024).

12. Krishnan V, Kumar V, Variane GFT, Carlo WA, Bhutta ZA, Sizonenko S, et al. Need for more evidence in the prevention and management of perinatal asphyxia and neonatal encephalopathy in low and middle-income countries: a call for action. *Semin Fetal Neonatal Med.* (2021) 26(5):101271. doi: 10.1016/j.siny.2021.101271

13. Sarracanie M, LaPierre CD, Salameh N, Waddington DEJ, Witzel T, Rosen MS. Low-cost high-performance MRI. *Sci Rep.* (2015) 5:15177. doi: 10.1038/srep15177

14. Turpin J, Unadkat P, Thomas J, Kleiner N, Khazanehdari S, Wanchoo S, et al. Portable magnetic resonance imaging for ICU patients. *Crit Care Explor.* (2020) 2(12):e0306. doi: 10.1097/CCE.0000000000000306

15. Sheth KN, Mazurek MH, Yuen MM, Cahn BA, Shah JT, Ward A, et al. Assessment of brain injury using portable, low-field magnetic resonance imaging at the bedside of critically ill patients. *JAMA Neurol.* (2021) 78(1):41–7. doi: 10.1001/jamaneurol.2020.3263

16. Sabir H, Kipfmueller F, Bagci S, Dresbach T, Grass T, Nitsch-Felsecker P, et al. Feasibility of bedside portable MRI in neonates and children during ECLS. *Crit Care.* (2023) 27(1):134. doi: 10.1186/s13054-023-04416-7

17. Padormo F, Cawley P, Dillon L, Hughes E, Almalbis J, Robinson J, et al. *In vivo* T1 mapping of neonatal brain tissue at 64 mT. *Magn Reson Med.* (2023) 89(3):1016–25. doi: 10.1002/mrm.29509

18. Sien ME, Robinson AL, Hu HH, Nitkin CR, Hall AS, Files MG, et al. Feasibility of and experience using a portable MRI scanner in the neonatal intensive care unit. *Arch Dis Child Fetal Neonatal Ed.* (2023) 108(1):45–50. doi: 10.1136/archdischild-2022-324200

19. Beekman R, Crawford A, Mazurek MH, Prabhat AM, Chavva IR, Parasuram N, et al. Bedside monitoring of hypoxic ischemic brain injury using low-field, portable brain magnetic resonance imaging after cardiac arrest. *Resuscitation.* (2022) 176:150–8. doi: 10.1016/j.resuscitation.2022.05.002

20. Cawley P, Padormo F, Cromb D, Almalbis J, Marenzana M, Teixeira R, et al. Development of neonatal-specific sequences for portable ultralow field magnetic resonance brain imaging: a prospective, single-centre, cohort study. *EClinicalMedicine.* (2023) 65:102253. doi: 10.1016/j.eclinm.2023.102253

21. Deoni SCL, Bruchhage MMK, Beauchemin J, Volpe A, D'Sa V, Huentelman M, et al. Accessible pediatric neuroimaging using a low field strength MRI scanner. *Neuroimage.* (2021) 238:118273. doi: 10.1016/j.neuroimage.2021.118273

22. Yamasaki M, Shohuda T, Sakamoto H, Nonaka M, Kanemura Y. Prenatal diagnosis of L1CAM gene mutations in X-linked hydrocephalus. *Fluids Barriers CNS.* (2006) 3(S1):S47. doi: 10.1186/1743-8454-3-S1-S47

23. Etchegaray A, Juarez-Peñalva S, Petracchi F, Igarzabal L. Prenatal genetic considerations in congenital ventriculomegaly and hydrocephalus. *Childs Nerv Syst.* (2020) 36(8):1645–60. doi: 10.1007/s00381-020-04526-5

24. Fox NS, Monteagudo A, Kuller JA, Craigo S, Norton ME. Mild fetal ventriculomegaly: diagnosis, evaluation, and management. *Am J Obstet Gynecol.* (2018) 219(1):B2–9. doi: 10.1016/j.ajog.2018.04.039

25. Pisapia JM, Sinha S, Zarnow DM, Johnson MP, Heuer GG. Fetal ventriculomegaly: diagnosis, treatment, and future directions. *Childs Nerv Syst.* (2017) 33(7):1113–23. doi: 10.1007/s00381-017-3441-y

26. Alluhaybi AA, Altuhaini K, Ahmad M. Fetal ventriculomegaly: a review of literature. *Cureus.* (2022) 14(2):e22352. doi: 10.7759/cureus.22352

27. Parveez MQ, Yaddanapudi LN, Saini V, Kajal K, Sharma A. Critical events during intra-hospital transport of critically ill patients to and from intensive care unit. *Turk J Emerg Med.* (2020) 20(3):135–41. doi: 10.4103/2452-2473.290067

28. Balaji S, Wiley N, Poorman ME, Kolind SH. Low-field MRI for use in neurological diseases. *Curr Opin Neurol.* (2024) 37(4):381–91. doi: 10.1097/WCO.0000000000001282

29. Mazurek MH, Parasuram NR, Peng TJ, Beekman R, Yadlapalli V, Sorby-Adams AJ, et al. Detection of intracerebral hemorrhage using low-field, portable magnetic resonance imaging in patients with stroke. *Stroke.* (2023) 54(11):2832–41. doi: 10.1161/STROKEAHA.123.043146

30. Yuen MM, Prabhat AM, Mazurek MH, Chavva IR, Crawford A, Cahn BA, et al. Portable, low-field magnetic resonance imaging enables highly accessible and dynamic bedside evaluation of ischemic stroke. *Sci Adv.* (2022) 8(16):eabm3952. doi: 10.1126/sciadv.abm3952

31. Abbas A, Hilal K, Rasool AA, Zahidi U-F, Shamim MS, Abbas Q. Low-field magnetic resonance imaging in a boy with intracranial bolt after severe traumatic brain injury: illustrative case. *J Neurosurg Case Lessons.* (2023) 6(1):CASE23225. doi: 10.3171/CASE23225

32. Altaf A, Baqai MWS, Urooj F, Alam MS, Aziz HF, Mubarak F, et al. Intraoperative use of ultra-low-field, portable magnetic resonance imaging—first report. *Surg Neurol Int.* (2023) 14:212. doi: 10.25259/SNI_124_2023

33. Altaf A, Baqai MWS, Urooj F, Alam MS, Aziz HF, Mubarak F, et al. Utilization of an ultra-low-field, portable magnetic resonance imaging for brain tumor assessment in lower middle-income countries. *Surg Neurol Int.* (2023) 14:260. doi: 10.25259/SNI_123_2023

34. Altaf A, Shakir M, Malik MJA, Arif A, Islam O, Mubarak F, et al. Intraoperative use of low-field magnetic resonance imaging for brain tumors: a systematic review. *Surg Neurol Int.* (2023) 14:357. doi: 10.25259/SNI_510_2023

Frontiers in Neurology

TYPE Original Research
PUBLISHED 24 April 2025
DOI 10.3389/fneur.2025.1573060

OPEN ACCESS

EDITED BY
Ye Wu,
Nanjing University of Science and Technology, China

REVIEWED BY
Jiquan Ma,
Heilongjiang University, China
Lifang Wei,
Fujian Agriculture and Forestry University, China
Jiahao Huang,
Zhejiang University of Technology, China

*CORRESPONDENCE
Jun Ma
✉ dr_ma@sina.com
Yun Peng
✉ ppengyun@hotmail.com

RECEIVED 08 February 2025
ACCEPTED 03 April 2025
PUBLISHED 24 April 2025

CITATION
Xi F, Tu L, Zhou F, Zhou Y, Ma J and Peng Y (2025) Automatic segmentation and quantitative analysis of brain CT volume in 2-year-olds using deep learning model. *Front. Neurol.* 16:1573060.
doi: 10.3389/fneur.2025.1573060

Automatic segmentation and quantitative analysis of brain CT volume in 2-year-olds using deep learning model

Fengjun Xi[1], Liyun Tu[2], Feng Zhou[2], Yanjie Zhou[2], Jun Ma[1]* and Yun Peng[3]*

[1]Department of Radiology, Beijing Tiantan Hospital, Capital Medical University, Beijing, China, [2]School of Artificial Intelligence, Beijing University of Posts and Telecommunications, Beijing, China, [3]Imaging Center, Beijing Children's Hospital, National Center for Children's Health, Capital Medical University, Beijing, China

Objective: Our research aims to develop an automated method for segmenting brain CT images in healthy 2-year-old children using the ResU-Net deep learning model. Building on this model, we aim to quantify the volumes of specific brain regions and establish a normative reference database for clinical and research applications.

Methods: In this retrospective study, we included 1,487 head CT scans of 2-year-old children showing normal radiological findings, which were divided into training (n = 1,041) and testing (n = 446) sets. We preprocessed the Brain CT images by resampling, intensity normalization, and skull stripping. Then, we trained the ResU-Net model on the training set and validated it on the testing set. In addition, we compared the performance of the ResU-Net model with different kernel sizes ($3 \times 3 \times 3$ and $1 \times 3 \times 3$ convolution kernels) against the baseline model, which was the standard 3D U-Net. The performance of the model was evaluated using the Dice similarity score. Once the segmentation model was established, we derived the regional volume parameters. We then conducted statistical analyses to evaluate differences in brain volumes by sex and hemisphere, and performed a Spearman correlation analysis to assess the relationship between brain volume and age.

Results: The ResU-Net model we proposed achieved a Dice coefficient of 0.94 for the training set and 0.96 for the testing set, demonstrating robust segmentation performance. When comparing different models, ResU-Net (3,3,3) model achieved the highest Dice coefficient of 0.96 in the testing set, followed by ResU-Net (1,3,3) model with 0.92, and the baseline 3D U-Net with 0.88. Statistical analysis showed that the brain volume of males was significantly larger than that of females in all brain regions ($p < 0.05$), and age was positively correlated with the volume of each brain region. In addition, specific structural asymmetries were observed between the right and left hemispheres.

Conclusion: This study highlights the effectiveness of deep learning for automatic brain segmentation in pediatric CT imaging, providing a reliable reference for normative brain volumes in 2-year-old children. The findings may serve as a benchmark for clinical assessment and research, complementing existing MRI-based reference data and addressing the need for accessible, population-based standards in pediatric neuroimaging.

KEYWORDS

brain volume, deep learning, segmentation, CT, children

1 Introduction

Abnormalities in brain volumetrics have been associated with congenital and acquired diseases in children, such as hydrocephalus (1), brain trauma (2), and neuropsychiatric disorders (3). Most *in vivo* studies have used magnetic resonance imaging (MRI) of healthy volunteers to measure global and regional volume loss (4–7). However, this approach encounters difficulties when applied to pediatric populations, resulting in a lack of an accepted normative database, which limits quantitative reporting (4, 5, 8).

CT is a fast, cost-effective, and widely accessible imaging modality, providing a viable alternative for pediatric patients unable to undergo MR examination, enabling the generation of a large reference database for statistical analysis (9, 10). Research indicates that CT-based visual classifications and quantitative metrics are comparable to MRI results for certain pathological features and show significant correlations with cognitive test outcomes (11–13). However, MRI is widely used for high-resolution brain volume measurements due to its strong soft tissue contrast. However, MRI remains the preferred modality for high-resolution brain volume measurements due to its superior soft tissue contrast. Previous CT volume assessments have primarily used semi-quantitative methods, which are time-intensive and require trained specialists. Recent advances in automated brain CT segmentation, particularly through deep learning, have demonstrated faster and more accurate segmentation, with results strongly correlating with those from MRI segmentation (14–16).

In this study, we focused on children aged 2 years, applying an automated segmentation algorithm to a large set of retrospectively identified head multidetector computed tomography (MDCT) scans with normal radiological findings to develop a clinical reference database for regional brain volumes. This database can serve as a quantitative benchmark for evaluating cases within similar clinical peer groups.

2 Materials and methods

2.1 Study cohort and imaging protocol

This study was a retrospective analysis of head CTs identified from the clinical PACS, with institutional review board approval and a consent waiver obtained prior to data collection.

We consecutively collected scans from a CT scanner between October 2017 and May 2022. Cases consisted of patients with nonspecific symptoms (e.g., head injury, headache, fever, vomiting) and no known systemic disease. All control cases were reviewed by two board-certified neuroradiologists and confirmed as normal, without acute or chronic abnormalities. Cases with image artifacts or a history of brain conditions-such as intracranial hemorrhage, skull fracture, or neurodevelopmental impairments-were excluded. Additionally, patients with prior or follow-up CT/MRI revealing intracranial abnormalities (e.g., cysts, hyperintense FLAIR lesions) were excluded from the analysis.

2.2 CT segmentation with ResU-Net model

In this study, we applied the ResU-Net (17) model to segment brain anatomical regions on CT images. First, this study involved 1,487 patients with multidetector computed tomography (MDCT) scans. We trained and tested the ResU-Net model on this dataset. Then, we used the trained ResU-Net model to obtain segmentation results on the CT data set. Further details on data acquisition, preprocessing, and model training and testing methodologies are provided below.

2.2.1 Data acquisition

To train the ResU-Net model, 1,487 patients were enrolled. All enrolled patients underwent multidetector computed tomography (MDCT) scans. MDCT images were used for the brain segmentation task and volume analysis task. All scans were performed using a 256-row detector CT scanner (Revolution CT, GE Healthcare) in axial scan mode. The detector coverage was adjusted based on the patient's head size, with options of 12, 14, or 16 cm. The tube voltage was set at 120 kVp, and the gantry rotation time was 0.8 s. The tube current was tailored to the children's age, ranging from 150 mA for children aged 0–2 years, 170 mA for children aged 3–6 years, 190 mA for children aged 7–12 years, and 210 mA for children aged 13 years and older. Additionally, radiologic technologists could adjust the tube current by ±10 mA based on their experience.

The scan matrix size was 512 × 512, with both slice thickness and slice spacing set to 0.625 mm. The volume CT dose index ($CTDI_{VOL}$) was approximately 16–20 mGy. The original scan data were then reconstructed into standard window images with a slice thickness of 0.625 mm and a slice spacing of 0.625 mm. Bone window images were also reconstructed using a window width of 4,000 and a window level of 700, while standard window images had a window width of 100 and a window level of 30. These images were subsequently uploaded to the PACS system.

The scans were performed in a single rotation with the patient in a fixed, supine position. The scanning range extended from the base of the skull to the top of the skull. For children unable to cooperate during the procedure, sedation was administered using oral chloral hydrate (10%, 0.4 mL/kg) before the scan.

The dataset was divided into training ($n = 1{,}041$) and test ($n = 446$) sets in a 7:3 ratio. The training set was utilized to train the ResU-Net model, while the test set was reserved for independent evaluation to assess the model's performance. This approach ensures that the model is trained on a sufficiently large sample while also enabling an unbiased assessment of its ability to generalize to new, unseen data.

2.2.2 Data preprocessing

Before training and testing the model, we applied a series of preprocessing steps to all the images, including resampling, intensity normalization, and skull stripping. First, we resampled all 3D images using linear interpolation to achieve a voxel spacing of $1 \times 1 \times 1\ mm^3$. Next, we performed intensity normalization through adaptive histogram equalization to enhance the contrast of the images. Finally, we used the Python library SimpleITK to perform skull stripping by applying threshold segmentation to remove the skull. This process eliminated the skull's occlusion of the brain tissue, allowing for clearer visualization of the brain tissue's morphology and density.

In this study, expert labeling was first established through manual labeling by a neuroradiologist with 6 years of experience, under the supervision of a pediatric neurodiagnostic specialist with over 15 years of expertise. Segmentation followed neuroanatomical atlases and previous studies (16, 18–21), with manual labeling performed on axial slices and adjusted in coronal and sagittal views. These expert labels were then used as the segmentation templates. To generate a large labeled dataset for model training, pseudo-labels were created through a template-based registration process using ANTs (Advanced Normalization Tools). The pseudo-labels were then roughly visually inspected by the experts to correct any evident segmentation errors. After correction, these pseudo-labels were treated as the ground truth labels for training the deep learning model.

The segmentation focused on 10 brain regions, including the right/left frontal lobes, parietal lobes, occipital lobes, temporal lobes, cerebellum, and brainstem. These regions were selected based on their clear anatomical boundaries and the feasibility of accurate segmentation in pediatric CT images. Due to the ongoing myelination process in children's brains, distinguishing gray and white matter is challenging. As a result, we prioritized larger brain lobes and structures that are more easily identifiable in CT scans. Manual labeling was performed on axial slices, with adjustments made in coronal and sagittal views to ensure accuracy. ITK-SNAP software (Version 3.6.0) was used for these manual annotations.

2.2.3 Model training and testing

The network architecture of the ResU-Net model used in this study is shown in Figure 1. The ResU-Net model processes 3D CT images through a combination of residual connections, U-Net skip connections, subsampling, and up-sampling operations. It uses 27 convolutional layers to achieve precise and detailed segmentation, enhancing convergence speed and computational efficiency.

We employed the ResU-Net model to segment brain structures. To enhance the robustness of the model, we selected data augmentation methods, including random flips and rotations, for the training data, while no augmentation was applied to the testing data to ensure a fair evaluation of the model's performance. Next, we built the deep learning model in PyTorch and trained it with five-fold cross-validation. Model parameters were updated using a multi-class cross-entropy loss function and the Adam optimizer, with a learning rate of 1×10^{-5}. Training was conducted over 200 epochs with a batch size of 4. Finally, the model's performance was evaluated using the Dice similarity score (22).

2.2.4 Comparison of ResU-Net configurations

In this study, we compared the performance of ResU-Net network with different kernel sizes by evaluating three configurations: ResU-Net model with a $3 \times 3 \times 3$ convolution kernel, ResU-Net model with a $1 \times 3 \times 3$ convolution kernel, and the baseline model, which was the standard 3D U-Net model. To assess segmentation accuracy, we calculated the average Dice coefficient over 10 training sessions to compare the performance of the different models. These results were analyzed to evaluate the impact of varying kernel sizes on model performance, with the baseline 3D U-Net serving as a reference for comparing the improvements or trade-offs introduced by modifying the kernel size in ResU-Net network.

2.3 Statistical analysis

All statistical analyses were performed on SPSS 26.0 software. Descriptive statistics are reported as mean ± standard deviation. We conducted one-sample t-tests and analysis of variance (ANOVA) to examine the age and sex distributions of the samples in both the training and testing sets, ensuring that no bias was introduced in the group assignments. Next, we assessed the effects of sex and age on brain structure volumes using multiple linear regression analyses. Specifically, sex was included as a categorical variable (coded as 1 for males and 2 for

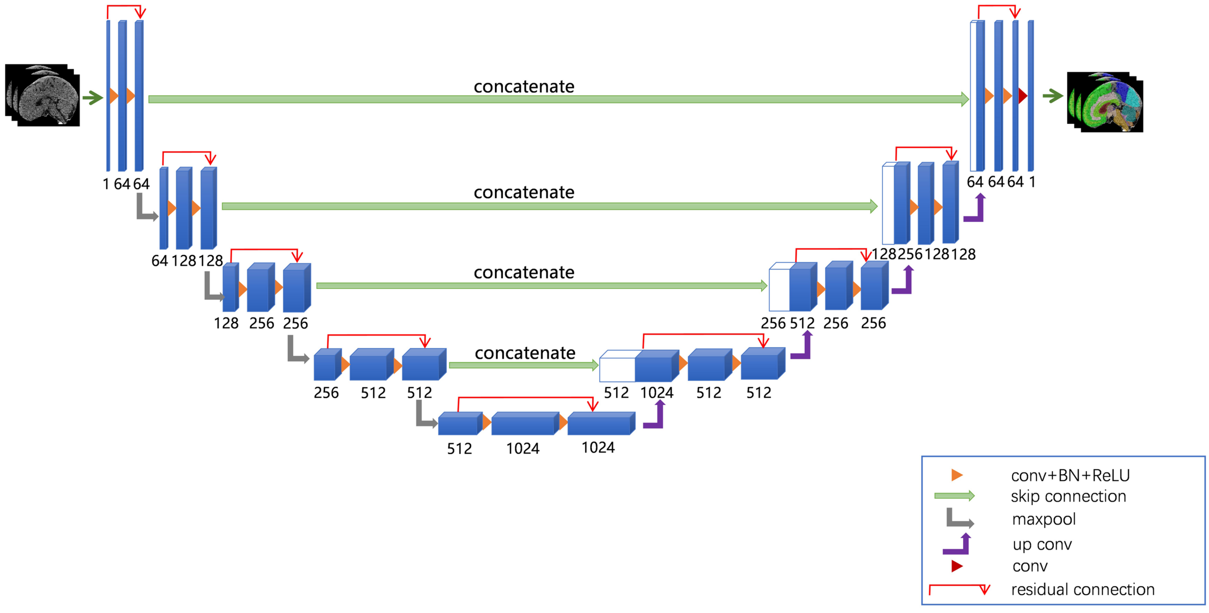

FIGURE 1
ResU-Net used in this study. The ResU-Net network processed 3D CT images through a combination of residual connections, U-Net skip connections, sub-sampling, and up-sampling operations.

females) in the regression models to isolate its impact on brain volume, while also adjusting for age. Additionally, a paired t-test was used to compare the left and right hemispheres, with the corresponding p-value calculated to evaluate the statistical significance of the difference. A p value of < 0.05 was considered statistically significant.

3 Results

3.1 Performance of ResU-Net model during training and testing

Overall, the ResU-Net model demonstrated strong performance in segmenting intracranial brain tissue, achieving an average Dice coefficient of 0.94 on the training set and 0.96 on the test set. Figure 2 presents representative segmentation results for 10 brain anatomical regions from a sample in the testing set. Figures 2a–c display axial, sagittal, and coronal sections with ground truth segmentation labels, while Figures 2d–f show the corresponding sections with ResU-Net model generated labels. Overall, our model results aligned closely with the ground truth, although some minor missed and extra labels appear at the edges in Figures 2d,e.

3.2 Comparison of model performance

In the training set, the Dice coefficients for the Baseline model, ResU-Net (1,3,3) model, and ResU-Net (3,3,3) models were 0.94, 0.93, and 0.92, respectively. These values indicate similar performance in segmentation accuracy, with the Baseline model slightly outperforming the ResU-Net configurations. The small differences in training Dice coefficients suggest that all models effectively learned to segment brain regions.

However, in the test set, the ResU-Net (1,3,3) models and ResU-Net (3,3,3) models showed substantial improvements, achieving Dice coefficients of 0.92 and 0.96, respectively, while the Baseline model dropped to 0.88. This indicates that the ResU-Net models, particularly the ResU-Net (3,3,3) model, generalize better to unseen data. This is likely due to their ability to capture more robust features and adapt to variations in test images more effectively than the Baseline model.

The decline in the Baseline model's performance from training (0.94) to testing (0.88) suggests overfitting to the training data. This reinforces the advantages of using ResU-Net network with residual connections, as these models maintained consistent performance across both training and testing, thereby reducing the risk of overfitting and improving the model's generalization ability.

3.3 Sample demographics

The cohort included 826 males and 661 females, totaling 1,487 participants. The ages of the participants ranged from 1.5 to 2.5 years, with a mean age of 1.98 ± 0.28 years. There were no statistically significant differences in age or gender distribution between the training and test sets ($p > 0.05$). Further details are provided in Table 1.

3.4 Influence of sex and age on brain volume

The average brain region volumes in healthy 2-year-old children were as follows: right frontal lobe (200.64 ± 19.15 cm^3), left frontal lobe (204.51 ± 19.61 cm^3), right parietal lobe (81.52 ± 7.91 cm^3), left parietal lobe (79.42 ± 7.65 cm^3), right occipital lobe (53.76 ± 5.21 cm^3), left occipital lobe (52.82 ± 5.33 cm^3), right temporal lobe (91.92 ± 9.07 cm^3), left temporal lobe (94.08 ± 9.27 cm^3). Additionally, the cerebellum volume was 127.97 ± 11.85 cm^3, and the brainstem volume was 15.47 ± 1.50 cm^3.

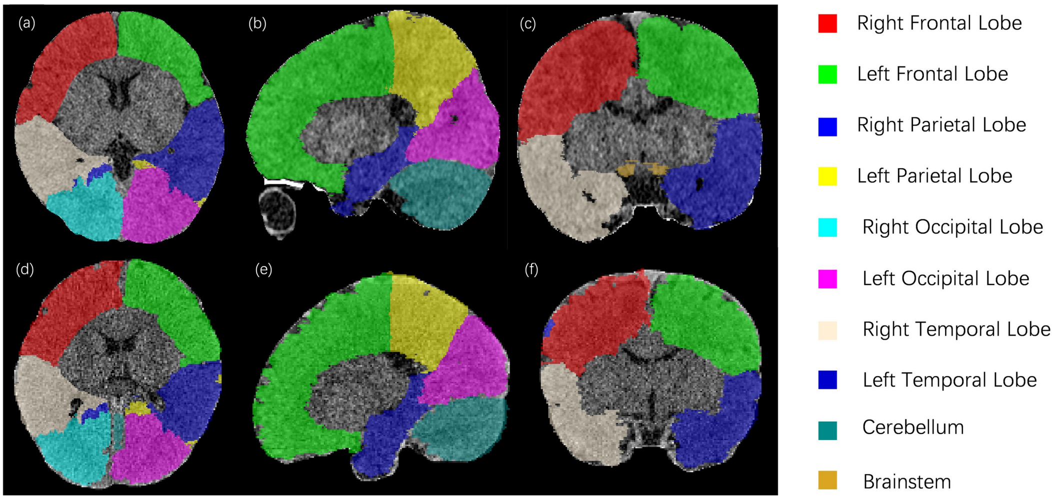

FIGURE 2
Segmentation results for a sample subject from the testing set. Panels **(a–c)** show axial, sagittal, and coronal CT sections with ground truth labels, while panels **(d–f)** display the corresponding sections with labels generated by the ResU-Net model. Ten brain regions—right and left frontal lobes, right and left parietal lobes, right and left occipital lobes, right and left temporal lobes, cerebellum, and brainstem—are color-coded and labeled on the right.

A more detailed description is provided in Table 2, which includes the distribution of brain volumes by sex.

We analyzed the effect of age and sex on brain volume using multiple regression analysis. The results in Table 3 demonstrate the effect of gender on volume. Statistical analysis showed that the brain volume of males was generally larger than that of females at the same age, and the results were statistically significant ($p < 0.001$).

The results in Table 4 present the effect of age on brain volume. Statistical results showed that age had a significant effect on each brain volume ($p < 0.001$). Brain volume increases with age in all brain regions. However, brain volumes in different regions grew at different rates because they had different regression coefficients. Figure 3 visualizes the relationship between age and brain volumes, showing how the volumes of these regions increase with age.

TABLE 1 Demographics characteristics between training and testing set.

Group	Age (years)	Sex (*n*)	
		Male	Female
Training set (n = 1,074)	1.97 ± 0.28	603	471
Testing set (n = 413)	1.98 ± 0.28	223	190
p value	0.554	0.491	

This table shows the demographic characteristics of the training and testing sets, including age and sex distribution. The age of the two groups was 1.97 ± 0.28 and 1.98 ± 0.28, respectively, and there was no significant difference in age distribution ($p = 0.554$). In addition, there was no statistically significant difference in gender distribution between the training and test groups ($p = 0.491$).

3.5 Comparison of brain volumes by hemisphere

We performed paired comparisons between the left and right sides of symmetrical structures in the brain, including frontal, parietal, occipital, and temporal lobes. The statistical results in Table 5 show that there are statistical differences in the left and right brain volumes of each lobe ($p < 0.001$), which indicates the asymmetry of the left and right sides.

4 Discussion

Childhood is a critical period for brain development, particularly in the first few years of life when the brain undergoes rapid growth and completes many developmental stages (6, 23). Brain development is

TABLE 2 Distribution of brain structure volumes (cm^3).

Brain regions	Overall	Male	Female
Right frontal lobe	200.64 ± 19.15	208.01 ± 18.51	191.43 ± 15.63
Left frontal lobe	204.51 ± 19.61	211.90 ± 18.99	195.28 ± 16.15
Right parietal lobe	81.52 ± 7.91	84.61 ± 7.51	77.66 ± 6.60
Left parietal lobe	79.42 ± 7.65	82.35 ± 7.31	75.76 ± 6.41
Right occipital lobe	53.76 ± 5.21	55.53 ± 5.02	51.55 ± 4.55
Left occipital lobe	52.82 ± 5.33	54.45 ± 5.25	50.78 ± 4.69
Right temporal lobe	91.92 ± 9.07	95.55 ± 8.66	87.40 ± 7.38
Left temporal lobe	94.08 ± 9.27	97.85 ± 8.81	89.38 ± 7.53
Cerebellum	127.97 ± 11.85	132.56 ± 11.36	122.23 ± 9.78
Brainstem	15.47 ± 1.50	16.04 ± 1.46	14.75 ± 1.21

This table shows the brain volume distribution in detail for the overall, male group, and female group. It shows the volumes (in cm^3) of different brain regions including the frontal, parietal, occipital, and temporal lobes as well as the cerebellum and brainstem.

TABLE 3 Effect of sex on brain volume.

Brain region	Sex coefficient (B)	Standard error (std. error)	t-value	*p*-value
Right frontal lobe	−15.282	0.851	−17.95	$p < 0.001$
Left frontal lobe	−15.356	0.882	−17.418	$p < 0.001$
Right parietal lobe	−6.482	0.356	−18.215	$p < 0.001$
Left parietal lobe	−6.108	0.344	−17.742	$p < 0.001$
Right occipital lobe	−3.743	0.246	−15.193	$p < 0.001$
Left occipital lobe	−3.464	0.258	−13.423	$p < 0.001$
Right temporal lobe	−7.622	0.406	−18.763	$p < 0.001$
Left temporal lobe	−7.962	0.416	−19.15	$p < 0.001$
Cerebellum	−9.766	0.544	−17.955	$p < 0.001$
Brainstem	−1.201	0.068	−17.745	$p < 0.001$

This table presents the effect of gender on brain volume in the multiple regression analysis. The results showed that the gender coefficients were all negative, indicating that the brain volume of the male group was generally larger than that of the female group in all brain regions ($p < 0.001$).

TABLE 4 **Effect of age on brain volume.**

Brain region	Age coefficient (B)	Standard error (std. error)	t-value	*p*-value
Right frontal lobe	21.179	1.488	14.236	$p < 0.001$
Left frontal lobe	20.714	1.541	13.446	$p < 0.001$
Right parietal lobe	7.691	0.622	12.37	$p < 0.001$
Left parietal lobe	7.833	0.602	13.021	$p < 0.001$
Right occipital lobe	3.884	0.43	9.021	$p < 0.001$
Left occipital lobe	3.39	0.451	7.518	$p < 0.001$
Right temporal lobe	8.642	0.71	12.174	$p < 0.001$
Left temporal lobe	8.359	0.726	11.507	$p < 0.001$
Cerebellum	9.264	0.95	9.747	$p < 0.001$
Brainstem	1.45	0.118	12.262	$p < 0.001$

This table shows the effect of gender on brain volume in the multiple regression analysis. The results showed that the coefficients of gender were all positive, indicating that there was a positive correlation between age and brain volume, that is, brain volume increased with age ($p < 0.001$). And the results show that the change rate of brain volume in different regions is not consistent because of the different coefficient values.

TABLE 5 **Comparison of left and right brain structure volumes.**

Brain regions	Sex	Right	Left	t value	Effect size	*p*-value
Frontal lobe	M	208.01 ± 8.51	211.90 ± 8.99	−30.54	1.06	<0.001
	F	191.43 ± 5.63	195.28 ± 6.15	−29.60	1.15	<0.001
Parietal lobe	M	84.61 ± 7.51	82.35 ± 7.31	26.72	0.93	<0.001
	F	77.66 ± 6.60	75.76 ± 6.41	22.39	0.87	<0.001
Occipital lobe	M	55.53 ± 5.02	54.45 ± 5.25	11.60	0.40	<0.001
	F	51.55 ± 4.55	50.78 ± 4.69	8.13	0.32	<0.001
Temporal lobe	M	95.55 ± 8.66	97.85 ± 8.81	−24.53	0.85	<0.001
	F	87.40 ± 7.38	89.38 ± 7.53	−19.34	0.75	<0.001

This table compares the brain structure volumes between the left and right hemispheres for both males and females. It includes the frontal, parietal, occipital, and temporal lobes. Statistically significant differences are observed in all regions, with the right hemisphere showing larger volumes in the frontal and parietal lobes, and the left hemisphere having larger volumes in the occipital and temporal lobes. Effect sizes are moderate to high, reflecting the magnitude of the differences.

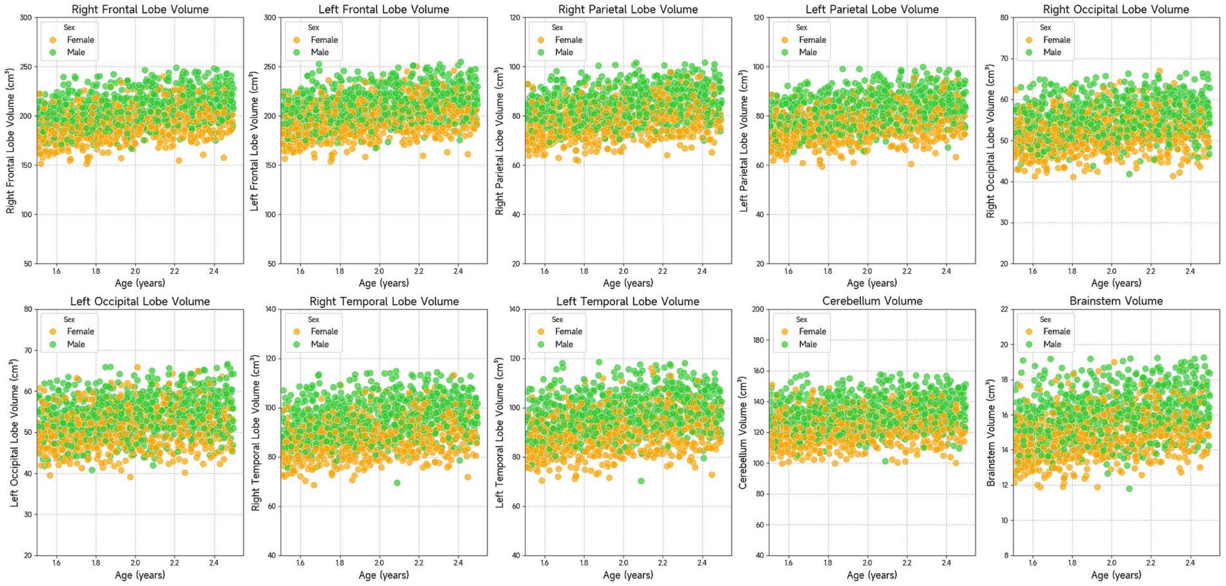

FIGURE 3
Scatter plots showing the volume of various brain regions (right frontal lobe, left frontal lobe, right parietal lobe, left parietal lobe, right occipital lobe, left occipital lobe, right temporal lobe, left temporal lobe, cerebellum, and brainstem) in relation to age. The data suggests that brain region volumes generally increase with age. Males and females are represented with green and orange dots, respectively.

influenced by various internal and environmental factors (24), and diseases during this period can significantly impact development (3, 7, 24–26). Brain volume is a key measure of brain development, obtained through non-invasive neuroimaging techniques such as high-resolution MRI, and is an important indicator of health and disease status in children. Quantitative assessments of brain volume are increasingly used in studies of neurological disorders (25, 27, 28). However, the lack of population-based reference standards for healthy brain volume complicates the clinical assessment of individual diseases (29, 30). Due to the limited availability of high-resolution MRI data in children and the small sample sizes in related studies, establishing a normative reference standard for brain volume remains challenging (4, 5, 31, 32). In addition, MRI may not be feasible in certain clinical scenarios, such as emergency situations or with patients who have medical devices that cause significant artifacts (e.g., endotracheal tubes or other hardware). These limitations can restrict the ability to obtain reliable brain volume measurements in diverse pediatric populations.

CT imaging, with its faster acquisition time and wider clinical application, offers an opportunity to accumulate large datasets, making it feasible for studies involving larger and more diverse populations. In this study, CT data were used to measure brain volumes, with the expectation that these findings will complement and extend results from MRI studies. By leveraging the strengths of CT imaging, we aim to address some of the limitations associated with MRI and provide a more comprehensive understanding of brain development and disease in children.

This study utilized the ResU-Net deep learning model for brain tissue segmentation. In recent years, deep learning has become increasingly prevalent in medical image processing, particularly in segmentation tasks, due to its speed and robustness (33–39). Previous research has shown that deep learning algorithms perform well in brain tissue segmentation, with results comparable to those from MRI (14, 16). The Dice coefficient of 0.96 obtained in this study demonstrates that the ResU-Net algorithm achieved good segmentation efficiency. Furthermore, the use of residual connections in ResU-Net model enhances feature propagation and helps mitigate the risk of overfitting, which is particularly crucial when working with complex and noisy medical imaging data. This advantage is supported by other studies, which have demonstrated that incorporating residual connections into network architectures leads to improvements in segmentation accuracy (40).

Our findings indicate that brain volume in males is generally larger than in females, which is consistent with previous studies (5, 7, 41, 42). Research suggests that male brain volume is larger than that of females across all ages (41, 43). This difference may be influenced by several factors, including gonadal hormones, neurosteroids, and epigenetic and environmental factors (44–47). These influences contribute to significant sex-based differences in brain development, which may also affect the manifestation of neuropsychiatric disorders, neurodegenerative diseases, and trauma-related conditions (44).

Brain volume development varies across regions and ages during childhood, which is essential for understanding cognitive and neurological development. The brain grows rapidly during childhood, with different regions maturing at different rates (6, 48, 49). Gray matter volume peaks around age 6 before gradually decreasing, whereas white matter continues to develop until approximately age 28. The growth trajectories of different regions are heterogeneous, with regions associated with sensory and motor control reaching developmental peaks earlier, while prefrontal regions related to higher cognitive functions develop more slowly. Although this study focused on 2-year-olds, we observed a positive correlation between brain region volume and age, confirming the rapid brain development occurring at this age.

Moreover, the study also revealed structural asymmetry in the brain: the left frontal and temporal lobes were larger than their right counterparts, while the right parietal and occipital lobes were larger than the left. Although the brain exhibits a high degree of left–right symmetry at a macroscopic anatomical and functional level, subtle structural differences exist between hemispheres (50). This asymmetry is closely linked to higher cognitive functions such as language processing, spatial cognition, facial recognition, and emotional response (51). For example, the left hemisphere is more involved in language production and comprehension, while the right hemisphere plays a key role in processing non-verbal information. Brain asymmetry is influenced by factors such as genetics, environment, and hormones (50). The study of brain lateralization is crucial for understanding brain mechanisms and identifying specific diseases. Previous studies have shown that changes in brain asymmetry are associated with neurodegenerative diseases and neuropsychiatric disorders (52, 53). These findings may provide useful biomarkers or clinical predictors of disease, offering insights into the neurobiology of these conditions.

Several factors should be considered when interpreting these results. One challenge is the reliance on a single manual segmentation template for brain CT data, particularly due to the lack of standardized templates for children. This reliance may affect the accuracy and generalizability of the findings. Therefore, future research should focus on developing multiple segmentation templates to enhance both accuracy and model robustness. Another limitation is that the data in this study were obtained from a single center and a single device, with no validation from multi-center or multi-device datasets. This could impact the model's adaptability to different scanning devices, scanning parameters, and image qualities. For instance, in real clinical settings, imaging data may be affected by noise, artifacts, or inadequate resolution. The robustness of the model in this study to such low-quality data has not been thoroughly tested, which could impact its reliability in practical applications. To address this issue, future studies will aim to expand data sources through multi-center collaborations and establish standardized data-sharing platforms to foster data exchange and promote collaborative research across various studies. Moreover, while this study focused on a "normal" population, the sample primarily consisted of trauma patients. Although efforts were made to exclude abnormal cases, minor trauma that was not identified by CT scans may have been overlooked, potentially affecting brain volume measurements. To improve detection of minor trauma, future research will develop deep learning-based detection techniques. Furthermore, collecting more detailed clinical information in subsequent studies will help to exclude such cases, ensuring that the findings are both accurate and comparable across different cohorts.

In conclusion, this study highlights the potential of deep learning for automatic brain tissue segmentation. Using existing clinical head CT data, our approach lays the groundwork for future clinical applications in diagnosis, treatment, and research.

Data availability statement

The original contributions presented in the study are included in the article, further inquiries can be directed to the corresponding authors.

Ethics statement

The studies involving humans were approved by Institutional Review Board of Beijing Children's Hospital. The studies were conducted in accordance with the local legislation and institutional requirements. Written informed consent for participation was not required from the participants or the participants' legal guardians/next of kin in accordance with the national legislation and institutional requirements.

Author contributions

FX: Data curation, Writing – original draft, Formal analysis, Methodology, Visualization. LT: Writing – review & editing, Methodology, Software, Supervision. FZ: Writing – original draft, Methodology, Software, Visualization. YZ: Writing – original draft, Methodology, Software, Visualization. JM: Writing – review & editing, Investigation, Supervision. YP: Writing – review & editing, Conceptualization, Funding acquisition, Investigation, Supervision.

Funding

The author(s) declare that financial support was received for the research and/or publication of this article. This work was supported by the National Natural Science Foundation of China (Grant No. 12171330), the STI 2030—Major Projects (Grant No. 2021ZD0200508), and Beijing Hospitals Authority's Ascent Plan (Grant No.DFL20221002). The funders had no role in the study design, data collection and analysis, decision to publish, or preparation of the manuscript.

Acknowledgments

The authors would like to express their sincere gratitude to all participants who took part in this study.

Conflict of interest

The authors declare that the research was conducted in the absence of any commercial or financial relationships that could be construed as a potential conflict of interest.

Generative AI statement

The authors declare that no Gen AI was used in the creation of this manuscript.

Publisher's note

References

1. Goo HW. Hydrocephalus: ventricular volume quantification using three-dimensional brain CT data and semiautomatic three-dimensional threshold-based segmentation approach. *Korean J Radiol*. (2021) 22:435–41. doi: 10.3348/kjr.2020.0671

2. Bigler ED, Volumetric MRI. Findings in mild traumatic brain injury (mTBI) and neuropsychological outcome. *Neuropsychol Rev*. (2023) 33:5–41. doi: 10.1007/s11065-020-09474-0

3. Boedhoe PSW, van Rooij D, Hoogman M, Twisk JWR, Schmaal L, Abe Y, et al. Subcortical brain volume, regional cortical thickness, and cortical surface area across disorders: findings from the ENIGMA ADHD, ASD, and OCD working groups. *AJP*. (2020) 177:834–43. doi: 10.1176/appi.ajp.2020.19030331

4. Schabdach JM, Schmitt JE, Sotardi S, Vossough A, Andronikou S, Roberts TP, et al. Brain growth charts for quantitative analysis of pediatric clinical brain MRI scans with limited imaging pathology. *Radiology*. (2023) 309:e230096. doi: 10.1148/radiol.230096

5. Zhang H, Li J, Su X, Hu Y, Liu T, Ni S, et al. Growth charts of brain morphometry for preschool children. *Neuroimage*. (2022) 255:119178. doi: 10.1016/j.neuroimage.2022.119178

6. Bethlehem RA I, Seidlitz J, White SR, Vogel JW, Anderson KM, Adamson C, et al. Brain charts for the human lifespan. *Nature*. (2022) 604:525–33. doi: 10.1038/s41586-022-04554-y

7. Alex AM, Aguate F, Botteron K, Buss C, Chong Y-S, Dager SR, et al. A global multicohort study to map subcortical brain development and cognition in infancy and early childhood. *Nat Neurosci*. (2024) 27:176–86. doi: 10.1038/s41593-023-01501-6

8. Raschle N, Zuk J, Ortiz-Mantilla S, Sliva DD, Franceschi A, Grant PE, et al. Pediatric neuroimaging in early childhood and infancy: challenges and practical guidelines. *Ann N Y Acad Sci*. (2012) 1252:43–50. doi: 10.1111/j.1749-6632.2012.06457.x

9. Cauley KA, Hu Y, Och J, Yorks PJ, Fielden SW. Modeling early postnatal brain growth and development with CT: changes in the brain Radiodensity histogram from birth to 2 years. *AJNR Am J Neuroradiol*. (2018) 39:775–81. doi: 10.3174/ajnr.A5559

10. Marin JR, Rodean J, Hall M, Alpern ER, Aronson PL, Chaudhari PP, et al. Trends in use of advanced imaging in pediatric emergency departments, 2009-2018. *JAMA Pediatr*. (2020) 174:e202209. doi: 10.1001/jamapediatrics.2020.2209

11. Adduru V, Baum SA, Zhang C, Helguera M, Zand R, Lichtenstein M, et al. A method to estimate brain volume from head CT images and application to detect brain atrophy in Alzheimer disease. *AJNR Am J Neuroradiol*. (2020) 41:224–30. doi: 10.3174/ajnr.A6402

12. Jaroenngarmsamer T, Benali F, Fladt J, Singh N, Bala F, Tymianski M, et al. Cortical and subcortical brain atrophy assessment using simple measures on NCCT compared with MRI in acute stroke. *AJNR Am J Neuroradiol*. (2023) 44:1144–9. doi: 10.3174/ajnr.A7981

13. Srikrishna M, Ashton NJ, Moscoso A, Pereira JB, Heckemann RA, van Westen D, et al. CT-based volumetric measures obtained through deep learning: association with biomarkers of neurodegeneration. *Alzheimers Dement*. (2024) 20:629–40. doi: 10.1002/alz.13445

14. Srikrishna M, Pereira JB, Heckemann RA, Volpe G, van Westen D, Zettergren A, et al. Deep learning from MRI-derived labels enables automatic brain tissue classification on human brain CT. *NeuroImage*. (2021) 244:118606. doi: 10.1016/j.neuroimage.2021.118606

15. Cai JC, Akkus Z, Philbrick KA, Boonrod A, Hoodeshenas S, Weston AD, et al. Fully automated segmentation of head CT neuroanatomy using deep learning. *Radiology*. (2020) 2:e190183. doi: 10.1148/ryai.2020190183

16. Wang T, Xing H, Li Y, Wang S, Liu L, Li F, et al. Deep learning-based automated segmentation of eight brain anatomical regions using head CT images in PET/CT. *BMC Med Imaging*. (2022) 22:99. doi: 10.1186/s12880-022-00807-4

17. IEEE Xplore. Deep Residual Learning for Image Recognition. (2016) IEEE Conference Publication|. Available online at: https://ieeexplore.ieee.org/document/7780459 (Accessed November 13, 2024).

18. Oishi K, Mori S, Donohue PK, Ernst T, Anderson L, Buchthal S, et al. Multi-contrast human neonatal brain atlas: application to Normal neonate development analysis. *NeuroImage*. (2011) 56:8–20. doi: 10.1016/j.neuroimage.2011.01.051

19. Lancaster JL, Woldorff MG, Parsons LM, Liotti M, Freitas CS, Rainey L, et al. Automated Talairach atlas labels for functional brain mapping. *Hum Brain Mapp*. (2000) 10:120–31. doi: 10.1002/1097-0193(200007)10:3<120::AID-HBM30>3.0.CO;2-8

20. NITRC. WFU_PickAtlas: Tool/Resource Info. (2015) Available online at: https://www.nitrc.org/projects/wfu_pickatlas/ (Accessed September 18, 2024).

21. Lin C-M, Tseng Y-C, Hsu H-L, Chen C-J, Chen DY-T, Yan F-X, et al. Arterial spin labeling perfusion study in the patients with subacute mild traumatic brain injury. *PLoS One*. (2016) 11:e0149109. doi: 10.1371/journal.pone.0149109

22. Jaskiewicz L, Filipowicz W. Role of dicer in posttranscriptional RNA silencing. *Curr Top Microbiol Immunol*. (2008) 320:77–97. doi: 10.1007/978-3-540-75157-1_4

23. Gilmore JH, Knickmeyer RC, Gao W. Imaging structural and functional brain development in early childhood. *Nat Rev Neurosci*. (2018) 19:123–37. doi: 10.1038/nrn.2018.1

24. Anderson V, Spencer-Smith M, Wood A. Do children really recover better? Neurobehavioural plasticity after early brain insult. *Brain*. (2011) 134:2197–221. doi: 10.1093/brain/awr103

25. Bourke NJ, Demarchi C, De Simoni S, Samra R, Patel MC, Kuczynski A, et al. Brain volume abnormalities and clinical outcomes following paediatric traumatic brain injury. *Brain*. (2022) 145:2920–34. doi: 10.1093/brain/awac130

26. Galler JR, Bringas-Vega ML, Tang Q, Rabinowitz AG, Musa KI, Chai WJ, et al. Neurodevelopmental effects of childhood malnutrition: a neuroimaging perspective. *Neuroimage*. (2021) 231:117828. doi: 10.1016/j.neuroimage.2021.117828

27. Giorgio A, De Stefano N. Clinical use of brain volumetry. *Magn Reson Imaging*. (2013) 37:1–14. doi: 10.1002/jmri.23671

28. Castellanos FX, Lee PP, Sharp W, Jeffries NO, Greenstein DK, Clasen LS, et al. Developmental trajectories of brain volume abnormalities in children and adolescents with attention-deficit/hyperactivity disorder. *JAMA*. (2002) 288:1740–8. doi: 10.1001/jama.288.14.1740

29. Marquand AF, Rezek I, Buitelaar J, Beckmann CF. Understanding heterogeneity in clinical cohorts using normative models: beyond case-control studies. *Biol Psychiatry*. (2016) 80:552–61. doi: 10.1016/j.biopsych.2015.12.023

30. Marquand AF, Kia SM, Zabihi M, Wolfers T, Buitelaar JK, Beckmann CF. Conceptualizing mental disorders as deviations from normative functioning. *Mol Psychiatry*. (2019) 24:1415–24. doi: 10.1038/s41380-019-0441-1

31. Howell BR, Styner MA, Gao W, Yap P-T, Wang L, Baluyot K, et al. The UNC/UMN baby connectome project (BCP): an overview of the study design and protocol development. *Neuroimage*. (2019) 185:891–905. doi: 10.1016/j.neuroimage.2018.03.049

32. Almli CR, Rivkin MJ, McKinstry RC. The NIH MRI study of normal brain development (Objective-2): newborns, infants, toddlers, and preschoolers. *Neuroimage*. (2007) 35:308–25. doi: 10.1016/j.neuroimage.2006.08.058

33. Chen X, Wang X, Zhang K, Fung K-M, Thai TC, Moore K, et al. Recent advances and clinical applications of deep learning in medical image analysis. *Med Image Anal*. (2022) 79:102444. doi: 10.1016/j.media.2022.102444

34. Wang L, Wang H, Huang Y, Yan B, Chang Z, Liu Z, et al. Trends in the application of deep learning networks in medical image analysis: evolution between 2012 and 2020. *Eur J Radiol*. (2022) 146:110069. doi: 10.1016/j.ejrad.2021.110069

35. Billot B, Magdamo C, Cheng Y, Arnold SE, Das S, Iglesias JE. Robust machine learning segmentation for large-scale analysis of heterogeneous clinical brain MRI datasets. *Proc Natl Acad Sci USA*. (2023) 120:e2216399120. doi: 10.1073/pnas.2216399120

36. Zhang Z, Keles E, Durak G, Taktak Y, Susladkar O, Gorade V, et al. Large-scale multi-center CT and MRI segmentation of pancreas with deep learning. *Med Image Anal*. (2025) 99:103382. doi: 10.1016/j.media.2024.103382

37. Sherifa CA, Kanisha B. A review on medical image segmentation using deep learning In: SM Basha, H Taherdoost and C Zanchettin, editors. Innovations in cybersecurity and data science. Singapore: Springer Nature (2024). 65–77.

38. Yoo H, Moon HE, Kim S, Kim DH, Choi YH, Cheon J-E, et al. Evaluation of image quality and scan time efficiency in accelerated 3D T1-weighted pediatric brain MRI using deep learning-based reconstruction. *Korean J Radiol*. (2025) 26:180–92. doi: 10.3348/kjr.2024.0701

39. Mahootiha M, Tak D, Ye Z, Zapaishchykova A, Likitlersuang J, Climent Pardo JC, et al. Multimodal deep learning improves recurrence risk prediction in pediatric low-grade gliomas. *Neuro Oncol*. (2025) 27:277–90. doi: 10.1093/neuonc/noae173

40. Yu L, Chen H, Dou Q, Qin J, Heng P-A. Automated melanoma recognition in Dermoscopy images via very deep residual networks. *IEEE Trans Med Imaging*. (2017) 36:994–1004. doi: 10.1109/TMI.2016.2642839

41. Kaczkurkin AN, Raznahan A, Satterthwaite TD. Sex differences in the developing brain: insights from multimodal neuroimaging. *Neuropsychopharmacology*. (2019) 44:71–85. doi: 10.1038/s41386-018-0111-z

42. Namburete AIL, Papież BW, Fernandes M, Wyburd MK, Hesse LS, Moser FA, et al. Normative spatiotemporal fetal brain maturation with satisfactory development at 2 years. *Nature*. (2023) 623:106–14. doi: 10.1038/s41586-023-06630-3

43. Kelly CE, Thompson DK, Adamson CL, Ball G, Dhollander T, Beare R, et al. Cortical growth from infancy to adolescence in preterm and term-born children. *Brain*. (2023) 147:1526–38. doi: 10.1093/brain/awad348

44. Panzica G, Melcangi RC. Structural and molecular brain sexual differences: a tool to understand sex differences in health and disease. *Neurosci Biobehav Rev*. (2016) 67:2–8. doi: 10.1016/j.neubiorev.2016.04.017

45. McCarthy MM, Arnold AP. Reframing sexual differentiation of the brain. *Nat Neurosci*. (2011) 14:677–83. doi: 10.1038/nn.2834

46. Jiang Z, Sullivan PF, Li T, Zhao B, Wang X, Luo T, et al. The X chromosome's influences on the human brain. *Sci Adv*. (2025) 11:eadq5360. doi: 10.1126/sciadv.adq5360

47. Mauvais-Jarvis F, Bairey Merz N, Barnes PJ, Brinton RD, Carrero J-J, DeMeo DL, et al. Sex and gender: modifiers of health, disease, and medicine. *Lancet*. (2020) 396:565–82. doi: 10.1016/S0140-6736(20)31561-0

48. Frangou S, Modabbernia A, Williams SCR, Papachristou E, Doucet GE, Agartz I, et al. Cortical thickness across the lifespan: data from 17, 075 healthy individuals aged 3–90 years. *Hum Brain Mapp*. (2022) 43:431–51. doi: 10.1002/hbm.25364

49. Dima D, Modabbernia A, Papachristou E, Doucet GE, Agartz I, Aghajani M, et al. Subcortical volumes across the lifespan: data from 18, 605 healthy individuals aged 3–90 years. *Hum Brain Mapp*. (2022) 43:452–69. doi: 10.1002/hbm.25320

50. Duboc V, Dufourcq P, Blader P, Roussigné M. Asymmetry of the brain: development and implications. *Annu Rev Genet*. (2015) 49:647–72. doi: 10.1146/annurev-genet-112414-055322

51. Wu X, Kong X, Vatansever D, Liu Z, Zhang K, Sahakian BJ, et al. Dynamic changes in brain lateralization correlate with human cognitive performance. *PLoS Biol*. (2022) 20:e3001560. doi: 10.1371/journal.pbio.3001560

52. Kong X, Postema MC, Guadalupe T, de Kovel C, Boedhoe PSW, Hoogman M, et al. Mapping brain asymmetry in health and disease through the ENIGMA consortium. *Hum Brain Mapp*. (2020) 43:167–81. doi: 10.1002/hbm.25033

53. Lubben N, Ensink E, Coetzee GA, Labrie V. The enigma and implications of brain hemispheric asymmetry in neurodegenerative diseases. *Brain Commun*. (2021) 3:fcab211. doi: 10.1093/braincomms/fcab211

Frontiers in
Pediatrics

Addresses ongoing challenges in child health and patient care

Explores research that meets ongoing challenges in pediatric patient care and child health, from neonatal screening to adolescent development.

Discover the latest Research Topics

See more →

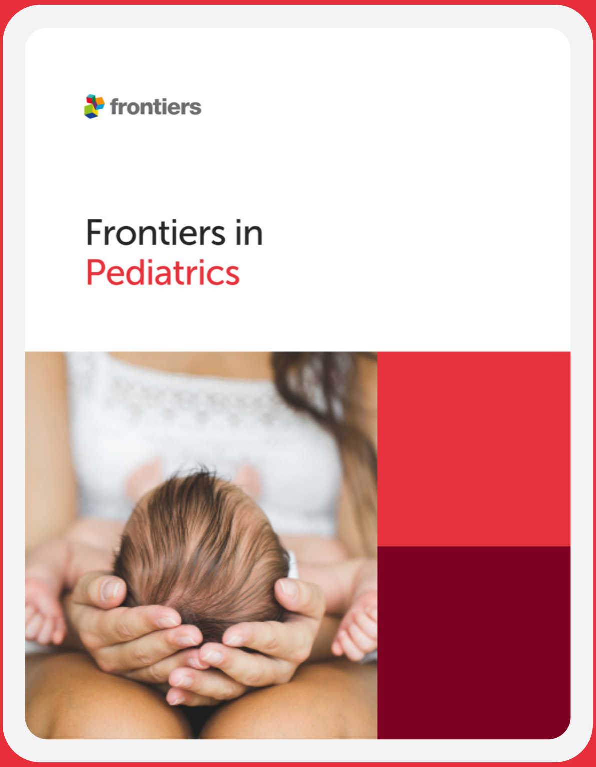
frontiers

Frontiers in
Pediatrics

Frontiers

Avenue du Tribunal-Fédéral 34
1005 Lausanne, Switzerland
frontiersin.org

Contact us

+41 (0)21 510 17 00
frontiersin.org/about/contact